UNIVERSITÀ DEGLI STUDI DELL' INSUBRIA

DIPARTIMENTO DI SCIENZA E ALTA TECNOLOGIA
Dottorato di Ricerca in Fisica e Astrofisica

PHD THESIS

Colour gradients in cluster ellipticals at z $\sim$ 1.4: the hidden content of the galaxy central regions

Candidate:
Federica Ciocca

Supervisors:
Dr. Paolo Saracco
Prof. Francesco Haardt

XXIX Cycle

Siamo tutti polvere di stelle

(André Brahic)

CONTENTS

CHAPTER

1

INTRODUCTION

The principal aim of this PhD thesis is the investigation of the formation and evolution of the elliptical galaxies. As I will discuss in Section 1, these galaxies are considered a crucial population in the observational cosmology, since they contain most of the present-day stars and baryons. Therefore, understanding their build-up and growth is very important to trace the assembly of the baryonic mass of galaxies in the Universe. Moreover, early-type galaxies (i.e. ellipticals and spheroidal galaxies) in the local Universe form an almost homogeneous family of systems mainly characterized by negligible star formation, relatively old stellar populations, red colours and tight correlations among observed quantities such as luminosity, colour, size, and velocity dispersion. However, despite their apparent simplicity, the physical processes involved in the formation and evolution of early-type galaxies are still unclear.

In this thesis, I studied a sample of 17 elliptical galaxies morphologically selected in the cluster XMMU J2235.3-2557 at z=1.39, when the Universe was $\sim$ 4.5 Gyr old, just 30% of the current age. Early-type galaxies at high redshift (hereafter with "high redshift" I mean $z > 1$) represent the best-suited benchmark to investigate and constrain the mechanisms driving their mass assembly due to the shorter time elapsed from their formation. Furthermore, studying galaxies at this redshift allows us to cut out 70% of the evolution the galaxies have undergone since their formation. Finally, since the ellipticals I have studied belong to a cluster, they are all in the same environment and at the same redshift. This allows us to remove from the analysis any uncertainty related to different environments or to different redshift singling out their intrinsic properties.

In order to investigate the mechanisms of mass accretion inside the elliptical galaxies I studied their colour gradients, that is the radial variation of the ratio of the fluxes at different wavelengths of their stellar populations. Indeed, the presence of a colour

gradient implies that one or more properties of the stellar population (mainly age and metallicity) are varying radially, allowing to put constraints for the mechanisms by which elliptical galaxies can have accreted their stellar mass.

1.1 The importance of the elliptical galaxies in understanding the galaxy formation

Early-type galaxies represent a fundamental class of galaxies to understand the galaxy formation and evolution. Indeed, even if early-type galaxies represent ∼20% of the galaxies in the local Universe (Baldry et al. 2004), they locked up at least 70% of the stellar mass (Fukugita, Hogan, and Peebles 1998; Hogg et al. 2002) (see fig. 1.1). Thus, understanding their build-up and growth is fundamental to trace the galaxy mass assembly in the Universe. A direct approach to test the models of galaxy formation and evolution is to follow the evolution of the stellar populations of the galaxies with redshift. The main difficulty is the lower quality of the data with increasing redshift.

In the local Universe (z ∼ 0), elliptical galaxies constitute a rather homogeneous class in term of morphology, colours and stellar populations, presenting red colours and cold and old (evolved) stellar populations (Renzini 2006), which present the peak of their emission towards red wavelengths. Generally their spectra show no emission lines, since the most of star formation is already quenched.

Furthermore, the kinematic and photometric properties of elliptical galaxies are correlated. Elliptical galaxies are not randomly distributed within the 3D space defined by the effective radius (R_e), the velocity dispersion (σ) and the effective surface brightness (I_e), but rather cluster close to a plane, known as the fundamental plane (FP), with $R_e \propto \sigma^a I_e^b$ (Dressler et al. 1987; Djorgovski and Davis 1987), where the exponents a and b depend on the specific band used for measuring the luminosity. For example, Jørgensen et al. (1996) obtained $a = 1.24 \pm 0.07$, $b = -0.82 \pm 0.02$ in the optical, while Pahre et al. (1998) obtained a = 1.53 ± 0.08, b = -0.79 ± 0.03 in the near-infrared. The projection of the FP over the (R_e,I_e) coordinate plane generates the Kormendy relation (Kormendy 1977), whereas a projection over the (σ,$L = 2\pi R_e^2 I_e$) plane generates the Faber-Jackson relation (Faber and Jackson 1976).

Of special interest is the comparison of the FP in cluster and in the field ellipticals, because all formation processes are expected to be faster in high-density peaks of the matter distribution. This was tested by Berardi et al. (2003; 2006) with a sample of ∼40,000 SDSS morphology- and colour-selected early-type galaxies, spanning a wide range of environmental conditions, from dense cluster cores to very low densities. The authors found that the average surface brightness is ∼0.08 mag brighter at the lowest density extreme compared to the opposite extreme, which implies an age difference of ∼1 Gyr, and therefore that galaxies in low-density environments are ∼1 Gyr younger compared to those in cluster cores.

Elliptical galaxies follow also a tight colour-magnitude (C-M) relation, which is first recognized by Baum (1959). Later, Visvanathan & Sandage (1977) and Sandage & Visvanathan (1978) established the universality of this relation, studying 9 local cluster

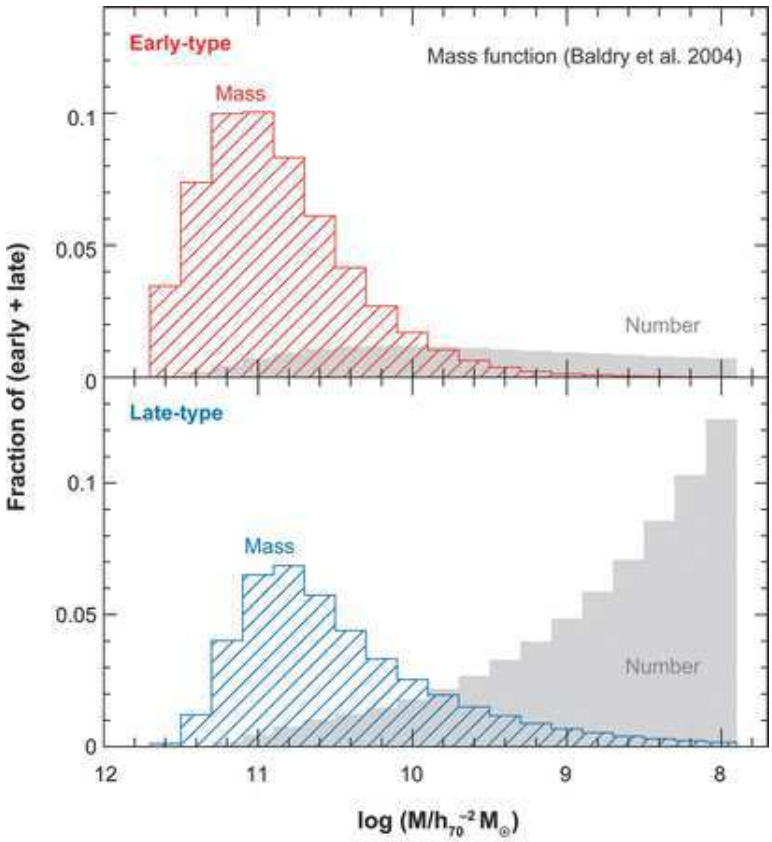

Figure 1.1: The contributions to the total stellar mass and to the number of galaxies by early-type galaxies (red) and late-type galaxies (blue) in various mass bins. The relative areas are proportional to the contributions of the early- and late-type galaxies to the total stellar mass and to the number of galaxies (Renzini 2006).

of galaxies and other groups. They also found the same correlation between all the analysed systems and estimated that both S0s and ellipticals had to be evolving passively since at least ~ 1 Gyr ago. Subsequently, Bower et al. (1992), studying the slope of the C-M of early-type galaxies in the Coma and Virgo clusters, provided constraints for the first time on the age of the stars in these galaxies, concluding that the bulk of the stellar component must have formed at $z \gtrsim 2$. Moreover, it was noticed that early-type galaxies and late-type occupy different positions in the C-M diagram, defining a "red sequence" and a "blue-cloud", respectively (see e.g., Bell et al. 2004; Gavazzi et al. 2010).

Finally, optical spectra of early-type galaxies present a number of absorption features whose strength depends on stellar ages, metallicities, and abundance ratios of their stellar populations. Historically, a correlation between the mass and metallicity of galaxies has been known from the 1970s. The fact that the most massive galaxies were the most metal-rich was interpreted by Larson et al. (1974) as a result of a more protracted star formation process than in the less massive galaxies. Indeed, outflows are expected to be

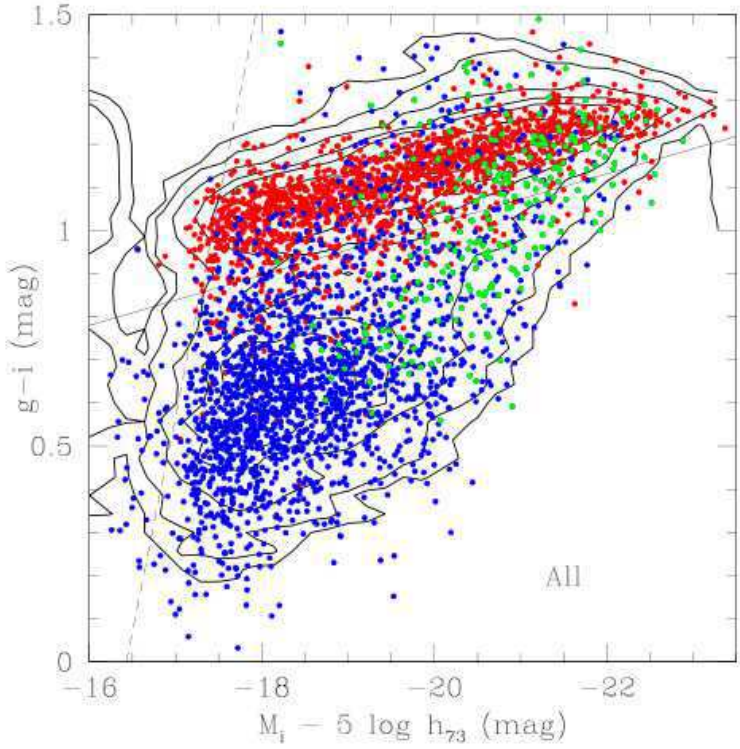

Figure 1.2: g - i color versus i-band absolute magnitude relation of all galaxies in the Coma Supercluster (CS) coded according to Hubble type: red = early-type galaxies (dE-E-S0-S0a); blue = disk galaxies (Sbc-Im-BCD); green = bulge galaxies (Sa-Sb) (Gavazzi et al. 2010).

more important in low mass galaxies, where the gravitational potential is lower and a smaller fraction of gas is retained. This could explain why the higher is the mass of the galaxies the larger is the chemical enrichment and the redder are the colours.

The situation at high redshift ($1 < z < 3$) is still far to be clear. The information available at these redshift is much more fragmentary than at $z < 1$, mostly due to the difficulty to identify large samples of early-type galaxies since they become rapidly very faint and the most prominent spectral features are redshifted to the near-infrared, where spectroscopy is difficult with the current telescopes.

The early-type galaxies spectroscopically identified so far up to $z \sim 2.5$ are composed by stellar populations formed in a strong and short burst of star formation happened at $z > 3$ (Cimatti et al. 2004) and are characterized by red colours (R-K > 5-6), passively evolving old stellar populations with ages of 1-4 Gyr, very low dust extinction and typical

masses of M > 10^{11} $M_{\odot}$ (Cimatti 2009).

With the identification of clusters at higher and higher redshifts, from the mid-1990s it has been possible to extend the studies of the relations described above also at intermediate and high redshift early-type galaxies. Pioneering studies showed a clearly recognizable red sequence in high-redshift clusters, and gave hints that the colour evolution up to z $\sim$ 1 was broadly consistent with pure passive evolution of the galaxies formed at high redshift (Dressler and Gunn 1990; Rakos and Schombert 1995). Subsequent studies provided new constraints and estimates on the formation redshift of the bulk of stars in cluster ellipticals. For instance, replicating the Bower et al. (1992) procedure for a sample of morphologically-selected early-type galaxies in clusters at z $\sim$ 0.5, Ellis et al. (1997) were able to conclude that most of the star formation in ellipticals in dense clusters was completed at z $\gtrsim$ 3. Extending these studies to clusters up to z $\sim$ 0.9, Stanford et al. (1998) showed that pure passive evolution continues all the way to such higher redshift, while the dispersion of the C-M relation remains as small as it is in Virgo and Coma. Thus, Stanford and colleagues concluded that cluster ellipticals formed the bulk of their stars at z > 3, with the small colour dispersion arguing for highly synchronized star-formation histories among galaxies within each cluster, and from one cluster to another.

As it concerns the scales relations, constructing the FP of high redshift cluster (and field) galaxies requires moderately high-resolution spectroscopy to measure the velocity dispersion σ, besides the high spatial resolution. All the quoted FP studies of high-z clusters conclude that the FP actually shifts nearly parallel to itself by an amount that increases with redshift and is consistent with the passive evolution of stellar populations that formed at high redshifts (see e.g. Holden et al. 2005b; Saracco et al. 2014). No field/cluster difference has clearly emerged at z = 0.3 (Treu et al. 1999), z $\sim$ 0.4 (Treu et al. 2001), z = 0.55 (van Dokkum et al. 2001). However, already at these modest redshifts there are hints that the brightest, most massive early-type galaxies in the field closely follow the FP evolution of their cluster counterparts, while less massive early-type galaxies appear younger. Similar results have been found at higher redshifts. Van der Wel et al. (2004, 2005a) constructed the FP for a total of 33 colour- and morphology-selected early-type galaxies at 0.60 < z < 1.15 in the GOODS South field. They also found the most massive galaxies (M_{*} > 2 x $10^{11}M_{\odot}$) to behave much like their cluster analogs at the same redshifts, while less massive galaxies appeared to be substantially younger. Recently, Saracco et al. (2017) found that cluster and field ellipticals at 1.2 < z < 1.4 follow the same scaling relations.

The spectra used for constructing the FP of distant cluster early-type galaxies were also used to measure age-sensitive line indices, that can provide further constraints on their formation epoch. For instance, Kelson et al. (2001) measured the H_{δ} lines of several clusters early-type galaxies up to z=0.83 and were able to set a lower limit to the formation redshift $z_F \gtrsim 2.5$. Moreover, all the above studies noted the higher proportion of weak [OII] emitters among the field early-type galaxies ($\sim$20%) compared to their cluster counterparts, as well as the higher proportion of galaxies with strong Balmer lines.

In summary, the study of the stellar populations in early-type galaxies belonging to distant clusters up to z $\sim$ 1.3 have shown that this class of galaxies have evolved passively from at least z $\sim$ 2-3. Moreover, the brightest cluster members at z $\sim$ 1-1.3 and the characteristic luminosity of the luminosity function appear to be brighter than their local counterpart by an amount that is fully consistent with a passive evolution, indicating that these galaxies were already fully assembled at this high redshift.

Although it is well established that early-type galaxies in distant clusters are progenitors to their local analogs and formed at high redshift, it is necessary to take into account a caveat. Indeed, the evidence summarized above indicate that at least some cluster galaxies evolved passively from z $\sim$ 1 to the present, but other local early-type galaxies may have z $\sim$ 1 progenitors that would not be classified as early-type at that redshift, either morphologically or photometrically. This "progenitor bias" (e.g. van Dokkum and Franx 1996) would therefore prevent us from identifying all the z $\sim$ 1 progenitors of local cluster early-type galaxies, some of which may well be still star forming.

In this thesis, I studied a sample of cluster ellipticals at z $\sim$ 1.4. Clusters of galaxies play a major role in galaxy evolution both since they provide a homogeneous environment for studying galaxy formation and evolution and because they provide large samples of galaxies at the same redshift; hence, the eventual differences in their properties do not depend on the fact that we are observing them at different epochs.

In the next section, I will briefly describe the main characteristics of the cluster environment and the different physical processes that galaxies can undergo in this peculiar environment.

1.2 Cluster environment

Galaxy clusters represent the largest known gravitationally bound structures in the Universe, with typical masses in the range $10^{14} - 10^{15}$ $M_{\odot}$. They are composed by hundreds to thousands of galaxies ($\sim$ 10% in mass), intracluster gas ($\sim$ 20% in mass) and dark matter ($\sim$ 70% in mass). Furthermore, these structures show high velocity dispersions ($\sigma \sim 1000$ km/s).

As early as the 1930s it was realized that the morphological mix of galaxies depends on environment, with denser environments (clusters) hosting larger fractions of early-type galaxies (Hubble and Humason 1931). This morphology-density relation was quantified more accurately by Dressler (1980), who studied the morphologies of galaxies in 55 clusters and found that the fraction of spiral galaxies decreases from $\sim$ 60% in the lowest density regions to less than 10% in the highest density regions, while the elliptical fraction basically reveals the opposite behaviour, as shown in fig. 1.3. This environmental effect has been confirmed both in the local (see e.g. Holden and Kelson 2007; Bamford et al. 2009) and intermediate redshift Universe (e.g. Treu et al. 2003; van der Wel et al. 2007; Tanaka et al. 2012).

It is well established that field and cluster galaxies experience different evolutionary processes due to the different environment they belong to. Cluster galaxies, unlike field galaxies, are subject to two main classes of processes: first, the gravitational ones,

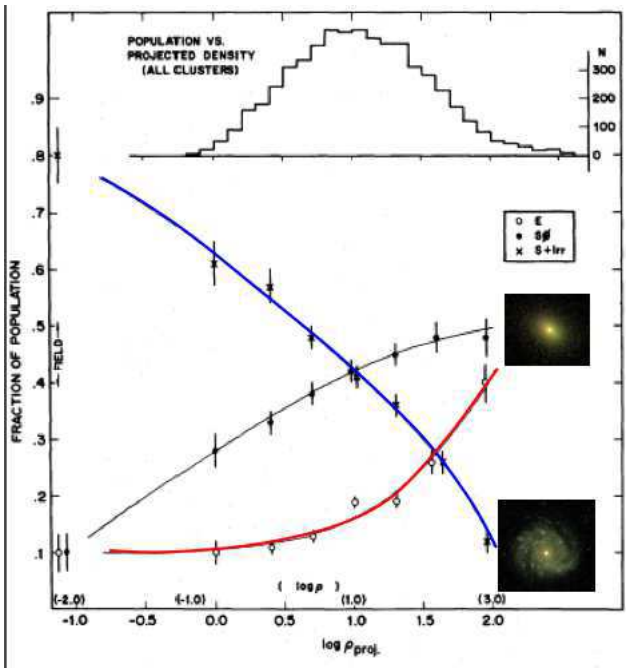

Figure 1.3: The fraction of E (open circles), S0 (solid circles) and S+I (crosses) galaxies as a function of the logarithm of the density. The fraction of S+I decreases with increasing density (blue line), conversely the fractions of S0 (black line) and E (red line) increase. The upper histogram shows the number distribution of galaxies over the bins of projected density (Dressler 1980).

including the tidal interactions (galaxy-galaxy, galaxy-cluster, harassment) (e.g. Fujita 1998; Merritt 1983; Merritt 1984; Mihos 1995) and secondly, the interactions taking place between the galaxy's ISM and the hot intergalactic medium (ram pressure, thermal evaporation, etc.) (e.g. Gunn and Gott 1972; Abadi, Moore, and Bower 1999; Cowie and Songaila 1977; Dressler and Gunn 1983). Processes like ram pressure stripping or thermal evaporation, removing the gas reservoir from the galaxy, can lead to a rapid quenching of star formation (e.g. Larson, Tinsley, and Caldwell 1980; Drake et al. 2000). These processes can either act at global galaxy scale or involve only a region of the galaxy, introducing a gradient of the stellar population properties (mainly age), whose steepness depends on the fraction of gas removed.

The main features of these processes are:

- **Galaxy-Galaxy**: Tidal interactions among galaxy pair act on gas, dust and stars, as well as on dark matter, with an efficiency depending on the gravitational bounding of the various components. If galaxy radii are not to small compared to the average separation between galaxies, tidal interactions can be quite efficient at removing matter from the peripheral parts (see e.g. Farouki and Shapiro 1981; Icke

1985; Merritt 1983). Tidal interactions among galaxies are boosted in the dense cores of galaxy clusters. However, due to the high relative velocities, these kind of processes, although very frequent, have significantly short duration ($t_{enc} \sim 10^8$ yr); thus, the effects of perturbations are slightly severe. Tidally interacting objects in clusters are relatively difficult to identify, since tidal tracers are very short lived; while in the field most of the ejected material in tidal tails remains bounded to the main galaxy, in clusters the tidal field strips the unbound material, possibly creating a diffuse intergalactic light (Mihos 2004).

- **Galaxy Harassment**: Moore et al. (1996; 1999) proposed that the evolution of cluster galaxies is governed by the combined effect of multiple high-speed galaxy-galaxy close ($\sim$ 50 kpc) encounters and the interaction with the potential of the cluster as a whole, a process they named "galaxy harassment". Harassment depends on the collisional frequency, the strength of the individual collisions, the cluster's tidal field, and the distribution of the potential within galaxies. Moore et al. simulations show that at a fixed mean orbital radius, galaxies on elongated orbits experience greater harassment than objects on circular orbits. The multiple encounters heat the stellar component, increasing the velocity dispersion and decreasing the angular momentum; meanwhile, they cause the gas to sink toward the galaxy centre. Because of their different potential distributions, massive and dwarf galaxies react differently to galaxy harassment. N-body simulations predict that the smallest spheroidals are destroyed in the inner cluster (half of the virial radius).

- **Ram Pressure**: Gunn & Gott (1972) first proposed that the ISM could also be efficiently roomed from galaxies moving at $\sim$ 1000 km s^{-1} through the hot ($\sim 10^7 - 10^8$ K) and dense ($\sim 10^{-3} - 10^{-4}$ atoms cm^{-3}) intergalactic medium by a ram pressure mechanism. Ram pressure can efficiently remove the ISM if it overcomes the gravitational pressure anchoring the gas to the galaxy. The efficiency of gas removal depends on the inclination of the galaxy with respect to the trajectory, with face-on interactions being more efficient than edge-on or inclined encounters (Abadi, Moore, and Bower 1999; Quilis, Moore, and Bower 2000; Vollmer et al. 2001).

- **Thermal evaporation**: As shown by Cowie & Songaila (1977), thermal evaporation can efficiently remove gas in cluster galaxies. If the IGM temperature is high compared to the galaxy velocity dispersion, at the interface between the hot IGM and the cold ISM, the temperature of the ISM rises rapidly and the gas evaporates and is not retained by the gravitational field.

1.2.1 Comparison between the various processes

The processes above described have different characteristics (timescale, probability, efficiency...), which mainly depend on the morphology of the galaxies involved and the distance from the cluster centre, as shown for instance by Treu et al. (2003), who studied

the morphology-radius and morphology-density relations for a sample of ~ 2100 galaxies in cluster CI 0024+16 at z ≈ 0.4 (see fig. 1.4). The principal effects are:

- *The effects of perturbation*: Spiral galaxies are more affected by the gravitational interactions compared to ellipticals. (a) Gravitational interactions can contribute to the heating of stellar disks and thus increase the bulge-to-disk ratio in spiral galaxies. Gravitational interactions are also able to modify the morphology of spiral galaxies by transforming them into lenticulars. (b) Interactions with the hot ICM can efficiently remove the outer disk gas and quench star formation (directly by gas removal or via starvation).

- *Timescales and probabilities*: Given the high velocity dispersion in clusters, the probability that galaxies are perturbed by tidal interactions with nearby companions is extremely low. The timescale for tidal interactions is $\sim 10^{10}$ yr. Timescales for ram pressure gas stripping ($\sim 10^9$ yr) are shorter than for harassment, where multiple encounters are necessary.

- *Efficiency as a function of the distance from the cluster centre*: The galaxy-cluster IGM interactions are most efficient close to the cluster centre, where the density and the temperature of the IGM reach their maxima. The perturbations induced by the cluster potential are also most efficient in the cluster centre, since the cluster tidal field is maximal at the core radius. Although the duration of the interaction might be shorter (because of the high relative velocity) than in the cluster outskirts, the frequency of galaxy - galaxy interactions reaches the maximum in the densest central regions. These processes thus seem confined to the inner part of the cluster. Because of the combined action of galaxy-galaxy and galaxy-cluster gravitational interactions, galaxy harassment might also be present at the cluster periphery. For similar reasons, starvation and preprocessing might be effective well outside the cluster core.

In the next section I will introduce the main proposed scenarios for the formation end evolution of the early-type galaxies together with the observational evidence so far collected and discussed in the previous sections.

1.3 Formation scenarios of early-type galaxies

Since the 1960s, a lot of theories on formation and evolution of the early-type galaxies have been proposed to explain the properties of this class of galaxies. These models not only have to fully describe what observed locally and at high redshift, but to match the constraints provided by cosmology on the formation of the dark matter haloes as well.

One of the first models proposed to describe the formation of the early-type galaxies is the so-called **monolithic collapse scenario** (Eggen, Lynden-Bell, and Sandage 1962; Larson 1974), which predicts that the massive early-type galaxies formed at z > 5 - 7 from the gravitational collapse of large clouds of gas. Stars are supposed to form in a

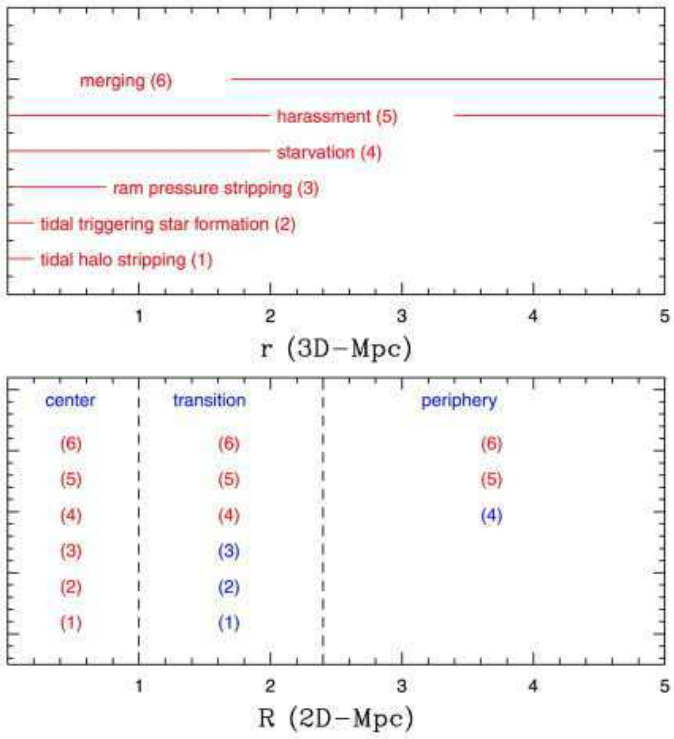

Figure 1.4: The figure summarizes the regions, where the key physical mechanisms are likely to operate (Treu et al. 2003). *Top*: Horizontal lines indicate the radial region where the mechanisms are most effective. *Bottom*: For each region within the cluster, the authors identify the mechanisms that could have affected the galaxies of their sample (red numbers). The blue numbers indicate processes that are marginally at work.

single violent and rapid episode of star formation (Chiosi and Carraro 2002; Pipino and Matteucci 2004). The gas is very quickly converted into stars through a very strong burst followed by a rapid quenching of the star formation due to the galactic winds powered by the supernovae explosions, which carry out the residual gas.

Numerous observational works, which have revealed the presence of old stellar populations in early-type galaxies and of a population of massive and passive galaxies already in place at high redshift, when the Universe was only a few Gyr old (see e.g. Cimatti et al. 2004; Saracco et al. 2005), are in agreement with this scenario.

However, this early phase dominated by *in situ* star formation could be followed by an extended phase of *ex situ* accretion of stars from dry minor mergers (not dissipative) with smaller satellite stellar systems, as recently proposed by e.g. Oser et al. 2010. These dry mergers are supposed to simply redistribute their stellar content in the outer regions, without mixing with the pre-existing stellar content and hence keeping unchanged the central bulge. The main effect of these dry minor mergers would be that to add an

external low-mass envelope to the compact core of the early type galaxies, enlarging the effective radius while leaving the stellar mass nearly constant. This scenario is motived by observational evidence of early-type galaxies at $1 < z < 2.5$ with effective radii 3-5 times smaller than the mean radius of local early-type galaxies with the same stellar mass (Daddi et al. 2005; Longhetti et al. 2007; Cimatti et al. 2008; Saracco, Longhetti, and Andreon 2009). Actually, this scenario shows some limitations, such as the large number of dry minor mergers needed to enlarge the early-type galaxies size and its failure to explain the presence of normal early-type galaxies observed at high redshift in number similar to the compact ones (Nipoti et al. 2009; Saracco, Longhetti, and Gargiulo 2010; Saracco, Longhetti, and Gargiulo 2011).

However, the fact that this scenario cannot be easily included in a global cosmological framework has led to the formulation of a *revised* monolithic model, according to which elliptical galaxies are formed in dissipational scenarios, such as gas-rich major merger in which most ($\sim 80\%$) of the stars is formed in the dissipative central starburst (Khochfar and Silk 2006; Naab et al. 2007; Sommer-Larsen and Toft 2010), or from primordial mergers of lumps of dark and baryonic matter occurring at very early epochs ($z > 4$) (Chiosi and Carraro 2002; Pipino and Matteucci 2004; Merlin and Chiosi 2006; Merlin et al. 2012). The following evolution is mainly characterized by aging of their stellar population, with small new episodes of star formation at $z < 1$, related, for instance, to the capture of small satellites (e.g. Katz 1991; Kawata 2001; Kobayashi 2004).

An alternative scenario of galaxy formation is the **hierarchical scenario**, supported by the cosmological ΛCDM model, which predicts that the dark matter halos, containing baryonic matter, evolve hierarchically with the small halos merging to form the biggest structures (Kauffmann 1996; De Lucia et al. 2006). Early-type galaxies would form by the wet (gas-rich) major mergers of disk galaxies. During these mergers, the star formation *in situ* is triggered by gas cooling and shock heating (Dekel and Birnboim 2006; Cattaneo et al. 2008) and provides only a minor fraction of the final stellar mass of the remnant, whose stars come principally from the disc progenitors.

An evidence in favor of this model comes from the sharp increasing of the merging rate with the redshift (see e.g., Patton et al. 1997). Moreover, this scenario is well supported by numerical simulations of the merging interactions among galaxies, which successfully reproduce also the kinematic and photometric properties of massive ellipticals (see Di Matteo, Springel, and Hernquist 2005; Naab, Khochfar, and Burkert 2006).

Even if the hierarchical model is considered the most convincing scenario of galaxy formation, some of its predictions are not in agreement with the observations. For instance, it is not yet completely clear how the prediction of ΛCDM model, which implies that massive systems assemble their stellar mass later than small ones, could be reconciled with the observational evidence of large and red galaxies already in place at high redshift (Marchesini et al. 2010; Mortlock et al. 2011). Furthermore, the number density of elliptical galaxies does not decrease with increasing redshift at least until $z \sim 2$, with the fraction of the early-type galaxies being constant at 20 - 30% (Tamburri et al. 2014; Im et al. 1996), contrary to what is predicted by the hierarchical scenario.

In order to solve the problem of the hierarchical scenario, Cowie et al. (1996) intro-

duced the "*downsizing scenario*", in which the baryonic matter has a mass-dependent assembly history, i.e. the most luminous and massive systems complete their formation first, while less massive systems prolong their star formation activity for a longer time. Studying a sample of ∼400 galaxies, the authors found that the massive galaxies formed their stars within short and highly peaked star formation interval at earlier cosmic time, while the less massive galaxies extended their star formation over longer period until more recent epoch. Similar results are also obtained by Chiosi & Carraro (2002) through a set of simulations, finding that the massive galaxies have a star formation characterized by a single episode peaked at very early epochs, while the smaller galaxies present intermittent star formation episodes protracted over time.

The only convincing alternative to the hierarchical formation of spheroids is the cold-accretion scenario (Dekel, Sari, and Ceverino 2009). In this context, the formation of early-type galaxies is driven by cosmological cold streams and violent disk instability rather than by mergers. After the hierarchical collapse of DM haloes, the primordial gas starts falling in the DM potential wells at a rate of about 100 $M_{\odot}$/yr at the highest z, forming a rotating disk. When the surface density is high enough and the circular velocity dispersion is sufficiently low, the disk breaks up into several giant clumps, of about 1 kpc in size and up to a few times 109 $M_{\odot}$ each (e.g. van den Bergh et al. 1996; Elmegreen and Elmegreen 2005; Genzel et al. 2008), that migrate towards the centre and dissipatively merge, forming a spheroid over short time-scales (< 1 Gyr). In this way, the galaxies acquired their gas through a continuous stream-fed of cold gas, that ensures instability and new clump formation in the disk as the older clumps migrate inward. During the gravitational collapse, the gas with high metallicity should flows towards the galaxy centre, producing a spheroids more metal-rich in the centre than in the external regions.

A systematic change in the stream properties is expected after $z \sim 1$, where the cosmological accretion rate becomes slower and the steady, narrow, cold streams no longer penetrate very effectively through the massive DM halos (Kereš et al. 2005; Dekel and Birnboim 2006; Cattaneo et al. 2006). The subsequent evolution of the spheroids should be mainly characterized by the ageing of their stellar populations, with small new episodes of star-formation at $z < 1$, that can derive from the minor merger with the capture of satellites. Hence, some of spheroids can further grow through inside-out accretion as in the hierarchical scenario, with the limitation to reproduce both the local scaling relations and their scatter (e.g. Nipoti et al. 2012; Saracco, Gargiulo, and Longhetti 2012).

Finally, some theoretical studies suggest that the formation and evolution of elliptical galaxies may be dependent on the environment. Ellipticals in dense environment would be formed at $z > 3$. The high peak of density fluctuations are expected to evolve very quickly and accelerate the formation of the elliptical galaxies through strong bursts of star formation. On the other hand, field environment does not present such high peak of density fluctuations. These fluctuations are expected to evolve more slowly and collapse at lower redshifts. Galaxies would evolve through bottom-up processes of smaller subgalaxies and could settle dawn to disk galaxies preferentially. In this case,

elliptical galaxies are more likely to form through major mergers of disk galaxies at lower redshift (e.g., z < 2) (e.g. Peacock 1999). Indeed, some recent observational and theoretical studies suggest that elliptical galaxies formed through major mergers tend to inhabit in field environments and they have experienced mergers inducing star formation until recent epochs, such as $z \lesssim 1$ (e.g. Baugh, Cole, and Frenk 1996; Governato et al. 1999; Menanteau, Abraham, and Ellis 2001).

1.4 Colour gradients and the different mechanisms of mass assembly

The picture described so far shows how the origin and the mass assembly history of early-type galaxies still remain an open issue. All these different predictions show how spatially resolving the properties of the stellar populations inside the galaxies represents an important tool to constrain the assembly and the shaping of elliptical morphology of the elliptical galaxies. The most viable way to carry out information on the radial variation of the stellar content of a galaxy is to study its colour variation, being the colour of a stellar population strongly dependent on its age, metallicity, (eventual) presence of dust...

The presence of a colour gradient indicates that the properties of the stellar population inside a galaxy are not homogeneous suggesting that, for instance, stars may not be the result of a single burst of star formation, or they may have been formed in regions characterized by different physical condition of the interstellar medium (ISM), or be the result of later episodes of accretion of small satellites. The history and mechanisms of galaxy assembly have significantly different consequences for the internal distribution of stellar populations probed by the colour gradients.

If elliptical galaxies are formed in dissipative scenarios, such as gas-rich major merger in which most ($\sim 80\%$) of the stars is formed in the dissipative central starburst or from primordial mergers of lumps of dark and baryonic matter occurring at very early epochs ($z > 4$), like predicted by the revised monolithic model, steep gradients are expected to be observed inside early-type galaxies. During the gravitational dissipative collapse, the gas should naturally flow towards the centre of the galaxies due to the deeper potential well, where it is enriched by the stellar evolutionary processes. This would produce a negative metallicity gradient and a mild positive age gradient since star formation is expected to last longer towards the centre (Kobayashi 2004). More massive galaxies are expected to have steeper gradients because of the mass dependent effect of the winds (Carlberg 1984).

However, if this early phase dominated by *in situ* star formation is followed by an extended phase of *ex situ* accretion of stars from dry minor mergers with smaller satellite stellar systems, the above gradients could be strongly affected. In this two-phase process, early-type galaxies would continue to grow from the inside-out redistributing the stellar content of the satellites in the outer regions, without mixing with the pre-existing central bulge. If the satellite stellar systems are coeval to the central early-type galaxy, that is if the age and the metallicity of their stars are similar, the resulting gradients may flatten

going towards the outer regions or, opposite, steepen if the satellites are younger.

On the other hand, if ellipticals formed through major mergers, these will tend to mix the stellar content of the progenitors producing nearly flat gradients in the remnant. Hereafter, the remnant may experience minor dry mergers whose effects are those discussed above.

1.4.1 Colour gradients in the local Universe

Since the early 1970s (Faber 1972), colour gradients in local early-type galaxies have been largely studied. Many studies have shown that local and intermediate redshift elliptical galaxies present negative optical or optical-NIR rest-frame colour gradients (e.g., B-R, U-R, V-K), i.e. they are redder towards the centre. However, it is not clear yet which is/are the stellar population property/ies (age, metallicity, IMF...) that is/are radially varying in order to produce the observed colour variations. Almost all these works agree that a metallicity gradient is the principal origin of the observed colour variation (e.g. Peletier, Valentijn, and Jameson 1990; Tamura and Ohta 2000; Saglia et al. 2000; Wu et al. 2005; La Barbera et al. 2005; Tortora et al. 2010): the cores are metal-rich compared to the outer region. Metallicity gradients can be produced through different mechanisms. Winds generated by supernovae (Larson 1974) or active galactic nuclei (AGNs) (Begelman, de Kool, and Sikora 1991) can provide the metallicity enrichment of the intergalactic medium. This enrichment does not necessary happen in a symmetrical way and, thus, it can produce strong metallicity gradients. In high mass galaxies typically $\nabla_Z = -0.3$ (e.g. Saglia et al. 2000; Wu et al. 2005; La Barbera and de Carvalho 2009), which is shallower than the value predicted by simulations of dissipative 'monolithic' collapse (where -0.5 or steeper values are expected, see e.g. Larson 1974; Kobayashi 2004).

Another open question is the presence of a correlation of colour gradients with galaxy mass and luminosity. Earlier studies have claimed a weak correlation with the physical properties of galaxies (e.g. Peletier, Valentijn, and Jameson 1990; Kobayashi and Arimoto 1999). Recently, a stronger correlation with mass and luminosity has started to emerge, pointing to a metallicity gradient decreasing with the mass of the galaxy. For instance, Tamura et al. (2003), studying the B-R colour gradients in a sample of ellipticals in cluster Abell 2199, found that brighter galaxies as well as galaxies with larger effective radii tend to have steeper colour gradients, suggesting that these galaxies might have been formed through the monolithic collapse scenario. In Coma, den Brok et al. (2011) find that the magnitude of the gradients correlates with galaxy mass, suggesting that all galaxies form in a quasi-monolithic scenario.

A few studies, besides negative metallicity gradients, have found that slightly positive age gradients are necessary to explain the observed radial colour variation, i.e. early-type galaxies tend to have younger and more metal-rich cores (e.g. Saglia et al. 2000; Clemens et al. 2009; Rawle, Smith, and Lucey 2010; La Barbera and de Carvalho 2009). In fact, local studies all agree in considering the observed radial colour variations as mainly driven by a metallicity variation, with, however, the contribution played by radial age variation still controversial.

The presence or otherwise of an age gradient is a key piece in understanding of the mass assembly of elliptical galaxies. However, its detection from colour gradients in low redshift galaxies is a challenging task, while high-z early-type galaxies constitute the ideal place to investigate the presence of an age gradient. Indeed, at fixed age radial variation, its effect on colour variation is much more enhanced when stellar populations are young. This effect is clearly shown in fig. 1.5, where I report the U-R colour variation of two stellar populations with age, which differs of 1 Gyr, as a function of the mean age of the two stellar populations. It results that an age variation of 1-2 Gyr in a stellar population with a mean age of about 8-9 Gyr reflects a variation of ~ 0.05 mag in the U-R colour, much smaller than the one produced by the observed metallicity gradient and comparable to typical photometric errors. On the contrary, a variation of just 1 Gyr in a stellar population ∼2-3 Gyr old, as in ellipticals at $z \sim 1.5$, would produce a colour variation $\sim 0.2 - 0.3$ mag, comparable to the one produced by a metallicity variation. Hence, an age variation, if present, would be detectable in high redshift early-type galaxies. These simple considerations highlight the relevance to study colour gradients in high redshift elliptical galaxies to properly investigate their assembly and shaping of their elliptical morphology.

1.4.2 Colour gradients at high redshift

Only few studies of colour gradients in high-redshift elliptical galaxies have been conducted so far. These galaxies represent an important benchmark to investigate the mechanisms of stellar mass assembly due to the short time elapsed from their formation. Anyway, because of the instrumental limitations, it is very difficult to derive colour gradients in early-type galaxies at high redshift. For instance, ground-based observations suffer from poor resolution. Indeed, the typical full width half-maximum (FWHM) of the point spread function (PSF) of Very Large Telescope (VLT) ISAAC Ks-band images is ∼0.5", corresponding to ∼4 kpc at z ∼ 2. This size is almost four times the average effective radius of early-type galaxies at z ∼ 2 (Cassata et al. 2010, and references therein). In the last years, the advent of the HST Advanced Camera for Surveys (HST/ACS) and HST Wild Field Camera 3 (HST/WFC3) has open new possibilities to study colour gradients of high-z early-type galaxies and to constrain their origin.

For instance, Guo et al. (2011) derived negative rest-frame U-R colour gradients for six massive and passively evolving galaxies at redshift $1.3 < z < 2.5$ and they found that the gradient of a single parameter (age/metallicity) cannot fully explain the observed colour variation.

Gargiulo et al. (2012) studied the rest-frame optical U-R and UV-U (Gargiulo, Saracco, and Longhetti 2011) colour gradients in a sample of field ellipticals at $1 < z < 2$ and they found that only for half of the sample an age/metallicity gradient can account for the observed gradients. For the remaining half of the sample, the variation of more than one parameter is required to account for the observed colour variation.

Recently, Chan et al. (2016) found that the rest-frame optical U-R colour gradients in passive cluster galaxies at z=1.39 are mostly negative, with a median value twice the value in the local Universe (Wu et al. 2005). To reproduce the colour gradients locally

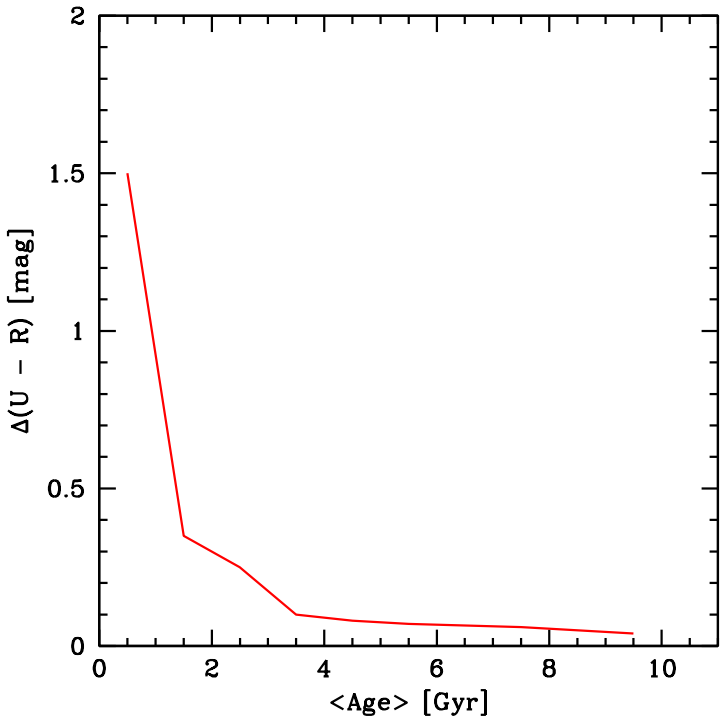

Figure 1.5: U-R colour variation of two stellar populations with age differentiating of 1 Gyr as a function of the mean age (<Age>) of the two stellar population. The same ΔAge produces a difference in the U-R colour of the two stellar populations higher for Age $\leq$ 4 Gyr than for old stellar populations.

observed, the presence both of age and metallicity gradient is needed. De Propris et al. (2015; 2016) found similar conclusions on the presence of metallicity and age gradients.

1.5 My thesis

The main aim of my Ph.D. thesis is to study how the colour of a sample of cluster ellipticals radially changes and to study its origin in term of variation of the stellar population properties. In particular, I jointly studied the rest-frame UV-U and U-R colour gradients for a sample of 17 elliptical galaxies morphologically selected in the cluster XMMU J2235.3-2557 at z=1.39, whose centre has coordinates α=$22^{h}35^{m}20^{s}.6$ and δ=-25°$57^{m}42^{s}$ (Mullis et al. 2005; Rosati et al. 2009; Strazzullo et al. 2010). At this redshift the age of the Universe was only $\sim$ 4.5 Gyr instead of the current $\sim$ 13.5 Gyr. Thus, this allows to cut out 70% of the evolution the galaxies have undergone since their formation. Finally, I focused on cluster galaxies since they are all in the same

environment and at the same redshift.

Colour gradients are based on HST optical and near-IR archive data sampling, at $z \simeq 1.4$, the rest-frame UV- and U-band (ACS F775W and F850LP), dominated by the emission of young stellar populations, and the rest-frame R-band (WFC3 F160W), dominated by the emission of old stellar populations.

This thesis is organized as follows:

- In Chapter 2 I describe the data and the criteria imposed in order to select the final sample composed by 17 cluster ellipticals. I also describe how the structural parameters (effective radius, index of concentration n) and the physical parameters (stellar mass, age, absolute magnitude) of these galaxies have been derived.
- In Chapter 3 I describe the methods used to derive the F775W-F850LP and F850LP - F160W colour gradients and I show that the results I obtain do not depend on the method used.
- In Chapter 4 I investigate the origin of the observed colour gradients in term of radial variation of the stellar population properties (age/metallicity) and dust content.
- In Chapter 5 I study the dependance of colour gradients on the global properties of galaxies and on their cluster centric distance. This is to probe the influence of the local environment on their shaping and to put constraints on the mechanisms of stellar mass accretion.
- In Chapter 6 I compare my results with colour gradients in other clusters and field ellipticals at a comparable redshift ($1.3 < z < 1.6$) and with colour gradients in local ellipticals, investigating, through the evolution of colour gradients, how cluster ellipticals have evolved from z=1.39 to z=0.

Throughout this thesis magnitudes are in the Vega system and I used a standard cosmology with $H_0 = 70$ km s^{-1} Mpc^{-1}, $\Omega_0 = 0.3$ and $\Omega_\Lambda = 0.7$. With these parameters, the age of the Universe at z = 1.39 is ~ 4.5 Gyr.

CHAPTER

2

DATA AND SAMPLE SELECTION

In this Chapter I describe the data and the criteria imposed in order to select the sample of 17 cluster ellipticals, that I have studied in my Ph.D. thesis. These galaxies have been selected to belong to the cluster XMMU J2235.3-2557 at z=1.39, which was serendipitously detected as an extended X-ray source in a archival XMM-Newton observation of NGC 7314 (Mullis et al 2005). Subsequent FORS2 multiobjects spectroscopy confirmed the presence of a massive cluster based on 12 concordant redshifts in the interval $1.38 < z < 1.40$. The cluster velocity dispersion is 762 ± 265 km s^{-1}. The authors estimated a X-ray luminosity $L_X = (3.0 \pm 0.2) \times 10^{44}\ h_{70}^{-2}$ ergs s^{-1} in the 0.5-2.0 keV band and a temperature of $kT = 6.0\ ^{+2.5}_{-1.8}$ keV.

The cluster has also been observed with HST, Spitzer, VLT and *Chandra*. Rosati et al. (2009) measured with *Chandra* a global X-ray temperature of $kT = 8.6^{+1.3}_{-1.2}$ keV and, in the hypothesis of hydrostatic equilibrium, they obtained a total mass of $M_{tot}(< 1\ \mathrm{Mpc}) = (5.9 \pm 1.3) \times 10^{14}\ M_\odot$.

2.1 Data description

2.1.1 Optical and near-IR data

The analysis presented in this thesis is based on Hubble Space Telescope (HST) and Spitzer data and on ground-based observations carried out at the Very Large Telescope (VLT).

The HST data retrieved from the archive are composed of optical ACS observations and near-IR WFC3 observations. ACS observations covering a field of about 11 arcmin^2 surrounding the cluster XMMUJ2235-2557 were obtained in the F775W (5060 s) and

F850LP (6240 s) filters (i_{775} and z_{850} hereafter) and they are described in Rosati et al. 2009 (see also Strazzullo et al. 2010). The two filters are centred at $\lambda_{obs} = 7692.4$ Å and $\lambda_{obs} = 9033.1$ Å, respectively, which, at z = 1.39, according to the relation

$$\lambda_{obs} = \lambda_{rest}(1 + z) \tag{2.1}$$

where λ_{obs} is the observed wavelength and λ_{rest} is the wavelength in the rest frame, correspond to $\lambda_{rest} \sim 3200$ Å ($\sim$ UV band) and $\lambda_{rest} \sim 3800$ Å ($\sim$ U band).

The ACS images have a pixel scale of 0.05 arcsec/pix and a resolution of $\mathrm{FWHM}_{850} \simeq 0.11$ arcsec, corresponding to a minimum resolved linear size of ~ 1 kpc at the cluster distance.

WFC3 observations sampling a field of about 5 arcmin^2 centered on the cluster were obtained in the F160W filter ($\sim$1200 s), which is centred at $\lambda_{obs} = 15369$ Å corresponding to $\lambda_{rest} \sim 6430$ Å ($\sim$ R band). The original WFC3 images have a pixel scale of 0.123 arcsec/pix and a resolution $\mathrm{FWHM}_{160} \simeq 0.2$ arcsec (~ 1.7 kpc at z=1.39). The HST-ACS images in the archive were already reduced and the mosaic images were already available. On the contrary, the WFC3 F160W mosaic image available in the archive had a pixel scale not suitable for my analysis (0.09 arcsec/pix). I have, hence, reduced the raw images using the Pyraf task `calwf3` to subtract the bias, dark current and cosmic-rays contributions and I have created the mosaic F160W image with the software `multidrizzle` (Koekemoer et al. 2003) reducing the pixel scale from the original value of 0.123 arcsec/pix to the pixel scale of the ACS images (0.05 arcsec/pix). The software, through a drizzle algorithm, operates on the input image by shrinking the pixels by a scale factor called "*pixfrac*" and dividing up the flux of each input pixel into the output smaller pixels. If the *pixfrac* value is too small, the flux of each input pixel can not be well divided up in the output pixels; if, instead, it is too large, an input pixel "footprint" can remain in the output images. Starting from the raw WFC3-F160W images, I have created different output images varying the *pixfrac* value. After checking that the drizzle procedure had not introduced any artificial effects, I have chosen as WFC3-F160W final image the one with $pixfrac = 0.8$.

VLT-HAWKI observations sampling a region of about 13'×13' centered on the cluster were obtained in the J ($\lambda_{obs} = 12580$ Å, $\lambda_{rest} \sim 5200$ Å) and Ks ($\lambda_{obs} = 21460$ Å, $\lambda_{rest} \sim 8900$ Å) filters under excellent seeing conditions (FWHM(J)$\simeq$0.5 arcsec and FWHM(Ks)$\simeq$0.35 arcsec). The exposure time is ~ 10500 s for each image. These data are described in detail in Lidman et al. (2008) and Lidman et al. (2013). VLT-VIMOS U-band ($\lambda_{obs} = 3700$ Å, $\lambda_{rest} \sim 1500$ Å) data were obtained in 2007 for a total exposure time of about 21000 s with a seeing of about 0.8 arcsec. The images were reduced and stacked as described in Nonino et al. (2009).

Spitzer data were obtained in the four IRAC bandpasses [3.6, 4.5, 5.8, 8.0]μm ($\lambda_{rest} \sim$ [1.5, 1.9, 2.4, 3.3] μm). The fully co-added mosaics (0.6 arcsec/pix) produced by the standard Spitzer reduction pipeline resulting in a mean exposure time of $\sim$2100 s in the 3.6 μm, 4.5 μm and 5.8 μm bands and in about 1990 s in the 8.0 μm were used.

The characteristics of the 10 filters used in the analysis are summarized in table 2.1.

As I will show in §2.3.5, the colour gradients have been derived using the three

Filter	λ_e Å	FWHM arcsec	Pixel scale arcsec/px	Exp. Time s
U	3780	0.80	0.20	21000
i (F775W)	7692	0.11	0.05	5060
z (F850LP)	9033	0.11	0.05	6240
J	12550	0.47	0.15	10560
H (F160W)	15369	0.20	0.12	1200
Ks	21630	0.32	0.15	10740
3.6 μm	35620	>2.7	0.60	2100
4.5 μm	45120	>2.7	0.60	2100
5.8 μm	56860	>2.7	0.60	2100
8.0 μm	79360	>2.7	0.60	1990

Table 2.1: Characteristics of the 10 photometric bands available.

HST images thanks to their good resolution, which allows to spatially resolve the stellar properties inside the galaxies.

2.2 Catalogue construction

The sample analyzed in my thesis is composed of 17 ellipticals selected to belong to the cluster XMMUJ2235-2557 at $z = 1.39$ (Mullis et al. 2005; Rosati et al. 2009). In the following section I describe the method used to construct the catalogue of galaxies in the cluster and the criteria adopted to select the sample of elliptical galaxies. In particular, the sample has been selected according to the following criteria:

1. $z_{850} < 24$ mag
2. D < 1 Mpc (Abell's radius) from the cluster centre
3. colour concordance
4. morphological classification

2.2.1 Detection of the sources

To select the sample of elliptical galaxies belonging to the cluster, I first constructed the catalogue containing all the sources in the field surrounding the cluster region. To detect all the sources in the images and estimate their magnitudes I used the software SExtractor (*Source Extractor*, Bertin and Arnouts 1996), that builds a catalogue of objects from an astronomical image. The detection has been done on the F850LP image since it has a better resolution ($\simeq$ 0.11 arcsec) and the smaller native pixel scale (0.05 arcsec/px). In this section I will discuss the input parameter required by SExtractor.

A group of connected pixels (DETECT_MINAREA) that exceeds a threshold (DETECT_THRESH) above the background is identified as a detection. I have fixed the DETECT_THRESH value at 1.5σ above the local background. Below this threshold the number of spurious sources significantly increased. To determinate the minimum number of pixels that are considered as a detection, I took as reference the FWHM of the PSF. For the HST-ACS the FWHM is ∼0.11", which corresponds to 3 pixels. I hence set as DETECT_MINAREA an area of 9 pixels.

As concerns the photometry, the main input parameters required by the software are: the zeropoint (MAG_ZEROPOINT) and the PSF FWHM (SEEING_FWHM). Magnitudes are computed through the formula:

$$mag = -2.5\ log\left(\frac{ADUs}{t_{exp}}\right) + mag\ ZP \tag{2.2}$$

where ADUs are the counts, t_{exp} is the exposure time and ZP is the zeropoint, which depends on the filter used. For the F850LP band ZP = 24.326 mag in Vega system and $t_{exp} = 6240$ s. SExtractor provides four magnitudes, among which the *corrected-isophotal* (MAG_ISOCOR) and the *adaptive-aperture* (MAG_AUTO). The first one is computed using the detection threshold as isophote and corrected by also considering the flux falling outside the isophote; the second one, instead, is computed inside the aperture at the Kron radius, which contains $\geq 90\%$ of the total flux of the source. For isolated sources the best estimate of the magnitude is MAG_AUTO; it is, instead, suggested to use MAG_ISOCOR when a source is to close to its neighbours. This is automatically done by the software when using the MAG_BEST magnitude. For this reason, I adopted MAG_BEST as the best estimator of the magnitude.

On the basis of these input parameters, SExtractor detected 3012 sources. Magnitudes in the F775W and F160W filters have been obtained by running the procedure in double image mode using the F850LP image as reference. Through this procedure, the software uses for the detection of the sources the F850LP image and it computes the magnitudes in the other filter. It is thus important that the images have the same dimensions and they are alined.

2.3 Selection criteria

2.3.1 $z_{850} < 24$ mag

The sources detected by SExtractor include both stars and galaxies. The software allows to separate between galaxies and stars through the parameter CLASS_STAR, which can vary between 0 and 1. In particular, a CLASS_STAR value ∼1 is assigned to point sources, whereas a CLASS_STAR value ∼0 is assigned to extended sources. In fig. 2.1, the stellar index computed by SExtractor is shown as a function of the F850LP apparent magnitude. For magnitudes brighter than $z_{850} = 24$, point like sources (CLASS_STAR $\simeq$ 1) and extended sources (CLASS_STAR $\simeq$ 0) are well segregated, whereas they tend to mix at fainter magnitudes. For this reason, only sources with

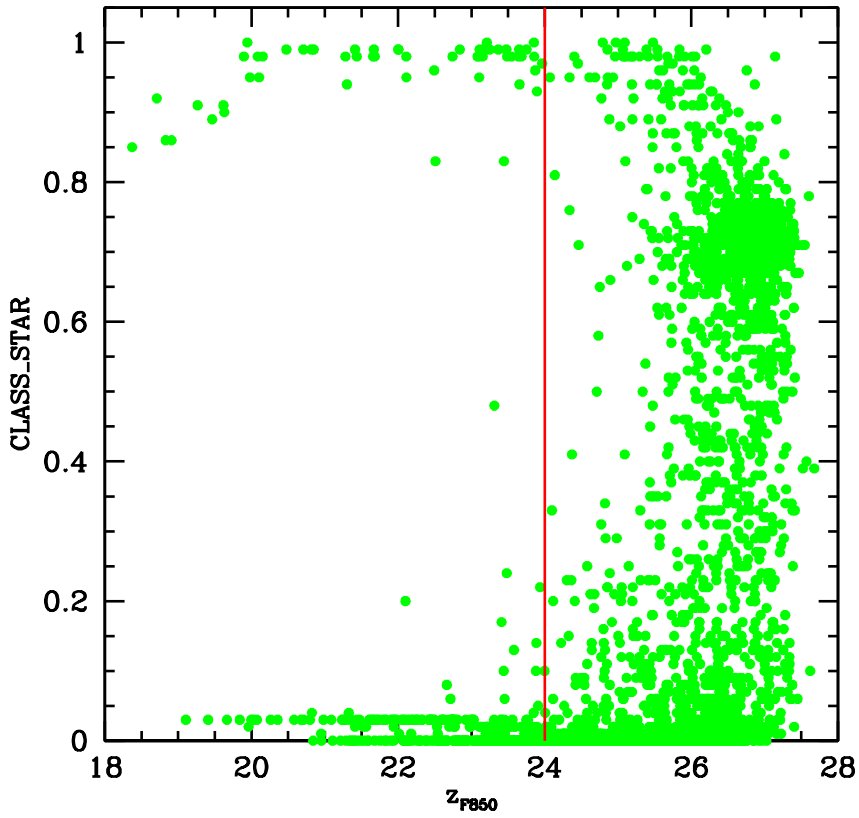

Figure 2.1: SExtractor stellar index (CLASS_STAR) as a function of the F850LP magnitude for all the sources detected.

CLASS_STAR < 0.9 have been selected. Furthermore, following previous works (see e.g., Saracco et al. 2014), in order to perform a reliable and robust visual morphological classification, only galaxies with magnitudes $z_{850} \leq 24$ have been selected. At this magnitude limit, the sample is 100% complete. According to this selection, 381 galaxies have been selected.

2.3.2 Distance from the cluster centre

In order the select galaxies belonging to the cluster, I restricted the selection to those galaxies within a radius D $\leq$ 1 Mpc (typical radius of galaxy cluster) from the cluster centre. This criterion is due to Abell (1958), who selected 1682 galaxy clusters from the Palomar Sky Survey, which are now referred to as the Abell clusters, setting a compactness criterion: only galaxies with distances to the cluster centre smaller than 1 Mpc (the Abell radius) are selected as cluster members. Hence, for each of the 381 galaxies

brighter than $z_{850} = 24$ mag, its distance from the cluster centre has been computed. The angular distance of two sources (given their right ascension and declination) is

$$d_A = \sqrt{(\Delta\alpha \cdot \cos\delta_m)^2 + (\Delta\delta)^2} \tag{2.3}$$

where $\Delta\alpha$ and $\Delta\delta$ are the differences of right ascensions and declinations, respectively, and $cos\ \delta_m$ is the cosine of the mean declination.

From cosmology, we know that a source of proper length l (in kpc) at redshift z subtends an angle $\Delta\theta$ (in rad), such that

$$\frac{l}{\Delta\theta} = \frac{d_L}{(1+z)^2} \tag{2.4}$$

where d_L is the luminosity function, which depends on the cosmological parameters and on the redshift z through the relation (see e.g. Hogg 1999)

$$d_L = \frac{c}{H_0}\,(1+z)\int_0^z \frac{dz'}{E(z')} \tag{2.5}$$

where $E(z') = \sqrt{\Omega_m(1+z)^3 + \Omega_\Lambda}$, H_0 is the Hubble constant , c is the speed of light e Ω_m e Ω_Λ are the matter density and dark energy density parameters, respectively. We thus obtain that, at z = 1.39, $1''$ corresponds to 8.427 kpc, from which 1 Mpc corresponds to $120''$. Hence, only galaxies with a distance $Dist \leq 120''$ from the cluster centre have been selected. On the basis of this criterium, I obtained a sample of 352 galaxies, 219 of which covered also by WFC3-F160W observations.

2.3.3 Colour concordance

This sample contains the 5 central cluster member galaxies spectroscopically identified by Rosati et al. (2009), three out of which, #1740, #1758 and #1782 of Tab. 2.3, are ellipticals. In tabel 2.2 the colour $i_{775} - z_{850}$ of the 5 cluster members with spectroscopic redshift is reported.

ID	i_{775} [mag]	z_{850} [mag]	$i_{775} - z_{850}$ [mag]	$\sigma_{i_{775}-z_{850}}$ [mag]
1740	22.42	21.48	1.12	0.02
1755	23.88	22.67	1.14	0.03
1758	24.16	23.13	1.08	0.03
1782	23.45	22.49	0.97	0.02
1786	24.30	23.30	1.08	0.04

Table 2.2: I report, from left to right, the ID of the galaxies as identified in SExtractor catalogue, the magnitude in the F775W band, the magnitude in the F850LP band, the colour $i_{775} - z_{850}$ and its error.

The mean colour of these five cluster member galaxies is $\langle i_{775} - z_{850}\rangle = 1.08$ with a dispersion $\sigma = 0.06$. This colour well traces the redshift of the galaxies. In particular,

for z $<$ 0.8 the $i_{775} - z_{850}$ colour is always $<$ 0.8 mag, while for z $>$ 0.8 - 0.9 its value rapidly increases and remains always $>$ 0.8 mag, independently from the age of the stellar population considered (see e.g. Saracco et al. 2014). In Fig. 2.2 (right panel) I show the $i_{775} - z_{850}$ colour distribution of the 352 galaxies with $z_{850} \leq 24$, which reflects the behavior described above. Two peaks are present. The first peak is centered to a value of $\sim 0.3 - 0.4$ mag suggesting, on the basis of the considerations above, that these galaxies are all at z $<$ 1. The remaining galaxies form a second peak centered at $\simeq$ 1.1 mag, the mean colour of the 5 cluster member red sequence galaxies, suggesting that they are at $z > 1$. Hence, I selected all the galaxies in the colour range $0.96 < i_{775} - z_{850} < 1.2$ mag, defining the second peak of the colour distribution centred at the mean colour (marked by red solid line in the figure) of the 5 cluster member galaxies. The dashed red lines represent $\pm 2\sigma$ from the mean colour of the 5 cluster members. According to these criteria, 50 galaxies have been selected as cluster member candidates.

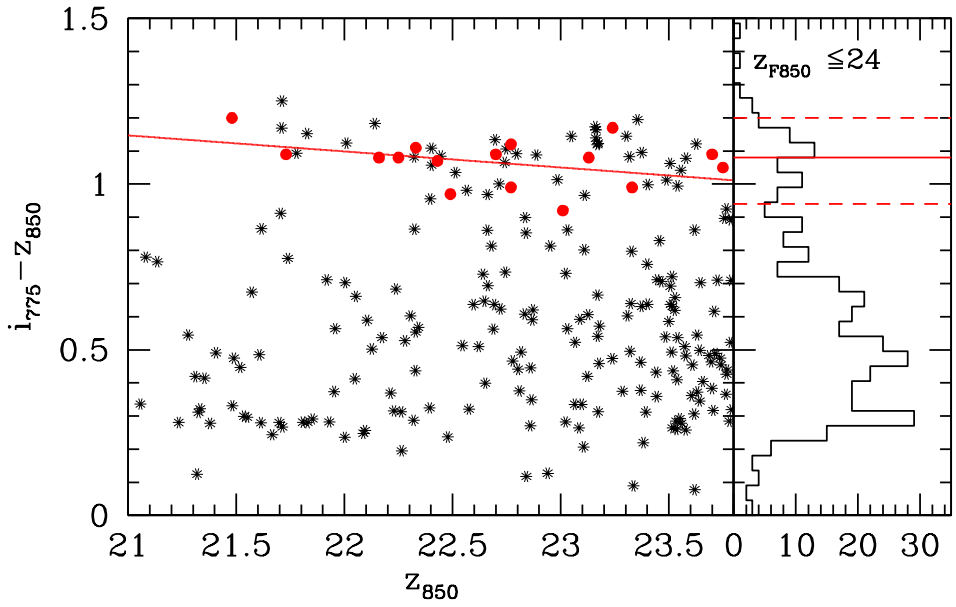

Figure 2.2: *Left panel*: Colour-magnitude relation. The i_{775} - z_{850} colours of the 17 selected ellipticals (red points) as a function of z_{850} are shown together with those of the 352 galaxies with $z_{850} < 24$ (black asterisks). The solid red line is the colour-magnitude relation (i_{775} - z_{850}) = 2.16($\pm$0.58) - 0.048($\pm$0.026)z_{850} best-fitting the 17 ellipticals. *Right panel*: The $i_{775} - z_{850}$ colour distribution of the 352 galaxies brighter than $z_{850} < 24$ falling within 1 Mpc from the cluster centre is shown. The red solid line marks the mean color $\langle i_{775} - z_{850} \rangle = 1.08 \pm 0.06$ of the 5 cluster members spectroscopically confirmed (Rosati et al. 2009). The dashed lines represent $\pm 2\sigma$. A second peak in the distribution centered at the mean colour of the 5 cluster galaxies is evident.

2.3.4 Morphological Classification

In order to identify the elliptical galaxies, I have performed a morphological classification based on the visual inspection of the galaxies on the ACS-F850LP image and on the fitting of their surface brightness profile as described in § 2.4. In particular, I classified as ellipticals those galaxies having a regular shape with no sign of a disc on the F850LP image and no irregular or structured residuals resulting from the profile fitting. On the basis of this morphological classification 17 galaxies out of the 50 turned out to be ellipticals. Their coordinates are reported in table 2.3.

#ID	RA	Dec	z_{spec}
358	22:35:26.99	-25:58:14.77	—-
595	22:35:26.22	-25:56:46.17	—-
684	22:35:25.81	-25:56:46.62	—-
692	22:35:25.68	-25:56:59.11	—-
837	22:35:24.90	-25:56:37.65	—-
1284	22:35:22.82	-25:56:25.54	—-
1539	22:35:22.48	-25:56:15.78	—-
1740	22:35:20.83	-25:57:40.41	1.39
1747	22:35:20.58	-25:58:21.34	—-
1758	22:35:20.91	-25:57:36.55	1.39
1782	22:35:20.70	-25:57:45.09	1.39
1790	22:35:20.70	-25:57:38.35	—-
2054	22:35:19.06	-25:58:27.99	—-
2147	22:35:19.04	-25:57:52.08	—-
2166	22:35:18.15	-25:59:06.58	—-
2429	22:35:17.87	-25:56:13.68	—-
2809	22:35:18.26	-25:56:06.79	—-

Table 2.3: Sample of 17 ellipticals selected as cluster members at $z_{850} < 24$, within 1 Mpc radius from the cluster center and having a colour $i_{775} - z_{850} = 1.08 \pm 0.12$, i.e. within 2σ from the mean colour of the 5 galaxies spectroscopically confirmed cluster members (Rosati et al. 2009). For three galaxies (#1740, #1782, #1790) spectroscopic redshift is available.

In order to estimate the expected contamination from field foreground/background galaxies, I derived the density of galaxies in the GOODS-South field over a region of ~ 1 Mpc (as for cluster galaxies). Field control sample has been selected following the same selection criteria adopted for cluster galaxies (see above). Two galaxies out of the 17 are expected not to be cluster members.

Fig. 2.2 (left panel) shows the i_{775} - z_{850} colours of the 17 selected ellipticals (red points) as a function of z_{850} together with those of the 352 galaxies with $z_{850} < 24$ mag (black asterisks). The selected ellipticals define a red sequence, as expected. The solid red line is the colour-magnitude relation (i_{775} - z_{850}) = 2.16($\pm$0.58) - 0.048($\pm$0.026)z_{850}

best-fitting the 17 ellipticals. This result is in good agreement with the relations found by Holden et al. (2005) for cluster RDCS J1252.9-2927 at z=1.23, by Mei et al (2012) for the cluster in the Linx structure and by Saracco et al. (2014) for the cluster RDCS J0848+4453 at z =1.27.

2.3.5 Multiwavelength photometry

Magnitudes for the 17 selected galaxies have been measured in all the available bands using SExtractor and MAG_BEST has been adopted as best estimator of the magnitude.

As mentioned in §2.1.1, the field of view of the WFC3 is smaller than the ACS field (5 arcmin^2 instead of 11 arcmin^2); hence, only 13 ellipticals out of the 17 are covered by WFC3 observations, with galaxies #358, #1539, #2166 and #2809 falling outside.

VIMOS U-band observations cover the whole sample to a limiting depth of U$\simeq$ 28. Thank to this depth, 6 of them have been detected at this wavelength.

HAWKI J- and Ks-band images cover the whole sample. Thank to the excellent resolution of the images all the galaxies are resolved in both the filters.

Also Spitzer-IRAC observations cover the whole sample. Magnitudes have been estimated in the four IRAC bands using SExtractor in double image mode adopting the 3.6 μm image as reference. The reliability of the flux measurement has been tested by comparing the flux measured with SExtractor for some stars in the field with the flux obtained using the IRAF task phot. Due to the low resolution (FWHM$>$ 2.7 arcsec) 8 galaxies (#2809, #595, #692, #358, #1740, #1790, #1782 and #1758) are not resolved but appear fully blended with other close sources. For these galaxies, their magnitudes in the four IRAC bands have been derived by redistributing the total IRAC flux of the blended sources according the fluxes measured for each of them in the F160W and Ks filters. In figure 2.3 I show as example galaxy #2809, which is closed to another galaxy, in the ACS-F850LP (*upper left panel*), HAWKI J (*upper right panel*) and Spitzer-IRAC 3.6 μm (*lower panel*) images. The two galaxies are clearly resolved in the F850LP band image, they are resolved but their light profiles overlap in the HAWKI J band image and finally they are fully blended in the Spitzer-IRAC 3.6 μm image.

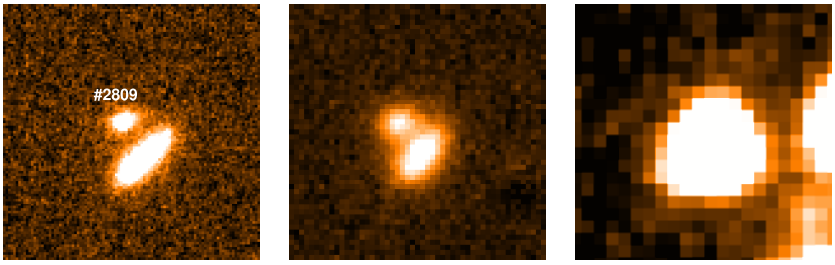

Figure 2.3: Galaxy #2809, which is closed to another galaxy, is shown. The two galaxies are resolved both in the F850LP band image (*left panel*) (FWHM $\sim$ 0.12") and in the HAWKI J band image (FWHM $\sim$ 0.5") (*central panel*), whereas they are completely blended in the Spitzer - IRAC 3.6 μm band image due to the lower resolution (FWHM $>$ 2.7") and bigger pixel size (0.6"/px) (*right panel*). The F850LP and J images are 5" x 5", the IRAC 3.6 μm image is 10" x 10".

Fig. 2.4 shows the cluster image obtained with the ACS F850LP band. The 17 selected ellipticals are circled in blue. The three central ellipticals spectroscopically identified are circled in yellow. From left to right they are: #1758, #1740 and #1782. The red circle set a distance of 1 Mpc from the cluster centre (Abell's radius). We can see the presence of a group of galaxies (including #595, #684, #692 and #837) that are very closed (the mean distance between the galaxies is $\sim$ 50-60 kpc) and seem to form a substructure, which has recently fallen inside the cluster due to its distance from the centre ($\gtrsim$ 650 kpc) (see Chapter 5). This group is circled in white. In table 2.4 I report the photometry in the 10 photometric bands for the 17 ellipticals of the sample.

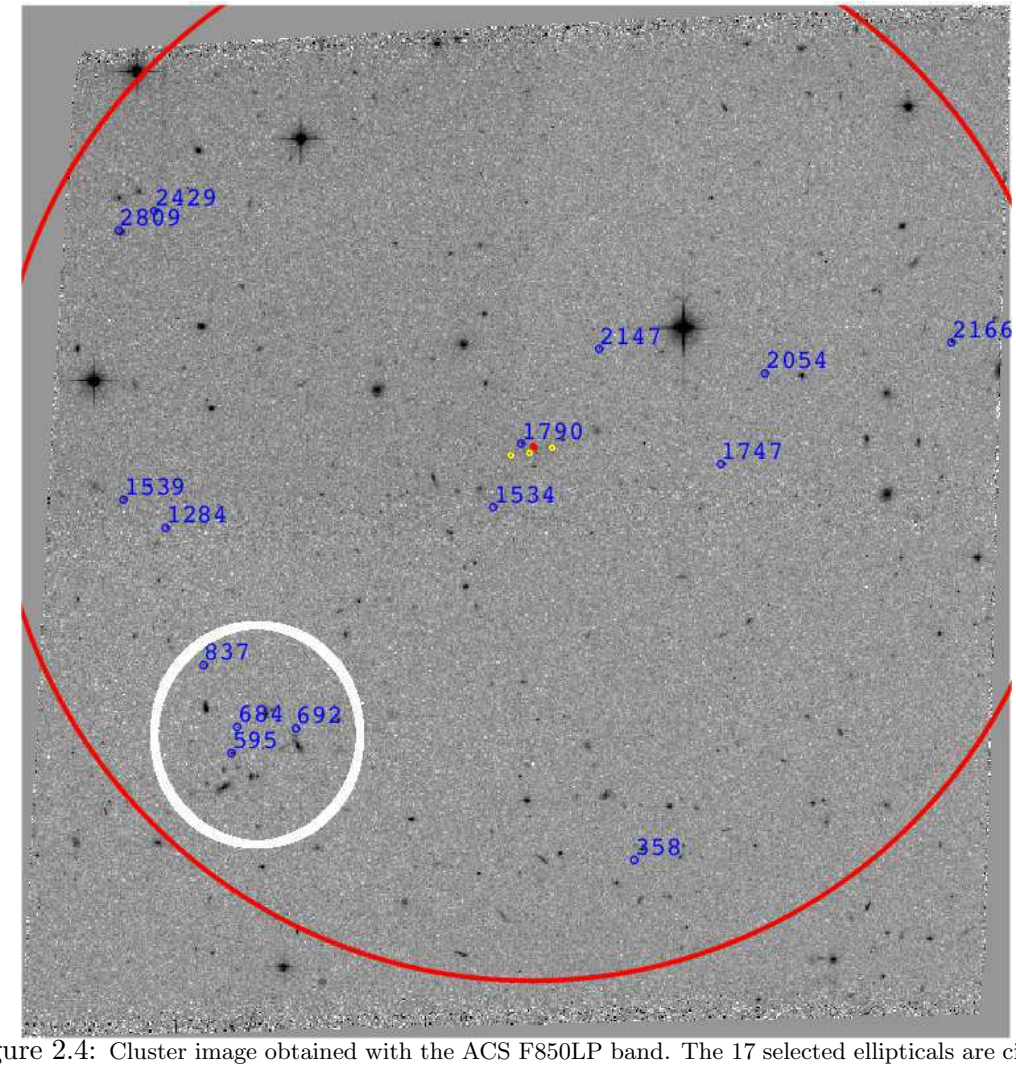

Figure 2.4: Cluster image obtained with the ACS F850LP band. The 17 selected ellipticals are circled in blue. The three central ellipticals spectroscopically identified are circled in yellow. From left to right they are: #1758, #1740 and #1782. The red point indicates the cluster centre. The red circle set a distance of 1 Mpc from the cluster centre (Abell's radius). Galaxies that are supposed to form a group falling into the cluster (see Chapter 5) are circled in white.

#ID	U	i_{775}	z_{850}	J	H_{160}	Ks	m3.6	m4.5	m5.8	m8.0
358	>28 99	24.85±0.05	23.91±0.04	22.14±0.1	—	20.41±0.05	19.84±0.1	19.69±0.1	19.53±0.4	19.33±0.4
595	27.8±0.3	23.17±0.02	22.16±0.01	20.23±0.03	19.35±0.03	18.35±0.01	16.70±0.1	16.23±0.1	15.99±0.1	15.94±0.2
684	25.9±0.1	24.19±0.03	23.33±0.03	21.92±0.07	21.10±0.06	20.11±0.03	18.15±0.02	17.79±0.03	17.31±0.1	17.41±0.2
692	>28 99	24.80±0.06	23.75±0.04	21.90±0.08	21.12±0.06	19.97±0.03	18.69±0.1	18.46±0.1	18.29±0.3	18.03±0.3
837	>28 99	23.76±0.03	22.77±0.03	20.59±0.05	19.83±0.04	18.61±0.02	16.99±0.01	16.49±0.02	16.38±0.08	16.10±0.1
1284	>28 99	23.65±0.02	22.70±0.02	20.91±0.04	20.22±0.04	19.16±0.02	17.56±0.01	17.09±0.02	16.77±0.09	16.84±0.1
1539	26.02±0.1	23.86±0.02	23.01±0.02	21.28±0.05	—	19.34±0.02	17.63±0.01	17.20±0.03	17.14±0.1	16.87±0.1
1740	24.30 0.05	22.42±0.02	21.48±0.02	18.55±0.02	18.68±0.02	17.44±0.01	15.60±0.1	15.17±0.1	15.17±0.1	14.82±0.2
1747	>28 99	24.79±0.05	23.70±0.04	22.06±0.09	21.25±0.06	20.08±0.03	18.73±0.02	18.41±0.04	18.56±0.3	99.00±99.0
1758	>28 99	24.16±0.03	23.13±0.02	20.46±0.04	20.33±0.04	19.09±0.01	17.58±0.1	17.14±0.1	16.70±0.1	16.89±0.2
1782	24.6±0.5	23.45±0.02	22.49±0.02	19.97±0.03	19.60±0.04	18.40±0.01	16.99±0.1	16.58±0.1	16.55±0.1	16.49±0.2
1790	>28 99	23.22±0.02	22.25±0.02	19.70±0.02	19.35±0.03	18.18±0.01	16.34±0.1	15.91±0.1	15.91±0.1	15.56±0.2
2054	>28 99	23.43±0.02	22.43±0.02	20.67±0.03	19.86±0.04	18.83±0.01	16.96±0.01	16.61±0.03	16.27±0.1	15.79±0.1
2147	>28 99	23.78±0.03	22.77±0.03	20.90±0.04	20.15±0.04	19.02±0.02	16.82±0.02	16.36±0.03	16.37±0.1	15.42±0.1
2166	26.50±0.1	22.80±0.01	21.73±0.01	20.53±0.03	—	18.73±0.01	17.33±0.01	17.13±0.03	17.02±0.1	16.68±0.1
2429	>28 99	24.41±0.03	23.24±0.02	21.96±0.08	21.04±0.06	20.05±0.03	18.15±0.02	17.98±0.04	17.91±0.2	17.36±0.2
2809	>28 99	23.41±0.01	22.33±0.01	20.92±0.03	—	19.28±0.01	18.36±0.1	17.99±0.1	17.96±0.2	16.71±0.2

Table 2.4: For each galaxy of the sample I report the photometry in the 10 photometric bands. Optical U-band and near-IR J- and Ks-band magnitudes come from VIMOS and HAWKI VLT observations respectively; i_{775}, z_{850} and H_{160} from ACS and WFC3 HST observations in the F775W, F850LP and F160W filters respectively; m3.6, m4.5, m5.8 and m8.0 from the Spitzer archival images in the corresponding filters. I adopted the MAG_BEST provided by SExtractor as total magnitude. A detailed description of the photometric measurements is given in §2.3.5.

2.4 Structural parameters

The structural parameters (effective radius, Sérsic index, axis ratio, position angle...) of the 17 selected ellipticals have been derived in the F775W, F850LP and F160W bands by fitting their surface brightness profile with a single Sérsic law

$$\mu(r) = \mu_e + \frac{2.5 b_n}{ln(10)}[(r/r_e)^{1/n} - 1] \tag{2.6}$$

where r_e is the effective radius (in arcsec) (the radius containing the 50% of the light of the galaxy), n is the Sérsic index and μ_e is the surface brightness at the effective radius. For large values of n the light is more concentrated towards the centre of the galaxy; for small n, instead, the profile has a flatter core with a sharp truncation at large radii (fig.2.5). Fixing n = 1 and n = 4, the Sérsic profile coincides with the exponential and the de Vaucouleurs profiles (de Vaucouleurs 1948), which are often used to describe the profiles of spiral and elliptical galaxies, respectively.

The two-dimensional fitting has been performed using `Galfit` software (Peng et al. 2002), a semiautomatic tool that, starting from initial parameters provided by the user, models the light profile of a galaxy. In the fitting procedure, the software convolves the model with the *point spread function* (PSF) of a star to take into account the diffraction and the spread of the light due to its passing through the telescope optics. In `Galfit` the indicator of the goodness of the fit is the reduced χ^2

$$\chi^2_\nu = \frac{1}{N_{DOF}} \sum_{x=1}^{nx} \sum_{y=1}^{ny} \frac{(f_{data}(x,y) - f_{model}(x,y))^2}{\sigma(x,y)^2} \tag{2.7}$$

where nx and ny are the total pixel number along the x and the y axis, N_{DOF} is the degree of freedom, f_{data} is the observed flux at the pixel (x, y), $\sigma(x, y)$ is the error associated to the observed flux and f_{model} is the flux of the model generated by `Galfit` by convolving the analytic function of the light profile with the PSF.

In order to provide the PSF for the fits, some stars spatially distant in the field have been selected and their light profiles have been analyzed through the IRAF task *imexamine* to check they were not saturated. After this analysis, the two brightest isolated and not saturated stars have been chosen as PSFs for the fits. In order to test for the dependence of our results on the PSF used, for each galaxy I have convolved the Sérsic profile with the two different PSFs. In fact, since the analytic function used to model the surface brightness profile of the galaxy is always the same, different values of χ^2_ν are due to the different PSFs used. The residual maps were lacking of any structure in both the cases and the returned χ^2 values were not statistically different, showing that the results do not depend on the PSF used. Thus, I chose the mean values of the fitting results as best fitting value for the structural parameters.

The output the software returns are the total magnitude m_{tot}, the Sérsic index n, the semimajor axis a and the axial ratio b/a, which are related to the surface brightness profile parameters by the following relations:

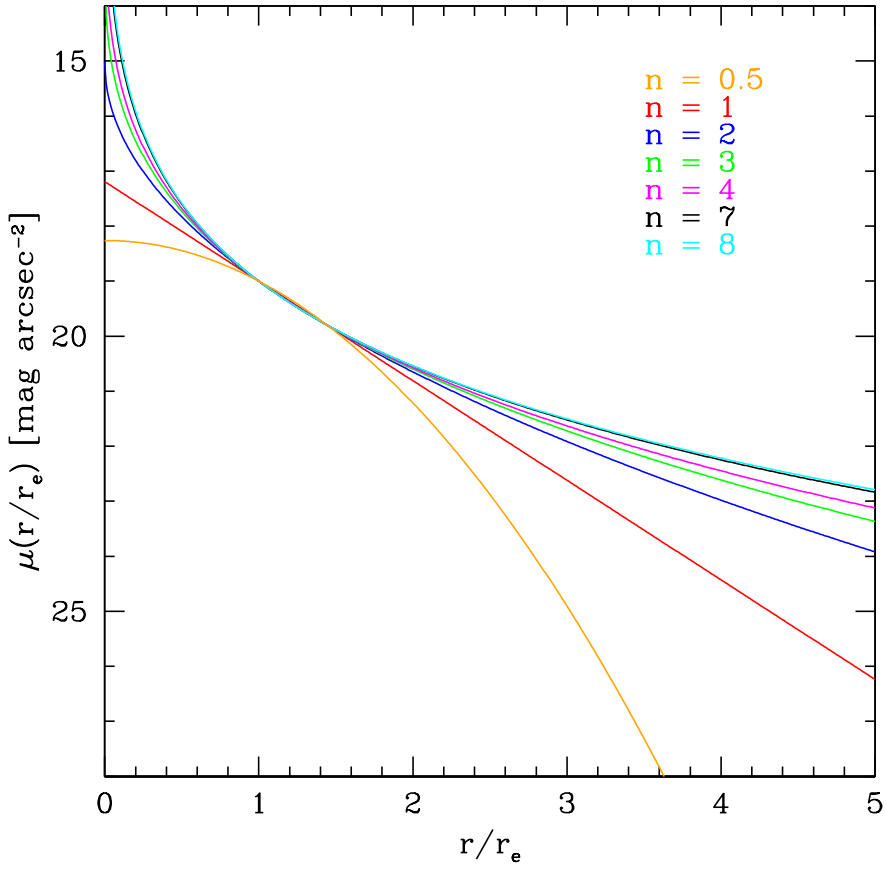

Figure 2.5: The Sérsic profile for different values of n. By increasing the value of n, the light is more concentrated towards the centre of the galaxy.

$$r_e = a\sqrt{(b/a)} \tag{2.8}$$

and

$$\mu_e =< \mu >_e + 2.5log[ne^b\Gamma(2n)/b^{2n}] \tag{2.9}$$

where $< \mu >_e = m_{tot} + 2.5log(2\pi r_e^2)$, $\Gamma(2n)$ is the complete Gamma function and $b = 2n - 1/3 + 0.009876/n$ (Prugniel and Simien 1997).

The first analysis has been performed keeping free all the input parameters required by `Galfit`, which are: the position of the galaxy in the image, the effective radius, the Sérsic index, the integrated magnitude, the axis ratio and the position angle. For the effective radius and for the Sérsic index indicative values have been chosen as initial guess: I have initialized the effective radius at 0.3" and the Sérsic index at 2; for the

remaining parameters the estimates obtained through SExtractor have been used.

The fitting was performed over a box of 7.5″x 7.5″ centered on the centroid of each galaxy derived by SExtractor. To derive the fitting box and the convolution box size (7.5″x 7.5″), I repeatedly fitted the surface brightness profiles by increasing the boxes size until the best-fitting parameters values converged. I masked every sources distant from the targets using the segmentation image generated by SExtractor, while I fitted simultaneously the sources close to the galaxies of the sample. These processes prevent the profile of the surrounding galaxies from overlapping the target profile.

For some galaxies (#358 and #684 both in the F775W and F850LP band, #1758 and #2429 only in the F160W band and #837 in all the three bands), the fitting procedure was not able to converge keeping free all the parameters. Hence, I re-performed the fit several times for different values of n and for each of them I obtained a set of structural parameters as output. I chose as best solution the set of structural parameters for which the reduced χ^2_ν was minimum. In table 2.5 I report for each galaxy the best-fitting n, R_e [kpc] and m_{tot} in the F775W, F850LP and F160W bands. The effective radii R_e, as derived by fitting the Sérsic law in the F850LP image, are in the range 0.9-7.8 kpc, with the exception of the dominant central galaxy of the cluster, which has an effective radius $R_e = 12.8$ kpc. The Sérsic index varies in the range 2.1 - 6, while the total magnitude m_{tot} varies in the range 20.78 - 23.47 mag. These galaxies follow the same scale relations of local ellipticals (Saracco et al. 2017). In particular, the comparison with the local Kormendy relation shows that the luminosity evolution due to the aging of the stellar content already assembled at z$\sim$1.4 brings them on the local relation.

In fig. 2.6 the 17 ellipticals of the sample selected according to the criteria described in the previous sections are shown (upper panels), together with the best-fitting surface brightness model (middle panels) and the residuals (lower panels). The goodness of the fit is shown by the lack of residuals obtained for all the galaxies. It is also worth noting that no structures are visible in the residuals, showing the regularity and the symmetry of the true profile.

The goodness of the fits is also shown in figure 2.7, where the observed surface brightness profiles of the galaxies are compared with the best fitting models generated by `Galfit`. The surface brightness has been measured within circular annuli centered on each galaxy

$$\mu = -2.5\ log\ \left(\frac{\Delta F}{A_{annulus}}\right) + Z_p \tag{2.10}$$

where ΔF is the difference between the flux in the aperture i and the flux in the aperture $i-1$ and $A_{annulus}$ is the area of the circular annulus between the radii R_{i-1} and R_i. The surface brightness profiles are plotted in blue (F775W), red (F850LP) and green (F160W) in figure 2.7. The error bars are obtained by propagating the errors on fluxes measured within the concentric annuli. In all the cases, a range of at least five magnitudes in surface brightness has been covered in the profiles of the galaxies which extend up to at least $\sim 2r_e$ for the largest galaxies. For the galaxies with a small r_e ($\sim 0.1'' - 0.2''$) the observed brightness profiles extend up to $\sim$ 4 - 5 r_e. I used

simulations to test the reliability of the surface brightness profile fitting and to estimate the uncertainties affecting the resulting structural parameters (see §2.4.1).

To derive the colour variation along a fixed radius (see Chapter 3) it is necessary to evaluate the galaxies light profiles in each band along ellipses with the same orientation and ellipticity in order to prevent any artificial gradients. Hence, I re-run `Galfit` on the F775W and the F160W images keeping fixed the position angle PA and the axial ratio b/a at the values derived on the F850LP image by `Galfit`. I chose the F850LP band as reference image for its better resolution (FWHM $\sim 0.11''$) and good sampling of the PSF (pixel size $= 0.05''$). Moreover, given the shallower surface brightness, it determines the maximum radius at which we can reliably estimate radial gradients (see discussion in the next Chapter). In table 2.6 I report for each galaxy the best-fitting n, R_e [kpc] and m_{tot} in the F775W, F850LP and F160W bands obtained taking as reference the position angle and the axis ratio derived in the F850LP image. In the same table, I also report in the second row the parameters obtained assuming $n = 4$, i.e. a de Vaucouleur's profile.

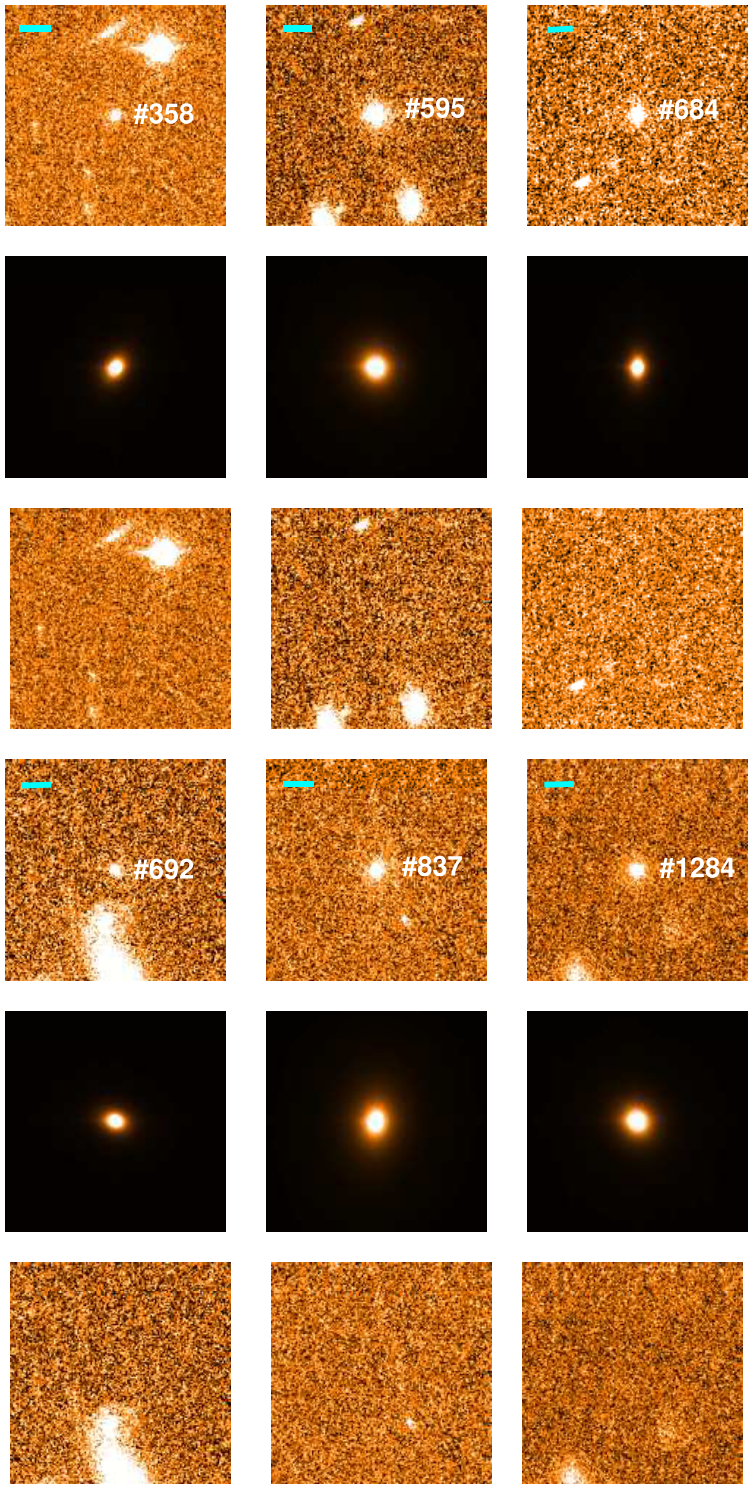
#358
#595
#684
#692
#837
#1284

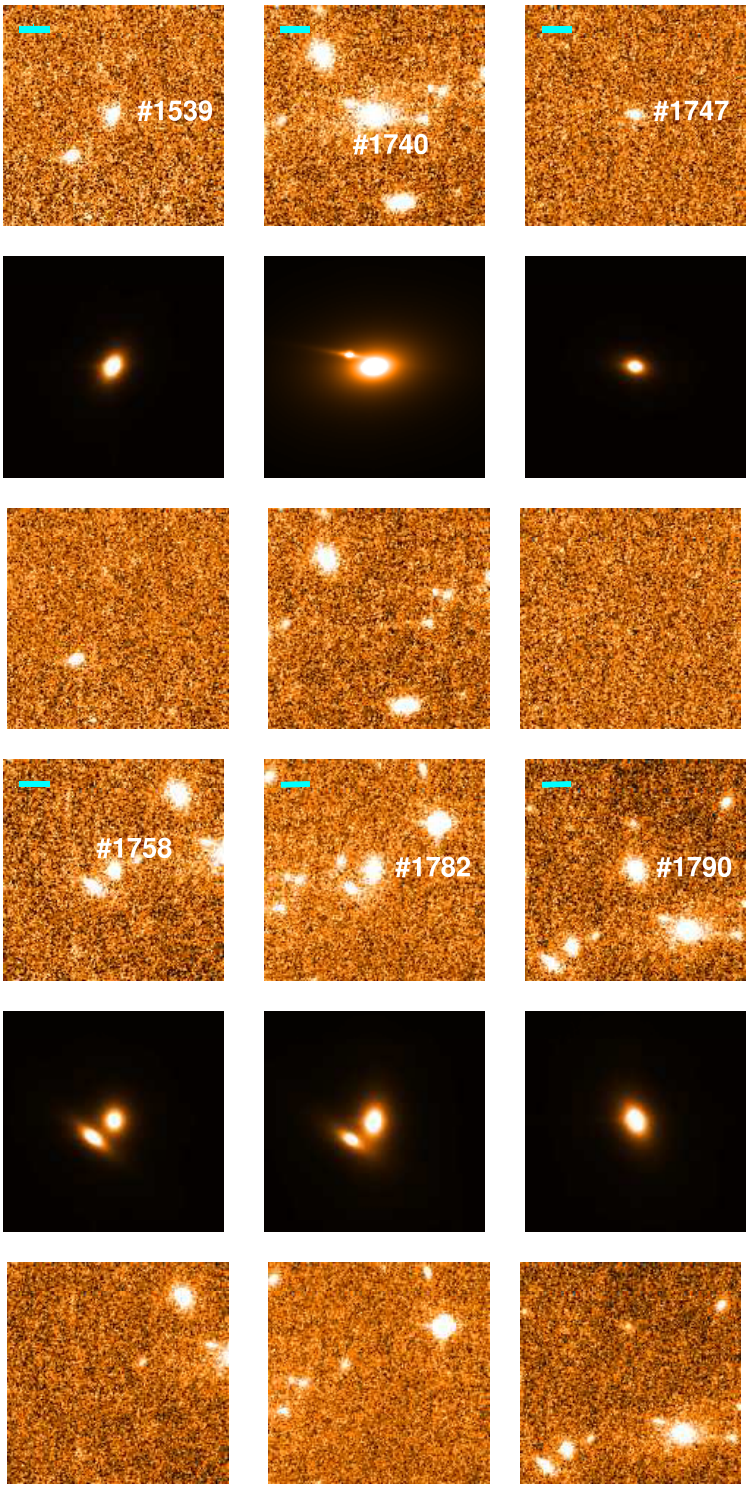
#1539
#1740
#1747
#1758
#1782
#1790

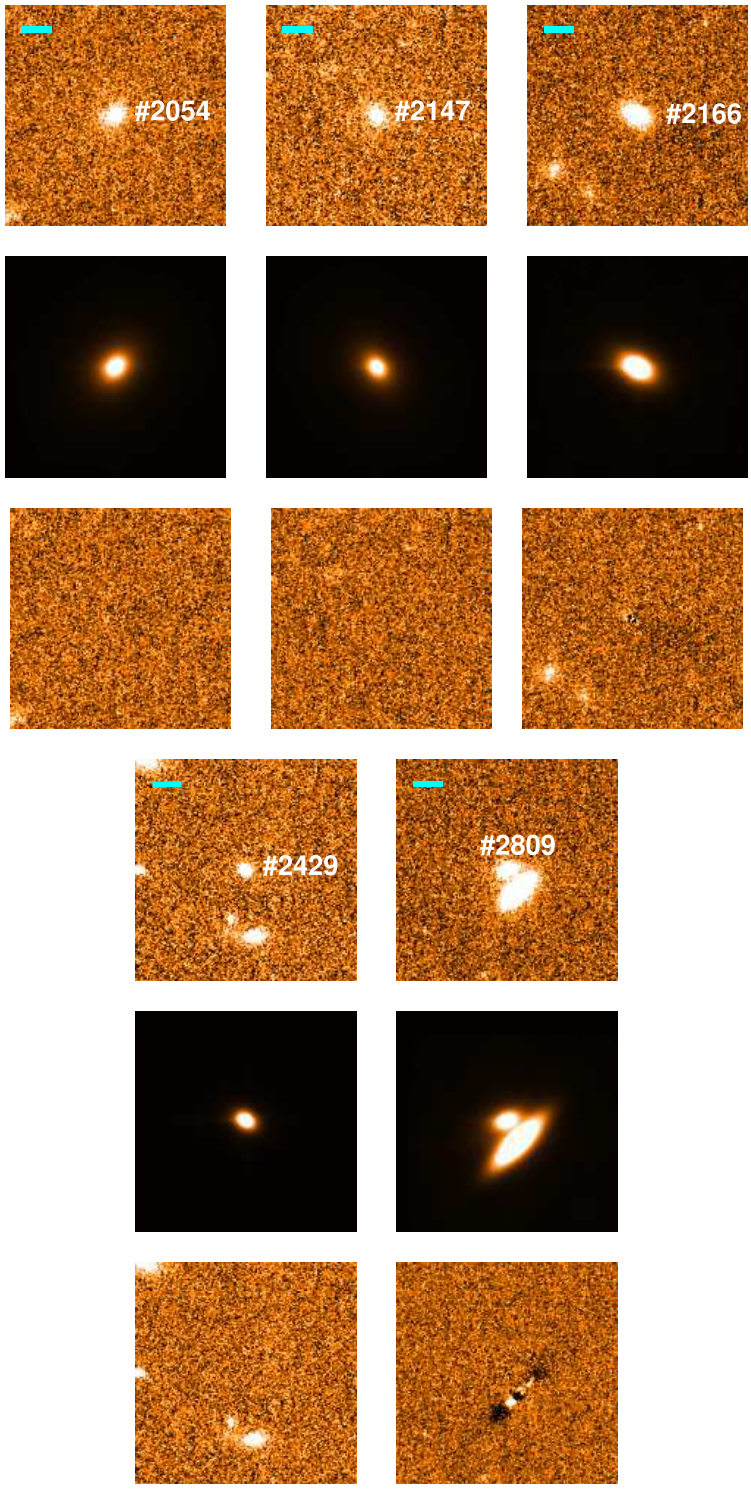

Figure 2.6: Each column shows the GALFIT input and output for the 17 cluster ellipticals at z = 1.45: ACS F850LP band image of the galaxy (upper box), best-fitting Sérsic model profile (middle box) and residual image (lower box) obtained by subtracting the model from the image. Galaxies are (from top left to bottom right): #358, #595, #684, #692, #837, #1284, #1539, #1740, #1747, #1758,#1782, #1790, #2054, #2147, #2166, #2429 and #2809. Each image is 7.5 x 7.5 arcsec^2. The cyan line corresponds to 1".

Table 2.5: For each galaxy of the sample I report the ID number, the Sérsic index n, the total magnitude and the effective radius R_e [kpc] as derived from the fitting of the surface brightness profile in the F775W, F850LP and F160W images, respectively. For the F850LP band I also report the axial ratio $(b/a)_{850}$.

ID	n_{775}	i_{775}^{fit} [mag]	R_e^{775} [kpc]	n_{850}	z_{850}^{fit} [mag]	R_e^{F850} [kpc]	$(b/a)_{850}$	n_{160}	H_{160}^{fit} [mag]	R_e^{F160} [kpc]
358	6.0±0.4	24.5±0.2	1.1±0.1	6.0±0.4	23.5±0.1	1.5±0.2	0.6±0.1	—	—	—
595	5.7±0.3	22.9±0.1	2.1±0.3	5.6±0.3	21.6±0.1	3.5±0.5	0.9±0.1	4.5±0.1	19.2±0.1	2.5±0.1
684	6.0±0.4	24.1±0.2	0.6±0.1	6.0±0.4	22.9±0.1	1.4±0.2	0.6±0.1	4.0±0.1	20.9±0.1	0.8±0.1
692	4.0±0.2	24.7±0.2	1.3±0.1	4.1±0.2	23.5±0.2	1.5±0.2	0.7±0.1	3.0±0.1	21.0±0.1	0.9±0.1
837	6.0±0.2	23.3±0.1	4.3±0.6	6.0±0.4	21.9±0.1	7.8±1.1	0.7±0.1	6.0±0.2	19.4±0.1	5.2±0.2
1284	4.3±0.3	23.4±0.1	2.0±0.3	4.3±0.2	22.3±0.1	2.4±0.3	0.9±0.1	4.0±0.1	20.0±0.1	1.7±0.1
1539	4.8±0.3	23.7±0.2	1.1±0.1	3.5±0.2	22.7±0.1	1.5±0.2	0.6±0.1	—	—	—
1740	3.3±0.2	21.8±0.1	13.3±2.0	3.3±0.2	20.8±0.1	12.8±1.9	0.6±0.1	4.6±0.1	17.8±0.1	20.7±0.9
1747	4.3±0.2	24.7±0.2	0.7±0.1	4.8±0.3	23.3±0.1	1.7±0.2	0.6±0.1	4.0±0.2	21.1±0.1	0.9±0.1
1758	2.9±0.2	23.9±0.2	1.9±0.2	2.9±0.2	22.6±0.1	2.5±0.3	0.8±0.1	2.90±0.04	20.3±0.1	1.5±0.1
1782	2.6±0.2	23.5±0.1	1.6±0.1	3.6±0.2	22.5±0.1	3.4±0.5	0.6±0.1	3.11±0.04	19.5±0.1	2.2±0.1
1790	4.4±0.3	23.1±0.1	1.9±0.2	4.4±0.3	21.9±0.1	2.4±0.3	0.6±0.1	4.1±0.1	19.3±0.1	2.3±0.1
2054	5.0±0.3	23.2±0.1	2.7±0.4	4.4±0.3	21.9±0.1	4.2±0.6	0.7±0.1	5.0±0.1	19.5±0.1	3.7±0.2
2147	5.4±0.3	23.5±0.1	3.6±0.5	5.3±0.3	22.2±0.1	5.3±0.8	0.7±0.1	4.0±0.1	20.0±0.1	2.3±0.1
2166	3.6±0.2	22.6±0.1	1.2±0.1	3.0±0.2	21.5±0.1	1.4±0.1	0.6±0.1	—	—	—
2429	2.1±0.4	24.3±0.2	0.6±0.1	2.1±0.2	23.0±0.1	0.9±0.1	0.6±0.1	2.1±0.1	21.0±0.1	0.9±0.1
2809	4.8±0.3	23.3±0.1	1.2±0.1	3.2±0.2	22.7±0.1	1.4±0.2	0.6±0.1	—	—	—

Table 2.6: For each galaxy of the sample I report the ID number, the Sérsic index n, the total magnitude and the effective radius R_e [kpc] as derived from the fitting of the surface brightness profile in the F775W, F850LP and F160W images, taking as reference the position angle and the axis ratio b/a_{850} obtained in the F850LP image. For each galaxy I report, in the second row, the values obtained for a de Vaucouleur's profile ($n = 4$).

ID	n_{775}	i_{775}^{fit} [mag]	R_e^{775} [kpc]	n_{850}	z_{850}^{fit} [mag]	R_e^{F850} [kpc]	$(b/a)_{850}$	n_{160}	H_{160}^{fit} [mag]	R_e^{F160} [kpc]
358	6.0±0.4	24.5±0.2	1.1±0.1	6.0±0.4	23.5±0.1	1.5±0.2	0.6±0.1	—	—	—
”	—	24.8±0.2	0.8±0.1	4.0	23.7±0.1	1.0±0.2	—	—	—	—
595	5.7±0.3	22.9±0.1	2.2±0.3	5.6±0.3	21.6±0.1	3.5±0.5	0.9±0.1	4.5±0.1	19.2±0.1	2.5±0.1
”	—	23.1±0.1	1.5±0.3	4.0	21.9±0.1	2.2±0.5	—	—	19.2±0.1	2.3±0.1
684	6.0±0.4	24.0±0.2	0.7±0.1	6.0±0.4	22.9±0.1	1.4±0.2	0.6±0.1	4.1±0.1	20.9±0.1	0.8±0.1
”	—	24.2±0.2	0.5±0.1	4.0	23.1±0.1	1.0±0.2	—	—	20.9±0.1	0.8±0.1
692	4.5±0.2	24.3±0.2	1.3±0.1	4.1±0.2	23.5±0.2	1.5±0.2	0.7±0.1	3.0±0.1	21.0±0.1	0.9±0.1
”	—	24.7±0.2	1.3±0.1	4.0	23.5±0.2	1.5±0.2	—	—	20.9±0.1	1.1±0.1
837	6.0±0.2	23.3±0.1	5.2±0.6	6.0±0.4	21.9±0.1	7.8±1.1	0.7±0.1	6.0±0.2	19.4±0.1	5.2±0.2
”	—	23.6±0.1	2.3±0.6	4.0	22.3±0.1	8.0±1.1	—	—	19.7±0.1	7.2±0.2
1284	4.3±0.3	23.4±0.1	1.8±0.3	4.3±0.2	22.3±0.1	2.4±0.3	0.9±0.1	4.0±0.1	20.0±0.1	1.7±0.1
”	—	23.4±0.1	1.9±0.3	4.0	22.3±0.1	2.3±0.3	—	—	20.0±0.1	1.7±0.1
1539	4.8±0.3	23.7±0.2	1.1±0.1	3.5±0.2	22.7±0.1	1.5±0.2	0.6±0.1	—	—	—
”	—	23.8±0.2	1.0±0.1	4.0	22.6±0.1	1.7±0.2	—	—	—	—
1740	3.3±0.2	21.8±0.1	12.7±1.9	3.3±0.2	20.8±0.1	12.8±1.9	0.6±0.1	4.6±0.1	17.8±0.1	20.7±0.9
”	—	21.5±0.1	20.1±2.0	4.0	20.5±0.1	19.5±1.9	—	—	18.0±0.1	15.4±0.9
1747	4.3±0.2	24.6±0.2	0.8±0.1	4.8±0.3	23.3±0.1	1.7±0.2	0.6±0.1	4.0±0.2	21.1±0.1	0.9±0.1
”	—	24.7±0.2	0.7±0.1	4.0	23.4±0.1	1.5±0.2	—	—	21.1±0.1	0.9±0.1
1758	2.9±0.2	23.9±0.2	1.9±0.2	2.9±0.2	22.6±0.1	2.5±0.3	0.8±0.1	2.90±0.04	20.3±0.1	1.5±0.1
”	—	23.7±0.2	1.9±0.2	4.0	22.4±0.1	3.8±0.3	—	—	20.1±0.1	1.0±0.1
1782	2.5±0.2	23.5±0.1	1.7±0.1	3.6±0.2	22.5±0.1	3.4±0.5	0.6±0.1	3.11±0.04	19.4±0.1	2.2±0.1
”	—	22.9±0.1	3.4±0.1	4.0	22.0±0.1	3.5±0.5	—	—	19.4±0.1	2.0±0.1
1790	4.4±0.3	23.1±0.1	1.9±0.2	4.4±0.3	21.9±0.1	2.4±0.3	0.6±0.1	4.1±0.1	19.3±0.1	2.3±0.1
”	—	23.2±0.1	1.8±0.2	4.0	22.0±0.1	2.2±0.3	—	—	19.3±0.1	2.2±0.1
2054	5.1±0.3	23.2±0.1	2.9±0.4	4.4±0.3	21.9±0.1	4.2±0.6	0.7±0.1	5.1±0.1	19.5±0.1	3.7±0.2
”	—	23.3±0.1	2.2±0.4	4.0	22.0±0.1	3.7±0.6	—	—	19.6±0.1	2.9±0.2
2147	5.4±0.3	23.5±0.1	3.6±0.5	5.3±0.3	22.2±0.1	5.3±0.8	0.7±0.1	4.1±0.1	20.0±0.1	2.3±0.1
”	—	23.7±0.1	2.3±0.5	4.0	22.4±0.1	3.4±0.8	—	—	20.0±0.1	2.3±0.1
2166	3.6±0.2	22.6±0.1	1.2±0.1	3.0±0.2	21.5±0.1	1.4±0.1	0.6±0.1	—	—	—
”	—	22.6±0.1	1.3±0.1	4.0	21.4±0.1	1.7±0.1	—	—	—	—
2429	2.1±0.4	24.3±0.2	0.7±0.1	2.1±0.2	23.0±0.1	0.9±0.1	0.6±0.1	2.1±0.1	21.0±0.1	0.9±0.1
”	—	24.3±0.2	0.7±0.1	4.0	22.8±0.1	1.2±0.1	—	—	20.9±0.1	1.0±0.1
2809	4.8±0.3	23.3±0.1	1.2±0.1	3.2±0.2	22.7±0.1	1.4±0.2	0.6±0.1	—	—	—
”	—	23.3±0.1	1.1±0.1	4.0	22.0±0.1	1.6±0.2	—	—	—	—

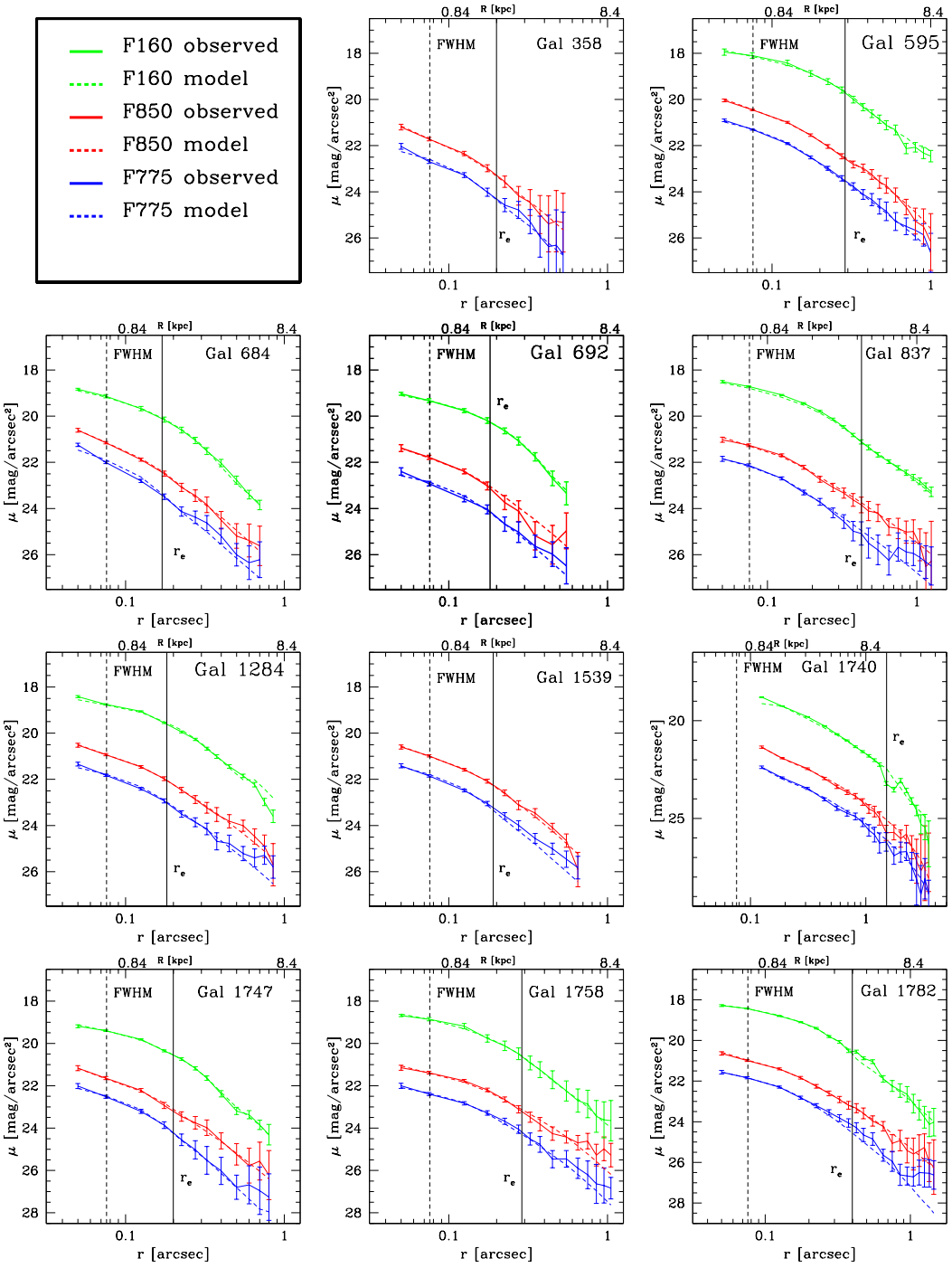
F160 observed
F160 model
F850 observed
F850 model
F775 observed
F775 model
Gal 358
Gal 595
Gal 684
Gal 692
Gal 837
Gal 1284
Gal 1539
Gal 1740
Gal 1747
Gal 1758
Gal 1782
FWHM
R [kpc]
0.84
8.4
μ [mag/arcsec²]
r [arcsec]
r_e

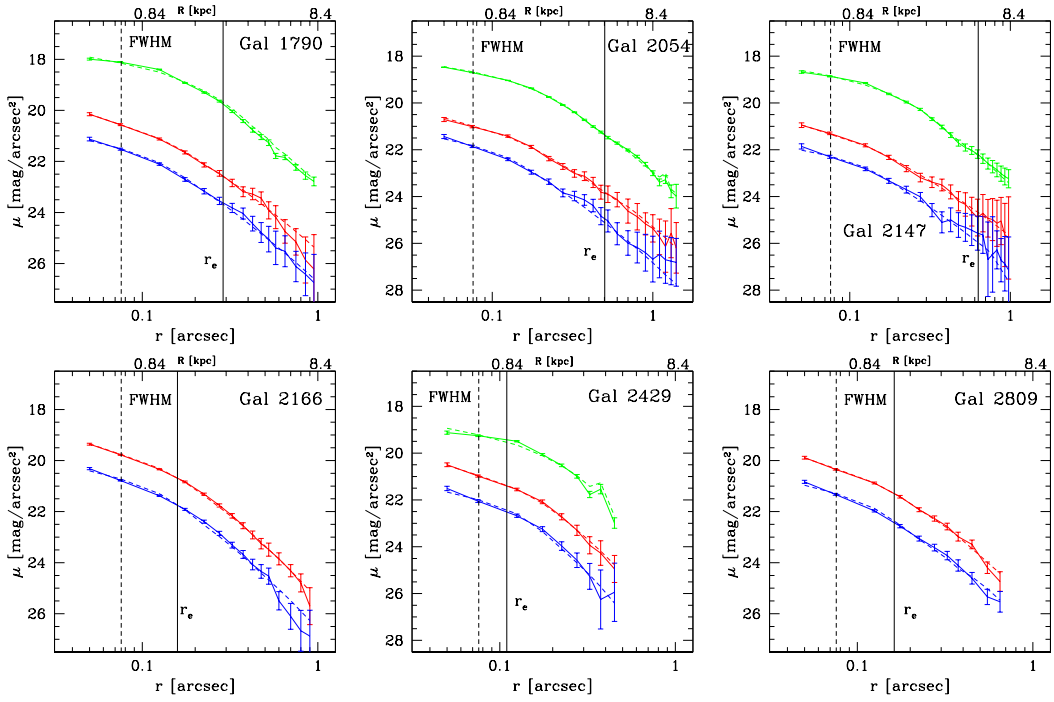

Figure 2.7: Comparison between the observed brightness profiles (solid lines) and the models obtained with `Galfit` (dashed lines) in the three HST bands for the 17 ellipticals of the sample. The surface brightness profiles in the F775W, F850LP and F160W bands are plotted in blue, red and green, respectively. The surface brightness has been measured within circular annuli centered on each galaxy. The black dashed vertical line represents the radius of the FWHM of the PSF ($\sim 0.06''$), while the black solid vertical line corresponds to the effective radius of the galaxy derived in the F850LP band.

2.4.1 Simulations

In order to test for the absence of systematics introduced by the fitting algorithm and to derive reliable statistical errors for the structural parameters, the same fitting procedure has been performed to a set of simulated galaxies. In particular, to test for the absence of systematics, I generated with `Galfit` a set of ~ 8000 galaxies described by a Sérsic profile with effective radius r_e, index of concentration n and magnitude m assigned in the ranges $0.1'' < r_e < 2''$ with a step of 0.03, $2 < n < 7$ with a step of 0.5 and $20 < m < 24.5$ mag with a step of 0.25. These selected ranges are a good representation of the cluster sample. The simulated galaxies have been convolved with the HST-ACS F850LP PSF and embedded in the real background, constructed by cutting different portions devoid of sources from the real image. For each structural parameters I verified how the output values vary as a function of the input values, keeping fixed the other two structural parameters.

In fig. 2.8 I plot the output values m_{out}, $r_{e,out}$ and n_{out} versus the input values m_{in}, $r_{e,in}$ and n_{in} (upper left panel, upper right panel and lower panel, respectively). For $m < 24$ mag, $n < 6$ and $r_e < 1''$ `Galfit` recovers exactly the input values. For $m > 24$ mag, $n > 6$ and $r_e > 1''$ the output m, r_e and n are, on average, underestimated of $\sim$ 9%, $\sim$ 8% and $\sim$ 15%, respectively. These underestimates are negligible compared to the statistical errors and they are possibly due to the fact that for galaxies having larger surface brightness profile tails we miss a larger fraction of the profile since it is dominated by the background. This would drop abruptly the brightness profile and favour lower values of n in the fitting. Since the selected galaxies have $m < 24$ mag, $r_e < 1''$ and $n < 6$, I did not apply any correction to the values of the structural parameters obtained by the fitting.

I repeated the same procedure for the F160W image in order to test for the absence of systematics for the HST-WFC3 as well. The simulated galaxies have been generated with $0.1'' < r_e < 2''$ and $2 < n < 7$ (as for the F850LP image) and $18 < m < 21$ mag. I found the same results obtained for the F850LP simulated galaxies.

I also verified for each structural parameter whether a dependence of the output values on the input values of the other structural parameters was present (e.g., output r_e versus input n and m) and no trend was found. As example, in fig. 2.9 I show $\Delta mag = m_{in}$ - m_{out} as a function of the input values of r_e and n (left and right panel, respectively). It results that no dependence of m_{out} on input r_e and n is present.

To derive the statistical uncertainties of each parameter, that is how the background RMS affects the estimates of the structural parameters, I have considered a subsample of the $\sim$ 200 simulated galaxies and I embedded each of them in ten different real backgrounds. Then, for each galaxy, I have run `Galfit` to derive the best fitting parameters for the ten different backgrounds. The standard deviation of the mean has been employed as indicator of the statistical fluctuations.

Finally, I exploited these simulations to assess a reliable magnitude estimator for the galaxies in our images. To this end, I compared the SExtractor MAG_BEST magnitude obtained for a subsample of $\sim$ 180 simulated galaxies to the input F850LP and F160W magnitude. Fig. 2.10 (upper panel) shows the comparison between magnitudes derived

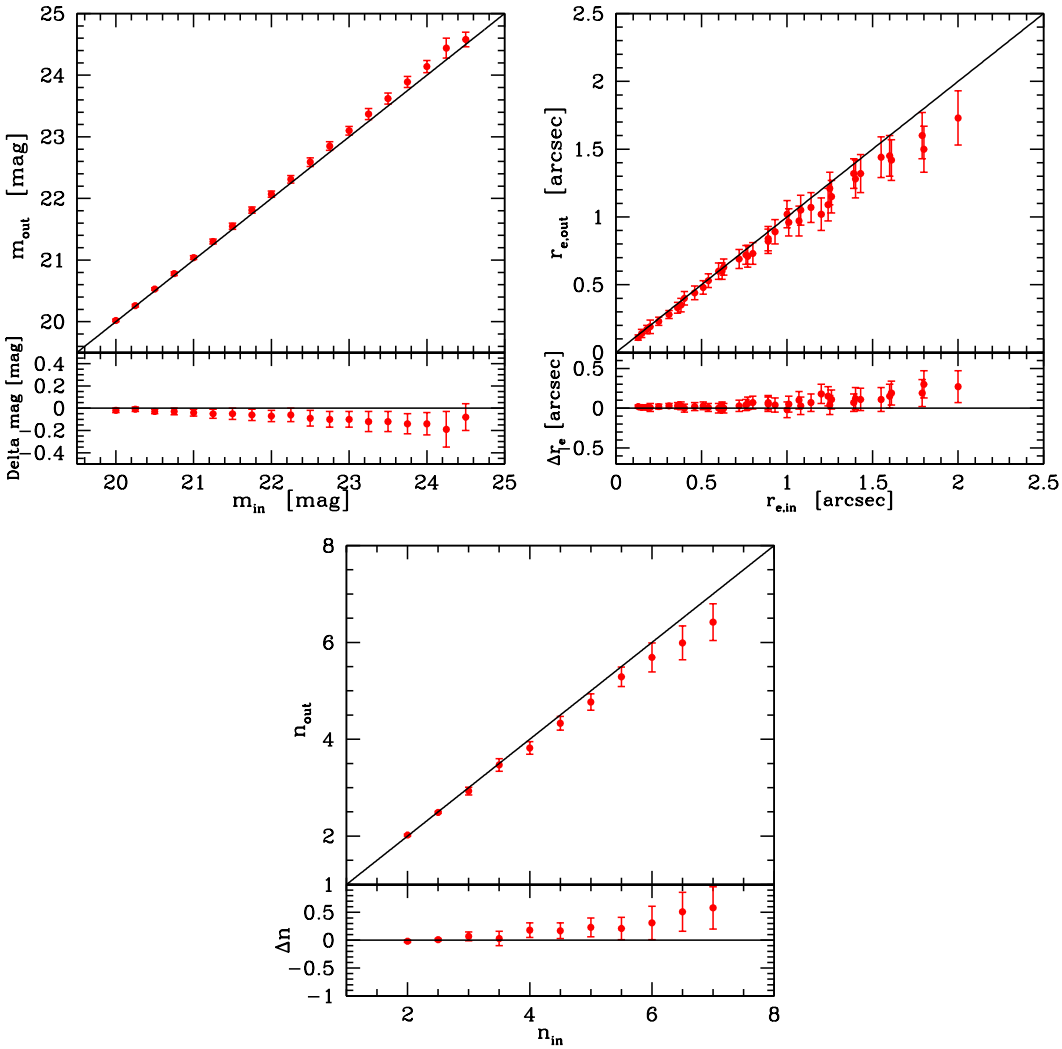

Figure 2.8: Comparison between the magnitude (m_{in}), the effective radius ($r_{e,in}$) and the index of concentration (n_{in}) of the simulated galaxies and the magnitude (m_{out}), the effective radius ($r_{e,out}$) and the index of concentration (n_{out}) obtained through the fitting with the Sérsic profile (upper left-hand and right-hand panel, respectively). The differences $\Delta r_e = r_{e,in} - r_{e.out}$ and $\Delta n = n_{in} - n_{out}$ are plotted as a function of the input parameters (lower left-hand and right-hand panel, respectively).

by SExtractor (m_{sex}) in the F850LP band and input magnitudes (m_{in}) for the simulated galaxies. The difference $\Delta mag = m_{sex} - m_{in}$ is plotted as a function of the input magnitude in the lower panel. I found that m_{sex} is systematically fainter than m_{in} and the offset increases with fainter magnitudes. In particular, for magnitudes $m_{in} < 23$ mag, the offset is ~ 0.18 mag; for $m_{in} > 23$ mag, instead, the offset increases becoming

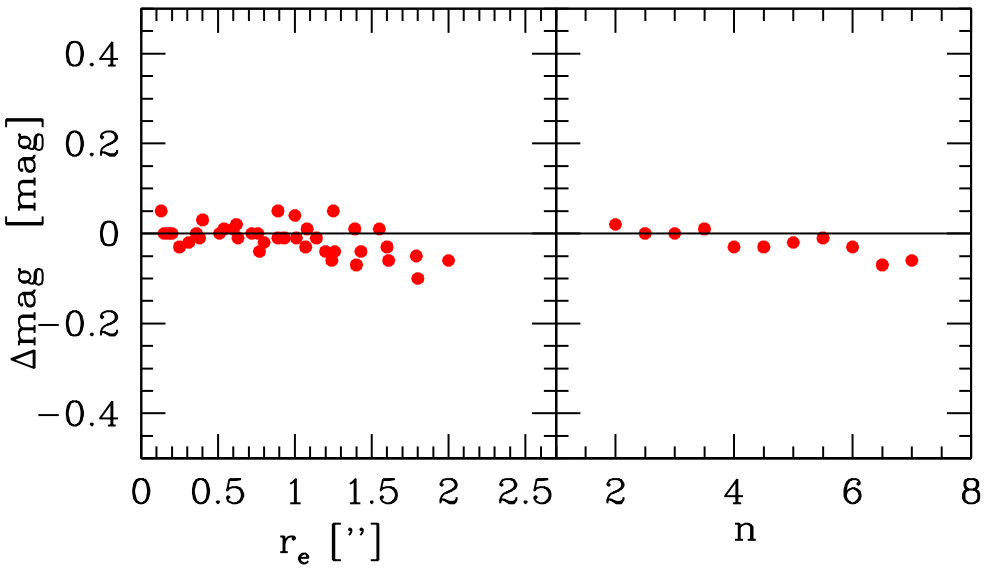

Figure 2.9: Comparison between $\Delta mag = m_{in} - m_{out}$ and the input values of r_e and n (left and right panel, respectively).

larger than 0.3 - 0.4 mag. The presence of the observed offset is due to the fact that we loose part of the flux of the external regions of the galaxies since it is dominated by the background. In the case of the F160W band, I obtained the same offset. Hence, the photometry needs to be corrected taking into account this offset. Anyway, these underestimates do not affect the colours of the galaxies. Indeed, since the offset is the same in each band, when the colour is computed via the fluxes ratio no spurious colour is introduced. In this case, I did not apply any correction to the photometry. On the contrary, these underestimates have been taken into account when I derived the global properties of the galaxies (i.e., the stellar mass) through the SED-fitting technique (see Chapter 4). In this case, an underestimate of the fluxes would lead to an underestimate of the global properties of the galaxies. The photometry reported in table 2.4 is the one derived through SExtractor with no corrections applied.

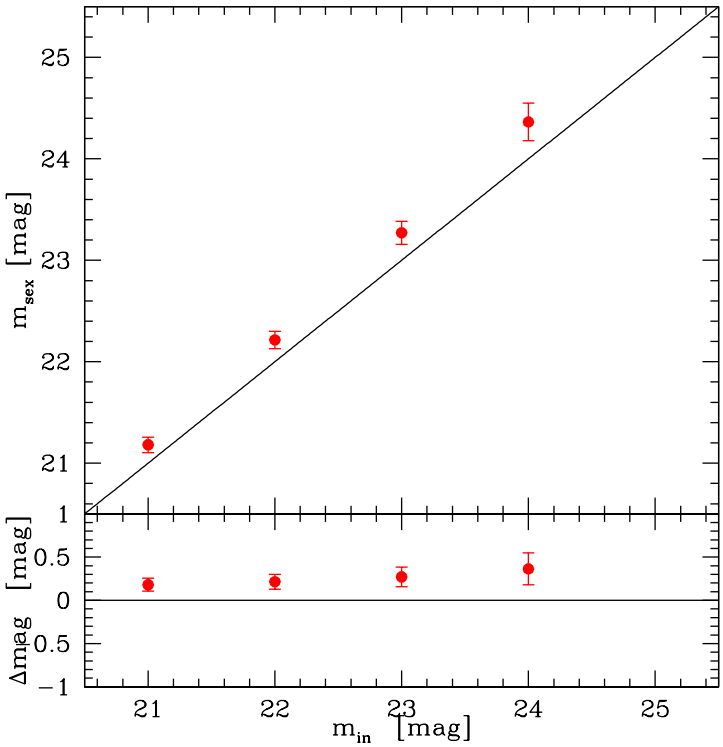

Figure 2.10: Comparison between magnitudes derived by SExtractor (m_{sex}) and input magnitudes (m_{in}) for the simulated galaxies (upper panel). The difference $\Delta mag = m_{sex} - m_{in}$ is plotted as a function of the input magnitude in the lower panel.

2.5 Global physical properties of the galaxies of our sample

2.5.1 The stellar population synthesis models

The analysis of the properties of the galaxy stellar populations (e.g. age and metallicity) is based on the comparison between their spectro-photometric characteristics and the predictions of the stellar population synthesis models. The basic idea of the stellar population synthesis models is that a galactic spectrum can be represented through the sum of the spectra of its stars (Tinsley 1972; Larson and Tinsley 1978). These models are based on a variety of stellar evolutionary tracks and on theoretical or observed stellar spectra. The first ones are built for any combination of the physical stellar parameters, i.e. surface temperature, chemical composition and gravity, on the basis of the stellar evolution theory; the second ones, instead, are composed by spectra of real stars. These models are able to reproduce the observed spectrum of a galaxy basing on a set of initial parameters: *initial mass function* (IMF), *metallicity* (Z) and *star formation rate* (SFR).

- *Initial Mass Function*: The initial mass function ($\xi(m)$) is a function, which defines the numbers of stars formed per stellar mass interval. The IMF is one of the factors that mostly affects the evolution of the spectro-photometric characteristics of a stellar population. Indeed, high mass stars (M $>$ 5 $M_\odot$) evolve very quickly and leave the main sequence in a very short time, not contributing anymore to the total light of stellar populations. On the contrary, low mass stars (M $<$ 1 $M_\odot$) evolve slowly and their contribution to the total emission is predominant over longer time-scales. The differences between high mass stars and low mass stars are reflected on their spectrum: the first ones present a dominant emission towards the blue/ultraviolet wavelengths, whereas the second ones emit mainly in the optical/infrared region.

  Generally, the IMF is assumed to have a simple power law

  $$\xi(m) = cM^{-\alpha} \tag{2.11}$$

  and to extend from a lower to an upper cutoff, chosen to be 0.1 $M_\odot$ and 125 $M_\odot$. The IMF in the field star population of the Milky Way more massive than our sun was first quantified by Edwin Salpeter (1955). His work favoured an exponent of α =2.35. Recently, other IMFs have been assumed in order to take into account observational indications of a flattening of the IMF at low masses (e.g. Chabrier 2003).

  The IMF is assumed to universal, i.e. invariant both throughout the different classes of galaxies and across the cosmic time, even if recently some works have casted doubts on the IMF universality (e.g., Bastian et al. 2013; Kroupa et al. 2013).

- *Metallicity*. Another important parameter to build a model is the metallicity (Z) of the stellar population, which is defined as the fraction of mass of elements different

from hydrogen (X) or helium (Y), so that X + Y + Z = 1. In particular, for the Sun Z = 0.02. Metal-rich stars have a slightly redder spectrum than metal-poor stars. Indeed, the effect on the global properties of a stellar population is that the increasing of metallicity produces the redding of its continuum. As it will be shown in the next section, the same effect can be produced by the ageing of the stellar population itself, causing the well known age-metallicity degeneracy.

- *Star Formation Rate.* The simplest way to model a stellar population is through the Simple Stellar Population (SSP), which is defined as an assembly of stars formed at the same time and from the same nebular cloud. This population, thus, at each fixed age, is coeval and have the same metallicity.

  The simple stellar population model is an approximation of the stellar populations in galaxies. Indeed, in a real situation, galaxies are more complex structures, formed by the addition of more SSPs. Hence, galaxies may experience different bursts of star formation protracted over time, leading to the creation of a more complex model (*composite stellar population or CSP*). The CPSs are characterized by a more complex star formation rate (SFR) and star formation history compared to a SSP.

  In the stellar population synthesis models it is generally assumed for a CSP a star formation history with a SFR exponentially declining with a time-scale τ (Tosi 1988):

$$SFR = SFR_0 \, e^{-\frac{t}{\tau}} \tag{2.12}$$

  where SFR_0 is the initial star formation rate. Typically, ellipticals heve low SFR; the comparison with models shows that they are well described by $\tau < 1$ Gyr. The longer the time-scale τ, the larger the spread of the star formation over the time, tending to 0 for $\tau \to \infty$; on the contrary, if τ is very small, the burst of star formation is very short, reproducing the instantaneous burst of a SSP for $\tau \to 0$.

In my analysis, I used the stellar population models of Bruzual & Charlot (2003, hereafter BC03). These models consist on a matrix of data that, at fixed age, lists the fluxes for each wavelength available in the spectra. The age range covered is between $1 \cdot 10^5$ yr and $2 \cdot 10^{10}$ yr and the fluxes are normalized at $1 M_\odot$. The authors provide the template spectra in a wide range, from 91 Å to 1600000 Å, at low resolution with the theoretical spectral library BaSeL. Template spectra based on library of observed stellar spectra, named STELIB, are available in a wavelength range from 3200 Å to 9500 Å with an high resolution. The metallicity range covered is $0.004 < Z < 0.04$.

2.5.2 Dependence of the SED of a galaxy on age, metalliticity and star formation rate

As mentioned above, the SED of a galaxy strongly depends on the age, metallicity and star formation rate of its stellar populations. In fig 2.11 (upper left panel) it is shown the model SEDs for different values of ages of the stellar population at fixed τ=0.1 Gyr, Z=$Z_{\odot}$, Chabrier IMF. At increasing age it can be observed the growth of the infrared emission due to the ageing of the stellar populations. This is due to the fact that the emission of a star strongly depends on its age: young massive stars emit mostly in the UV range, whereas old low mass stars emit mostly at infrared wavelength. Moreover a stellar population of 3 Gyr has a spectral shape more similar to a 10 Gyr one than to a 0.5 Gyr, since the time elapsed from the star formation epoch for t = 3 Gyr is much longer than the star formation time-scale (t $\gg \tau$) than for t = 0.5 Gyr. Hence, the stellar component is much more similar to the 10 Gyr population. The SEDs are normalized at 4000 Å $\leq \lambda \leq$ 5000 Å.

The role played by star formation time-scale is shown in fig. 2.11 (upper right panel), where it is shown how the SED of a stellar population changes by fixing the age (3 Gyr), the metallicity (Z=$Z_{\odot}$) and Chabrier IMF and varying the star formation time-scale from 0.1 Gyr (blue curve) to 5.0 Gyr (magenta curve). If the star formation time-scale is of the same order of the age of the stellar population (e.g. magenta curve in figure 2.11 left panel), the star formation process is still ongoing, that is the stellar population is seen while it is forming most of its stars. The contribution due to the massive and hot stars is dominant and the emission is peaked towards the bluest wavelengths (emission peak at $\lambda \approx$ 1000 Å). On the contrary, if τ is smaller than the age of the stellar population (e.g. blue curve in fig. 2.11 left panel), then the star formation is already finished. Hence, very massive stars have already evolved and the most contribute in the SED is due to the old and low mass stars, which are still in the main sequence phase and whose emission dominates at infrared wavelengths (emission peak at $\lambda \approx$ 7000 Å).

Finally, in fig. 2.11 (lower panel) it is shown how the SED of a stellar population changes as a function of metallicity, fixing the other parameters (Age = 1 Gyr, τ = 0.1 Gyr and Chabrier IMF). The metallicity variation does not strongly affect the shape of the SED of stellar population, but, at fixed age, a model with an higher metallicity (red curve) produces a reddening of the spectrum with an infrared emission more pronounced.

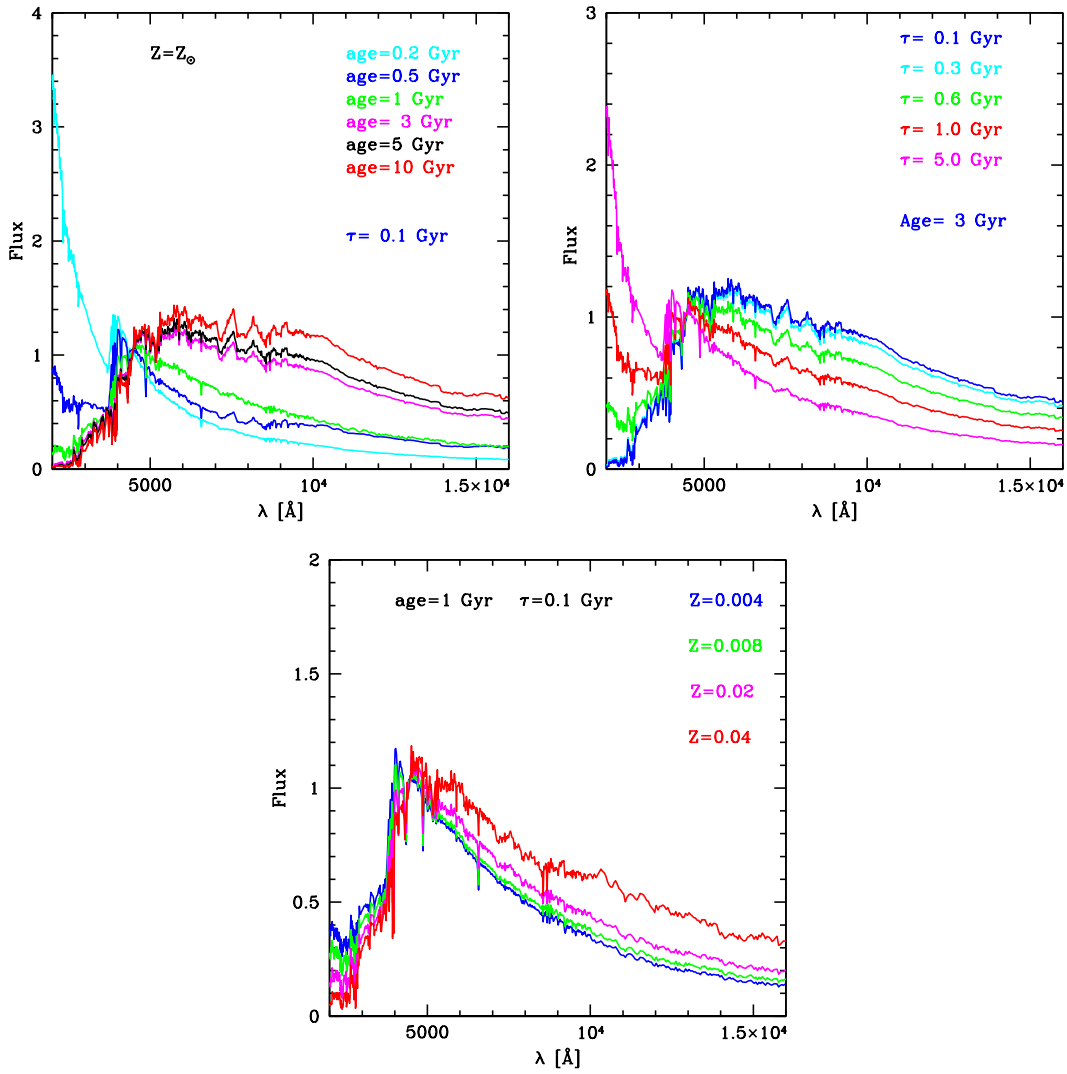

Figure 2.11: *Upper left panel*: BC03 models at different ages with fixed τ=0.1 Gyr, Z=Z$_\odot$ and Chabrier IMF. The cyan spectrum is the most younger with a pronounced emission of young stars in the UV range, whereas the red SED represents an evolved population of stars with an high contribution at the infrared wavelengths. *Upper right panel*: Comparison of BC03 models for stellar population with different star formation time-scales at fixed age (1 Gyr), metallicity (Z=Z$_\odot$) and Chabrier IMF. *Lower panel*: Comparison of BC03 models for stellar population with different metallicity at fixed age = 1 Gyr, τ = 0.1 Gyr and Chabrier IMF. The increasing of metallicity produces the redding of the stellar population spectrum. The normalization of the spectra is at 4000 Å $\leq \lambda \leq$ 5000 Å

2.5.3 The SED-*fitting* technique

For each galaxy I derived the mean global stellar parameters (stellar mass, age, absolute magnitudes) by fitting the spectral energy distribution (SED) defined by the 10 available photometric points. The fit has been performed with the software `hyperzmass` (Bolzonella, Miralles, and Pelló 2000), which returns the best-fitting SED by minimizing the χ^2 between observed ($f_{obs,i}$) and model fluxes ($f_{temp,i}$) for galaxies at fixed known redshift:

$$\chi^2 = \sum_{i=1}^{N_{filters}} \left[\frac{F_{obs,i} - b \cdot F_{temp,i}}{\sigma_i} \right]^2 \tag{2.13}$$

where $F_{\rm obs,}i$, $F_{\rm temp,}i$ and σ_i are the observed and template fluxes and their uncertainty in filter i, respectively, and b is a normalization constant needed to transform the template fluxes normalized to a total mass of 1 $M_\odot$ into the fluxes of the galaxy, thus it is related to the stellar mass. The software requires as input a catalogue with the apparent magnitudes of the galaxies and the relative errors and their redshift. After reading the observed magnitudes, with the corresponding errors, it transforms them in fluxes. Subsequently, it builds up an hypercube, with the model fluxes of the reference templates reddened for an extinction law convolved with the filter response function and shifted at the galaxy redshift. Then, the program proceeds with the χ^2 calculation, finding the best-fit model among a set of models with different masses, ages, star formation history (SFH), metallicity and dust reddening.

The observed spectral energy distribution (SED) of our galaxies from the UV to the 8 μm (10 points) has been fitted using a set of templates characterized by the BC03 models, Chabrier IMF and an exponentially declining star formation history (SFH $\propto exp^{-t/\tau}$). In all the cases, I considered 5 star-formation time scale ($\tau = [0.1, 0.3, 0.4, 0.6, 1]$ Gyr) and solar metallicity $Z_\odot$. For the extinction curve the Calzetti law (Calzetti et al. 2000) has been adopted. In the fitting procedure the extinction parameter A_V has been left as free parameter and allowed to vary in the range 0 - 0.6 mag.

Since the F775W, F850LP and F160W bands sample $\lambda_{rest} \sim 3200$ Å , $\lambda_{rest} \sim 3800$ Å and $\lambda_{rest} \sim 6400$ Å, respectively, at the redshift of the cluster, the absolute magnitudes have been derived in the UV, U and R bands (M_{UV}, M_U and M_R, respectively). The k-correction term, needed to derive the absolute magnitudes, was derived from the best fitting template. In table 2.7 I report the best fitting values for the age, the logarithm of the stellar mass, M_{UV}, M_U and M_R for the 17 galaxies of the sample. For the stellar masses and the ages I assume the errors provided by Saracco et al (2014) for a sample of cluster ellitpicals at z =1.27. The authors derived the physical properties of these galaxies through the best-fitting of their SEDs with the stellar population synthesis models of Maraston (2005; MA05), Bruzual & Charlot (2003; BC03), Charlot & Bruzual (2007; CB07), and with the Salpeter and Chabrier stellar initial mass functions. The typical variation in the best fitting parameters due to the different models and IMF is about 18% in stellar mass and 25% in age. The absolute magnitudes depend neither on the model nor on the IMF adopted since the color k-correction term can vary with different

Table 2.7: For each of the 17 galaxies of the sample I report the age, the logarithm of the stellar mass and the absolute magnitudes M_{UV}, M_U and M_R derived from the best fitting template. The typical variation in the best fitting parameters due to the different models and IMF is about 18% in stellar mass and 25% in age (as described in Section 2.5.3). The photometric errors have been assumed as errors on the absolute magnitudes (see Tab. 2.5). They represent a lower limit on the error of the absolute magnitude.

#ID	Age [Gyr]	log M_* [$M_\odot$]	M_{UV} [mag]	M_U [mag]	M_R [mag]
358	0.72	10.08	-20.14	-20.19	-21.18
595	3.00	11.56	-21.83	-21.95	-23.62
684	1.70	10.56	-20.71	-20.79	-21.91
692	1.14	10.56	-20.23	-20.35	-21.87
837	2.50	11.47	-21.22	-21.36	-23.22
1284	1.01	11.05	-21.29	-21.41	-22.88
1539	1.80	11.01	-21.07	-21.15	-22.67
1740	3.50	11.93	-22.56	-22.65	-24.39
1747	1.02	10.55	-20.22	-20.34	-21.77
1758	1.80	11.14	-20.85	-20.99	-22.73
1782	1.90	11.57	-21.52	-21.65	-23.43
1790	4.25	11.60	-21.76	-21.89	-23.71
2054	1.70	11.22	-21.55	-21.66	-23.21
2147	1.14	11.01	-21.20	-21.31	-22.90
2166	0.90	10.99	-22.19	-22.27	-23.39
2429	0.72	10.58	-20.66	-20.76	-21.98
2809	0.65	10.73	-21.59	-21.67	-22.74
Mean	1.73	10.45	-21.21	-21.32	-22.80

models of hundredth of a magnitude. Hence, the photometric errors have been assumed as errors on the absolute magnitudes. They represent a lower limit on the error of the absolute magnitude.

In fig. 2.12 I show the SEDs obtained for the 17 ellipticals of the sample. For 14 galaxies out of the 17, the best fitting template is defined by a SFH with $\tau = 0.1$ Gyr, whereas the remaining 3 galaxies are characterized by SFHs with $\tau = 0.3$ Gyr (#837 and #1539) and with $\tau = 0.6$ Gyr (#1740). The longest time-scale (τ=1 Gyr) is never found as solution by the best fit. This suggests that the observed SEDs of the galaxies are consistent with a stellar population rather coeval that formed in a very short time. The 17 ellipticals have stellar masses in the range 1.2 x 10^{10} $M_\odot$< M_* < 8.5 x 10^{11} $M_\odot$ with a mean value $M_* \simeq 3$ x 10^{10} $M_\odot$ and ages in the range 0.6 Gyr <t≤ 4.3 Gyr with a mean value of $\sim$ 1.7 Gyr. The central elliptical is the most massive in the sample ($M_{*,1740} = (8.5 \pm 1.5) \times 10^{11}$ $M_\odot$). This estimate is consistent with the stellar mass derived by Rosati et al. (2009) ($M_{*BCG} \approx 9 \times 10^{11}$ $M_\odot$).

We can see that in some cases (#837, #1284, #1539, #1740, #1758, #1790, #2054,

#2147 and #2409) the observed fluxes are not well fitted by the best-fitting SEDs, especially in the IR wavebands. Hence, I have re-performed the fits excluding these photometric points and I found that the derived stellar population properties do not change.

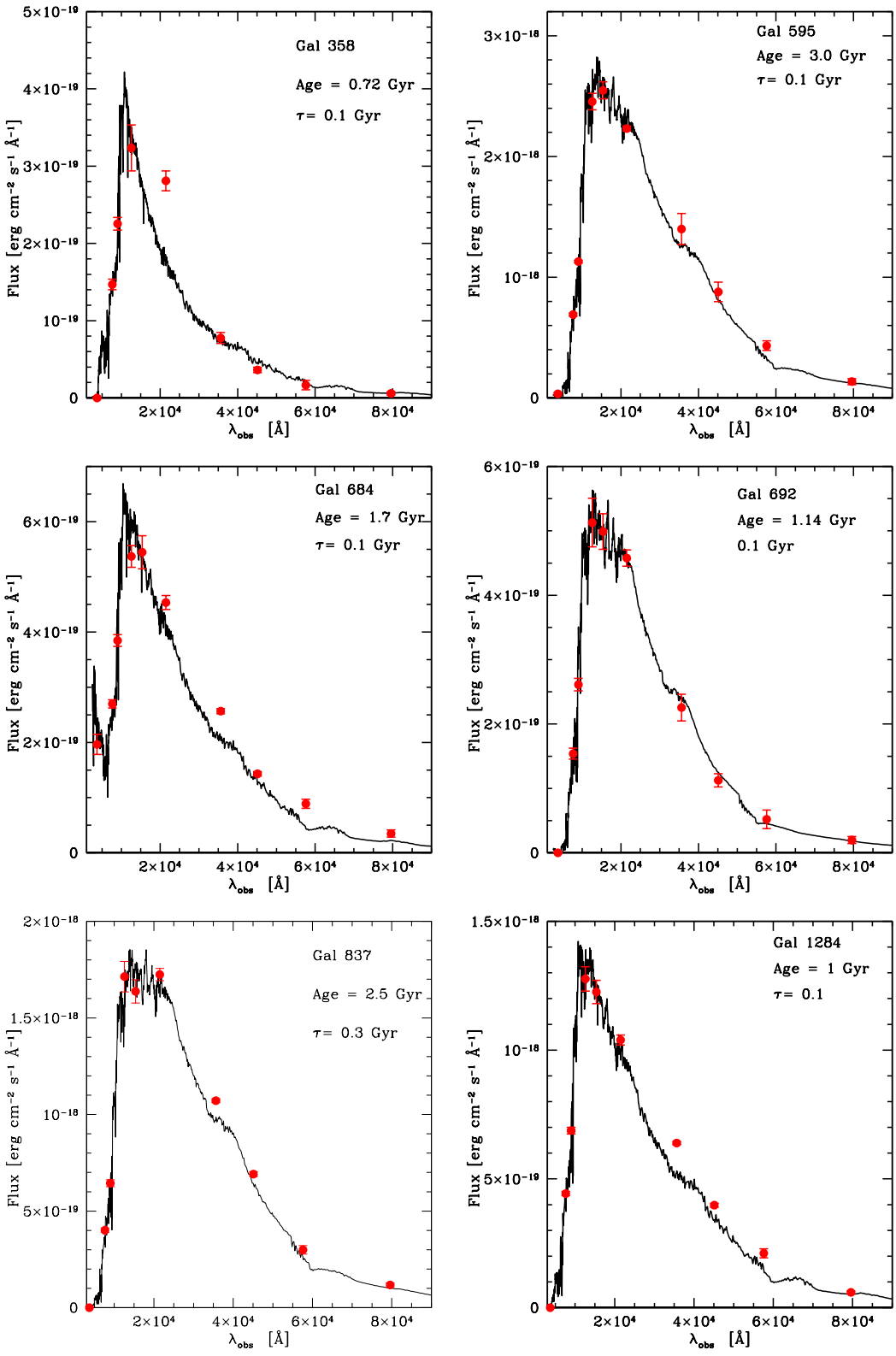
Gal 358
Age = 0.72 Gyr
τ= 0.1 Gyr
Gal 595
Age = 3.0 Gyr
τ= 0.1 Gyr
Gal 684
Age = 1.7 Gyr
τ= 0.1 Gyr
Gal 692
Age = 1.14 Gyr
0.1 Gyr
Gal 837
Age = 2.5 Gyr
τ= 0.3 Gyr
Gal 1284
Age = 1 Gyr
τ= 0.1
Flux [erg cm⁻² s⁻¹ Å⁻¹]
λobs [Å]

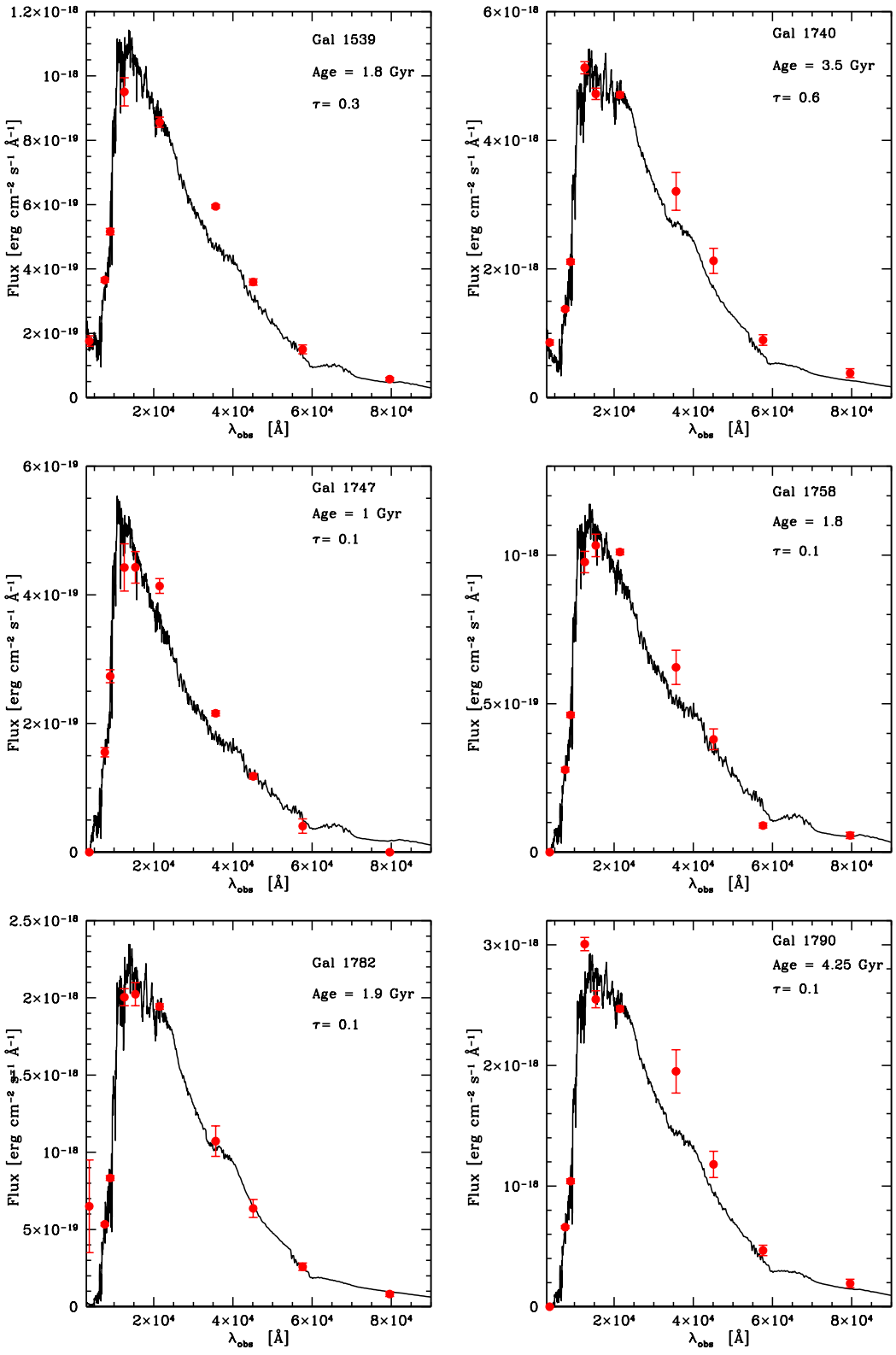
Gal 1539
Age = 1.8 Gyr
τ= 0.3
Gal 1740
Age = 3.5 Gyr
τ= 0.6
Gal 1747
Age = 1 Gyr
τ= 0.1
Gal 1758
Age = 1.8
τ= 0.1
Gal 1782
Age = 1.9 Gyr
τ= 0.1
Gal 1790
Age = 4.25 Gyr
τ= 0.1
Flux [erg cm⁻² s⁻¹ Å⁻¹]
λobs [Å]

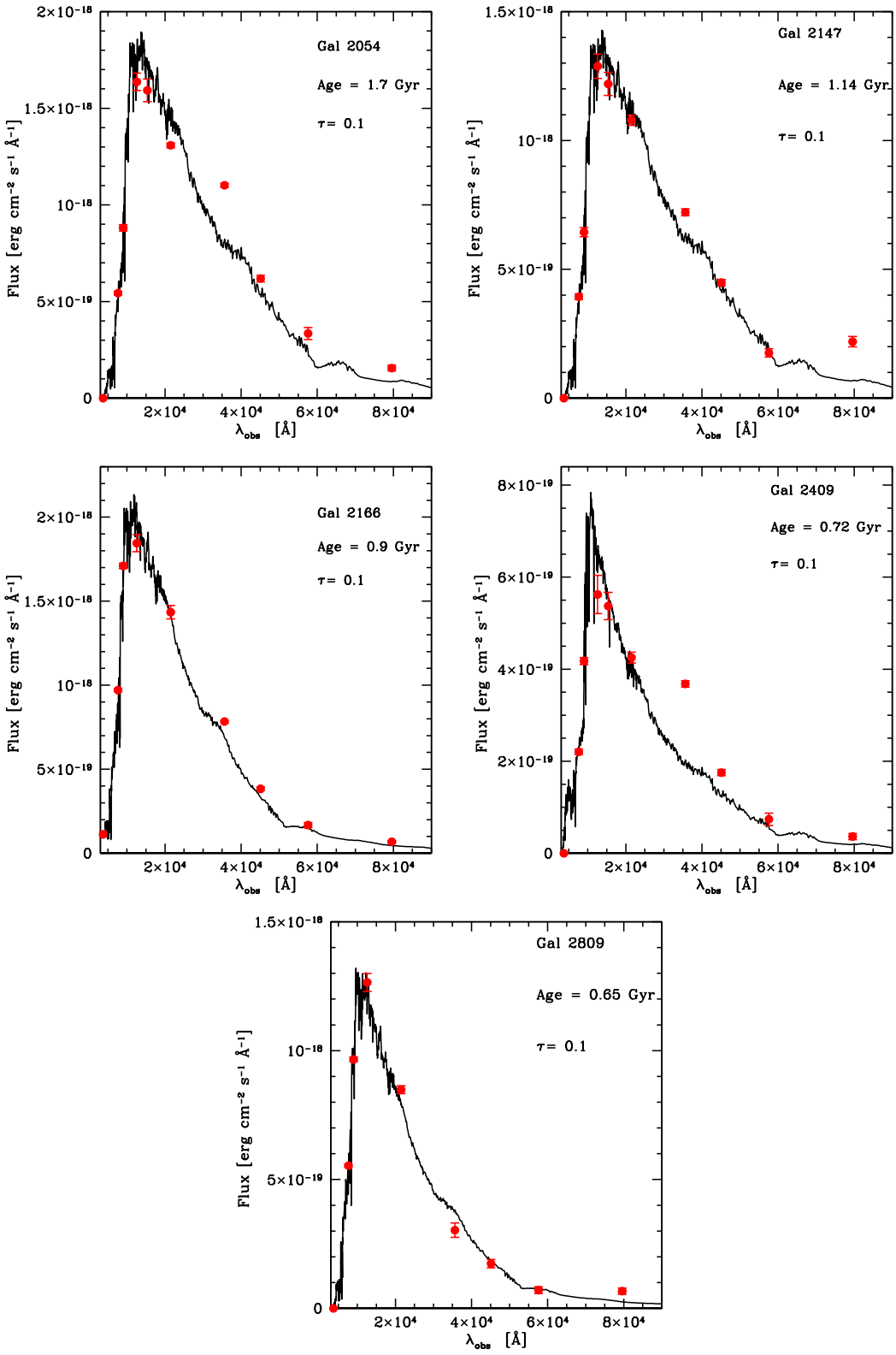

Figure 2.12: SED fitting performed on the observed SEDs of the 17 ellipticals of the sample. Red points are the fluxes measured through the 10 photometric bands U_{VIMOS}, F775W, F850LP, J, F160W, Ks, [3.6, 4.5, 5.8 and 8.0] μm. The solid black line is the best-fitting template to the observed SED.

CHAPTER

3

COLOUR GRADIENTS

In this Chapter I present the F775W-F850LP and F850LP-F160W colour gradients derived for the 17 ellipticals of the sample. In order to test the independence of the results from the method used, colour gradients have been derived using three different methods: the logarithmic slope of the deconvoluted colour profiles, the ratio of the effective radii as measured in the three different filters and through the observed colour profiles. While the first two methods are both dependent on the best-fitting procedure of the colour profiles, the third method does not involve any fit of the light profiles of the galaxies.

The origin of the observed colour variation will be discussed in Chapter 4.

3.1 Dependence of the colour gradients on the structural parameters

Colour gradient is classically defined as the logarithmic slope of the colour profile (e.g. Peletier, Valentijn, and Jameson 1990)

$$\nabla_{X-Y} = \frac{\Delta(\mu_X(R) - \mu_Y(R))}{\Delta \log R} \tag{3.1}$$

where μ_X(R) and μ_Y(R) are the surface brightness profiles of the galaxy in the generic X and Y band, respectively, and R is the distance from the galaxy centre in kiloparsec.

As describe in 2.4, the surface brightness profiles have been derived by fitting a Sérsic law, which depends on the effective radius r_e, the Sérsic index n and the surface brightness at the effective radius μ_e.

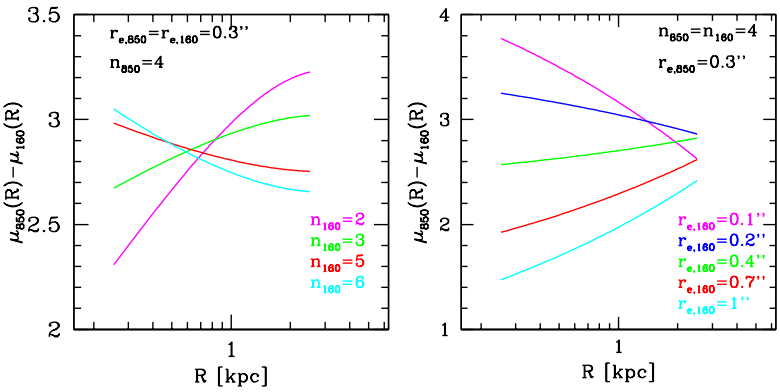

Figure 3.1: *Left panel*: I show how the colour profiles vary keeping fixed r_e ($r_{e,850} = r_{e,160} = 0.3''$) and $n_{850} = 4$ and varying n_{160} between 2 and 6. *Right panel*: I show how the colour profiles vary keeping fixed n ($n_{850} = n_{160} = 4$) and $r_{e,850} = 4$ and varying $r_{e,160}$ between 0.1" and 1".

Fig. 3.1 shows the dependence of the colour profiles on the structural parameters. As reference bands I used the F850LP and F160W. A Sérsic profile is assumed for both the bands. In the left panel, I fixed the value of $r_e = 0.3$" in both bands, which corresponds to the mean value of the effective radii of the galaxy of the sample, and $n_{850} = 4$. The index n_{160}, instead, varies in the range $2 < n < 6$, which corresponds to THE range covered by the galaxies of the sample. If $n_{160} < n_{850}$, that is the light profile is more concentrated in the F850LP band, the colour profile increases by increasing the distance from the centre: the galaxy is redder towards the outskirt. If $n_{160} > n_{850}$, the trend is opposite. In fig. 3.1 (right panel) I fixed $n = 4$ in both the bands and the effective radius $r_{e,850} = 0.3''$, while $r_{e,160}$ varies between 0.1" and 1.5", which corresponds to the range covered by the galaxies of the sample. If $r_{e,160} < r_{e,850}$, that is the light profile is more concentrated in the F160W band, the colour profile decreases by increasing the distance from the centre: the galaxy is redder towards the centre. If $r_{e,160} > r_{e,850}$, the trend is opposite.

In fig. 3.2, instead, I fixed the value of r_e and n in both bands and I studied how the colour profiles vary on the basis of the four possible combinations. As reference values, I considered 0.3" and 0.6" for r_e and 2 and 4 for n, which are a good representation of the values of the galaxies of the sample. The colour profiles obtained are plotted in fig 3.2. If $n_{160} > n_{850}$, the colour profile decreases by increasing the distance from the centre both for $r_{e,850} < r_{e,160}$ and for $r_{e,850} > r_{e,160}$: the galaxy is redder towards the centre. On the contrary, when $n_{160} < n_{850}$, if $r_{e,850} < r_{e,160}$ the colour profile increases by increasing the distance from the centre, if instead $r_{e,850} > r_{e,160}$ colour profile decreases by increasing the distance from the centre.

In the following section I quantitative derive the radial colour variations inside the 17 ellipticals of the sample.

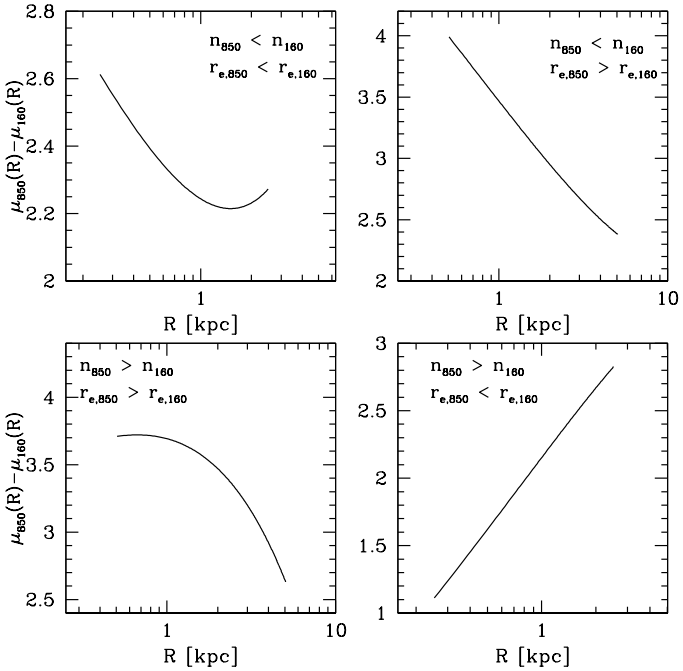

Figure 3.2: I show how the colour profiles vary for four different combinations of r_e and n. As reference values, I considered 0.3" and 0.6" for r_e and 2 and 4 for n, which are a good representation of the values of the galaxies of the sample. If $n_{160} > n_{850}$, the colour profile decreases by increasing the distance from the centre both for $r_{e,850} < r_{e,160}$ and for $r_{e,850} > r_{e,160}$: the galaxy is redder towards the centre. On the contrary, when $n_{160} < n_{850}$, if $r_{e,850} < r_{e,160}$ the colour profile increases by increasing the distance from the centre, if instead $r_{e,850} > r_{e,160}$ colour profile decreases by increasing the distance from the centre.

3.2 Colour gradients

To quantify the radial variation of the colour along a fixed radius of the ellipticals of the sample, I have derived their F775W - F850LP and F850LP - F160W colour gradients. I remind that the F775W, F850LP and F610W bands sample the rest-frame ∼UV ($\lambda_{rest} \sim 3200$ Å), ∼U ($\lambda_{rest} \sim 3800$ Å) and ∼R ($\lambda_{rest} \sim 6400$ Å) bands respectively. In order to obtain the rest-frame UV-U and U-R colours, I derived for each band the k-correction (k), which takes into account the effects of the expansion of the Universe on the flux of a source; for example, for the F160W band:

$$k = mag(F160W; z = 1.39) - mag(R; z = 0) \tag{3.2}$$

where the two magnitudes are derived from the best-fitting SED reproducing each galaxy. The transformations to obtain the rest-frame colours are: UV-U= (F775W-F850LP) - 0.8 mag and U-R = (F850LP-F160W) - 1.1 mag.

In order to test the independence of the results from the method used and to a proper comparison to previous works both at high and low redshift (see Chapter 6), colour gradients have been estimated using three different methods.

3.2.1 Intrinsic colour gradients

As anticipated in the previous Section, I first derived the colour gradient following the classical definition, that is as the logarithmic slope of the colour profile (see equation 3.1). The slope of the colour profile has been fitted between $0.1R_e$, and $1R_e$ to be consistent with the previous works present in literature. In fig. 3.6 and 3.7 I report the F775W - F850LP and F850LP-F160W colour gradients fitted between $0.1R_e$ and $1R_e$ for the whole sample. In each image I plotted on the y axis on the right side the rest-frame UV-U and U-R colours that correspond to the observed F775W-F850LP and F850LP-F160W colours, respectively. The black curves represent the deconvolved colour profiles, whereas the red lines are the best-fitting slopes. The red dashed lines set 1σ error. In all the figures, the variation Δcolour on the y axis is 1 mag for the F775W-F850LP colour and it is 0.9 mag for the the F850LP-F160W colour. The values of the colour gradients and their relative errors are reported in table 3.1.

I assigned as error on the colour gradient the error on the observed colour estimated within a thin circular annulus of width 0.1" and centered at $1R_e$. This represents an upper limit to the error on the colour gradient. Indeed, I verified that, due to the lower S/N, the error at $1R_e$ is, on average, ~ 3 times the error at $0.1R_e$.

The analysis shows that the 17 ellipticals present positive or null rest-frame UV-U gradients. Indeed, 2 galaxies (#692, #1740) have a colour gradient comparable with zero at 1σ, whereas the remaining galaxies present a significant positive gradient at $> 1\sigma$, showing the presence of a bluer stellar population towards the centre in this colour. On the contrary, these galaxies have negative or null rest-frame U-R colour gradients. In particular, 4 galaxies (#595, #1740, #1790 and #2429) have a U-R colour gradients comparable with zero at 1σ, whereas the remaining ones present a significant negative gradient at $> 1\sigma$, showing that the stellar populations are redder towards the centre in this colour. The ranges covered by the two colour gradients are: $0 < \nabla_{F775W-F850LP} < 0.7$ mag and $0 < \nabla_{F850LP-F160W} <$ -0.7 mag. The distributions of the two colour gradients are shown in fig. 3.3.

These results do not depend on the fitted region. The intrinsic profile derived through `Galfit` well reproduces the observed profile up to $2R_e$ for the majority ($\sim 80\%$) of the sample, as shown in Chapter 2. Hence, I have estimated the colour gradients at most up to this distance from the centre confirming the UV-U and U-R gradients for all the galaxies of our sample. Beyond $2R_e$, the surface brightness profiles of the galaxies in the ACS images fall below the sky noise and cannot be reliably fitted, preventing us to obtain reliable colour gradients at radii larger than this (see also below).

The first main result of my analysis is that, even if the galaxies in the sample are relatively young (< 4 Gyr old), their stellar content is not homogeneous, but they already exhibit significant differences among their stellar population properties. Furthermore, the observed colour gradients present systematically opposite slopes: the F775W - F850LP gradients are positive or flat, whereas the F850LP - F160W are negative or flat. The interpretation on the origin of these observed radial colour variations will be discussed in Capter 4.

I have also derived the two colour gradients for the galaxies in our sample by pa-

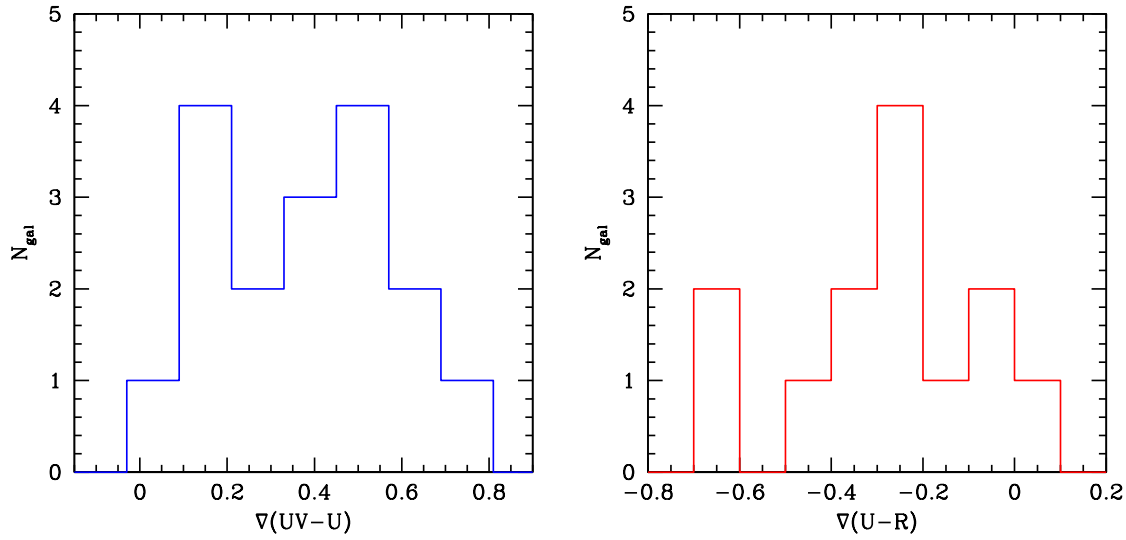

Figure 3.3: The F775W-F850LP (blue histogram) and F850LP - F160W (red histogram) distributions of the colour gradients of the 17 cluster ellipticals.

rameterizing the gradients via the ratio of the effective radii as measured in the F775W, F850LP and F160W: $\Delta logR_e$=$log(R_e(X)/R_e(Y))$, where X stands for the bluer band and Y stands for the redder band. This method is not independent on the first one, anyway I used it to compare the colour gradients with other studies in literature, which derive the colour gradients in this way (see e.g. La Barbera et al. 2003; De Propris, Bremer, and Phillipps 2015).

In fig. 3.4 I show the ratios $log(R_{e,775}/R_{e,850})$ (upper panel) and $log(R_{e,850}/R_{e,160})$ (lower panel) vs. the effective radius in the F850LP band ($R_{e,850}$) for the 17 ellipticals of the sample. Grey crosses indicate the colour gradients of the red sequence galaxies belonging to four clusters (included this cluster) at $1 < z < 1.4$ selected by De Propris et al. (2015). A detailed comparison with this sample will be shown in Chapter 6. The most of the selected galaxies shows significant negative $log(R_{e,775}/R_{e,850})$ and simultaneously significant positive $log(R_{e,850}/R_{e,160})$, with the exception of galaxy #1740 (the central elliptical) for which $log(R_{e,775}/R_{e,850}) = 0.02$ and $log(R_{e,850}/R_{e,160}) = -0.2$. This implies positive UV-U and negative U-R colour gradients for most of the galaxies in agreement with the previous methods. The values of $\Delta\log(R_e)$ are reported in table 3.1.

3.2.2 Observed colour gradients

To test for the robustness of the colour profiles derived by fitting the brightness profiles with `Galfit`, I have derived the observed surface brightness profiles, and hence the colour profiles, by measuring the fluxes in each band within circular apertures with a width of 0.05" centered on the galaxy. This method is not based on any fit of the surface brightness profile; hence, no dependence either on any assumption on the analytic

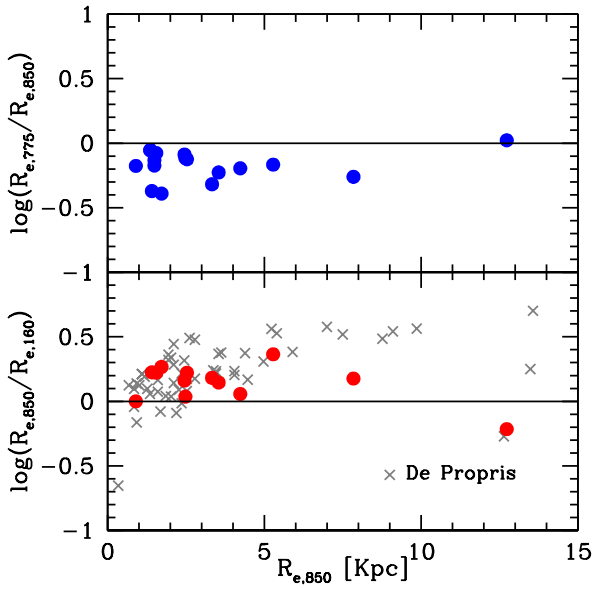

Figure 3.4: Colour gradients derived as $log(R_e(775)/R_e(850))$ (upper panel) and as $log(R_{e,850}/R_{e,160})$ (lower panel) vs. the effective radius in the F850LP band ($R_{e,850}$). I plotted with grey crosses the cluster galaxies at <z> $\sim$ 1.25 from De Propris et al. (2015) sample with n consistent with our ellipticals.

function of the profile or on the fitting procedure is present. Since ACS F850LP images and WFC3 F160W images have a different resolution, in order not to introduce spurious gradients, I have degraded the F850LP image to the same PSF of the F160W image before deriving the F850LP - F160W observed colour profiles. Indeed, the observed profile of a galaxies is given by the convolution of the intrinsic profile with the PSF: $P_{obs} = P_{int} \star PSF$. Hence, when the ratio of the fluxes in the two bands is computed, if the PSF is different, a spurious radial colour variation could be introduced, since the ratio between the two PSFs is $\neq 1$. For this reason, I have degraded the F850LP image (PSF $\sim$ 0.11") to the same resolution of the F160W image (PSF $\sim$ 0.2") using the transformation kernel $K(r)$, defined by the relation

$$PSF_{850} \star K(r) = PSF_{160} \tag{3.3}$$

To compute the kernel function I used the IRAF task *psfmatch*. I adopted as PSF_{850} and PSF_{160} images the isolated and unsaturated star used in *Galfit*. I tested the effectiveness of PSF matching by comparing the fractional encircled energy of each PSF before (fig. 3.5, left panel) and after the procedure (fig. 3.5, right panel). We can see that, after matching, the PSFs in the two bands have an identical profile, especially within the central region ($\lesssim$ 0.4"), which is the one mainly affecting the galaxy light profile. Differences smaller than 2% appear at r > 0.4". Thus, I neglect them, since they

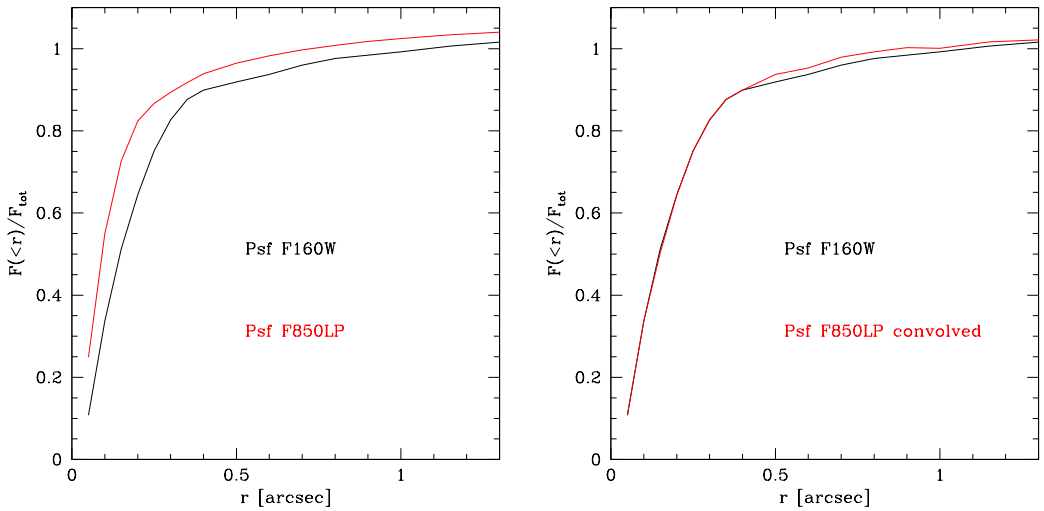

Figure 3.5: *Left*: Profile of the PSF_{850} (red line) and of the PSF_{160} (black line). *Right*: Profile of the PSF_{160} (black line) and of the PSF_{850} convolved with the kernel function $k(r)$ (red line).

would not affect the analysis.

In fig. 3.8 I show as an example the observed colour profiles for galaxies #1284 and #1747 up to $1R_e$. Errors have been estimated by propagating the uncertainties on the observed brightness profiles. These gradients cannot be easily compared to the results discussed in the previous subsection, as they depend on the PSF. However, both the methods provide the same systematics for all the galaxies as shown in fig. 3.9, where we compare the 'intrinsic' and 'observed' F775W-F850LP (upper panel) and F850LP-F160W (lower panel) colour gradients up to $1R_e$. The 'observed' F775W-F850LP gradients are, on average, slightly less steep than the intrinsic gradients (with an offset < 0.1 mag) due to the PSF that smooths both the profiles. The F850LP-F160W colour gradients, instead, are, on average, steeper with an offset of ~ 0.3 mag. This is mainly due to the psf-match procedure. Indeed, degrading the F850LP image to the same PSF of the F160W image, the same amount of flux of the F850LP image has been redistributed over a larger area. This implies a decrease of the flux in the inner region in favour to the outer region and, consequently, the gradients become steeper.

I have also checked the effect of estimating colour gradients beyond $2R_e$. Fig. 3.10 shows as example the observed F850LP-F160W colour profiles for galaxies #595 and #837, which have a large effective radius (3.5 kpc and 7.8 kpc, respectively), up to $3R_e$. We can see that at $R \gtrsim 1.5\text{-}2R_e$ the colour profiles reverse because the sky noise dominates the surface brightness profiles in the F850LP band image (see fig. 2.7), introducing a spurious colour gradient. This artificially flattens the colour gradient from the steeper one measured within $2R_e$ (and with Galfit). In particular, for the galaxies with a large

R_e ($R_e \gtrsim 3$ kpc) (∼20% of the sample), the S/N of the F850LP image at $R \gtrsim 1.5R_e$ is not good enough to derive reliable colour profiles and, consequently, colour gradients. In particular, galaxies #595 and #837 have S/N ∼ 3 at $2R_e$. For lower S/N ratios, a reliable estimate of colour gradients cannot be derived. For the remaining ∼80% of the galaxies, the S/N in the F850LP band is good enough (see fig. 2.6) to derive reliable gradients up to ∼ $2R_e$ and they are in agreement with the gradients derived through the intrinsic profiles. For $R \gtrsim 2R_e$ the estimates of the colour gradients are completely affected by the noise introduced by the F850LP image for 10 out to the 13 galaxies (∼76% of the sample) and, hence, their estimates of the colour gradients are not reliable. Figure 3.9 (right panel) shows the comparison between the F850LP-F160W colour gradients derived from the intrinsic surface brightness profiles and the observed profiles up to $3R_e$. As we can see, the values of the colour gradients are more scattered due to the high noise of the F850LP image at $3R_e$ that tends to flatten the observed colour gradients of the galaxies with a large R_e. Hence, to derive reliable colour gradients from the observed colour profiles, it is very important to select a region where the S/N is good in both the bands. Up to the distance where we have a reliable estimate of the observed colour profile of the galaxies, the gradients derived through the two methods are in good agreement. At larger radii the measure of the colour gradients from the observed profiles is completely affected by the background introduced by the F850LP band (in agreement with what previously found with the *Galfit* fitting). This is the reason why I derived the colour gradients at most up to $2R_e$.

These three different methods used to derive colour gradients are mutually consistent, implying that the results are independent on the method used.

I find that the UV-U colour gradients are systematically positive (∼ 80%) or null (∼ 20%), never negative. On the contrary, the U-R colour gradients are systematically negative (∼ 70%) or null (∼ 30%), never positive.

The presence of colour gradients implies that one or more properties of the stellar population of these galaxies are radially varying. In the next Chapter I present the analysis aimed at investigate the nature of the observed colour variation.

Table 3.1: For each of the 17 galaxies of the sample I report the F775W - F850LP and F850LP - F160W colour gradients derived as the logarithmic slope of the colour profile within $1R_e$ and $2R_e$ and via the ratio of the effective radii as measured in the F775W, F850LP and F160W filters. The error on the observed colour estimated within a thin circular annulus of width 0.1" and centered at $1R_e$ and $2R_e$ has been assigned as error on the colour gradients.

#ID	$\nabla_{F775W-F850LP}$	$(\nabla_{F775W-F850LP})_{2r_e}$	$\nabla_{F850LP-F160W}$	$(\nabla_{F850LP-F160W})_{2r_e}$	$log(R_{775}/R_{850})$	$log(R_{850}/R_{160})$
358	0.2±0.1	0.3±0.2	–	–	-0.2	–
595	0.4±0.2	0.4±0.2	-0.1±0.1	-0.2±0.2	-0.2	0.1
684	0.6±0.1	0.6±0.2	-0.3±0.1	-0.5±0.2	-0.4	0.2
692	0.2±0.2	0.2±0.2	-0.3±0.1	-0.5±0.3	-0.1	0.2
837	0.4±0.3	0.4±0.3	-0.3±0.2	-0.3±0.2	-0.3	0.2
1284	0.2±0.1	0.2±0.2	-0.3±0.1	-0.3±0.2	-0.1	0.2
1539	0.5±0.2	0.4±0.2	–	–	-0.1	–
1740	0.0±0.2	0.0±0.2	0.05±0.10	0.06±0.2	0.02	-0.2
1747	0.7±0.2	0.8±0.3	-0.4±0.1	-0.6±0.2	-0.4	0.3
1758	0.4±0.2	0.5±0.2	-0.7±0.2	-0.7±0.3	-0.1	0.2
1782	0.6±0.1	1.0±0.3	-0.3±0.2	-0.4±0.2	-0.3	0.2
1790	0.2±0.1	0.2±0.2	0.0±0.1	-0.04±0.02	-0.1	0.2
2054	0.5±0.1	0.4±0.2	-0.2±0.2	-0.2±0.2	-0.2	0.1
2147	0.3±0.2	0.3±0.3	-0.6±0.3	-0.7±0.3	-0.1	0.1
2166	0.3±0.1	0.3±0.2	–	–	-0.2	–
2429	0.5±0.1	0.6±0.1	0.00±0.04	0.0±0.1	-0.1	0.4
2809	0.5±0.1	0.4±0.2	–	–	-0.2	–

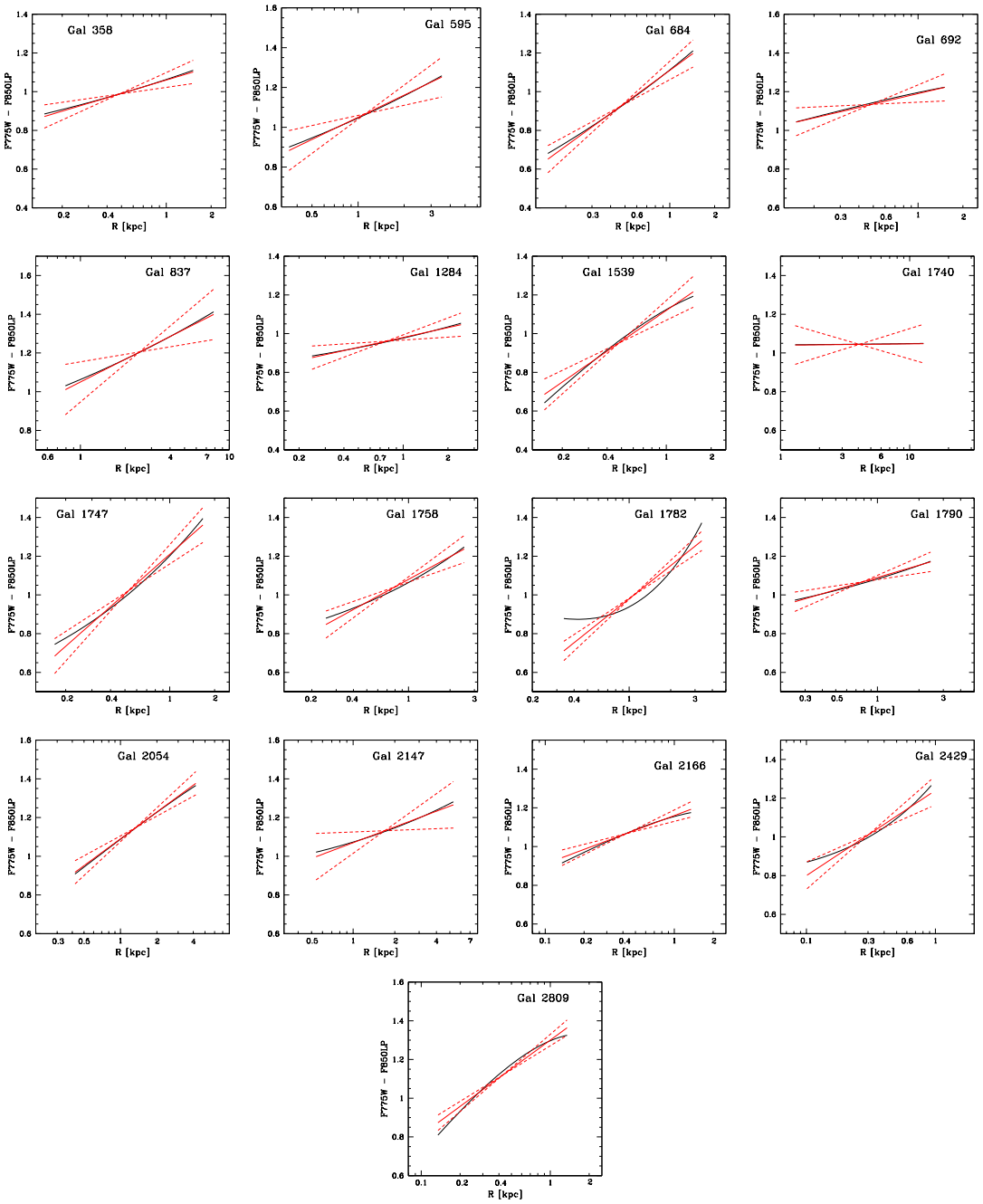

Figure 3.6: The F775W - F850LP colour gradients for the galaxies of our sample. Black lines represent the deconvolved colour profiles between $0.1R_e$ and $1R_e$ and the red solid lines are the best-fitted lines to the models. The red dashed lines set 1σ errors. For all the galaxies in the y axis Δcolour = 1 mag. The transformation to obtain the UV-U colours is: UV-U = (F775W-F850LP) - 0.8 mag.

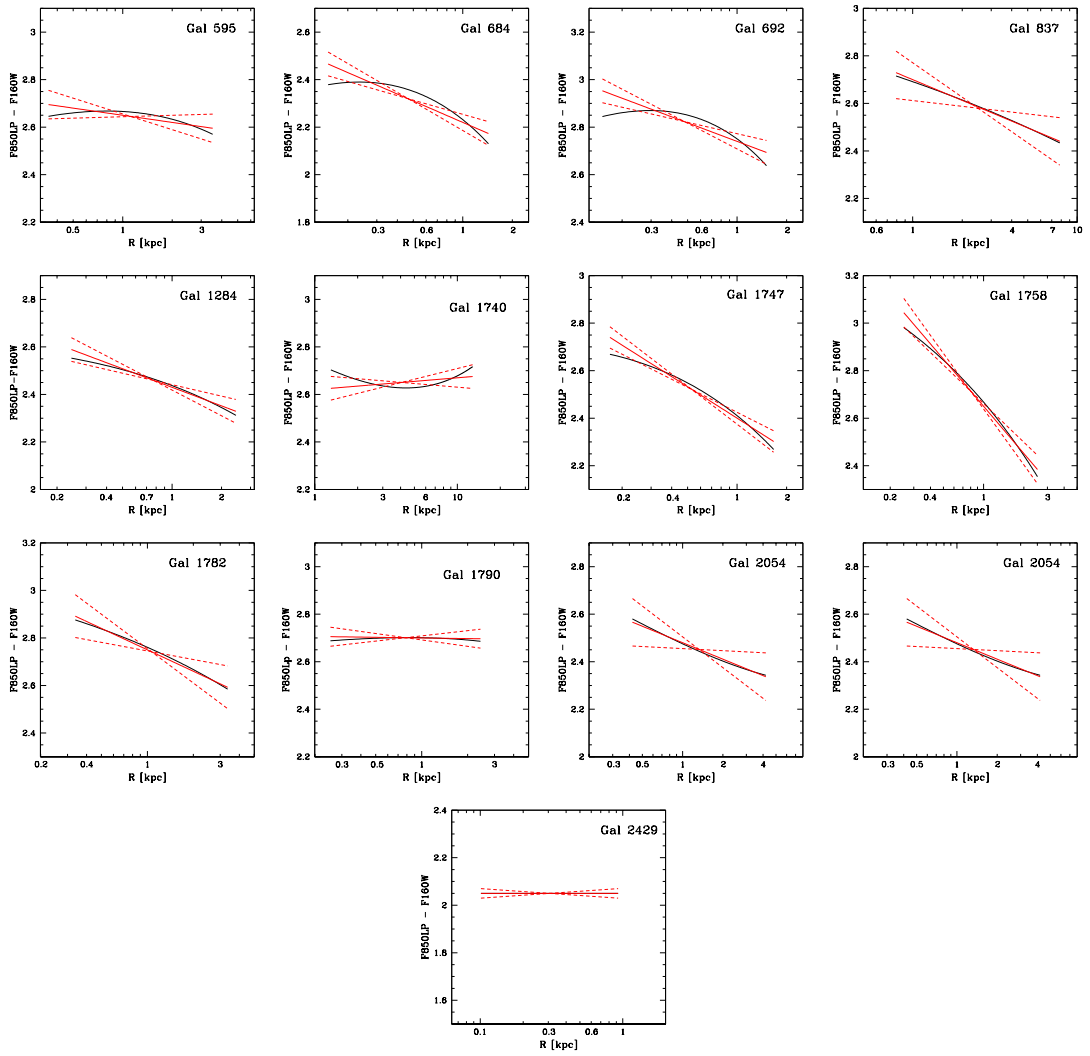

Figure 3.7: The F850LP - F160W colour gradients for the galaxies of our sample. Black lines represent the deconvolved colour profiles between $0.1R_e$ and $1R_e$ and the red solid lines are the best-fitted lines to the models. The red dashed lines set 1σ errors. For all the galaxies in the y axis Δcolour = 0.9 mag. The transformation to obtain the U-R colours is: U-R = (F850LP-F160W) - 1.1 mag.

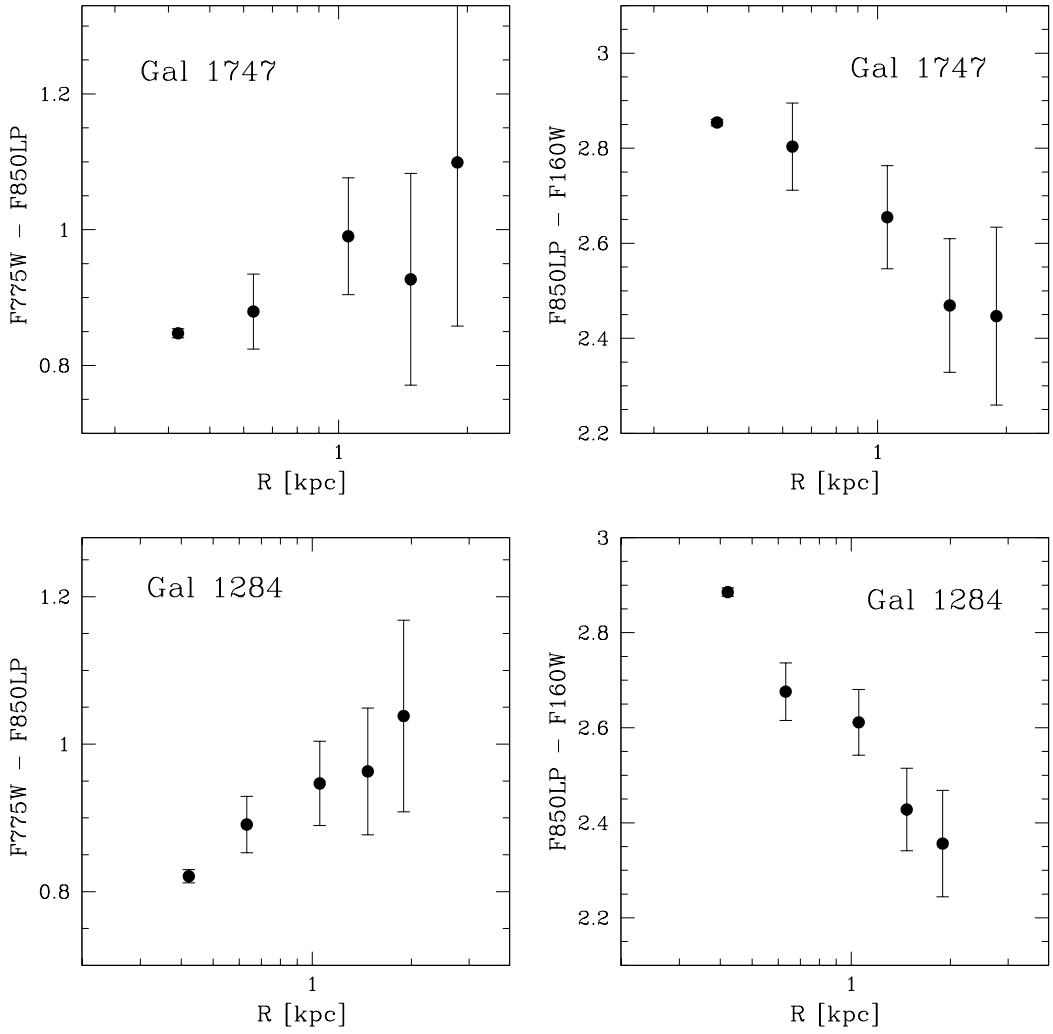

Figure 3.8: Observed 775W - F850LP (upper panels) and F850LP - F160W (lower panels) colour profiles derived by measuring the fluxes within circular apertures centered on each galaxy. Errors have been estimated by propagating the uncertainties on the observed brightness profiles.

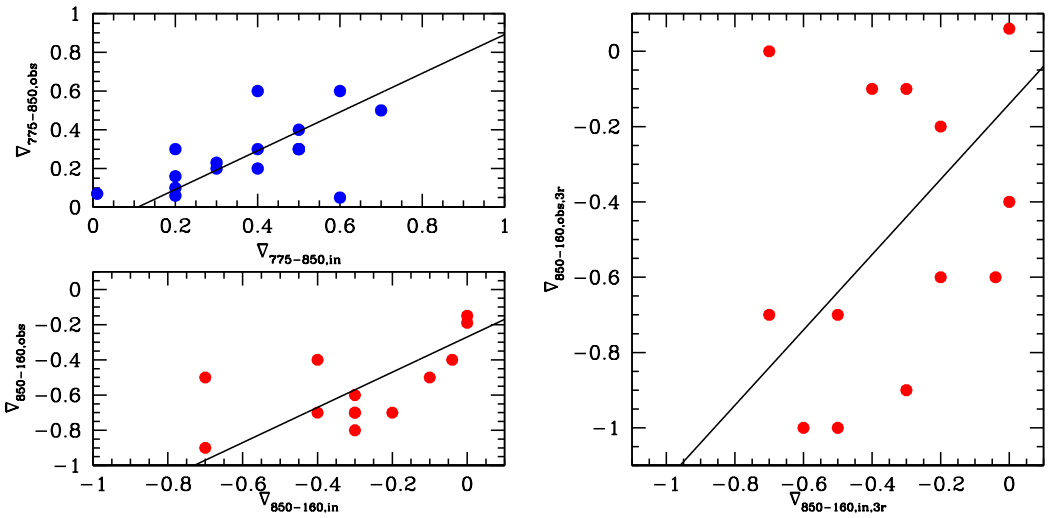

Figure 3.9: *Left panel*: Comparison between the F775W-F850LP (upper panel) and the F850LP-F160W (lower panel) colour gradients derived from the intrinsic surface brightness profiles and the observed profiles. *Right panel*: Comparison between the F850LP-F160W colour gradients derived from the intrinsic surface brightness profiles and the observed profiles up to $3R_e$.

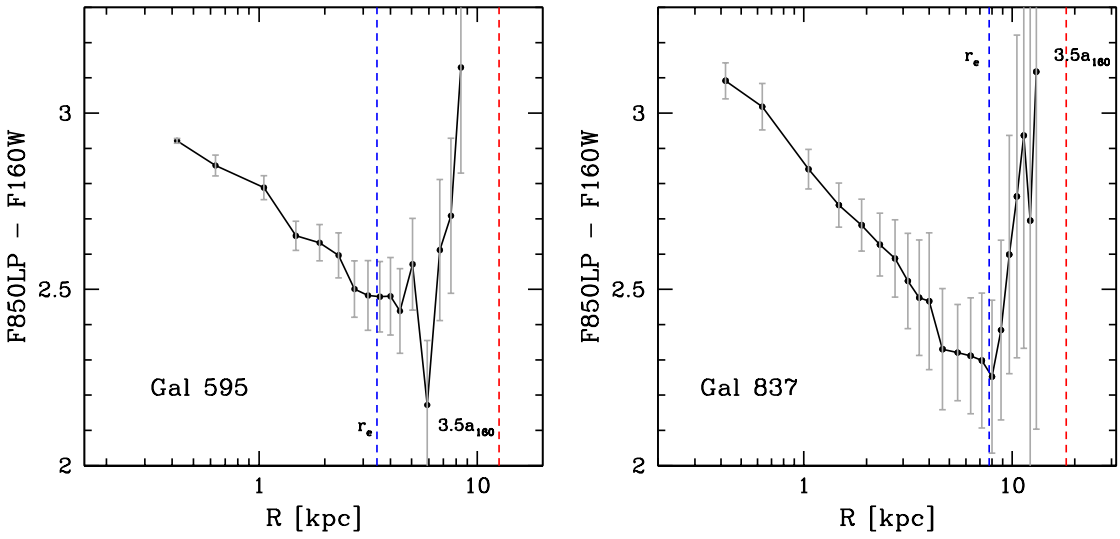

Figure 3.10: Observed F850LP - F160W colour profiles derived by measuring the fluxes within circular apertures centered on each galaxy. Blue dashed line represents the effective radius of the galaxies as we derived in the F850LP band, while red dashed line represents 3.5a (major axis) as derived in the F160W band by Chan et al.

CHAPTER

4

THE NATURE OF THE OBSERVED COLOUR GRADIENTS

The analysis presented in the previous Chapter shows that for most of the galaxies of the sample ($\sim 80\%$) the stellar content is not homogeneous. The presence of colour gradients implies that one or more properties of the stellar population are radially varying.

In this Chapter I investigate the origin of the observed colour gradients in the 17 ellipticals in term of radial variation of the stellar properties (age and metallicity) and of dust content. In particular, I will show that the rest-frame ultraviolet gradient is a very important key to correctly interpret the properties of the stellar populations of the galaxies and to constrain their history of mass accretion.

4.1 Radial variation of a single parameter: age, metallicity and dust

In this Section, I will probe whether the variation of a single property of the stellar population (metallicity or age) can account for the opposite trend of the UV-U and U-R colour gradients.

Since most of the studies agree in ascribing the observed radial colour variations in local elliptical galaxies as mainly driven by a metallicity gradient, with the contribution played by age variation still controversial, I have first verified whether the detected colour gradients can be reproduced by a pure metallicity gradient as for the local ellipticals. Fig. 4.1 (upper left panel) shows the UV-U and U-R colour gradients for different

radial metallicity variations. To this aim, I modeled the central region of the galaxy with a simple stellar population (SSP) 3 Gyr old (the results are independent on this assumption) with supersolar metallicity (2 $Z_\odot$), while I modeled the external region with the same SSP (i.e., no radial age variation is assumed) but with metallicity 2 $Z_\odot$ (*red solid line*), $Z_\odot$ (*blue dot-long dashed line*) and 0.2 $Z_\odot$ (*green short dashed line*). It can be seen that a metallicity gradient affects more strongly the optical U-R colour gradient than the UV-U gradient, but the slope is always negative. For instance, by considering in the central region Z_{in}=2 $Z_\odot$ and in the external region Z_{out}=0.2 $Z_\odot$ (the most extreme metallicity variation), we obtain $\nabla_{UV-U} \sim -0.1$ mag, while $\nabla_{U-R} \sim -0.7$ mag. These results are independent on the age assumed. Indeed, by repeating the same analysis for different ages (2 Gyr, 3 Gyr and 4 Gyr), I found the same result: the only metallicity variation can not account for the opposite slopes of the observed colour gradients. For obvious reasons, by reversing the direction of the metallicity radial variation, hence from less metal-rich stellar population in the centre towards more metal-rich stellar population in the outskirts, both the colour gradients would be positive. Therefore, we cannot explain both gradients at z=1.4 with a simple metal abundance gradient as in the local Universe.

I have repeated the same exercise in the case of a pure age (fig. 4.1, upper right panel) and dust variation (fig. 4.1, lower panel). In particular, to investigate the effect of a pure age variation on UV-U and U-R colours, I have modeled the central region of the galaxy with a SSP 4 Gyr old and with solar metallicity, and the external region with a SSP with the same metallicity and three different ages: 4 Gyr (*red solid line*), 3 Gyr (*blue dot-long dashed line*) and 1 Gyr (*green short dashed line*). Also in this case the U-R colour is more sensitive to age variation. For instance, by considering in the central region Age_{in}=4 Gyr and in the external region Age_{out}=1 Gyr, we obtain $\nabla_{UV-U} \sim -0.05$ mag, while $\nabla_{U-R} \sim -0.6$ mag. By reversing the direction of the age radial variation both the colour gradients would be positive. As for the case of metallicity variation, an age variation is not able to reproduce opposite colour gradients. These results are independent on the metallicity assumed.

Finally, to probe the effect of the dust variation, I fixed both the metallicity and the age and I assumed that the dust is concentrated in the inner region of the galaxies. The dust extinction produces an attenuation of the intrinsic flux of the galaxy that depends on the wavelength: $f_{\rm obs}(\lambda) = f_{\rm int}(\lambda)10^{-0.4A_\lambda}$, where $f_{\rm obs}$ and $f_{\rm int}$ are the observed and the intrinsic fluxes, respectively, and $A_\lambda = k(\lambda)A_V/R_V$ is the extinction at a wavelength λ, $k(\lambda)$ is the Calzetti law and $R_V = 4.05\pm0.80$ (Calzetti et al. 2000). In the lower panel of fig. 4.1 it is shown how the two colour gradients vary as a function of the dust extinction for three different values of A_V: 0.5, 1 and 1.5. Also in this case, the radial variation of dust produces concordant UV-U and U-R gradients, which become steeper for increasing values of A_V.

The main result of this analysis is that the radial variation of a single stellar population parameter is not able to produce UV-U and U-R gradients with opposite slopes. In particular, a radial decrease in metallicity (age) from the central to external regions produces a UV-U and U-R negative colour gradients, whereas a radial increase of metal-

licity (age) from the central to external regions produces a UV-U and U-R positive colour gradients. Beside this, fig. 4.1 shows also that the UV-U colour is less sensitive to metallicity and age variation than the U-R colour. In fact, while the U-R colour variations induced by the age/metallicity variations are comparable to those observed in our galaxies, the same age/metallicity variations do not produce UV-U colour variations as large as those observed (see fig. 3.6), but the maximum amplitude is $\sim$ 0.1 mag. To verify whether this result is just related to our choice of the input values of metallicity/age chosen, in the next section I have check whether an age or a metallicity variation is able to reproduce the amplitude of the observed gradients for the 17 ellipticals of the sample or it is easier to reproduce a certain colour gradient than the other one.

4.2 Modeling of the real data

In order to investigate the origin of the observed colour gradients, following the analysis technique proposed by Gargiulo et al. (2012), I modeled the stellar content of a galaxy as composed of two main stellar populations, one population dominating towards the centre and the other one dominating the external regions of the galaxy. The two populations have been modeled by using BC03 composite stellar populations. On the basis of the colour profiles (see Chapter 2 fig. 2.7), I have chosen as inner region the one enclosed within the FWHM, that is within a radius of $\sim$ 0.06 arcsec ($\sim$0.5 kpc) and, as outer region, a circular annulus $\sim$ 1 kpc width centered at 1.5R_e in order to maximize the distance between the two regions and, hence, their colour difference. This should facilitate in detecting differences between the stellar populations parameters of the two components. I verified that for each galaxy 1.5R_e corresponds to at least $\sim$3 times the radius of the PSF.

To test for the radial age (metallicity, Z) variation as origin of the observed colour gradients, I fixed, as initial guess, Z (age), A_V and τ of the two populations to those derived from the fit to the global SED and leave age (Z) as free parameter of the fit. The best-fitting age of the central (external) stellar population is the one that better reproduces the UV-U and U-R colours observed in the inner (outer) region of the galaxy. In addition, the sum of the internal and external populations has to reproduce the global SED.

For all the galaxy, the best-fitting procedure finds a solution to the observed U-R colour gradients ($-0.7 < \nabla < 0$ mag) at 1σ both in the case of an age gradient and a metallicity gradient. The results are shown in table 4.1. For a pure metallicity variation, the resulting metallicity gradients are in the range $\nabla_Z = d\log(Z)/d\log(R)$<-0.8, with a median value of $\sim$ -0.4, consistent with the metallicity gradients derived in local and intermediate redshift ellipticals, where ∇_Z ranges from -0.2 to -0.4 (e.g. Saglia et al. 2000; Wu et al. 2005; La Barbera and de Carvalho 2009). For a pure age variation, instead, the resulting age gradients are in the range $\nabla_{age}=d\log(age)/d\log(R) \lesssim$ -0.4. Such age gradients would be barely detectable locally. For instance, ∇_{age}=-0.3 due to an age variation of 2 Gyr corresponds at z=0 to a colour gradient of -0.07 mag, smaller than the typical errors on colour gradients. On the contrary, the procedure does not

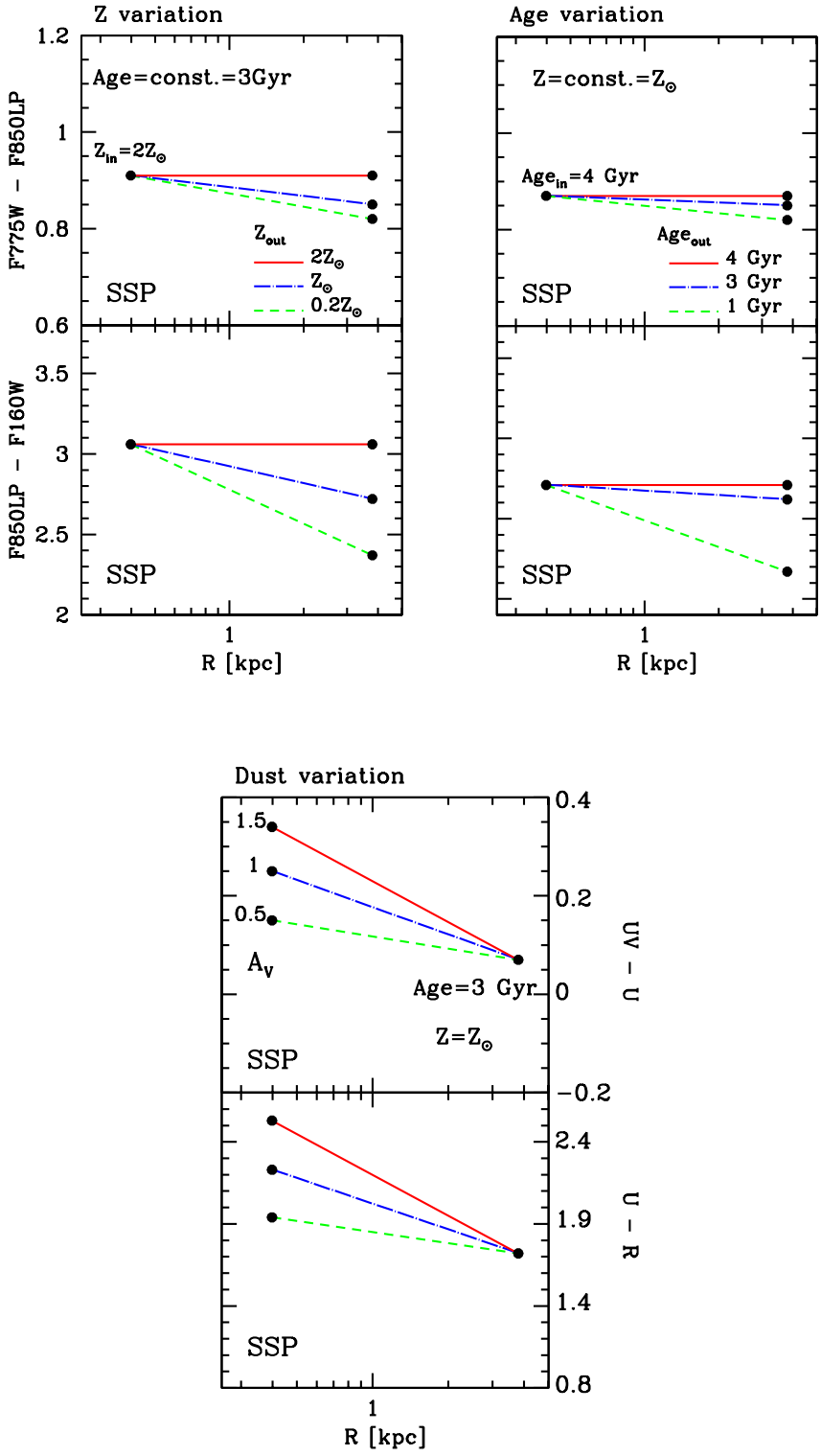

Figure 4.1: F775W-F850LP and F850LP-F160W colour gradients variation as a function of metallicity, age and dust. *Upper left panel*: we fixed the age of the stellar population at 3 Gyr and varied the metallicity from the central region (2 $Z_\odot$) to the outer region [2 $Z_\odot$ (red solid line), $Z_\odot$ (blue dot-long dashed line) and 0.2 $Z_\odot$ (green short dashed line)]. *Upper right panel*: we fixed the metallicity at $Z_\odot$ and varied the age from the central region (4 Gyr) to the outer region [4 Gyr (red solid line), 3 Gyr (blue dot-long dashed line) and 1 Gyr (green short dashed line)]. *Lower panel*: the gradient variation as a function of the dust extinction A_V at fixed age and metallicity for three different values of A_V: 0.5 (green short dashed line), 1 (blue dot-long dashed line) and 1.5 (red solid line) is shown.

find a solution for the observed large UV-U colour gradients and for the opposite slopes shown by the two gradients.

In fig. 4.2, I show as example the result obtained for the galaxy #1758, the one showing the most extreme color gradients. In the left panels I show the colour gradients obtained considering a pure age variation, whereas in the right panels I show those obtained considering a pure metallicity variation. Metallicity variation has been modeled on a grid of subsolar and supersolar metallicity values: 0.2 $Z_{\odot}$, 0.4 $Z_{\odot}$, $Z_{\odot}$ and 2 $Z_{\odot}$. The black curves represent the colour profiles of the galaxy, whereas the red lines are the observed colour gradients. The blue dashed lines represent the best-fitting colour gradients as resulting from the two-component model. The magenta points represent the mean colour of the stellar population in the inner and in the outer region. It results that the rest-frame U-R colour gradient of this galaxy (∇ = -0.7$\pm$0.3 mag) is well reproduced both by an age gradient and by a metallicity gradient. In particular, by considering a pure metallicity variation the best fit slope for the colour profile is -0.72 mag, which corresponds to a metallicity gradient $\nabla_Z = d\log(Z)/d\log(R) \sim$ -0.7. By considering a pure age variation, instead, the best fit slope for the colour profile of -0.66 mag, which corresponds to an age gradient $\nabla_{age} = d\log(age)/d\log(R) \sim$ -0.4. On the contrary, the same radial variation of age/metallicity is not able to reproduce the rest-frame ultraviolet gradient. In both the cases we obtain a flat rest-frame ultraviolet gradients ($\nabla = 0.01$ and $\nabla = 0$ in case of age and metallicity variation, respectively).

In the case of dust variation, instead, to produce even the mean amplitude (-0.3 mag) of the U-R gradients an $A_V >> 1$ mag would be needed in the inner regions, values never obtained from the fitting to the global SED of our galaxies. Hence, dust can play only a marginal role, if it has one, in the origin of the observed colour gradients.

Hence, this analysis shows that it is easier to reproduce the negative U-R colour gradients rather than the positive UV-U colour gradients. UV-U colour gradients can not be accounted for by age and/or by metallicity variations. Actually, what the data show is that galaxies are bluer in the center when the UV-U colour is considered. Hence, there is an UV excess towards the galaxy central regions with respect to the external ones. Starting from this evidence, in the next section, I try to constrain the scenario best able to reproduce simultaneously both the colour gradients, focusing on the nature of the bluer UV-U colour in the galaxy central regions.

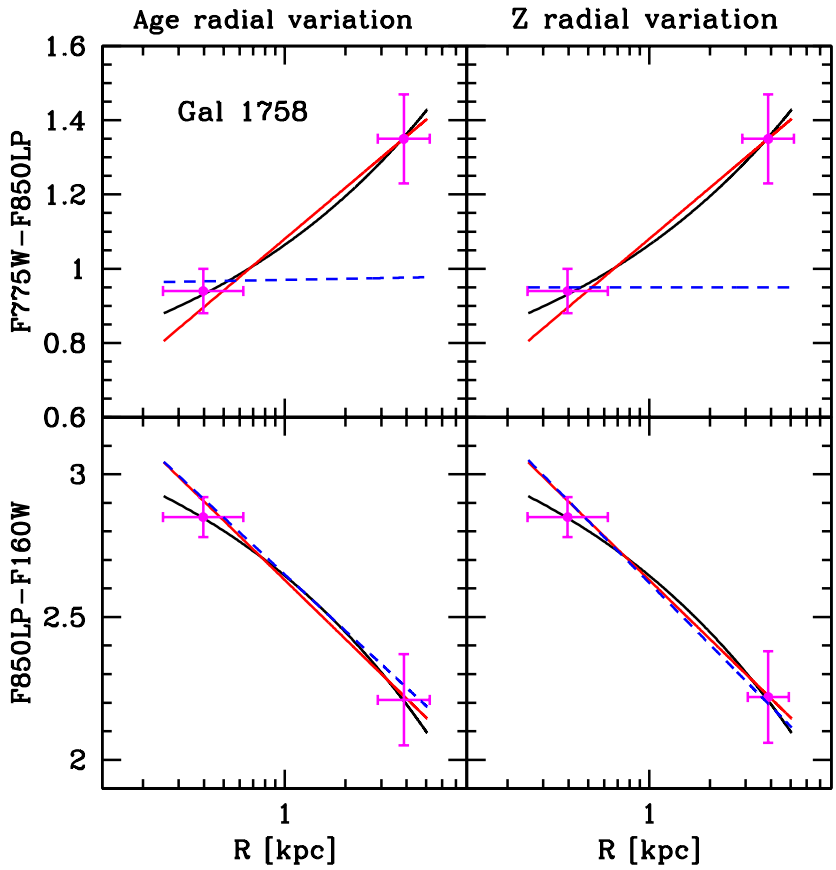

Figure 4.2: *Left*: radial age variation as origin of the observed colour gradients. The upper panel shows the F775W-F850LP colour profile (black line) and best fitting slope (red line); the lower panel on this side shows the same information but for the F850LP-F160W gradient. In both panels, the blue dashed lines show the effect of a pure age variation as a function of radius on colour. The magenta points show the mean colour of the stellar populations in the inner and outer regions. *Right*: same as above but for metallicity.

ID	$\nabla_{F775W-F850LP}$|$\nabla_{F850LP-F160W}$ [mag]	$\nabla_{F775W-F850LP,age}$| $\nabla_{F850LP-F160W,age}$ [mag]	$\nabla_{F775W-F850LP,Z}$| $\nabla_{F850LP-F160W,Z}$ [mag]	∇_Z	∇_{age}
595	0.4|-0.1	0.01|-0.20	0.00|-0.15	-0.37	-0.10
684	0.6|-0.3	0.00|-0.28	0.00|-0.33	-0.80	-0.15
692	0.2|-0.3	0.03|-0.36	-0.01|-0.27	-0.51	-0.27
837	0.4|-0.3	0.00|-0.18	0.00|-0.20	-0.30	-0.10
1284	0.2|-0.3	-0.03|-0.28	0.04|-0.29	-0.32	-0.15
1740	0.0|0.05	0.00|0.00	0.00|0.00	0.00	0.00
1747	0.7|-0.4	0.03|-0.38	0.04|-0.28	-0.74	-0.20
1758	0.4|-0.7	0.01|-0.66	0.00|-0.72	-0.72	-0.39
1782	0.6|-0.3	0.01|-0.30	0.00|-0.21	-0.29	-0.15
1790	0.2|0.0	0.01|0.02	0.00|0.00	0.00	-0.19
2054	0.5|-0.2	0.00|-0.18	0.00|-0.40	-0.57	-0.10
2147	0.3|-0.6	0.00|-0.48	0.00|-0.39	-0.29	-0.25
2429	0.5|0.0	0.00|0.00	0.00|0.00	0.00	0.00

Table 4.1: Colour gradients produced by the variation of a single stellar population parameter from the internal to the external region. *Column 1*: galaxy ID number. *Column 2*: F775W-F850LP|F850LP-160W measured colour gradients. *Column 3*: F775W-F850LP|F850LP-F160W colour gradients produced by a pure age variation *Column 4*: F775W-F850LP|F850LP-F160W colour gradients produced by a pure metallicity variation. *Column 5*: ∇_Z: metallicity gradient derived as $d\log(Z)/d\log(R)$. *Column 6*: ∇_{age}: age gradient derived as $d\log(age)/d\log(R)$. The errors on colour gradients are those reported in table 3.1.

4.3 The hidden content of the galaxy central regions

From this analysis it results that a metallicity gradient, as the one observed in local elliptical galaxies (e.g. Saglia et al. 2000; Wu et al. 2005; La Barbera et al. 2005; Tortora et al. 2010), or an age gradient can produce the observed U-R colour gradients but the same variation cannot justify the opposite (positive) UV-U gradient. Thus, to produce the positive UV-U colour gradient without affecting the observed negative U-R gradient, a mechanism able to efficiently enhance UV emission without altering longer wavelengths has to be hypothesized in the galaxy central regions. Possible mechanisms able to fulfil these requirements are the star formation, the presence of a QSO, stars in the He-burning phase or He- rich stars. In the following, I will discuss each of these mechanisms.

4.3.1 An ongoing weak star formation?

One mechanism that produces UV emission is the star formation. In order to test whether a weak star formation can produce positive UV-U gradients without affecting the negative U-R gradients, I have added in the centre a young stellar component seen while it is forming most of its stars, i.e. characterized by τ=0.1 Gyr and an age of 0.1 Gyr. The results are shown in Fig. 4.3. In particular, in the left panel, I fixed the age of the bulk of stellar population (4 Gyr) and varied the metallicity from the centre ($Z_{\odot}$) to the external region (0.2 $Z_{\odot}$) and added different percentages (in terms of stellar mass) of star formation towards the centre. In the right panel, instead, I show the same model of the left panel (metallicity varies from the central region to the outer region with different percentages of star formation in the centre) but for different constant age of the bulk of the stellar population.

It can be seen that, although the radial decrease of metallicity (at constant age) would reflect in negative UV-U colour gradient (e.g. see fig. 4.1), the presence of a very weak star formation in the centre is able to reverse the UV-U gradient turning it from negative to positive. Moreover, it can be seen that the older the mean age of the stellar population the easier to produce positive UV-U colour gradients. This is because the UV emission of the star-forming component tends to dominate the UV and U emission of the stellar population when it is old, enhancing the gradient with respect to the outer regions. For instance, the ratio between the UV emission of 0.3% (in stellar mass) of star-forming component and the UV emission of 1 Gyr old component is $\sim$ 0.08. This ratio increases to $\sim$ 0.7 in the case of a 4 Gyr old component.

In order not to affect the negative U-R colour gradients, the percentage in stellar mass of this star-forming component must be less than $\sim$ 0.5% of the total stellar mass.

I applied this model to the galaxies of the sample. I built a grid where the percentage of the star-forming component ranges from 0.1% to 3% with a step of 0.2 up to 1.5% and of 0.5 form 1.5% to 3%. At fixed percentage of the starforming component I varied the age and the metallicity of the stellar population in the centre and in the external region. The ages considered range from 1 Gyr to 4 Gyr (the age of the Universe at z = 1.39 is $\sim$ 4.5 Gyr) with a step of 0.5. Metallicity variation has been modeled on a grid of subsolar and supersolar metallicity values: 0.2 $Z_{\odot}$, 0.4 $Z_{\odot}$, $Z_{\odot}$ and 2 $Z_{\odot}$. I found that

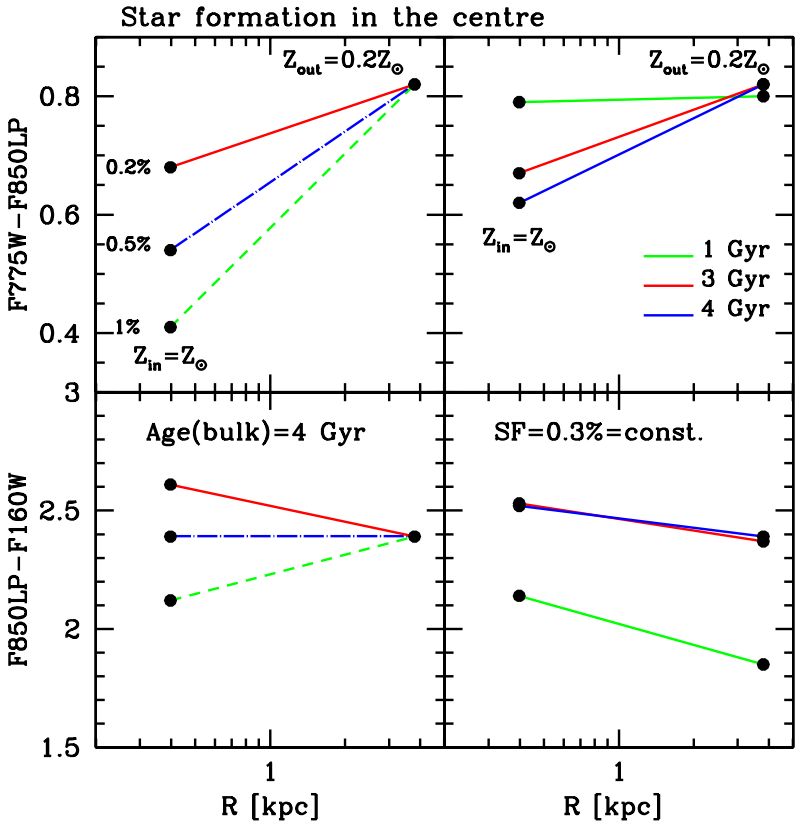

Figure 4.3: Figure shows how the F775W-F850LP and F850LP-F160W colour gradients change by adding a weak star formation towards the centre. *Left-hand panel*: I fixed the age of the main stellar population at 4 Gyr and varied the metallicity from the centre ($Z_\odot$) to the outer region (0.2 $Z_\odot$), adding a weak star formation towards the centre. The percentages indicate the contributes in term of stellar mass of the stellar population, which is producing stars. *Right-hand panel*: I show how both colours change if we add a star-forming component equivalent to 0.3% in stellar mass for three different ages of the main stellar population [1 Gyr (green line), 3 Gyr (red line) and 4 Gyr (blue line)] and with the same metallicity gradient.

0.7% represent an upper limit to the percentage of the star forming component, since larger percentages produce flat or even positive U-R gradients.

Six galaxies (#595, #1740, #1790, #2054, #2429, #837) present U-R colour gradients consistent with a null gradient at 1σ. Hence, no age or metallicity variation is required to produce the U-R gradients. However, these galaxies present significant positive UV-U gradients at 1σ. The only addition of star formation towards the centre produces positive UV-U gradients, but also slightly positive U-R gradients. The best solutions provide for these galaxies a contribution of 0.2% in mass of star formation

together with either an age gradient of $\sim$ - 0.3 (Age_{in}= 4 Gyr and Age_{out}= 2 Gyr) or with a metallicity gradient of $\sim$ -0.4 (Z_{in} = $Z_{\odot}$ and Z_{out}= 0.4 $Z_{\odot}$), consistent with the metallicity gradients found in local ellipticals.

Four galaxies (#692, #1284, #1782, #2147), instead, show opposite colour gradients at 1σ. For them, the best-fitting model producing simultaneously both the observed colour gradients is composed of 0.2% of star-forming component in the centre superimposed to an age gradient of $\sim$ - 0.3 (Age_{in}= 4 Gyr and Age_{out}= 2 Gyr) and a metallicity gradient $\sim$ -0.4 (Z_{in} = $Z_{\odot}$ and Z_{out}= 0.4 $Z_{\odot}$).

Galaxy #1758 presents an extreme value of the U-R gradient at 1σ (∇= -0.55 mag). In order to produce such steep U-R gradient, it is needed to consider a even lower metallicity towards the external region (Z_{out}= 0.2 $Z_{\odot}$). This would imply a steeper metallicity gradient ($\nabla_Z \sim$ -0.7$\pm$0.1). Such steep metallicity gradients are rarely observed in the local ellipticals. For instance, Spolaor et al. (2009), studying a sample of 51 Virgo and Fornax cluster early-type galaxies, found that the metallicity gradients range up to -0.6, even if only 5 out to the 51 galaxies have $\nabla_Z <$ -0.4 (see also Ogando et al. 2005). For this galaxy, we are able to simultaneously produce both the colour gradients by adding 0.3% of star formation together with both an age gradient of $\sim$ - 0.3 (Age_{in}= 4 Gyr and Age_{out}= 2 Gyr) and a metallicity gradient of $\sim$ -0.7 (Z_{in} = $Z_{\odot}$ and Z_{out}= 0.2 $Z_{\odot}$). This galaxy is shown in fig. 4.4 as example. The upper panel shows the F775W-F850LP colour profile (black line) with the best-fitting slope (red line), while the lower panel the F850LP-F160W colour profile. The blue dashed line is the colour gradient derived by considering also the star formation in the centre in the case of a metallicity gradient (left) and both metallicity and age gradient (right). The magenta points represent the mean colour of the stellar population in the inner and in the outer region.

Finally, two galaxies (#684 and #1747) present an extreme value of the UV-U gradients at 1σ (∇= 0.47, 0.58 mag, respectively). For these galaxies, we are not able to simultaneously produce both the colour gradients. Indeed, in order to produce the steep observed UV gradients, $\gtrsim$ 1% in mass of star formation is needed, but this produces null or positive U-R gradients, even if we consider the lowest metallicity available in the external region (Z_{out}= 0.2 $Z_{\odot}$). These galaxies are isolated; they are not the faintest in the sample and their structural parameters are not extreme. Hence, we have no reason to suppose that the colour gradients of these galaxies are overestimated.

In conclusion, by applying a model with star formation in the centre together with a metallicity and/or an age gradient, we are able to simultaneously produce at 1σ both the colour gradients for 11 out of the 13 ellipticals ($\sim$ 85% of the sample). On the basis of this model, the ellipticals of the sample would be composed by a younger and less metal-rich stellar population towards the external regions and by an older and more metal-rich stellar population with the presence of a weak star formation towards the centre.

Taking as reference the mean value of the stellar mass ($<M_*> \sim 3 \cdot 10^{10}$ $M_{\odot}$) of the galaxies of our sample, this young star-forming component would contribute in stellar mass for just $\sim 2.7 \cdot 10^8$ $M_{\odot}$. Since the BC03 models are normalized at 1 $M_{\odot}$ and a stellar population of 0.1 Gyr with τ=0.1 Gyr is characterized by a SFR = $3.6 \cdot 10^{-9}$

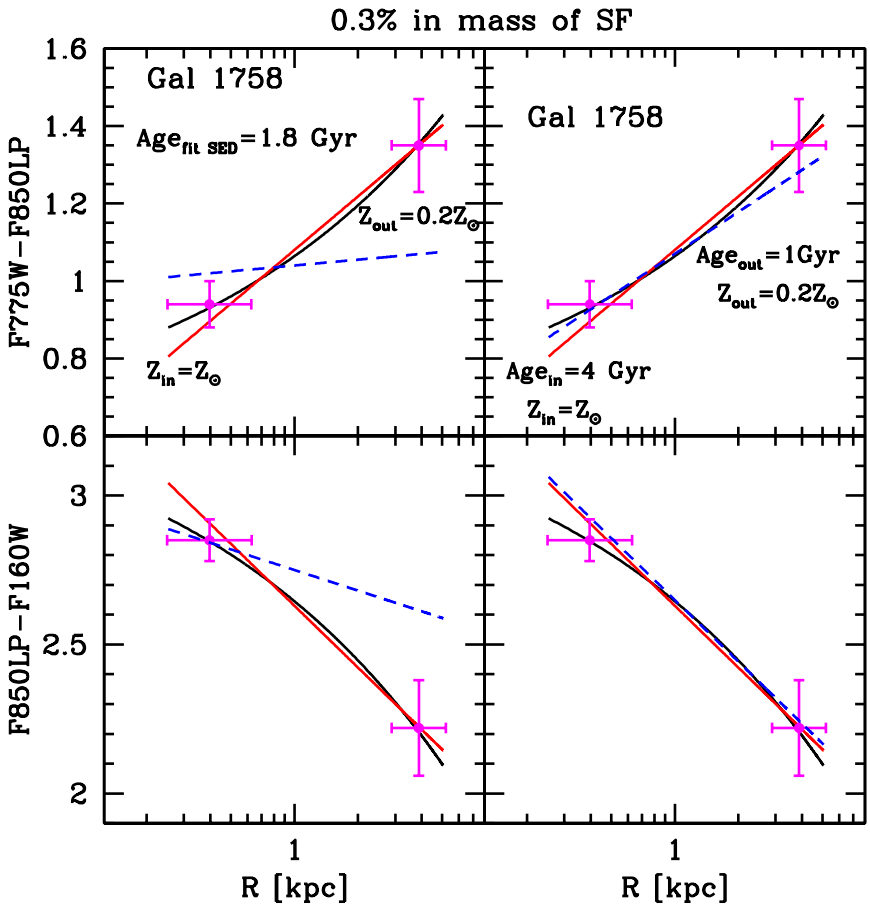

Figure 4.4: The two panels show the F775W-F850LP (upper panel) colour profile (black line) with the best fit slope (red line) and the F850LP-F160W (lower panel) colour profile (black line) with the best fit slope (red lines). The blue dashed lines represent the colour gradients derived from the model described in 4.3.1. In the left panel, a metallicity gradient and a weak star formation in the center have been considered. In the right panel an age gradient has been also added. The magenta points represent the mean colour of the stellar population in the inner and in the outer region.

$M_\odot$ yr^{-1}, the SFR associated with the young central star-forming component would be SFR $\sim$ 1 $M_\odot$ yr^{-1}. It is worth noting that this SFR is rather stable with respect to the assumptions made: at fixed SFH (e.g. $\tau = 0.1$ Gyr) a younger stellar population (<0.1 Gyr) would be characterized by a stronger UV emission and, consequently, the required mass percentage would be lower (<0.5%) leaving nearly unchanged the resulting SFR.

To test whether such a weak star formation would be detectable in a galaxy at z=1.39, I derived the flux f[OII]λ3727 associated with a SFR $\sim$ 1 $M_\odot$ yr^{-1}. Following

Kennicutt 1998

$$SFR\ (M_{\odot} yr^{-1}) = (1.4 \pm 0.4) \cdot 10^{-41}\ L[OII]\ (erg\ s^{-1}) \tag{4.1}$$

I obtained f[0II]λ3727 $\sim 6 \cdot 10^{-18}$ erg cm^{-2} s^{-1}. Such faint $f[OII]$ fluxes are barely detectable even at a 10 m class telescope. For instance, Cimatti et al. (2008) report the detection of such faint fluxes in 3 passive galaxies in the GMASS survey, all of them observed for more than 30 hr. Thus, it could not be directly confirmed whether such a weak star formation activity is actually present in the galaxies of our sample, since it is too low to be detectable with the current instrumentations. However, some works find indirect evidence of the presence of star formation in early-type galaxies both at high-z and in the local universe. For instance, Lonoce et al. (2014), measuring the spectral indices of a sample of 15 field early-type galaxies at $0.7 < z_{spec} < 1.1$, found that, for $\sim$60% of the sample, the measured H+K (Ca II) index is consistent with the presence of a small mass percentage (<1%) of a young stellar component (< 1 Gyr) with recent weak star formation. Also Wagner et al. (2015), studying a sample of massive ($M > 10^{10.1} M_{\odot}$) early-type galaxies in 11 high redshift ($1.0 < z < 1.5$) clusters, found that 12% of them are likely experiencing star formation activity (SFR > 26 $M_{\odot}$ yr^{-1}). In the local Universe, Kaviraj et al. (2008), studying $\sim$ 2100 early-type galaxies in the SDSS DR3 in the redshift range $0 < z < 0.11$, found that at least $\sim$ 30% of them have UV to optical (NUV - r) colour consistent with recent star formation within the last Gyr.

If the star formation is the origin of the UV excess in the galaxy central regions of the sample, this scenario requires a certain degree of fine-tuning. Indeed, the fact that positive UV-U (or null) gradients are observed in all the galaxies implies that all of them are experiencing star formation in their centre, otherwise we would have observed negative UV-U gradients in some of them at least. This implies, in turn, that the star formation cannot be either episodic or short, but that it protracts over time in a steady fashion at low levels to allow us to observe it as it is (low) in all the galaxies. Being protracted over long time (say $\sim$ 1 Gyr, being at $z \sim 1.4$), this SF even if weak, needs to be supplied with gas. The fuel cannot come from inflows of intracluster medium (ICM), since galaxies are in thermal equilibrium with the ICM. Furthermore, infall of metal-poor gas directly reduces the observed metallicity by diluting the metal-rich gas, as discussed, for example, by Finlator & Dave (2008). Hence, such star formation should be feeded by the residual processed gas in the galaxies (closed box). This process would efficiently enhance the metallicity towards the centre (e.g. Peng, Maiolino, and Cochrane 2015) producing naturally the observed negative U-R gradients. Assuming that this process continues with redshift to z=0, at maximum 10^9 $M_{\odot}$ of new stars would form in the galaxies' centre.

As already said, this scenario requires a fine-tuning in term of synchronism and duration of the star formation as possible origin of the observed UV excess in the centre of our galaxies. However, apart from this, there are no evidence to exclude it. Moreover, it is worth considering that this model gives rise to the observed colour gradients simultaneously reproducing both the UV-U and the U-R gradients (see fig. 4.4) and that it would naturally produce the metallicity gradient observed also in the local ellipticals.

4.3.2 The possible QSO contribution

Quasars or QSOs are sources showing broad (1000 - 20,000 km sec^{-1}) permitted (e.g. Balmer lines) and forbidden emission lines (e.g., OII, OIII, NeIII) and a bright, non-stellar, central point source visible at all wavelengths (Schmidt 1968). The optical to UV emission of quasars is characterized by the "big blue bump" (Shields 1978), where the peak of quasar emission is usually found. The peak energy is around $\sim$ 1500 Å and the spectrum can be well approximated with a power law. The 300 - 5000 Å continuum can be modeled with two power laws with slopes α_1 = -1.76 between 300 Å and ∼1200 Å and α_2 = -0.44 between 1200 Å and 5000 Å. At longer wavelengths, the spectrum appears to flatten significantly, probably due to the contribution of galactic emission in the quasar spectra (see Vanden Berk et al. 2001, for details).

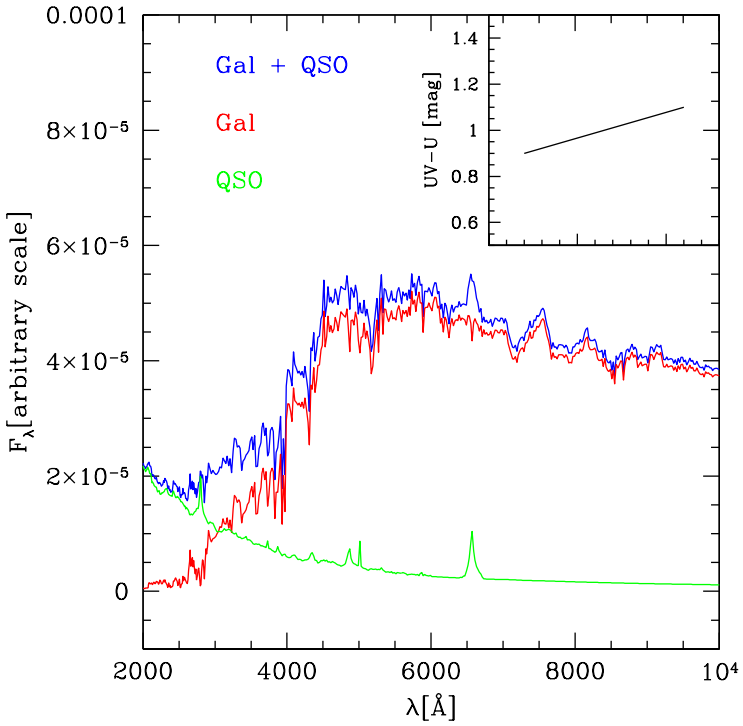

Figure 4.5: QSO contribution to the UV excess in the central galaxy regions. Green line represents the composite spectrum of a QSO (Francis et al. 1991), the red line is the template of a galaxy (4 Gyr old) and the blue line is the sum of the two components. The QSO is scaled to produce a UV-U colour gradient of $\sim$ 0.2 mag. In term of absolute magnitude, this QSO is $\sim$ 2 mag fainter than the galaxy in the B band rest-frame. The addition of this QSO component together with an age and metallicity gradient reproduces simultaneously gradients in the range $\nabla(UV-U) \leq 0.25$ mag and $\nabla(U-R) > -0.3$ mag. Brighter QSO component would flatten the U-R gradients and would make the integrated UV-U and U-R colours of the galaxies bluer than those observed.

To verify whether the UV excess in the galaxy central regions is the sign of the blue bump, I have added in the center a QSO component instead of the star forming one. I have considered the composite spectrum of Francis et al. (1991). In fig. 4.5 is shown, as an example, the case of the QSO component (green line) needed to produce a UV-U colour gradient of ~ 0.2 mag. In term of absolute magnitude, this QSO is ~ 2 mag fainter than the galaxy in the B band rest-frame. Red line is the template of a galaxy (4 Gyr old) and the blue line is the sum of the two components. In this case, the U-R gradient is not significantly affected and we can reproduce simultaneously gradients in the range $\nabla(UV - U) \leq 0.25$ mag and $\nabla(U - R) > -0.3$ mag, assuming a radial decrease of metallicity and age. For instance, for galaxies #692 and #1284, having gradients in the above ranges, the QSO would have an absolute magnitudes of $M_B \sim$ -18.7 mag and $M_B \sim$ -19.7 mag (Seyfert like), respectively. However, higher values of the UV-U gradient cannot be accounted for by further increasing the QSO luminosity. Indeed, in this latter case, the integrated UV-U and U-R colours of the galaxy would be affected resulting in significantly bluer (>0.3 mag in UV-U and in U-R) than those observed. Hence, a QSO could be present in the galaxies and contribute to the observed UV excess but cannot be the only cause. It should be superimposed to, e.g., star formation to account for the observed gradients without altering the colours of the galaxies.

4.3.3 Or, rather, evidence of the UV upturn phenomenon?

In the local Universe it has been observed that elliptical galaxies can present an UV excess in their SED. It is well known that the emission in the UV region is principally dominated by the hot and young stars (age < 1 Gyr) contributing to the whole galaxy emission. Hence, this UV excess was unexpected since ellipticals were supposed to contain mainly old and cold stellar populations. However, also old stars ($\gtrsim$ a few Gyr) metal-rich ($\gtrsim Z_\odot$) can become UV bright (Greggio and Renzini 1990; Horch, Demarque, and Pinsonneault 1992; Dorman, O'Connell, and Rood 1995). This phenomenon is called UV upturn (Yi 2008, for a review). The effect of the UV upturn on the spectrum shape of the galaxy is clearly visible in the extreme far UV (around 1000 - 2000 Å) (e.g. Code and Welch 1979; O'Connell et al. 1992; O'Connell 1999), but also many spectral indices at $\lambda > 2500$ Å are affected by this particular emission (e.g., MgII(2800), MgI(2852) and FeI(3000)). In particular, the MgII line strength was found to be stronger for bluer UV-optical colours, i.e. galaxies become bluer in the UV with increasing metallicity (Burstein et al. 1988; Donas et al. 2007).

Since its discovery, the UV upturn phenomenon in elliptical galaxies has generated a big discussion about its origin. From the shape of the SED in the UV, it derives that the temperature of the stars, which give rise to the UV excess, is in the range 20000 ± 3000 K (Brown et al. 1997). Young stars in star forming galaxies emit in the FUV band (Ferreras and Silk 2000; Yi et al. 2005) but have different features in spectral energy distributions from the observed UV upturn galaxies (e.g. C IV lines). The main mechanisms that are supposed to be the responsible of the UV upturn are He-burning stars with extremely thin hydrogen envelopes (<0.02 $M_\odot$) (e.g. Han et al. 2002; Han et al. 2003; Han, Podsiadlowski, and Lynas-Gray 2007; Han 2008) and He-rich stars

(e.g. Greggio and Renzini 1990; Yi et al. 2011; Carter et al. 2011). In the first case, there are competing models to explain the UV emission due to helium-burning stars. For instance, Han et al. propose a binary model, in which a star loses all its envelope near the tip of the red giant branch by mass transfer to a companion star or ejection in a common-envelope phase, or where two helium white dwarfs merge with a combined mass loss larger than $\sim$0.35 $M_\odot$. In each case, the remnant star ignites helium. The other accredited mechanism, instead, predicts that post main-sequence stars with an enough high metallicity content do increase significantly the opacity in their atmospheres causing mass loss during their long horizontal branch phase. Consequently, the internal hotter shells become the responsible of the dominant emission.

In the following subsections the two main scenarios will be discussed to test if they can explain the observed blue excess towards the center of ellipticals studied at $z \sim 1.4$. Indeed, even though the emission peak of the UV upturn is at wavelengths < 2100 Å, its tails extends up to ~ 3200 Å, affecting the F775W band (filter range 2700 Å $\lesssim \lambda_{rest} \lesssim$ 3600 Å).

4.3.3.1 He-burning stars

He-burning stars are stars that have already stopped burning hydrogen in their cores and they are burning helium. Assuming for the stellar population a formation redshift $z_f \sim 6$, at z=1.39 the population would be $\sim$ 4 Gyr old. Hence, at z = 1.39, only stars with 1.2 $M_\odot \lesssim M \lesssim$ 1.5 $M_\odot$ would be in the He-burning phase since their lifetime in the Main Sequence (MS) is $\sim$3-4 Gyr (Iben 1967). Stars with M<1.2 $M_\odot$ would still be in the MS (lifetime in MS phase $> 10^{10}$ yr), whereas stars with M>1.4$M_\odot$ have already evolved (lifetime in MS phase $< 10^8$ yr). The He-burning phase is characterized by a very short time-scale if compared to the MS phase and, for stars with 1.2 $M_\odot$<M<1.5 $M_\odot$ it lasts just $\sim 10^8$ yr. Hence, this very short time makes highly unlikely that the UV excess seen in the galaxy central regions is due to an excess of intermediate mass stars in the He-burning phase.

4.3.3.2 He-rich stars

One other possibility is that the cores of elliptical galaxies host an He-rich subpopulation of stars. These stars are formed from the gas enriched by the evolution of very high mass stars. In the ΛCDM model the first stars are predicted to be composed principally by hydrogen (see e.g. Blumenthal et al. 1984; Komatsu et al. 2009). The absence of metals disadvantaged the formation of low and intermediate mass stars, since the cooling is less efficient. Results from recent numerical simulations of the collapse and fragmentation of primordial gas clouds suggest that the first stars were predominantly very massive, with typical masses $M_* > 100$ $M_\odot$ (Bromm, Coppi, and Larson 1999; Bromm, Coppi, and Larson 2002; Nakamura and Umemura 2001; Abel, Bryan, and Norman 2000; Abel, Bryan, and Norman 2002). These stars would evolve very quickly and the supernova (SN) explosions that ended their lives would enrich efficiently the interstellar medium (ISM) with heavy elements (see e.g. Ostriker and Gnedin 1996; Gnedin

and Ostriker 1997; Ferrara, Pettini, and Shchekinov 2000; Madau, Ferrara, and Rees 2001). These metals would fall towards the centre of the galaxies due to the potential well naturally explaining the observed negative metallicity gradients resulting from the subsequent generations of stars.

We know that these stars exist in local ellipticals, where they contribute to the classical UV upturn (e.g. O'Connell 1999). Moreover, the UV gradients in Coma galaxies observed by Carter et al. 2011 imply that there exists an He abundance gradient, established at very early times. He-enriched stars are known to be bluer than their counterparts of standard metal abundances. When the initial helium content is higher, the opacity due to Thomson scattering is reduced in the stellar interior, and the nuclear burning luminosity increases during the main sequence. Consequently, the evolution tracks are shifted towards higher luminosities and effective temperatures, and the main sequence lifetime is significantly shortened. For instance, while the 0.8 $M_{\odot}$ model with Y_{in}=0.2 (i.e., the primordial helium abundance predicted by standard Big Bang nucleosynthesis) spends 12.9 Gyr on the main sequence (90% of its total lifetime), those with Y_{in}=0.4 and 0.8 have main sequence lifetimes of 4.62 Gyr and 158 Myr, respectively, which corresponds to 86% and 60% of their total evolution (see Chantereau, Charbonnel, and Decressin 2015).

This behaviour is observed in the bluer UV colours of He-enriched red giants in Lardo et al. 2012 and in the bluer secondary main sequences of several globular clusters (e.g. Bedin et al. 2004; Piotto et al. 2005). Similar results are also found by Kaviraj et al. 2007, who, studying the ultraviolet and optical properties of 38 globular clusters (GCs) in the Virgo elliptical M87, found that the majority of them present a FUV excess justified with the presence of a super-He-rich ($\Delta Y/\Delta Z > 90$) stellar component.

Since these stars will be bluer, they will naturally produce an excess in the UV in the centre, but they will not strongly affect optical colours, as also shown by the above observations in globular clusters. Thus, an He abundance gradient, which is known to exist in the local Universe, would reproduce the observed positive UV-U gradients without fine-tuning. Unfortunately, we lack population synthesis models for He-enriched populations to study this issue in detail.

CHAPTER

5

COLOUR GRADIENTS VS. GALAXIES GLOBAL PROPERTIES

In this Chapter I will investigate whether the observed colour gradients depend on the global properties of the galaxies and/or on the local density within the cluster. In the first section, I will describe the mechanisms typical of the cluster environment, which may affect colour gradients inside the galaxies. In the second section, I will describe the analysis performed to investigate whether and how the observed colour gradients correlate with the global properties of the galaxies and on the local density.

5.1 Dependence of colour gradients on the global properties of galaxies and on the position in the cluster

The presence of correlations between colour gradients and the global properties of the galaxies may provide clues about the different possible mechanisms of stellar mass assembly. There are contradictory evidences of a correlation of colour gradients with the physical properties of galaxies. Earlier studies have claimed a weak correlation with the galaxy mass (e.g. Peletier, Valentijn, and Jameson 1990), at variance with the monolithic collapse predictions. Recently, a stronger correlation with mass has started to emerge (e.g. Tortora et al. 2010; den Brok et al. 2011): high-mass galaxies have steeper gradients than dwarfs, accordingly with the monolithic scenario. During the dissipative collapses, the most of the stellar mass of the galaxies ($\sim$ 80%) form through a violent central burst of star formation, producing a radial variation of the stellar population properties. Indeed, the gas falls towards the centre of the galaxies due to the the deeper potential

well, where it is enriched by the stellar evolutionary processes, producing a radial metal abundance gradient. As this process is regulated by the galaxy potential depth, which is related to the galaxy mass, high-mass galaxies are expected to have steeper gradients than lower-mass ones (Carlberg 1984).

Furthermore, the environment can also affect the colour gradients. The studied galaxies belong to a particular environment (cluster), which, as discussed in Chapter 1.2, is subject to peculiar processes of interactions between galaxies and between galaxies and the hot ICM. In the following, I will describe how the main processes typical of the cluster environment (mergers and ram pressure) can affect colour gradients.

The interactions between galaxies and with the cluster ICM are more efficient close to the cluster centre, where the galaxy density and the temperature of the IMC reach their maxima. Hence, galaxies in the external regions are expected to experience less interactions with other galaxies than in the inner regions. Thus, it is reasonable to suppose that for these galaxies the observed colour gradients are mainly due to the mechanisms of formation and that the interaction processes slightly affect the colour gradients. On the contrary, in the inner region the probability that galaxies are subjects to mergers with other galaxies or to ram pressure is higher than towards the external region and the interaction processes can significantly affect the colour gradients.

Recent simulations predict different effects on colour gradients depending on the type of merger considered. Major mergers (i.e. mergers between galaxies with a comparable mass) produce a significant mixing of the stellar populations, which flattens the colour gradients (see e.g. White 1980; Kobayashi 2004). On the contrary, it has been predicted that minor mergers show a different behavior. The stars of the galaxies satellites accreted are predominantly added at large radii and, assuming lower metallicity for the satellites, lead to steeper colour gradients at large radii (Villumsen 1983). If, instead, the satellites present similar properties of the principal galaxy, the colour gradients would be flattened.

Also ram pressure may affect the colour gradients. This mechanism is more efficient in removing gas from the outskirts of the galaxies, introducing a gradient of the stellar population properties (mainly age), whose steepness depends on the fraction of the gas removed. However, the efficiency of this process in stripping the gas content depends on the mass and density of the galaxy as well as its position in the cluster. Ram pressure is expected to be more efficient at removing gas from low-mass galaxies than from massive galaxies due to their higher potential depth. Furthermore, at equal mass, denser galaxies are expected to be less affected by ram pressure since the gas is more strongly retained.

In the following Section, I will investigate the dependence of the observed colour gradients on the global properties of the galaxies of the sample and on the local density within the cluster.

5.2 Observed colour gradients vs. global properties of galaxies

The analysis described in the previous Chapter has shown that the stellar properties inside the galaxies of the sample are not homogeneous, implying a radial variation in the M/L. In particular, the negative restframe U-R gradients are well produced by a metallicity variation (like observed in the local Universe), even if an age contribution is not excluded. More complex is, instead, the interpretation of the positive restframe UV-U gradient, which is very weakly dependent on age/metallicity of the stellar population and, thus, requires other mechanisms producing an UV excess towards the centre of the galaxies.

To gain insight the mechanisms that could have produced these observed colour variations, I have looked for the presence of correlation of the observed colour gradients with the global properties of the studied galaxies. Indeed, the presence of a correlation between the colour gradients and the physical and structural parameters (e.g. stellar mass, effective radius, stellar mass surface density...) of the galaxies and their position from the cluster centre could allow us to put some constraints on the mechanisms through which the galaxies have accreted their stellar mass.

I considered the stellar mass $\mathcal{M}_*$, the mean age as derived by the SED fitting, the effective stellar mass density $\Sigma_{R_e} = \mathcal{M}_*/(2\pi R_e^2)$ and the central stellar mass density $\Sigma_{1kpc} = \mathcal{M}_{1kpc}/(2\pi R_1^2)$ within 1 kpc radius. Following Saracco et al. (2017), M_{1kpc} has been derived as

$$\mathcal{M}_1 = L_{1kpc} \times \left(\frac{\mathcal{M}_*}{L_{tot}}\right) = \frac{\gamma(2n,x)}{\Gamma(2n)} \tag{5.1}$$

where

$$L_{1kpc} = 2\pi I_e R_e^2 n \frac{e^{b_n}}{b_n^{2n}} \gamma(2n,x) \tag{5.2}$$

is the luminosity within the central region of 1 kpc, L_{tot} is the total luminosity obtained by replacing in eq. 5.2 $\gamma(2n,x)$ with the complete gamma function $\Gamma(2n)$ (Ciotti 1991) and $\mathcal{M}_*$ is the stellar mass of the galaxy obtained from the SED fitting. In eq. 5.2 n is the Sérsic's index, $x = b_n(R_1/R_e)^{1/n}$, $\gamma(2n,x)$ is the incomplete gamma function and $b_n = 1.9992n - 0.3271$ (Capaccioli and Corwin 1989).

Fig. 5.1 shows the relation between colour gradients and global properties of galaxies. I did not plot the giant central elliptical (#1740), which has a very extended halo that incorporates small galaxies satellites (especially in the F160W image). Hence, the uncertainties on the physical and structural parameters of this galaxy are larger difficult to properly evaluate. No correlation was detected with the global properties of galaxies, both considering the UV-U (upper panel) and the U-R (lower panel) colour gradients. This is not surprising since colour gradients trace principally the variation of the stellar component dominating the galaxy within 1-2R_e while the other properties involve the whole galaxy mass. Similar results are also found by De Propris et al. (2015; 2016) for

cluster red sequence galaxies at a comparable redshift and by Gargiulo et al. (2012) for a sample of field early-type galaxies at $0.9 < z < 1.92$.

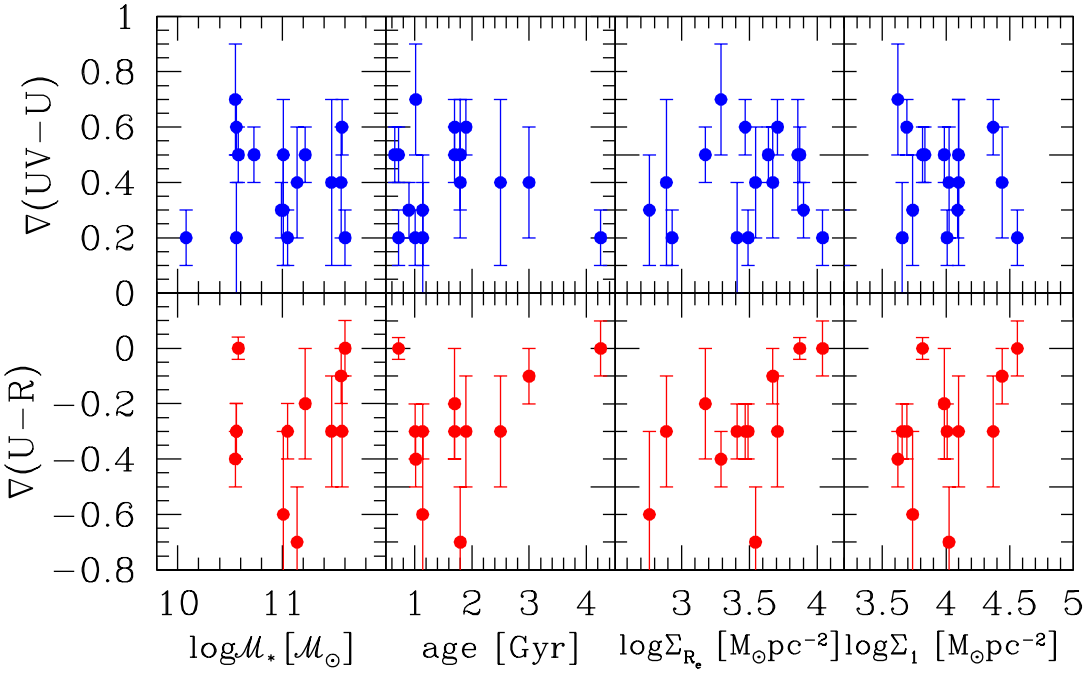

Figure 5.1: The UV-U gradients (upper panels) and U-R gradients (lower panels) versus, from left to right, log$\mathcal{M}_*$, the mean age as derived by the SED fitting, logΣ_{R_e} and logΣ_1 within 1 kpc radius.

Actually, the U-R colour gradient seems to be weakly correlated with the effective stellar mass density of galaxies in the sense that the larger the gradient the lower the density. However, the Spearmen rank test provides a probability of just 90% significance (Spearman's rank coefficient r_s=0.5). To derive Σ_{R_e} I used as reference the effective radius as derived in the F850LP band for the reasons discussed in Chapter 2. I thus tested if this weak correlation is present even if I use the effective radius as derived in the F160W band to derive the stellar mass surface density. The effective radius encloses the 50% of the light of the galaxies. Since $R_{e.850}$ and $R_{e,160}$ are different, the stellar mass inside the two effective radii will be different as well. Hence, I assumed a spherical distribution of the stellar mass inside the effective radii and I have scaled the stellar mass inside $R_{e,850}$ by a factor $(R^3_{e,850}/R^3_{e,160})$ to derive the stellar mass inside $R_{e,160}$ and Σ_{R_e} at $R_{e,160}$. The same weak correlation with the colour gradients has been found.

I have also verified if the amplitude of the colour gradients depends on the local density within the cluster. I used the radial distance from the cluster centre as tracer

of the local density. Also in this case the U-R colour gradient seems to be weakly correlated with the distance with a probability of just 90% significance: galaxies in the denser regions present steeper colour gradients, as shown in fig. 5.2 (left panel). I have, thus, tested if Σ_{R_e} correlates with the distance of the cluster centre, but no correlation has been found, as shown in Fig. 5.2 (right panel). However, as anticipated in Chapter 2 (see fig. 2.4), galaxies #595, #684, #692 and #837 are very closed (the mean distance between the galaxies is $\sim$ 50-60 kpc) and seem to form a group of galaxies, which has recently fallen inside the cluster due to its distance from the centre ($\gtrsim$ 650 kpc). These galaxies are circled in black in Fig. 5.2. Even if we consider this substructure as separated from the cluster, no correlation is found: the Spearmen rank test provides a probability of just 90% significance.

The absence of correlations does not allow us to establish whether the local environment has affected the colour gradients of the galaxies of the sample. However, the observed trend (galaxies with steeper colour gradients are in denser regions) would suggest that major mergers are not responsible of the observed colour variations. Indeed, predictions of the simulations and theoretical models show that this process tends to mix the stellar populations inside the remnant producing flat colour gradients and this does not match with our observations. On the contrary, ram pressure stripping could have affected the observed colour gradients. This process is more efficient in the inner region of the cluster, thus it could explain the steeper gradients observed in the galaxies closer to the cluster centre.

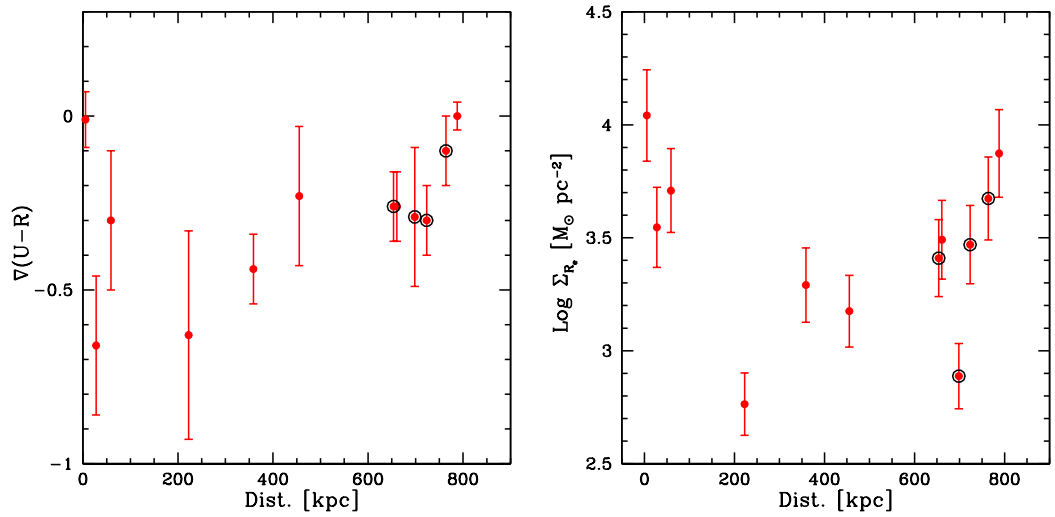

Figure 5.2: *Left panel*: The U-R gradients versus the radial distance from the cluster centre. *Right panel*: The log Σ_{R_e} versus the radial distance from the cluster centre. Galaxies #595, #684, #692 and #837, that are supposed to belong to a group, are circled in black.

CHAPTER

6

CONSTRAINING THE EVOLUTION OF CLUSTER ELLIPTICAL GALAXIES SINCE Z=1.39: COMPARISON WITH COLOUR GRADIENTS IN THE LOCAL UNIVERSE

In this Chapter I investigate, through the evolution of colour gradients and the comparison with colour gradients studied in local ellipticals, how cluster ellipticals have evolved from z=1.39 to z=0.

Furthermore, I compare the colour gradients derived for the 17 cluster ellipticals at z=1.39 with other studies present in literature to verify if we found consistent results.

6.1 Colour gradients at high redshift

6.1.1 Cluster environment

To test whether galaxies belonging to the cluster environment present similar colour gradients, I have compared the colour gradients derived for the 17 cluster ellipticals with those presented by De Propris et al. (2015), Allen et al. (2015) and Chan et al. (2016).

De Propris et al. (2015) studied the F850LP - F160W colour gradients of red sequence galaxies belonging to four clusters (one of which in common with us) at $1 < z < 1.4$ using the ratio of their effective radii measured in the two bands. The authors divide their red sequence galaxies in red discs ($n < 2$) and red spheroids ($n > 2$). My sample has been selected following different criteria: I selected only galaxies on the basis of their elliptical morphology and not on the basis of their concentration index n. Mei et al. (2012 showed that a classification based on $n > 2.5$ to separate early-type and late-type galaxies is not efficient. Indeed, analyzing a sample of $\sim$ 160 galaxies morphologically classified in the Lynx supercluster at z $\approx$ 1.3, the authors found that if they classified galaxies with $n > 2.5$ as early-type, their sample would be contaminated at $\approx 40\%$ by late-type galaxies (especially S0 and Sa galaxies). These results are in agreement with Tamburri et al. (2014), who, analyzing a sample of field galaxies morphologically selected over the redshfit range 0.6 < z < 2.5, also found that a selection criterion based on the Sérsic index does not allow to separate between early-type and late-type galaxies.

De Propris et al. found that the galaxies in their sample present significant positive $log(R_e(z)/R_e(H))$, hence negative colour gradients, larger than those observed locally (e.g. in Virgo cluster), where typical values of $\Delta logR_e$ are < 0.1 (e.g. Ferrarese et al. 2006). Since 16 out to 17 of our ellipticals have n>3, for a proper comparison, in Chapter 3 fig. 3.4 I plotted with grey crosses the galaxies of De Propris et al. (2015) sample with n>3. The median value of the $log(R_e(F850LP)/R_e(F160W))$ of their cluster galaxies with n>3 is 0.18$\pm$0.11, consistent with the median value (0.21$\pm$0.15) of our cluster ellipticals. The authors interpret the negative observed F850LP - F160W gradient in term of radial age gradients, with a younger stellar population towards the outskirts, due to the fact that star formation may have continued for a longer time in the outer regions of the galaxies (e.g. Tacchella et al. 2016). Our interpretation, as resulting from the analysis shown in Chapter 4, does not exclude a contribution of age gradient, specially to justify the most extreme U-R gradients. However, it seems that the major role is played by the metallicity, as also seen in the local ellipticals. Anyway, the similarities in the colour gradients, independently found in the range $1 < z < 1.4$, suggest that cluster galaxies have experienced similar evolutionary processes in their past.

Colour gradients in cluster and field galaxies are also derived by Allen et al. 2015 at $z \sim 2$. The authors selected a mass-completed sample of 59 cluster galaxies at $z = 2.095$ and 478 field galaxies at $2 < z < 2.2$ with $\log(M_*/M_\odot) \geq 9$. Galaxies in both samples are separated in quiescent and star-forming galaxies using the UVJ rest-frame colour - colour diagram (e.g. Williams et al. 2009; Williams et al. 2010; Wuyts et al. 2009; Wild et al. 2014). The authors stacked galaxies images both for cluster and field sample to

measure average F814W - F160W ($(U-V)_{restframe}$) radial colour profiles as a function of the mass. They found that negative colour gradients are only present for massive star-forming field and cluster galaxies with $\log(M_*/M_\odot) > 10.4$. On the contrary, no colour gradients have been found either in field or in cluster quiescent galaxies. Unlike Allen et al. 2015, most of my cluster elliptical galaxies present significative colour gradients. This suggests that from $z \sim 2$ to $z \sim 1.4$ cluster galaxies may have experienced some evolutionary processes, which have increased the amplitude of their colour gradients producing a significant radial variation of their stellar population properties.

Finally, I also compared our results with Chan et al. (2016), who studied a sample of 36 passive galaxies selected in the same cluster considered in my analysis, XMMUJ2235-2557. They base their analysis only on the rest-frame U-R gradient. Since I selected elliptical galaxies, only 12 galaxies are in common. A detailed comparison will be shown in the next subsection. They derived colour U-R gradients from the observed colour profile up to $3.5a_e$ (a_e=major axis), whereas I derived colour gradients from the intrinsic colour profile and at most up to 2 effective radii. For the 12 galaxies in common I found a median value of the F850LP-F160W colour gradients of -0.3±0.1 mag, consistent with the median value (∼-0.4 mag) found by Chan et al. (2016). However, they find both negative gradients (78% of their galaxies) and positive colour gradients, while all the ellipticals of my sample show negative or null F850LP - F160W gradients.

They explain the evolution of the color gradients from $z = 1.39$ to $z \sim 0$ through the presence of an age gradient ($\nabla_{age} \sim -0.33$) besides a metallicity gradient ($\nabla_Z \sim -0.2$). In agreement with Chan et al. 2016, I also found that the rest-frame U-R gradients can be produced by the radial variation of age and metallicity. However, our analysis shows that a relevant information is stored in the UV-U gradient. As pointed out in the previous Chapter, the rest-frame ultraviolet gradient is a very important key to correctly interpret the property of the stellar population of the galaxies and to constrain their history of mass accretion.

6.1.1.1 Comparison with Chan et al. 2016

In this subsection I compare in detail my sample with the one by Chan et al. (2016). The criteria adopted to select the two samples are different. In my analysis, I adopted the ACS-F850LP image for the object detection with SExtractor and as reference in the morphological and structural analysis, given its high resolution (≃ 0.11 arcsec) and small pixel scale (0.05 arcsec/px) when compared to the WFC3-F160W image (FWHM≃ 0.22 arcsec; 0.123 arcsec/px). Furthermore, I selected galaxies (see Section 2.2) at magnitudes F850LP< 24, where the sample is 100% complete, according to their F775-F850 colour and on the basis of their elliptical morphology. Chan et al., instead, used the WFC3-F160W image for object detection with SExtractor and as reference, and selected 36 passive galaxies according to their red sequence colour from the colour–magnitude diagram ((F850LP-F160W) versus F160W). They also applied a magnitude cut of $H_{160} <$ 22.5 mag, which corresponds to a completeness of ∼ 95%.

I verified that 12 out to the 17 ellipticals of my sample are in common with Chan et al. Four of our galaxies (#358, #1539, #2166, #2809) are not included in their sample

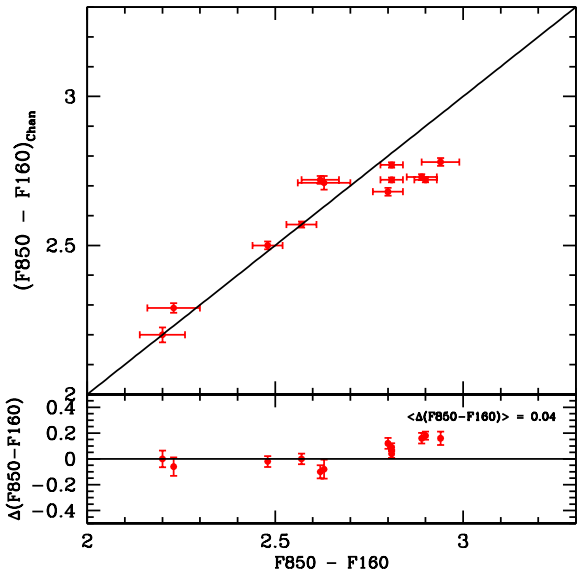

Figure 6.1: Comparison between the F850LP-F160W colours derived by Chan et al. (2016) and our F850LP-F160W colours for the 12 galaxies in common (upper panel). The difference $\Delta(F850 - F160)$=(F850-F160) - $(F850\text{-}F160)_{Chan}$ is plotted as a function of our colours in the lower panel.

since they fall outside the smaller field covered by the WFC3 (5 arcmin^2 instead of 11 arcmin^2 of the ACS). Moreover, also galaxy #1747 is not included in their sample. I verified that its F850LP-F160W colour would be consistent with their colour selection. However, its magnitude (F160W = 22.6 mag, in my sample) seems to be slightly fainter than the cut they applied. Most probably, this is the reason why it is not included in their sample. In fig. 6.1 the comparison between the F850LP-F160W colour of the 12 galaxies in common is shown, after having transformed the colours of the Chan et al. sample from AB to Vega magnitudes. I found that my F850LP-F160W colours (mean value 2.66±0.25 mag) are consistent with those derived by Chan et al. (mean value 2.62±0.19 mag).

The structural parameters of the galaxies have been derived, in both the analyses, using the software *Galfit*. Since the authors do not report the structural parameters derived in the F775W and F850LP bands, I only compare the structural parameters derived in the F160W band. The results are shown in fig. 6.2, where in the left panel I compare the Sérsic indices n and in the right panel I compare the effective radii R_e. I found a good agreement between mine and their estimate of the effective radii ($<R_e/R_{e,Chan}> \simeq 1$) and also between the indices n. For three galaxies (#595, #684 and #837) I obtained from the fit a smaller value of the index n ($< n - n_{Chan} >$ = -1.78). However, I verified through the simulations that an eventual underestimate of n does not affect the estimate of the effective radii and, hence, of the colour gradients.

Finally, I compared the colour gradients. Chan et al. derived only the F850LP-

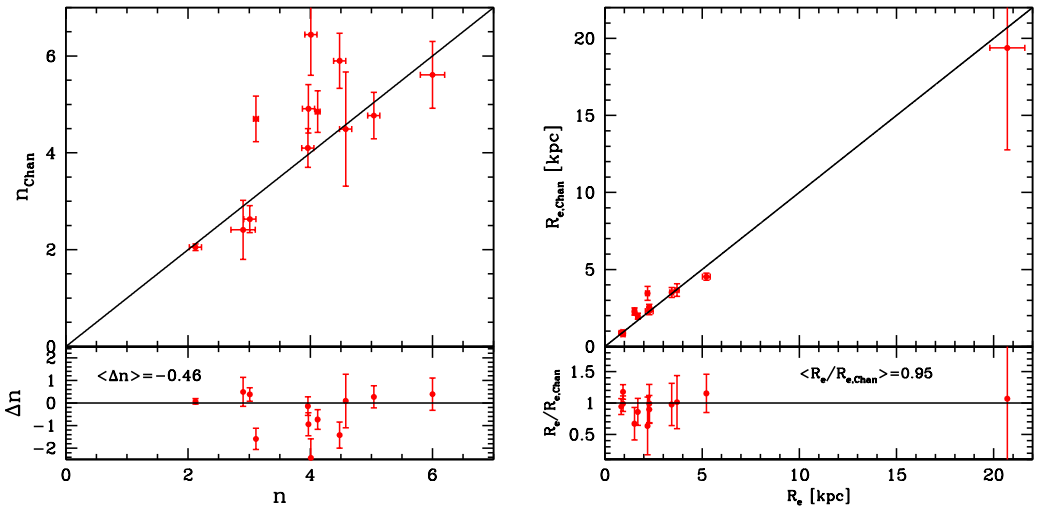

Figure 6.2: *Left panel*: Comparison between the Sérsic indices n derived by Chan et al. (2016) and mine Sérsic indices n for the 12 galaxies in common (upper panel). The difference $\Delta n = n$ - n_{Chan} is plotted as a function of mine n in the lower panel. *Right panel*: Comparison between $R_{e,Chan}$ derived by Chan et al. (2016) in the F160W band and mine R_e for the 12 galaxies in common (upper panel). The ratio $R_e/R_{e,Chan}$ is plotted as a function of mine R_e in the lower panel.

F160W gradients. They derived the colour gradients only from the observed colour profile up to 3.5a (major axis) using elliptical apertures taking as reference the axis ratio and the position angle as derived in the F160W image, whereas I derived colour gradients from the observed colour profiles measuring the fluxes within circular aperture. For this reason, a proper comparison between our results and the colour gradients they derive can not be done. The different apertures used can affect the estimates of the colour gradients, causing a scatter between the measured colour gradients. Most importantly, as I have discussed in Chapter 3, in order to obtain reliable estimates of colour gradients from the observed profiles, it is very important to select a region where the S/N is good in both the bands. I show again fig. 6.3, which shows the observed F850LP - F160W colour profiles for galaxies #595 and #837, which have a large effective radius (3.5 kpc and 7.8 kpc, respectively), up to 3.5a. Blue dashed line represents the effective radius of the galaxies as derived in the F850LP band, while red dashed line represents 3.5a (major axis) as derived in the F160W band by Chan et al. We can see that for $R > 1.5R_e$, the colour profiles of the two galaxies are dominated by the sky noise of the F850LP band, which introduces a spurious contribution in the estimate of the colour gradients. This is the reason why I derived the colour gradients at most up to $2R_e$. For $R \gtrsim 2R_e$ the estimates of the colour gradients are completely affected by the noise introduced by the F850LP image for 10 out to the 13 galaxies ($\sim$76% of the sample) and, hence, their estimates of the colour gradients are not reliable given the depth reached by the ACS image.

Furthermore, for 2 galaxies (#595 and #684) Chan et al. derived a positive gradient, whereas I measured a negative gradient. Actually, to one of the two (#684 in my sample) they assign a large uncertainty that makes it consistent even also with a negative gradient. In fig. 2.7 I show the surface brightness profiles I derived for these galaxies in the three HST bands (third and fourth panel, respectively) and in fig. 3.7 I show their colour profiles, which clearly present a negative trend. Since the authors do not report the effective radii in the F850LP band, to investigate why they derived positive gradients for these two galaxies, I compare my R_e in the F850LP with their R_e in the F160W image. The results are shown in fig. 6.4 (right panel). I plotted in blue the effective radii of galaxies #595 and #684. These galaxies have a ratio $R_{e,850}/R_{e,160} > 1$, so they should present a negative colour gradient. Indeed, if this ratio is > 1, the light is more concentrated in the reddest band considered and the colour gradient is negative; the opposite happens for values < 1 of the ratio. Since, instead, Chan et al. measured a positive gradient for these two galaxies, it follows that the R_e they derived in the F850LP image is smaller than the R_e they derived in the F160W image. However, as shown in fig. 6.4 (left panel), I find that systematically all the galaxies (with the exception of the central one) have the R_e in the F160W smaller than the R_e in the F850LP: $< R_{e.850}/R_{e,160} > \sim 1.5$. I am not able to explain the reason why the radii of #595 and #684 should deviate from this behaviour.

The comparisons shown in the previous sections show that cluster ellipticals at $1 < z < 1.4$ present comparable colour gradients, suggesting that cluster galaxies have experienced similar evolutionary processes in their past.

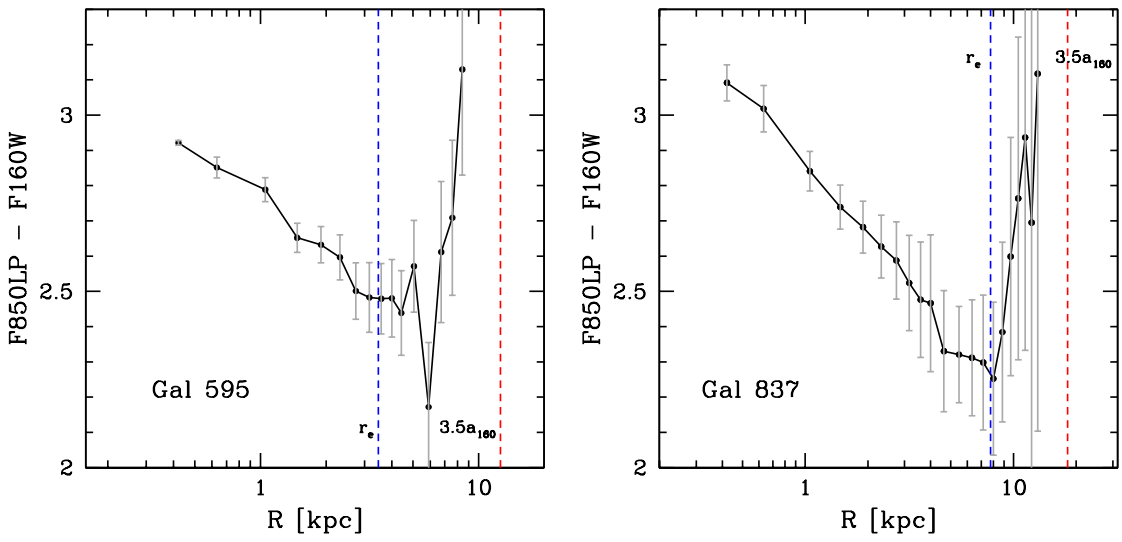

Figure 6.3: Observed F850LP - F160W colour profiles derived by measuring the fluxes within circular apertures centered on each galaxy. Blue dashed line represents the effective radius of the galaxies as we derived in the F850LP band, while red dashed line represents 3.5a (major axis) as derived in the F160W band by Chan et al.

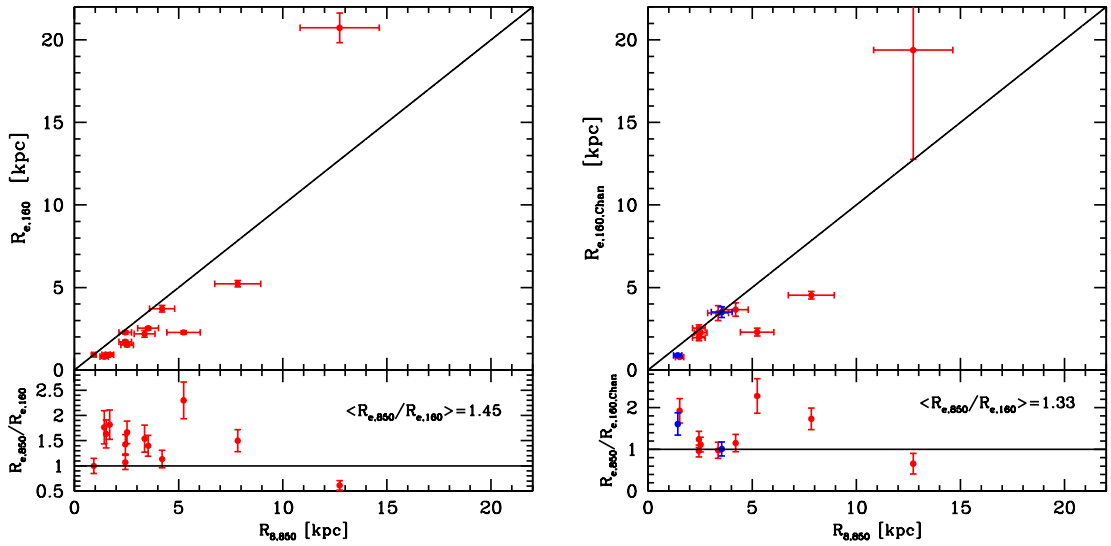

Figure 6.4: *Left panel.* Comparison between R_e we derived in the F850LP image and the R_e derived in the F160W image (upper panel). The ratio $R_{e,850}/R_{e,160}$ is plotted as a function of $R_{e,850}$ in the lower panel. *Right panel.* Comparison between R_e we derived in the F850LP image and the R_e Chan et al. derived in the F160W image (upper panel). In blue we plotted the two galaxies for which Chan et al. derived positive F850LP-F160W gradients. The ratio $R_{e,850}/R_{e,160,Chan}$ is plotted as a function of our $R_{e,850}$ in the lower panel.

6.1.2 Cluster versus field

In this Section I compare the colour gradients derived in the cluster ellipticals of my sample with the colour gradients derived in field ellipticals in order to investigate the role of the environment.

I first compared the colour gradient I have derived with those of Gargiulo et al. (2012). The authors have derived the F850LP - F160W colour gradients for 11 ellipticals morphologically selected at $1 < z < 1.9$ in the GOODS-South region. Structural parameters and colour gradients have been derived as in this work. They found significant at 1σ negative $\nabla(F850LP-F160W)$ within $1R_e$ in $\sim 70\%$ of the galaxies, a fraction that rises up to 100% when R>R_e is considered, as for my sample. By considering the 8 galaxies of their sample in redshift range $1.2 < z < 1.6$, to avoid evolutionary effects, our cluster ellipticals show U-R (F850LP - F160W) colour gradients of amplitudes ($< \nabla >= -0.3\pm0.2$ mag) comparable to those of field ellipticals ($< \nabla >= -0.5\pm0.3$ mag). As for my cluster ellipticals, the authors do not find any correlation between colour gradients and age/stellar mass/effective radii of the galaxies.

In a previous work, the authors studied the F606W - F850LP ($(UV-U)_{restframe}$) for 20 early-type galaxies at $0.9 < z < 1.92$, only 4 of these in common with the other study.

They detected significant radial UV-U colour variation in 10 out of the 20 galaxies, five showing negative gradients and the remaining ones showing positive gradients. Hence, contrary to cluster galaxies, field galaxies at similar redshift ($1.2 < z < 1.6$) seem to present both positive and negative ultraviolet gradients. Their analysis shows that, for $\sim 50\%$ of the sample, the observed gradients can be well reproduced by a pure radial age variation or by a pure metallicity variation while, for the remaining galaxies, more than one property of the stellar population must simultaneously vary to account for the observed gradients. Hence, although the small statistic, this comparison may suggest that the environment could have already influenced the evolution of elliptical galaxies at $z \sim 1.4$.

I also compared my results with those of Guo et al. (2011), who studied the F850LP - F160W colour gradients for 6 massive ($M_* > 10^{10}$ $M_\odot$) early-type galaxies selected at redshift $1.3 < z < 2.5$ in the Hubble Ultra Deep Field (HUDF) on the basis of their early-type morphology and low SSFRs (SSFR = SFR/$M_* \leq 10^{-11}$ yr^{-1}). By deriving colour gradients in concentric annular apertures up to ≈ 10 R_e, they found, in agreement with my results, that the inner regions are redder than the outskirts. A radial variation of a single stellar parameter (age/metallicity) does not account for the observed colour gradients, but they found a correlation between the dust and the observed colour gradients: the redder the inner regions the higher the central dust obscuration. Like Guo et al. (2011) I also found that the radial variation of a single stellar parameter can not account for the observed colour gradients, but I do not confirm the correlation between the observed colour gradients and the dust content. However, their analysis considered only the $\sim$(U-R) colour gradients.

Finally, the structure and the intrinsic properties of the cluster elliptical galaxies of my sample do not differ from those in the field (see Saracco et al. 2017, of which I am a co-author). The authors compared a sample of 56 cluster elliptical galaxies selected in the three clusters XMMJ2235-2557 at $z = 1.39$ (the ellipticals are those selected and studied in this thesis), RDCS J0848+4453 at $z = 1.27$ and XLSS-J0223-0436 at $z = 1.22$ with a sample of 31 field elliptical galaxies in the GOODS-South field at the same redshift. Cluster and field elliptical galaxies are characterized by the same structural parameters at fixed mass and follow the same scaling relations. However, their results suggest that dense environment is more efficient in assembling high-mass elliptical galaxies. Indeed, there is a significant lack of massive ($M_* > 2 \times 10^{11}$ $M_\odot$) and large ($R_e > 4$ - 5 kpc) elliptical galaxies in the field with respect to the cluster. Nonetheless, at $M_* < 2 \times 10^{11}$ $M_\odot$, the two populations are similar. However, there seems to be also a lack of elliptical galaxies in the field as old as the oldest ellipticals in cluster.

6.2 Constraining the evolution of galaxies through the evolution of the colour gradients

In this Section, I investigate, through the evolution of colour gradients, how cluster ellipticals have evolved from $z = 1.39$ to $z = 0$.

Since the early 1970s (Faber 1972), colour gradients in local early-type galaxies have been largely studied. Many studies have shown that local and intermediate redshift elliptical galaxies present negative optical or optical-NIR rest-frame colour gradients (e.g., B-R, U-R, V-K), i.e. they are redder towards the centre. However, it is not clear yet which is/are the stellar population property/ies (age, metallicity, IMF...) that are radially varying in order to produce the observed colour variations. Almost all these works agree that a metallicity gradient is the principal origin of the observed colour variation (e.g. Peletier, Valentijn, and Jameson 1990; Tamura and Ohta 2000; Saglia et al. 2000; Wu et al. 2005; La Barbera et al. 2005; Tortora et al. 2010): the cores are metal-rich compared to the outer region. The metallicity gradient is found to range from -0.1 to -0.3.

A few studies, besides negative metallicity gradients, have found that slightly positive age gradients are necessary to explain the observed radial colour variation, i.e. early-type galaxies tend to have younger and more metal-rich cores (e.g. Saglia et al. 2000; Clemens et al. 2009; Rawle, Smith, and Lucey 2010; La Barbera and de Carvalho 2009).

The colour gradients I derived for 17 ellipticals at $z = 1.39$ are steeper (-0.7 mag $>$ ∇ $>$ -0.1 mag) than colour gradients derived in local ellipticals, where colour gradients range from $\sim$ -0.1 to $\sim$ -0.2 mag (e.g. Peletier, Valentijn, and Jameson 1990; Wu et al. 2005; La Barbera et al. 2005). Hence, in order to flatten the colour gradients from z $\sim$1.4 to z=0, the presence of an age gradient added to a metallicity gradient is needed. Indeed, with no age gradient at $z \sim 1.4$ the evolution of colour gradients would produce steeper colour gradients ($<\nabla> \sim$ -0.6 mag), not observed locally. On the contrary, an age-driven gradient evolution with a metallicity gradient close to the local value is able to reproduce (as we will see below) the smaller amplitude of the colour gradients in the local Universe. Similar results are also found by De Propris et al. (2015) and Chan et al. (2016).

To investigate the evolution of the observed colour gradients, I have passively evolved (that is I simply aged the inner and outer stellar population of 9 Gyr) the model I have discussed in Chapter 4, which are able to simultaneously produced both the colour gradients of the ellipticals of the sample at z=1.39 and I have computed the colour gradients predicted by these models at z=0. I have, then, applied to the colour gradients of each galaxy the difference between the colour gradients predicted by its best model at z=0 and the colour gradients predicted at z=1.39. The results are shown in fig. 6.5, where the colour gradients are plotted as a function of the effective radii of the galaxies. Solid blue and red points represent the UV-U and U-R colour gradients at z=1.39, respectivelyy, whereas black circles represent the evolved colour gradients at z=0. In both the case, a passive evolution of the galaxies flattens the colour gradients of the galaxies a z=0. The grey solid line corresponds to the mean value of the observed

U-R gradients at z=0 by Wu et al. (2005). The mean value of the UV-U gradients at z=0 is 0.20±0.04 mag, while the mean value of the U-R gradients is -0.14±0.04 mag, which is consistent with other studies in literature.

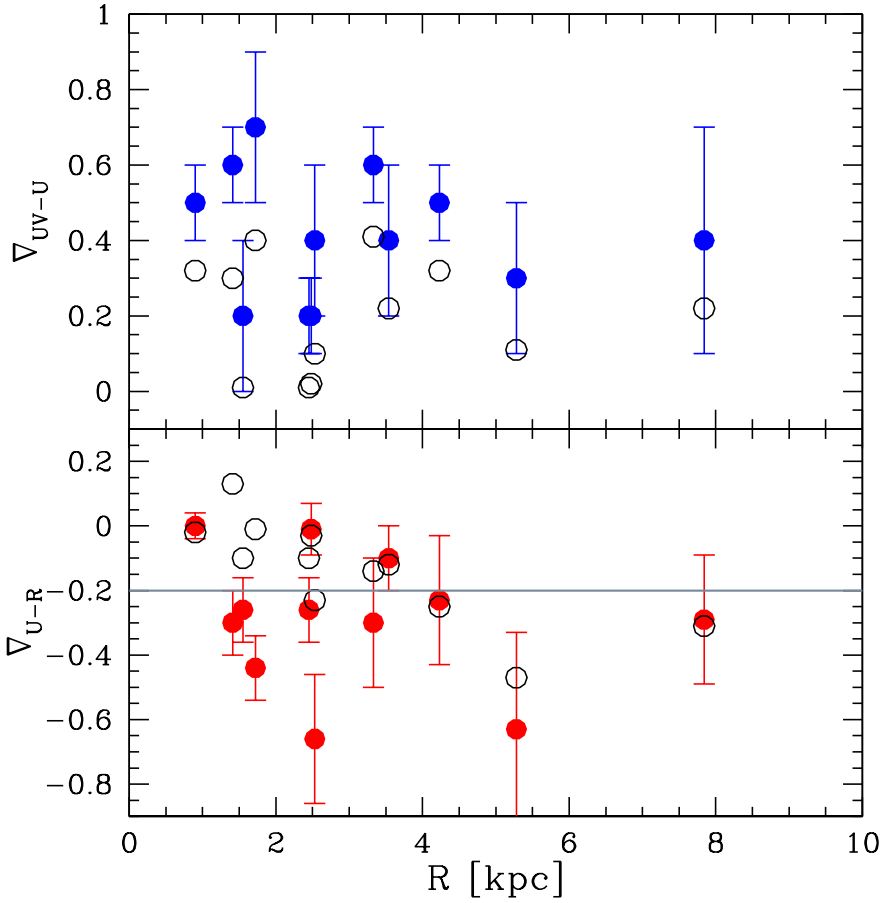

Figure 6.5: Solid blue and red points represent the UV-U and U-R colour gradients at z=1.39, respectively, whereas black circles represent the evolved colour gradients at z=0. The grey solid line corresponds to the mean value of the observed U-R gradients at z=0 by Wu et al. (2005).

For instance, Peletier et al. (1990) studied the U-R and B-R colour gradients, derived as the logarithmic slope of the colour profiles, for 39 local ellipticals belonging to local clusters or groups. Their mean value of the U-R gradients is -0.20±0.02 mag and it is consistent with a metallicity gradient of -0.2.

Also Wu et al. (2005) derived colour gradients of 36 nearby early-type galaxies. The mean value of their U-R gradients is -0.21±0.04 mag. Using simple stellar population models, they derived a metallicity gradient of -0.25±0.03 and an age gradient of 0.02± 0.04. Hence, they conclude that a metallicity gradient is the main of responsible the

observed colour variations.

La Barbera et al. (2005) derived the $g-r$ colour gradients for 1700 early-type galaxies in 159 clusters spanning a range of 0.05 - 0.2. The authors find that colour gradients can be explained by a metallicity gradient ($\nabla_Z \approx -0.2 \div$ -0.4) and, for rich clusters, also by an age gradient ($\nabla_{age} \sim$ -0.15).

Ko et al. (2005) studied the environmental effect on optical-NIR (V-K) colour gradients of 273 nearby elliptical galaxies. The authors derived colour gradients as $\log(r_e(V)/r_e(K))$, finding that $r_e(V)$ is about 33% larger than $r_e(V)$. They divided their sample into different environments and found that elliptical galaxies in the denser environment have flatter colour gradients than those in less dense environment. The median value for rich cluster Abell 2199 is 0.037, for poor cluster Fornax is 0.176 and for field ellipticals is 0.260. Hence, the authors suggest that elliptical galaxies in the denser environment have undergone many merging events and the mixing of stars through merging have flattened the colour gradients. Also in my sample the effective radii in the optical band (rest-frame U) are larger than the effective radii derived in the NIR band (rest-frame R), with a median value of the $\log(r_e(U)/r_e(R))$ of 0.21.

From these comparisons, it results that the evolution of the colour gradients from z=1.39 to z=0 can be explained by a passive evolution of the galaxies. The analysis discussed in the previous Chapters has shown that the metallicity gradient plays the major role in producing the observed colour gradients at z=1.39, with a contribution of an age gradient of $\sim$ 2 Gyr ($\nabla_{Age} \sim$ -0.3).

Assuming a passive evolution, the metallicity gradient observed at z=1.39 ($\nabla_Z \sim$ -0.38) is consistent with those observed at z=0 ($\nabla_Z \approx -0.1 \div$ -0.4) (e.g. Peletier, Valentijn, and Jameson 1990; Wu et al. 2005; La Barbera et al. 2005). The age gradient $\nabla_{age} \sim$ -0.3 corresponds at z=0 to $\nabla_{age} \sim$ -0.05, which is consistent with a flat gradient as found, for instance, by Wu et al. (2005).

Furthermore, the fact that cluster ellipticals passively evolve up to z=0 is consistent with other studies present in literature. For instance, Saracco et al. (2014) studied the size-surface brightness and the size-mass relations of a sample of 16 cluster elliptical galaxies at z=1.27 and they conclude that these galaxies have, for the most part, completed their stellar mass growth at the redshift they are and that, consequently, their evolution at $z < 1.27$ will be dominated by the aging of their stellar content.

Also Andreon et al. (2008) and De Propris et al. (2013), studying the luminosity function and mass function of cluster galaxies at $1 \lesssim z \lesssim 0.2$, found that the evolution of these galaxies is consistent with an aging of their stellar populations.

CHAPTER

7

CONCLUSIONS

In this PhD thesis I investigated the radial variation of the stellar population properties in a sample of 17 ellipticals belonging to the cluster XMMU J2235.3-2557 at z=1.39 with the aim to put some constraints on the mechanisms thorough which these galaxies could have accreted their stellar mass. Indeed, colour gradients represent a powerful tool to gather insight into the processes that concur to accrete the stellar mass in elliptical galaxies, being the colour of a stellar population strongly dependent on its age, star formation time-scale, metallicity and (eventual) presence of dust. Hence, the presence of a colour gradient indicates that the properties of the stellar population inside a galaxy are not homogeneous, but they are radially varying, allowing to constrain the mechanisms driving the mass assembly of early-type galaxies.

The sample of the 17 ellipticals studied has been selected according to four criteria:

- **F850 < 24**: only galaxies brighter than this magnitude has been selected to carry out a robust morphological classification.
- **D < 1 Mpc**: only galaxies within 1 Mpc (Abell's radius) from the cluster centre has been selected.
- **Colour concordance**: I selected galaxies with F775W-F850LP colour consistent with the colour of the 5 elliptical galaxies with known spectroscopic redshift: 0.96 mag < F775W - F850LP < 1.2 mag.
- **Morphological classification**: I classified as ellipticals those galaxies having a regular shape with no signs of disk on the F850LP images and no irregular or structured residuals resulting from the profile fitting.

Making use of the ACS images in the F775W and F850LP bands and of the WFC3 images in the F160W band, I derived their rest-frame UV-U (F775W-F850LP) and U- R (F850LP-F160W) colour gradients using three different methods: the logarithmic slope of the deconvoluted colour profiles, the ratio of the effective radii as measured in the three different filters and through the observed colour profiles. While the first two methods are both dependent on the best-fitting procedure of the colour profiles, the third method does not involve any fit of the light profiles of the galaxies.

The main results of this analysis are:

- The restfreame UV-U colour gradients are systematically positive ($\sim 80\%$) or null ($\sim 20\%$), never negative. On the contrary, the U-R colour gradients are systematically negative ($\sim 70\%$) or null ($\sim 30\%$), never positive. The mean value of the UV-U gradients is 0.4 ± 0.2 mag, slightly larger than the mean value of the U-R gradients (-0.3 ± 0.2 mag) in spite the much narrower wavelength interval of the UV-U gradient.

- The three different methods used to derive color gradients are mutually consistent, implying that the colour gradients I have obtained are independent from the method used to derive them.

- The presence of colour gradients implies that, even if the galaxies in the sample are relatively young (< 4 Gyr old), their stellar content is not homogeneous, but they already exhibit significant differences among their stellar population properties.

I have, thus, investigated the origin of the observed colour gradients making use of BC03 stellar population models. The results are the following:

- The opposite slopes of the observed colour gradients cannot be accounted for by the radial variation of a single parameter (age, metallicity and dust). A variation of these parameters produces ever gradients with concordant slopes. In particular, a radial decrease in metallicity/age/dust from the central to external regions produces negative UV-U and U-R colour gradients; a radial variation in the opposite direction of these properties produces positive UV-U and U-R colour gradient.

- The amplitude of the U-R colour variations observed in the ellipticals of the sample can be easily accounted for by an age or a metallicity radial decrease at 1σ. On the contrary, we are not able to reproduce the amplitude of the UV-U colour gradients observed in our galaxies through age or metallicity variation.

The detected UV-U colour gradients show the presence of an UV excess toward the center of the galaxies with respect to the outer regions and call into question others mechanisms able to efficiently produce UV and U emission in the galaxy central regions. The UV emission sources considered are: star formation, presence of a QSO stars in the He-burning phase and He-rich stars.

- *Star formation*: The analysis discussed in Chapter 4 shows that a weak star formation ($\sim$ 1 $M_\odot$ yr^{-1}) superimposed to an old stellar component towards the centre and to a negative metallicity gradient can reverse the UV-U colour gradient simultaneously reproducing the amplitude and the opposite slopes of the UV-U and U-R colour gradients. The required central star forming component should not exceed $\sim$0.5% in stellar mass not to affect the U-R gradient. In this way, we are able to reproduce both the colour gradients for 11 out of the 13 ellipticals ($\sim$ 85% of the samle), for which both colour gradients are available. However, if this is the cause of the bluer UV-U color toward the center, this implies that all the galaxies are currently experiencing SF in the center since all of them have positive or null UV-U gradients. This in turn implies that the star formation should be steady and protracted over a long time ($>$ 1 Gyr) and not episodic and/or erratic. Being protracted over long time, this SF even if weak should be feeded by the residual processed gas in the galaxies (closed box). This process would efficiently enhance the metallicity towards the centre (e.g. Peng, Maiolino, and Cochrane 2015) producing naturally the observed negative U-R gradients.

- *QSO*: The presence of a QSO could contribute to the UV excess, but it cannot justify alone the observed UV-U gradient unless flattening the U-R gradient and significantly altering the integrated colours of the galaxies.

- *Helium-burning stars*: He-burning stars are stars that have already stopped burning hydrogen in their cores and they are burning helium. At z=1.39, only stars with 1.2 $M_\odot \lesssim M \lesssim$ 1.5 $M_\odot$ would be in the He-burning phase. Since the He-burning timescale for stars in this range of mass is very short ($\sim 10^8$ yr), it would require a very strong fine-tuning in term of synchronism to justify the UV excess observed in almost all the galaxies of our sample. Hence, it is highly unlikely that the observed UV excess is due to the abundance of He-burning stars towards the centre of the galaxies.

- *He-rich stars*: An excess of He-rich stars towards the centre of the galaxies would qualitatively explain the positive UV-U gradients and the negative metallicity U-R gradients as well, without introducing any fine-tuning. It is worth noting that the presence of a population of He-rich stars in the center of elliptical galaxies would be in agreement with the NUV-UV colour gradients observed in some ellipticals in the local universe. Unfortunately, this scenario can not be tested since no suited models are available.

To gain insight the mechanisms that could have produced the observed colour variations, I have looked for the presence of correlation of the observed colour gradients with the global properties of the studied galaxies. Indeed, the presence of a correlation between the colour gradients and the physical and structural parameters (e.g. stellar mass, effective radius, stellar mass surface density...) of the galaxies and their position from the cluster centre could allow us to put some constraints on the mechanisms through which the galaxies have accreted their stellar mass.

The main results are:

- No correlation was detected with the global properties of galaxies, both considering the UV-U and the U-R colour gradients. Similar results are also found by De Propris et al. (2015; 2016) for cluster red sequence galaxies at a comparable redshift and by Gargiulo et al. (2012) for a sample of field early-type galaxies at $0.9 < z < 1.92$.

- Actually, the U-R colour gradient seems to be weakly correlated with the effective stellar mass density Σ_{R_e} of galaxies in the sense that the larger the gradient the lower the density. However, the Spearmen rank test provides a probability of just 90% significance.

I have also verified if the amplitude of the colour gradients depends on the position of the galaxy inside the cluster, namely on the radial distance from the cluster center (i.e. on the local density). Also in this case the U-R colour gradient seems to be weakly correlated with the distance with a probability of just 90% significance: galaxies in the denser regions present steeper colour gradients. I have, thus, tested whether Σ_{R_e} correlates with the distance of the cluster centre, but no correlation has been found. As shown in Fig. 2.4, it is evident the presence of a group of four galaxies (#595, #684, #692 and #837) that are very closed (the mean distance between the galaxies is $\sim$ 50-60 kpc) and seem to form a group of galaxies, which has recently fallen inside the cluster due to its distance from the centre. Even if we consider this substructure as separated from the cluster, no correlation is found.

The absence of correlations does not allow us to establish whether the local environment has affected the colour gradients of the galaxies of the sample. However, the observed trend (galaxies with steeper colour gradients are in denser regions) would allow us to exclude some mechanisms.

The interactions between galaxies and with the cluster ICM are more efficient close to the cluster centre, where the galaxy density and the temperature of the IMC reach their maxima. Hence, galaxies in the external regions are expected to experience less interactions with other galaxies than in the inner regions. Thus, it is reasonable to suppose that for these galaxies the observed colour gradients are mainly due the mechanisms of formation and that the interaction processes slightly affect the colour gradients. On the contrary, in the inner region the probability that galaxies are subjects to mergers with other galaxies or to ram pressure is higher than towards the external region and the interaction processes can significantly affect the colour gradients.

- Galaxies closer to the centre present steeper colour gradients. This would suggest that major mergers are not responsible of the observed colour variations. Indeed, predictions of the simulations and theoretical models show that this process tends to mix the stellar populations inside the remnant producing flat colour gradients and this does not match with our observations.

- Ram pressure may affect the colour gradients. This mechanism is more efficient in removing gas from the outskirts of the galaxies, introducing a gradient of the stellar population properties, whose steepness depends on the fraction of the gas removed. Furthermore, ram pressure is more efficient in the inner region of the cluster, thus it could explain the steeper gradients observed in the galaxies closer to the cluster centre.

Finally, I have investigated, through the evolution of colour gradients, how cluster ellipticals have evolved from z=1.39 to z=0. From the comparison with studies on colour gradients in the local Universe (see e.g., Peletier et al. 1990, Wu et al. 2005, La Barbera et al. 2005), it results that the evolution of the colour gradients from z=1.39 to z=0 can be explained by a passive evolution of the galaxies.

Assuming a passive evolution, the metallicity gradient observed at z=1.39 ($\nabla_Z \sim$ -0.38) is consistent with those observed at z=0 ($\nabla_Z \approx -0.1 \div$ -0.4) (e.g. Peletier, Valentijn, and Jameson 1990; Wu et al. 2005; La Barbera et al. 2005). The age gradient $\nabla_{Age} \sim$ -0.3 corresponds at z=0 to $\nabla_{Age} \sim$ -0.05, which is consistent with a flat gradient as found, for instance, by Wu et al. (2005).

The passive evolution of cluster galaxies is consistent with other studies present in literature. For instance, Saracco et al. (2014) studied the size-surface brightness and the size-mass relations of a sample of 16 cluster elliptical galaxies at z=1.27 and they conclude that these galaxies have, for the most part, completed their stellar mass growth at the redshift they are and that consequently, their evolution at $z < 1.27$ will be dominated by the aging of their stellar content.

Also Andreon et al. (2008) and De Propris et al. (2013), studying the luminosity function and mass function of cluster galaxies from $z \sim 1$ to z=0, found that the evolution of these galaxies is consistent with an aging of their stellar populations.

In the future, an important improvement to this study can be derived by studying colour gradients in field ellipticals at a comparable redshift (~ 1.4) in order to investigate whether and how the environment affects the formation and evolution of this class of galaxies. Indeed, theoretical simulations predict that the formation of these galaxies would differ in dense and sparse environments: ellipticals in dense environment would be formed at $z > 3$ through violent and rapid bursts of star formation; on the other hand, field galaxies are more likely to form through major mergers of disc galaxies at lower redshift (e.g. z < 2). This will reflect in different distributions of the stellar populations within these galaxies.

Finally, besides colour information, it would be useful to derive spectroscopic ages and metallicity through dedicated spatially resolved spectroscopic observations by fitting the features of indicative spectral indices (like Mgb(5175), Δ(4000), H+K(CaII)...) and by comparing them with spectrophotometric models. Indeed, spectroscopic gradients allow to break the age-metallicity degeneracy affecting the optical colours of the stellar populations (e.g. Worthey 1994). While Mg features allows to constrain the metallicity gradient and chemical composition of the galaxies, the combination with stellar age indicators, such as Δ(4000), would allow to detect the presence of an age gradient within the galaxies.

BIBLIOGRAPHY

[1] M. G. Abadi, B. Moore, and R. G. Bower. "Ram pressure stripping of spiral galaxies in clusters". In: *MNRAS* 308 (Oct. 1999), pp. 947–954.

[2] T. Abel, G. L. Bryan, and M. L. Norman. "The Formation and Fragmentation of Primordial Molecular Clouds". In: *ApJ* 540 (Sept. 2000), pp. 39–44.

[3] T. Abel, G. L. Bryan, and M. L. Norman. "The Formation of the First Star in the Universe". In: *Science* 295 (Jan. 2002), pp. 93–98. eprint: `astro-ph/0112088`.

[4] G. O. Abell. "The Distribution of Rich Clusters of Galaxies." In: *ApJS* 3 (May 1958), p. 211.

[5] R. J. Allen et al. "The Differential Size Growth of Field and Cluster Galaxies at z = 2.1 Using the ZFOURGE Survey". In: *ApJ* 806, 3 (June 2015), p. 3.

[6] S. Andreon et al. "Galaxy evolution in the high-redshift, colour-selected cluster RzCS 052 at z = 1.02". In: *MNRAS* 385 (Apr. 2008), pp. 979–985.

[7] I. K. Baldry et al. "Quantifying the Bimodal Color-Magnitude Distribution of Galaxies". In: *ApJ* 600 (Jan. 2004), pp. 681–694.

[8] S. P. Bamford et al. "Galaxy Zoo: the dependence of morphology and colour on environment". In: *MNRAS* 393 (Mar. 2009), pp. 1324–1352.

[9] N. Bastian et al. "Constraining globular cluster formation through studies of young massive clusters - I. A lack of ongoing star formation within young clusters". In: *MNRAS* 436 (Dec. 2013), pp. 2852–2863.

[10] C. M. Baugh, S. Cole, and C. S. Frenk. "Evolution of the Hubble sequence in hierarchical models for galaxy formation". In: *MNRAS* 283 (Dec. 1996), pp. 1361–1378.

[11] W. A. Baum et al. “The Main Sequence of the Globular Cluster M13.” In: *ApJ* 130 (Nov. 1959), p. 749.

[12] L. R. Bedin et al. “ω Centauri: The Population Puzzle Goes Deeper”. In: *ApJL* 605 (Apr. 2004), pp. L125–L128.

[13] M. Begelman, M. de Kool, and M. Sikora. “Outflows driven by cosmic-ray pressure in broad absorption line QSOs”. In: *ApJ* 382 (Dec. 1991), pp. 416–432.

[14] E. F. Bell et al. “Nearly 5000 Distant Early-Type Galaxies in COMBO-17: A Red Sequence and Its Evolution since z$\sim$1”. In: *ApJ* 608 (June 2004), pp. 752–767.

[15] M. Bernardi et al. “Early-Type Galaxies in the Sloan Digital Sky Survey. III. The Fundamental Plane”. In: *AJ* 125 (Apr. 2003), pp. 1866–1881.

[16] M. Bernardi et al. “Evolution and Environment of Early-Type Galaxies”. In: *AJ* 131 (Mar. 2006), pp. 1288–1317.

[17] E. Bertin and S. Arnouts. “SExtractor: Software for source extraction.” In: *A&AS* 117 (June 1996), pp. 393–404.

[18] G. R. Blumenthal et al. “Formation of galaxies and large-scale structure with cold dark matter”. In: *Nature* 311 (Oct. 1984), pp. 517–525.

[19] M. Bolzonella, J.-M. Miralles, and R. Pelló. “Photometric redshifts based on standard SED fitting procedures”. In: *A&A* 363 (Nov. 2000), pp. 476–492.

[20] R. G. Bower, J. R. Lucey, and R. S. Ellis. “Precision photometry of early-type galaxies in the Coma and Virgo clusters: A test of the universality of the colour-magnitude relation. I - The data. II. Analysis”. In: *MNRAS* 254 (Feb. 1992), pp. 589–613.

[21] V. Bromm, P. S. Coppi, and R. B. Larson. “Forming the First Stars in the Universe: The Fragmentation of Primordial Gas”. In: *ApJL* 527 (Dec. 1999), pp. L5–L8.

[22] V. Bromm, P. S. Coppi, and R. B. Larson. “The Formation of the First Stars. I. The Primordial Star-forming Cloud”. In: *ApJ* 564 (Jan. 2002), pp. 23–51.

[23] T. M. Brown et al. “A Far-Ultraviolet Analysis of the Stellar Populations in Six Elliptical and S0 Galaxies”. In: *ApJ* 482 (June 1997), pp. 685–707.

[24] G. Bruzual and S. Charlot. “Stellar population synthesis at the resolution of 2003”. In: *MNRAS* 344 (Oct. 2003), pp. 1000–1028.

[25] D. Burstein et al. “The far-ultraviolet spectra of early-type galaxies”. In: *ApJ* 328 (May 1988), pp. 440–462.

[26] D. Calzetti et al. “The Dust Content and Opacity of Actively Star-forming Galaxies”. In: *ApJ* 533 (Apr. 2000), pp. 682–695.

[27] M. Capaccioli and H. G. Corwin Jr. “Gérard and Antoinette de Vaucouleurs: a life for astronomy.” In: *Advanced Series in Astrophysics and Cosmology* 4 (1989).

[28] R. G. Carlberg. "Dissipative formation of an elliptical galaxy". In: *ApJ* 286 (Nov. 1984), pp. 403–415.

[29] D. Carter et al. "The spatial distribution and origin of the FUV excess in early-type galaxies". In: *MNRAS* 414 (July 2011), pp. 3410–3423.

[30] P. Cassata et al. "The Morphology of Passively Evolving Galaxies at z $\sim$ 2 from Hubble Space Telescope/WFC3 Deep Imaging in the Hubble Ultra Deep Field". In: *ApJL* 714 (May 2010), pp. L79–L83.

[31] A. Cattaneo et al. "Downsizing by shutdown in red galaxies". In: *MNRAS* 389 (Sept. 2008), pp. 567–584.

[32] A. Cattaneo et al. "Modelling the galaxy bimodality: shutdown above a critical halo mass". In: *MNRAS* 370 (Aug. 2006), pp. 1651–1665.

[33] G. Chabrier. "Galactic Stellar and Substellar Initial Mass Function". In: *PASP* 115 (July 2003), pp. 763–795.

[34] J. C. C. Chan et al. "Sizes, colour gradients and resolved stellar mass distributions for the massive cluster galaxies in XMMUJ2235-2557 at z = 1.39". In: *MNRAS* 458 (May 2016), pp. 3181–3209.

[35] W. Chantereau, C. Charbonnel, and T. Decressin. "Evolution of long-lived globular cluster stars. I. Grid of stellar models with helium enhancement at [Fe/H] = -1.75". In: *A&A* 578, A117 (June 2015), A117.

[36] C. Chiosi and G. Carraro. "Formation and evolution of elliptical galaxies". In: *MNRAS* 335 (Sept. 2002), pp. 335–357.

[37] A. Cimatti. "The formation and evolution of early-type galaxies: solid results and open questions". In: *American Institute of Physics Conference Series*. Ed. by G. Giobbi et al. Vol. 1111. American Institute of Physics Conference Series. May 2009, pp. 191–198. arXiv: 0901.1457.

[38] A. Cimatti et al. "GMASS ultradeep spectroscopy of galaxies at z $\sim$ 2. II. Superdense passive galaxies: how did they form and evolve?" In: *A&A* 482 (Apr. 2008), pp. 21–42.

[39] A. Cimatti et al. "Old galaxies in the young Universe". In: *Nature* 430 (July 2004), pp. 184–187.

[40] L. Ciotti. "Stellar systems following the R exp 1/m luminosity law". In: *ApJ* 249 (Sept. 1991), pp. 99–106.

[41] M. S. Clemens et al. "The history of star formation and mass assembly in early-type galaxies". In: *MNRAS* 392 (Jan. 2009), pp. L35–L39. arXiv: 0809.1189.

[42] A. D. Code and G. A. Welch. "Ultraviolet photometry from the Orbiting Astronomical Observatory. XXVI - Energy distributions of seven early-type galaxies and the central bulge of M31". In: *ApJ* 228 (Feb. 1979), pp. 95–104.

[43] L. L. Cowie and A. Songaila. "Thermal evaporation of gas within galaxies by a hot intergalactic medium". In: *Nature* 266 (Apr. 1977), pp. 501–503.

[44] L. L. Cowie et al. "New Insight on Galaxy Formation and Evolution From Keck Spectroscopy of the Hawaii Deep Fields". In: *AJ* 112 (Sept. 1996), p. 839.

[45] E. Daddi et al. "Passively Evolving Early-Type Galaxies at $1.4 \lesssim z \gtrsim 2.5$ in the Hubble Ultra Deep Field". In: *ApJ* 626 (June 2005), pp. 680–697.

[46] G. De Lucia et al. "The formation history of elliptical galaxies". In: *MNRAS* 366 (Feb. 2006), pp. 499–509.

[47] R. De Propris, M. Bremer, and S. Phillipps. "Morphological evolution of cluster red sequence galaxies in the past 9 Gyr". In: *ArXiv e-prints* (June 2016). arXiv: 1606.07192.

[48] R. De Propris, M. N. Bremer, and S. Phillipps. "Morphological evolution in situ: disc-dominated cluster red sequences at $z \sim 1.25$". In: *MNRAS* 450 (June 2015), pp. 1268–1278.

[49] R. De Propris, S. Phillipps, and M. N. Bremer. "Deep luminosity functions and colour-magnitude relations for cluster galaxies at $0.2 < z < 0.6$". In: *MNRAS* 434 (Oct. 2013), pp. 3469–3486.

[50] G. de Vaucouleurs. "Recherches sur les Nebuleuses Extragalactiques". In: *Annales d'Astrophysique* 11 (Jan. 1948), p. 247.

[51] A. Dekel and Y. Birnboim. "Galaxy bimodality due to cold flows and shock heating". In: *MNRAS* 368 (May 2006), pp. 2–20.

[52] A. Dekel, R. Sari, and D. Ceverino. "Formation of Massive Galaxies at High Redshift: Cold Streams, Clumpy Disks, and Compact Spheroids". In: *ApJ* 703 (Sept. 2009), pp. 785–801.

[53] M. den Brok et al. "The HST/ACS Coma Cluster Survey - VI. Colour gradients in giant and dwarf early-type galaxies". In: *MNRAS* 414 (July 2011), pp. 3052–3070. eprint: 1103.1218.

[54] T. Di Matteo, V. Springel, and L. Hernquist. "Energy input from quasars regulates the growth and activity of black holes and their host galaxies". In: *Nature* 433 (Feb. 2005), pp. 604–607.

[55] S. Djorgovski and M. Davis. "Fundamental properties of elliptical galaxies". In: *ApJ* 313 (Feb. 1987), pp. 59–68.

[56] J. Donas et al. "GALEX UV Color Relations for Nearby Early-Type Galaxies". In: *ApJS* 173 (Dec. 2007), pp. 597–606.

[57] B. Dorman, R. W. O'Connell, and R. T. Rood. "Ultraviolet radiation from evolved stellar populations. 2: The ultraviolet upturn phenomenon in elliptical galaxies". In: *ApJ* 442 (Mar. 1995), pp. 105–141.

[58] N. Drake et al. "X-ray wakes in Abell 160". In: *MNRAS* 314 (June 2000), pp. 768–774.

[59] A. Dressler. "Galaxy morphology in rich clusters - Implications for the formation and evolution of galaxies". In: *ApJ* 236 (Mar. 1980), pp. 351–365.

[60] A. Dressler and J. E. Gunn. "Spectral evolution of cluster galaxies". In: *Evolution of the Universe of Galaxies*. Ed. by R. G. Kron. Vol. 10. Astronomical Society of the Pacific Conference Series. 1990, pp. 200–208.

[61] A. Dressler and J. E. Gunn. "Spectroscopy of galaxies in distant clusters. II - The population of the 3C 295 cluster". In: *ApJ* 270 (July 1983), pp. 7–19.

[62] A. Dressler et al. "Spectroscopy and photometry of elliptical galaxies - A large-scale streaming motion in the local universe". In: *ApJL* 313 (Feb. 1987), pp. L37–L42.

[63] O. J. Eggen, D. Lynden-Bell, and A. R. Sandage. "Evidence from the motions of old stars that the Galaxy collapsed." In: *ApJ* 136 (Nov. 1962), p. 748.

[64] R. S. Ellis et al. "The Homogeneity of Spheroidal Populations in Distant Clusters". In: *ApJ* 483 (July 1997).

[65] B. G. Elmegreen and D. M. Elmegreen. "Stellar Populations in 10 Clump-Cluster Galaxies of the Hubble Ultra Deep Field". In: *ApJ* 627 (July 2005).

[66] S. M. Faber. "10-Color Photometry of Elliptical Galaxies and Globular Clusters." In: *Bulletin of the American Astronomical Society*. Vol. 4. BA&A. Mar. 1972, p. 224.

[67] S. M. Faber and R. E. Jackson. "Velocity dispersions and mass-to-light ratios for elliptical galaxies". In: *ApJ* 204 (Mar. 1976), pp. 668–683.

[68] R. Farouki and S. L. Shapiro. "Computer simulations of environmental influences on galaxy evolution in dense clusters. II - Rapid tidal encounters". In: *ApJ* 243 (Jan. 1981), pp. 32–41.

[69] A. Ferrara, M. Pettini, and Y. Shchekinov. "Mixing metals in the early Universe". In: *MNRAS* 319 (Dec. 2000), pp. 539–548.

[70] L. Ferrarese et al. "The ACS Virgo Cluster Survey. VI. Isophotal Analysis and the Structure of Early-Type Galaxies". In: *ApJS* 164 (June 2006), pp. 334–434.

[71] I. Ferreras and J. Silk. "How Young are Early-type Cluster Galaxies? Quantifying the Young Stellar Component in a Rich Cluster at z=0.41". In: *ApJL* 541 (Oct. 2000), pp. L37–L40.

[72] K. Finlator and R. Davé. "The origin of the galaxy mass-metallicity relation and implications for galactic outflows". In: *MNRAS* 385 (Apr. 2008), pp. 2181–2204. arXiv: 0704.3100.

[73] P. J. Francis et al. "A high signal-to-noise ratio composite quasar spectrum". In: *ApJ* 373 (June 1991), pp. 465–470.

[74] Y. Fujita. "Quantitative Estimates of Environmental Effects on the Star Formation Rate of Disk Galaxies in Clusters of Galaxies". In: *ApJ* 509 (Dec. 1998), pp. 587–594.

[75] M. Fukugita, C. J. Hogan, and P. J. E. Peebles. "The Cosmic Baryon Budget". In: *ApJ* 503 (Aug. 1998), pp. 518–530.

[76] A. Gargiulo, P. Saracco, and M. Longhetti. "Colour gradients in normal and compact early-type galaxies at $1 < z < 2$". In: *MNRAS* 412 (Apr. 2011), pp. 1804–1813.

[77] A. Gargiulo et al. "Spatially resolved colours and stellar population properties in early-type galaxies at $z \sim 1.5$". In: *MNRAS* 425 (Oct. 2012), pp. 2698–2714.

[78] G. Gavazzi et al. "A snapshot on galaxy evolution occurring in the Great Wall: the role of Nurture at $z = 0$". In: *A&A* 517, A73 (July 2010), A73.

[79] R. Genzel et al. "From Rings to Bulges: Evidence for Rapid Secular Galaxy Evolution at $z \sim 2$ from Integral Field Spectroscopy in the SINS Survey". In: *ApJ* 687, 59-77 (Nov. 2008), pp. 59–77.

[80] N. Y. Gnedin and J. P. Ostriker. "Reionization of the Universe and the Early Production of Metals". In: *ApJ* 486 (Sept. 1997), pp. 581–598.

[81] F. Governato et al. "On the Origin of Early-Type Galaxies and the Evolution of the Interaction Rate in the Field". In: *AJ* 117 (Apr. 1999), pp. 1651–1656.

[82] L. Greggio and A. Renzini. "Clues on the hot star content and the ultraviolet output of elliptical galaxies". In: *ApJ* 364 (Nov. 1990), pp. 35–64.

[83] J. E. Gunn and J. R. Gott III. "On the Infall of Matter Into Clusters of Galaxies and Some Effects on Their Evolution". In: *ApJ* 176 (Aug. 1972), p. 1.

[84] Y. Guo et al. "Color and Stellar Population Gradients in Passively Evolving Galaxies at $z \sim 2$ from HST/WFC3 Deep Imaging in the Hubble Ultra Deep Field". In: *ApJ* 735, 18 (July 2011), p. 18.

[85] Z. Han. "A possible solution for the lack of EHB binaries in globular clusters". In: *A&A* 484 (June 2008), pp. L31–L34.

[86] Z. Han, P. Podsiadlowski, and A. E. Lynas-Gray. "A binary model for the UV-upturn of elliptical galaxies". In: *MNRAS* 380 (Sept. 2007), pp. 1098–1118.

[87] Z. Han et al. "The origin of subdwarf B stars - I. The formation channels". In: *MNRAS* 336 (Oct. 2002), pp. 449–466.

[88] Z. Han et al. "The origin of subdwarf B stars - II". In: *MNRAS* 341 (May 2003), pp. 669–691.

[89] D. W. Hogg. "Distance measures in cosmology". In: *ArXiv Astrophysics e-prints* (May 1999). eprint: `astro-ph/9905116`.

[90] D. W. Hogg et al. "The Luminosity Density of Red Galaxies". In: *ApJ* 124 (Aug. 2002), pp. 646–651.

[91] B. Holden and D. Kelson. "Mass and the Morphology-Density Relation". In: *Cosmic Frontiers*. Ed. by N. Metcalfe and T. Shanks. Vol. 379. Astronomical Society of the Pacific Conference Series. Dec. 2007.

[92] B. P. Holden et al. "Evolution in the Cluster Early-Type Galaxy Size-Surface Brightness Relation at $z \sim 1$". In: *ApJ* 626 (June 2005), pp. 809–822.

[93] B. P. Holden et al. "The Fundamental Plane of Cluster Elliptical Galaxies at z=1.25". In: *ApJL* 620 (Feb. 2005), pp. L83–L86. eprint: `astro-ph/0412570`.

[94] E. Horch, P. Demarque, and M. Pinsonneault. "The evolution of high-metallicity horizontal-branch stars and the origin of the ultraviolet light in elliptical galaxies". In: *ApJL* 388 (Apr. 1992), pp. L53–L56.

[95] E. Hubble and M. L. Humason. "The Velocity-Distance Relation among Extra-Galactic Nebulae". In: *ApJ* 74 (July 1931), p. 43.

[96] I. Iben Jr. "Stellar Evolution Within and off the Main Sequence". In: *ARA&A* 5 (1967), p. 571.

[97] V. Icke. "Distant encounters between disk galaxies and the origin of S0 spirals". In: *A&A* 144 (Mar. 1985), pp. 115–123.

[98] M. Im et al. "Luminosity Functions of Elliptical Galaxies at Z $<$ 1.2". In: *ApJL* 461 (Apr. 1996), p. L79.

[99] I. Jorgensen, M. Franx, and P. Kjaergaard. "The Fundamental Plane for cluster E and S0 galaxies". In: *MNRAS* 280 (May 1996), pp. 167–185.

[100] N. Katz. "Dissipationless collapse in an expanding universe". In: *ApJ* 368 (Feb. 1991), pp. 325–336.

[101] G. Kauffmann. "The age of elliptical galaxies and bulges in a merger model". In: *MNRAS* 281 (July 1996), pp. 487–492.

[102] S. Kaviraj et al. "The UV colours of high-redshift early-type galaxies: evidence for recent star formation and stellar mass assembly over the last 8 billion years". In: *MNRAS* 388 (July 2008), pp. 67–79.

[103] S. Kaviraj et al. "UV bright globular clusters in M87: more evidence for super-He-rich stellar populations?" In: *MNRAS* 377 (May 2007), pp. 987–996.

[104] D. Kawata. "The Role of Clustering of Subclumps in Bright Elliptical Galaxy Formation from a Low-Spin Seed Galaxy". In: *ApJ* 548 (Feb. 2001), pp. 703–711.

[105] D. D. Kelson et al. "The Evolution of Balmer Absorption-Line Strengths in E/S0 Galaxies from z=0 to z=0.83". In: *ApJL* 552 (May 2001), pp. L17–L21.

[106] R. C. Kennicutt Jr. "Star Formation in Galaxies Along the Hubble Sequence". In: *ARA&A* 36 (1998), pp. 189–232.

[107] D. Kereš et al. "How do galaxies get their gas?" In: *MNRAS* 363 (Oct. 2005), pp. 2–28.

[108] S. Khochfar and J. Silk. "A Simple Model for the Size Evolution of Elliptical Galaxies". In: *ApJL* 648 (Sept. 2006), pp. L21–L24.

[109] J. Ko and M. Im. "Optical-Near Infrared Color Gradients of Elliptical Galaxies and Their Environmental Dependence". In: *Journal of Korean Astronomical Society* 38 (June 2005), pp. 149–151.

[110] C. Kobayashi. "GRAPE-SPH chemodynamical simulation of elliptical galaxies - I. Evolution of metallicity gradients". In: *MNRAS* 347 (Jan. 2004), pp. 740–758.

[111] C. Kobayashi and N. Arimoto. "Gradients of Absorption-Line Strengths in Elliptical Galaxies". In: *ApJ* 527 (Dec. 1999), pp. 573–599.

[112] A. M. Koekemoer et al. "MultiDrizzle: An Integrated Pyraf Script for Registering, Cleaning and Combining Images". In: *HST Calibration Workshop : Hubble after the Installation of the ACS and the NICMOS Cooling System*. Ed. by S. Arribas, A. Koekemoer, and B. Whitmore. 2003, p. 337.

[113] E. Komatsu et al. "Five-Year Wilkinson Microwave Anisotropy Probe Observations: Cosmological Interpretation". In: *ApJS* 180 (Feb. 2009), pp. 330–376.

[114] J. Kormendy. "Brightness distributions in compact and normal galaxies. II - Structure parameters of the spheroidal component". In: *ApJ* 218 (Dec. 1977), pp. 333–346.

[115] P. Kroupa et al. "The Stellar and Sub-Stellar Initial Mass Function of Simple and Composite Populations". In: *Planets, Stars and Stellar Systems. Volume 5: Galactic Structure and Stellar Populations*. Ed. by T. D. Oswalt and G. Gilmore. 2013, p. 115.

[116] F. La Barbera and R. R. de Carvalho. "The Origin of Color Gradients in Early-Type Systems and their Compactness at High-z". In: *ApJL* 699 (July 2009), pp. L76–L79.

[117] F. La Barbera et al. "Color Gradients in Early-Type Galaxies: Dependence on Environment and Redshift". In: *ApJL* 626 (June 2005), pp. L19–L22.

[118] F. La Barbera et al. "Evolution of UV-NIR structural properties of cluster galaxies". In: *A&A* 409 (Oct. 2003), pp. 21–35.

[119] C. Lardo et al. "Carbon and nitrogen abundances of stellar populations in the globular cluster M 2". In: *A&A* 548, A107 (Dec. 2012), A107.

[120] R. B. Larson. "Dynamical models for the formation and evolution of spherical galaxies". In: *MNRAS* 166 (Mar. 1974), pp. 585–616.

[121] R. B. Larson and B. M. Tinsley. "Star formation rates in normal and peculiar galaxies". In: *ApJ* 219 (Jan. 1978), pp. 46–59.

[122] R. B. Larson, B. M. Tinsley, and C. N. Caldwell. "The evolution of disk galaxies and the origin of S0 galaxies". In: *ApJ* 237 (May 1980), pp. 692–707.

[123] C. Lidman et al. "HAWK-I imaging of the X-ray luminous galaxy cluster XMMU J2235.3-2557. The red sequence at z = 1.39". In: *A&A* 489 (Oct. 2008), pp. 981–988.

[124] C. Lidman et al. "The importance of major mergers in the build up of stellar mass in brightest cluster galaxies at z = 1". In: *MNRAS* 433 (July 2013), pp. 825–837.

[125] M. Longhetti et al. "The Kormendy relation of massive elliptical galaxies at z $\sim$ 1.5: evidence for size evolution". In: *MNRAS* 374 (Jan. 2007), pp. 614–626.

[126] I. Lonoce et al. "Spectral detection of multiple stellar populations in z $\sim$ 1 early-type galaxies". In: *MNRAS* 444 (Nov. 2014), pp. 2048–2064.

[127] P. Madau, A. Ferrara, and M. J. Rees. "Early Metal Enrichment of the Intergalactic Medium by Pregalactic Outflows". In: *ApJ* 555 (July 2001), pp. 92–105.

[128] C. Maraston. "Evolutionary population synthesis: models, analysis of the ingredients and application to high-z galaxies". In: *MNRAS* 362 (Sept. 2005), pp. 799–825.

[129] D. Marchesini et al. "The Most Massive Galaxies at 3.0 < z < 4.0 in the Newfirm Medium-band Survey: Properties and Improved Constraints on the Stellar Mass Function". In: *ApJ* 725 (Dec. 2010), pp. 1277–1295.

[130] S. Mei et al. "Early-type Galaxies at z = 1.3. I. The Lynx Supercluster: Cluster and Groups at z = 1.3. Morphology and Color-Magnitude Relation". In: *ApJ* 754, 141 (Aug. 2012), p. 141. eprint: 1205.1785.

[131] F. Menanteau, R. G. Abraham, and R. S. Ellis. "Evidence for evolving spheroidals in the Hubble Deep Fields North and South". In: *MNRAS* 322 (Mar. 2001), pp. 1–12.

[132] E. Merlin and C. Chiosi. "Formation and evolution of early-type galaxies. II. Models with quasi-cosmological initial conditions". In: *A&A* 457 (Oct. 2006), pp. 437–453.

[133] E. Merlin et al. "Formation and evolution of early-type galaxies - III. Dependence of the star formation history on the total mass and initial overdensity". In: *MNRAS* 427 (Dec. 2012), pp. 1530–1554.

[134] D. Merritt. "Relaxation and tidal stripping in rich clusters of galaxies. I. Evolution of the mass distribution". In: *ApJ* 264 (Jan. 1983), pp. 24–48.

[135] D. Merritt. "Relaxation and tidal stripping in rich clusters of galaxies. II. Evolution of the luminosity distribution". In: *ApJ* 276 (Jan. 1984), pp. 26–37.

[136] J. C. Mihos. "Morphology of galaxy mergers at intermediate redshift". In: *ApJL* 438 (Jan. 1995), pp. L75–L78.

[137] J. C. Mihos. "The Evolution of Tidal Debris". In: *Recycling Intergalactic and Interstellar Matter*. Ed. by P.-A. Duc, J. Braine, and E. Brinks. Vol. 217. IAU Symposium. June 2004, p. 390.

[138] B. Moore et al. "Galaxy harassment and the evolution of clusters of galaxies". In: *Nature* 379 (Feb. 1996), pp. 613–616.

[139] B. Moore et al. "On the survival and destruction of spiral galaxies in clusters". In: *MNRAS* 304 (Apr. 1999), pp. 465–474.

[140] A. Mortlock et al. "A deep probe of the galaxy stellar mass functions at z$\sim$1-3 with the GOODS NICMOS Survey". In: *MNRAS* 413 (June 2011), pp. 2845–2859.

[141] C. R. Mullis et al. "Discovery of an X-Ray-luminous Galaxy Cluster at z=1.4". In: *ApJL* 623 (Apr. 2005), pp. L85–L88.

[142] T. Naab, S. Khochfar, and A. Burkert. "Properties of Early-Type, Dry Galaxy Mergers and the Origin of Massive Elliptical Galaxies". In: *ApJL* 636 (Jan. 2006), pp. L81–L84.

[143] T. Naab et al. "Formation of Early-Type Galaxies from Cosmological Initial Conditions". In: *ApJ* 658 (Apr. 2007), pp. 710–720.

[144] F. Nakamura and M. Umemura. "On the Initial Mass Function of Population III Stars". In: *ApJ* 548 (Feb. 2001), pp. 19–32.

[145] C. Nipoti et al. "Can Dry Merging Explain the Size Evolution of Early-Type Galaxies?" In: *ApJL* 706 (Nov. 2009), pp. L86–L90.

[146] C. Nipoti et al. "Size and velocity-dispersion evolution of early-type galaxies in a Λ cold dark matter universe". In: *MNRAS* 422 (May 2012), pp. 1714–1731.

[147] M. Nonino et al. "Deep U Band and R Imaging of Goods-South: Observations, Data Reduction and First Results". In: *ApJS* 183 (Aug. 2009), pp. 244–260.

[148] R. W. O'Connell. "Far-Ultraviolet Radiation from Elliptical Galaxies". In: *ARA&A* 37 (1999), pp. 603–648.

[149] R. W. O'Connell et al. "Ultraviolet imaging of old population in nearby galaxies". In: *ApJL* 395 (Aug. 1992), pp. L45–L48.

[150] R. L. C. Ogando et al. "Do Observed Metallicity Gradients of Early-Type Galaxies Support a Hybrid Formation Scenario?" In: *ApJL* 632 (Oct. 2005), pp. L61–L64. DOI: 10.1086/497824. eprint: astro-ph/0509142.

[151] L. Oser et al. "The Two Phases of Galaxy Formation". In: *ApJ* 725 (Dec. 2010), pp. 2312–2323.

[152] J. P. Ostriker and N. Y. Gnedin. "Reheating of the Universe and Population III". In: *ApJL* 472 (Dec. 1996), p. L63.

[153] M. A. Pahre, R. R. de Carvalho, and S. G. Djorgovski. "Near-Infrared Imaging of Early-Type Galaxies. IV. The Physical Origins of the Fundamental Plane Scaling Relations". In: *AJ* 116 (Oct. 1998), pp. 1606–1625.

[154] D. R. Patton et al. "Close Pairs of Field Galaxies in the CNOC1 Redshift Survey". In: *ApJ* 475 (Jan. 1997), pp. 29–42.

[155] Peacock. "Book Review: Cosmological physics / Cambridge U Press, 1999". In: *Nature* 399 (May 1999), p. 322.

[156] R. F. Peletier, E. A. Valentijn, and R. F. Jameson. "Near-infrared photometry of bright elliptical galaxies". In: *A&A* 233 (July 1990), pp. 62–81.

[157] C. Y. Peng et al. "Detailed Structural Decomposition of Galaxy Images". In: *AJ* 124 (July 2002), pp. 266–293.

[158] Y. Peng, R. Maiolino, and R. Cochrane. "Strangulation as the primary mechanism for shutting down star formation in galaxies". In: *Nature* 521 (May 2015), pp. 192–195.

[159] G. Piotto et al. "Metallicities on the Double Main Sequence of ω Centauri Imply Large Helium Enhancement". In: *ApJ* 621 (Mar. 2005), pp. 777–784.

[160] A. Pipino and F. Matteucci. "Photochemical evolution of elliptical galaxies - I. The high-redshift formation scenario". In: *MNRAS* 347 (Jan. 2004), pp. 968–984.

[161] P. Prugniel and F. Simien. "The fundamental plane of early-type galaxies: non-homology of the spatial structure." In: *A&A* 321 (May 1997).

[162] V. Quilis, B. Moore, and R. Bower. "Gone with the Wind: The Origin of S0 Galaxies in Clusters". In: *Science* 288 (June 2000), pp. 1617–1620.

[163] K. D. Rakos and J. M. Schombert. "Color evolution from Z = 0 to Z = 1". In: *ApJ* 439 (Jan. 1995), pp. 47–59.

[164] T. D. Rawle, R. J. Smith, and J. R. Lucey. "Stellar population gradients in early-type cluster galaxies". In: *MNRAS* 401 (Jan. 2010), pp. 852–866.

[165] A. Renzini. "Stellar Population Diagnostics of Elliptical Galaxy Formation". In: *ARA&A* 44 (Sept. 2006), pp. 141–192.

[166] P. Rosati et al. "Multi-wavelength study of XMMU J2235.3-2557: the most massive galaxy cluster at z > 1". In: *A&A* 508 (Dec. 2009), pp. 583–591.

[167] R. P. Saglia et al. "The evolution of the color gradients of early-type cluster galaxies". In: *A&A* 360 (Aug. 2000), pp. 911–934.

[168] E. E. Salpeter. "The Luminosity Function and Stellar Evolution." In: *ApJ* 121 (Jan. 1955), p. 161.

[169] A. Sandage and N. Visvanathan. "The color-absolute magnitude relation for E and S0 galaxies. II - New colors, magnitudes, and types for 405 galaxies". In: *ApJ* 223 (Aug. 1978), pp. 707–729.

[170] P. Saracco, A. Gargiulo, and M. Longhetti. "On the central stellar mass density and the inside-out growth of early-type galaxies". In: *MNRAS* 422 (June 2012), pp. 3107–3117.

[171] P. Saracco, M. Longhetti, and S. Andreon. "The population of early-type galaxies at 1 < z < 2 - new clues on their formation and evolution". In: *MNRAS* 392 (Jan. 2009), pp. 718–732.

[172] P. Saracco, M. Longhetti, and A. Gargiulo. "Constraining the star formation and the assembly histories of normal and compact early-type galaxies at 1 < z < 2". In: *MNRAS* 412 (Apr. 2011), pp. 2707–2716.

[173] P. Saracco, M. Longhetti, and A. Gargiulo. "The number density of superdense early-type galaxies at 1 < z < 2 and the local cluster galaxies". In: *MNRAS* 408 (Oct. 2010), pp. L21–L25.

[174] P. Saracco et al. "Cluster and field elliptical galaxies at z ∼1.3. The marginal role of the environment and the relevance of the galaxy central regions". In: *A&A* 597, A122 (Jan. 2017), A122.

[175] P. Saracco et al. "Scaling relations of cluster elliptical galaxies at z $\sim$ 1.3. Distinguishing luminosity and structural evolution". In: *A&A* 567, A94 (July 2014), A94.

[176] P. Saracco et al. "The density of very massive evolved galaxies to z$\sim$ 1.7". In: *MNRAS* 357 (Feb. 2005), pp. L40–L44.

[177] M. Schmidt. "Quasi-Stellar Sources". In: *Mitteilungen der Astronomischen Gesellschaft Hamburg* 25 (1968), p. 13.

[178] G. A. Shields. "Thermal continuum from acretion disks in quasars". In: *Nature* 272 (Apr. 1978), pp. 706–708.

[179] J. Sommer-Larsen and S. Toft. "Cosmological Simulations of Massive Compact High-z Galaxies". In: *ApJ* 721 (Oct. 2010), pp. 1755–1764.

[180] M. Spolaor et al. "The Mass-Metallicity Gradient Relation of Early-Type Galaxies". In: *ApJL* 691 (Feb. 2009), pp. L138–L141. DOI: 10.1088/0004-637X/691/2/L138. arXiv: 0901.0548 [astro-ph.GA].

[181] S. A. Stanford, P. R. Eisenhardt, and M. Dickinson. "The Evolution of Early-Type Galaxies in Distant Clusters". In: *ApJ* 492 (Jan. 1998), pp. 461–479.

[182] V. Strazzullo et al. "Cluster galaxies in XMMU J2235-2557: galaxy population properties in most massive environments at z $\sim$1.4". In: *A&A* 524, A17 (Dec. 2010), A17.

[183] S. Tacchella et al. "Evolution of density profiles in high-z galaxies: compaction and quenching inside-out". In: *MNRAS* 458 (May 2016), pp. 242–263.

[184] S. Tamburri et al. "The population of early-type galaxies: how it evolves with time and how it differs from passive and late-type galaxies". In: *A&A* 570, A102 (Oct. 2014), A102.

[185] N. Tamura and K. Ohta. "Color Gradients in Early-Type Galaxies in Abell 2199". In: *AJ* 126 (Aug. 2003), pp. 596–631.

[186] N. Tamura and K. Ohta. "Color Gradients in Early-Type Galaxies in Clusters at Redshift 0.37-0.56". In: *AJ* 120 (Aug. 2000), pp. 533–539.

[187] M. Tanaka et al. "X-Ray Groups of Galaxies at $0.5 < z < 1$ in zCOSMOS: Increased AGN Activities in High Redshift Groups". In: *PASJ* 64 (Apr. 2012).

[188] B. M. Tinsley. "Stellar Evolution in Elliptical Galaxies". In: *ApJ* 178 (Dec. 1972), pp. 319–336.

[189] C. Tortora et al. "Colour and stellar population gradients in galaxies: correlation with mass". In: *MNRAS* 407 (Sept. 2010), pp. 144–162.

[190] M. Tosi. "Models of galactic chemical evolution - The problem of uniqueness". In: *A&A* 197 (May 1988), pp. 33–46.

[191] T. Treu et al. "A Wide-Field Hubble Space Telescope Study of the Cluster Cl 0024+16 at z = 0.4. I. Morphological Distributions to 5 Mpc Radius". In: *ApJ* 591 (July 2003), pp. 53–78.

[192] T. Treu et al. "The properties of field elliptical galaxies at intermediate redshift - I. Empirical scaling laws". In: *MNRAS* 308 (Oct. 1999), pp. 1037–1052.

[193] T. Treu et al. "The properties of field elliptical galaxies at intermediate redshift - III. The Fundamental Plane and the evolution of stellar populations from z∼0.4 to z=0". In: *MNRAS* 326 (Sept. 2001), pp. 237–254.

[194] S. van den Bergh et al. "A Morphological Catalog of Galaxies in the Hubble deep Field". In: *AJ* 112 (Aug. 1996), p. 359.

[195] A. van der Wel et al. "The Evolution of the Field and Cluster Morphology-Density Relation for Mass-Selected Samples of Galaxies". In: *ApJ* 670 (Nov. 2007), pp. 206–220.

[196] P. G. van Dokkum and M. Franx. "The Fundamental Plane in CL 0024 at z = 0.4: implications for the evolution of the mass-to-light ratio." In: *MNRAS* 281 (Aug. 1996), pp. 985–1000.

[197] P. G. van Dokkum et al. "Luminosity Evolution of Field Early-Type Galaxies to Z=0.55". In: *ApJL* 553 (May 2001), pp. L39–L42.

[198] D. E. Vanden Berk et al. "Composite Quasar Spectra from the Sloan Digital Sky Survey". In: *AJ* 122 (Aug. 2001), pp. 549–564.

[199] J. V. Villumsen. "Simulations of galaxy mergers. II". In: *MNRAS* 204 (July 1983), pp. 219–236.

[200] N. Visvanathan and A. Sandage. "The color-absolute magnitude relation for E and S0 galaxies. I - Calibration and tests for universality using Virgo and eight other nearby clusters". In: *ApJ* 216 (Aug. 1977), pp. 214–226.

[201] B. Vollmer et al. "Ram Pressure Stripping and Galaxy Orbits: The Case of the Virgo Cluster". In: *ApJ* 561 (Nov. 2001), pp. 708–726.

[202] C. R. Wagner et al. "Star Formation in High-redshift Cluster Ellipticals". In: *ApJ* 800, 107 (Feb. 2015), p. 107.

[203] S. D. M. White. "Mixing processes in galaxy mergers". In: *MNRAS* 191 (Apr. 1980), 1P–4P.

[204] V. Wild et al. "A new method for classifying galaxy SEDs from multiwavelength photometry". In: *MNRAS* 440 (May 2014), pp. 1880–1898.

[205] R. J. Williams et al. "Detection of Quiescent Galaxies in a Bicolor Sequence from Z = 0-2". In: *ApJ* 691 (Feb. 2009), pp. 1879–1895.

[206] R. J. Williams et al. "The Evolving Relations Between Size, Mass, Surface Density, and Star Formation in 3 x 10^4 Galaxies Since z = 2". In: *ApJ* 713 (Apr. 2010), pp. 738–750.

[207] G. Worthey. "Comprehensive stellar population models and the disentanglement of age and metallicity effects". In: *ApJS* 95 (Nov. 1994), pp. 107–149.

[208] H. Wu et al. "Optical and Near-Infrared Color Profiles in Nearby Early-Type Galaxies and the Implied Age and Metallicity Gradients". In: *ApJ* 622 (Mar. 2005), pp. 244–259.

[209] S. Wuyts et al. "Color Distributions, Number, and Mass Densities of Massive Galaxies at $1.5 < z < 3$: Comparing Observations with Merger Simulations". In: *ApJ* 700 (July 2009), pp. 799–819.

[210] S. K. Yi. "The Current Understanding on the UV Upturn". In: *Hot Subdwarf Stars and Related Objects*. Ed. by U. Heber, C. S. Jeffery, and R. Napiwotzki. Vol. 392. Astronomical Society of the Pacific Conference Series. 2008, p. 3.

[211] S. K. Yi et al. "Galaxy Evolution Explorer Ultraviolet Color-Magnitude Relations and Evidence of Recent Star Formation in Early-Type Galaxies". In: *ApJL* 619 (Jan. 2005), pp. L111–L114.

[212] S. K. Yi et al. "The Ultraviolet Upturn in Elliptical Galaxies and Environmental Effects". In: *ApJS* 195, 22 (Aug. 2011), p. 22.

Monthly Notices of the ROYAL ASTRONOMICAL SOCIETY

MNRAS **466,** 4492–4514 (2017) doi:10.1093/mnras/stx003
Advance Access publication 2017 January 5

Colour gradients in cluster ellipticals at $z \sim 1.4$: the hidden content of the galaxy central regions

F. Ciocca,[1,2]★ P. Saracco,[1] A. Gargiulo[3] and R. De Propris[4]

[1]*INAF-Osservatorio Astronomico di Brera, Via Brera 28, I-20121 Milano, Italy*
[2]*Università degli Studi dell'Insubria, Via Valleggio 11, I-22100 Como, Italy*
[3]*INAF - Istituto di Astrofisica Spaziale e Fisica Cosmica (IASF), Via E. Bassini 15, I-20133 Milano, Italy*
[4]*Finnish Centre for Astronomy with ESO, University of Turku, Finland*

Accepted 2017 January 3. Received 2016 December 22; in original form 2016 July 15

ABSTRACT

We present *F775W–F850LP* (rest-frame $UV - U$) and *F850LP–F160W* (rest-frame $U - R$) colour gradients for a sample of 17 elliptical galaxies morphologically selected in the cluster XMMU J2235.3–2557 at $z = 1.39$. We detected significant negative (redder inwards) $U - R$ colour gradients in ∼70 per cent of the galaxies and flat gradients for the remaining ones. On the other hand, the $UV - U$ gradients are significant positive (bluer inwards) for ∼80 per cent of the galaxies and flat for the remaining ones. Using stellar population synthesis models, we found that the behaviour of the two colour gradients cannot be simultaneously explained by a radial variation of age, metallicity and/or dust. The observed $U - R$ gradients are consistent with a metallicity gradient (mean value $\nabla_Z = -0.4$) in agreement with the one observed in the local elliptical galaxies. The positive $UV - U$ gradients cannot be explained with age or metallicity variations and imply an excess of UV emission towards the galaxies' central regions. This excess calls into question mechanisms able to efficiently produce UV emission. The data require either steady weak star formation ($\lesssim 1\ M_\odot\ yr^{-1}$) or an He-rich population in the cores of these galaxies in order to simultaneously reproduce both the colour gradients. On the contrary, the presence of a Quasi-Stellar Object (QSO) cannot account for the observed UV excess on its own. We discuss these hypotheses on the basis of current observations and available models.

Key words: galaxies: ellipticals and lenticular, cD – galaxies: evolution – galaxies: high-redshift – galaxies: stellar content.

1 INTRODUCTION

The mass assembly and the shaping of the elliptical morphology of early-type galaxies (ellipticals and lenticulars) are not yet completely understood and they represent an important challenge for observational cosmology. Colour gradients represent a powerful tool to constrain the possible mechanisms ruling these two processes. The presence of colour gradients indicates that the properties of the stellar population within galaxy are not homogeneous. Stars may not have been formed in a single burst of star formation, or may have been formed in regions characterized by different physical conditions of the interstellar medium (ISM), or be the result of later episodes of accretion of small satellites. The different mechanisms of mass assembly that may have taken place affect in different ways the internal distribution of stellar populations probed by the colour gradients.

If elliptical galaxies are formed in dissipational scenarios, such as gas-rich major mergers in which most (∼80 per cent) of the stars are formed in a dissipative central starburst (e.g. Khochfar & Silk 2006; Naab et al. 2007; Sommer-Larsen & Toft 2010), or from primordial mergers of lumps of dark and baryonic matter occurring at very early epochs ($z > 4$) (e.g. Chiosi & Carraro 2002; Pipino & Matteucci 2004; Merlin & Chiosi 2006; Merlin et al. 2012), the radial variation of their stellar populations resembles the one expected in the classical monolithic scenario (Eggen, Lynden-Bell & Sandage 1962). In this scenario, gas is more efficiently retained in the centre of the galaxy and thus fuels both more prolonged star formation and chemical evolution, resulting in a negative metallicity gradient (galaxies are more metal-rich in the centre) and a mild positive age gradient (the mean age of stellar populations is younger in the centre) (Kobayashi 2004).

However, this early phase dominated by *in situ* star formation could be followed by an extended phase of *ex situ* accretion of stars from dry minor mergers with smaller satellite stellar systems, as recently proposed by e.g. Oser et al. (2010). In this case,

★ E-mail: federica.ciocca@brera.inaf.it

the above gradients could be strongly affected. In this two-phase process, early-type galaxies continue to grow from the inside-out redistributing the stellar content of the satellites in the outer regions, without mixing with the pre-existing central bulge. However, given the stochastic nature of merger, the resulting galaxies will not show systematics in their colour variation: if age and metallicity of the satellite stellar systems are similar to the central early-type galaxy, the gradients may flatten or, opposite, steepen if the satellites are younger.

In the classical hierarchical merging scenario (e.g. Kauffmann 1996; De Lucia et al. 2006), early-type galaxies form by the wet (gas-rich) major mergers of disc galaxies. During these mergers, star formation *in situ* is triggered by gas cooling and shock heating (e.g. Dekel & Birnboim 2006; Cattaneo et al. 2008) and provides only a minor fraction of the final stellar mass of the remnant, whose stars come principally from the disc progenitors. These major mergers will tend to mix the stellar content of the progenitors producing nearly flat gradients in the remnant. Hereafter, the remnant may later experience minor dry mergers whose effects are those discussed above.

The environment also plays an important role in the evolution of elliptical galaxies. Some theoretical studies suggest that ellipticals in dense environment are formed through bursts of star formation at $z > 3$, unlike field ellipticals that are formed through major mergers of disc galaxies at lower redshift (e.g. $z < 2$) (e.g. Peacock 1999). These different formation patterns would produce different colour gradients as discussed above. Field and cluster galaxies also experience different evolutionary processes due to the different environment. Cluster galaxies, unlike field galaxies, are subject to two main classes of processes: first, the gravitational ones, including the tidal interactions (galaxy–galaxy, galaxy–cluster, harassment) (e.g. Merritt 1983, 1984; Mihos 1995; Fujita 1998) and, secondly, the interactions taking place between the galaxy's ISM and the hot intergalactic medium (ram pressure, thermal evaporation, etc.) (e.g. Gunn & Gott 1972; Cowie & Songaila 1977; Dressler & Gunn 1983; Abadi, Moore & Bower 1999). Processes like ram-pressure stripping or thermal evaporation, removing the gas reservoir from the galaxy, can lead to a rapid quenching of star formation (e.g. Larson, Tinsley & Caldwell 1980; Drake et al. 2000). These processes can either act at global galaxy scale or involve only a region of the galaxy, introducing a gradient of the stellar population properties (mainly age), whose steepness depends on the fraction of gas removed.

All these different predictions show how spatially resolving the properties of the stellar populations within the galaxies may therefore constrain the history of mass assembly and evolution of elliptical galaxies.

Colour gradients in local early-type galaxies have been extensively studied during the last 30 years. Local and intermediate redshift elliptical galaxies show negative optical or optical-NIR rest-frame colour gradients (e.g. $B - R$, $U - R$, $V - K$), i.e. they are redder towards the centre. Almost all these works agree on the fact that a metallicity gradient is the main driver of the observed colour variation (e.g. Peletier, Valentijn & Jameson 1990; Saglia et al. 2000; Tamura & Ohta 2000; La Barbera et al. 2005; Wu et al. 2005; Tortora et al. 2010): the cores are metal-rich compared to the outer region. A few studies have also found that slightly positive age gradients, in addition to the metallicity gradient, are necessary to explain the observed radial colour variation, i.e. early-type galaxies tend to have younger and more metal-rich cores (e.g. Clemens et al. 2009; La Barbera & de Carvalho 2009; Rawle, Smith & Lucey 2010). However, the contribution played by radial age variation is still controversial.

The presence or otherwise of an age gradient is a key piece in understanding of the mass assembly of elliptical galaxies. However, its detection in low-redshift galaxies is a challenging task: an age variation of 1–2 Gyr in a stellar population with a mean age of about 8–9 Gyr reflects a variation of ∼0.05 mag in the $U - R$ colour, much smaller than the one produced by the observed metallicity gradient and comparable to typical photometric errors.

On the contrary, a variation of just 1 Gyr in a stellar population ∼2–3 Gyr old, as in ellipticals at $z \sim 1.5$, would produce a colour variation of ∼0.2 mag, comparable to the one produced by a metallicity variation (see Section 5). Hence, an age variation, if present, would be detectable in high-redshift early-type galaxies. Hence, age gradients, if present, would be more easily detectable in high-redshift galaxies.

Only a few studies of colour gradients in high-redshift elliptical galaxies have been carried out so far. Gargiulo et al. (2012) studied the rest-frame optical $U - R$ and $UV - U$ (Gargiulo, Saracco & Longhetti 2011) colour gradients in a sample of field ellipticals at $1 < z < 2$ and they found that only for half of the sample an age/metallicity gradient can account for the observed gradients. For the remaining half of the sample, the variation of more than one parameter is required to account for the observed colour variation. Recently, Chan et al. (2016) found that the rest-frame optical $U - R$ colour gradients in passive cluster galaxies at z=1.39 are mostly negative, with a median value twice the value in the local Universe (Wu et al. 2005). To reproduce the colour gradients locally observed, the presence of both age and metallicity gradient is needed. It is a conclusion also reached by De Propris, Bremer & Phillipps (2015, 2016) in cluster early-type galaxies at $z > 1$, where age gradients were associated with the presence of disc-like morphologies.

In this paper, we jointly studied the rest-frame $UV - U$ and $U - R$ colour gradients for a sample of 17 elliptical galaxies morphologically selected in the cluster XMMU J2235.3–2557 at z=1.39. Here, we focus on the study of the colour gradients in cluster ellipticals at $z \sim 1.4$, while we refer to a forthcoming paper for their evolution to z=0. Our colour gradients are derived from optical and near-IR data for this cluster in the *Hubble Space Telescope* (*HST*) archive (see the next section).

This paper is organized as follows. In Section 2 we describe the data and the sample selection. In Section 3 we derive the physical (stellar mass, age, absolute magnitudes) and structural (effective radius, index of concentration n) parameters of the galaxies of our sample. In Section 4 we derive the colour gradients with different methods. In Sections 5 and 6 we investigate the origin of the observed colour gradients showing the key role played by the $UV - U$ colour variation in the reconstruction of the history of the mass assembly of elliptical galaxies. In Section 7 we compare our results with previous works. In Section 8 we summarize our results and present our conclusions.

Throughout this paper magnitudes are in the Vega system and we used a standard cosmology with $H_0 = 70$ km s^{-1} Mpc^{-1}, $\Omega_0 = 0.3$ and $\Omega_\Lambda = 0.7$. With these parameters, the age of the Universe at $z = 1.39$ is ~ 4.5 Gyr.

2 DATA DESCRIPTION

2.1 Optical and near-IR data

The analysis presented in this paper is based on data obtained from the *HST*, *Spitzer Space Telescope* data and the Very Large Telescope (VLT).

The *HST* data are composed of archival images of cluster XMMU J2235–2557 (Mullis et al. 2005) at $z = 1.39$ obtained with the Advanced Camera for Surveys (ACS) in the *F775W* (5060 s) and *F850LP* (6240 s) filters (i_{775} and z_{850} hereafter) and with the Wide Field Camera 3 (WFC3) in the *F160W* (∼1200 s) filter. The ACS images have a pixel scale of 0.05 arcsec pixel^{-1} and a resolution of FWHM$_{850} \simeq 0.11$ arcsec. ACS observations cover a field of about 11 arcmin^2 surrounding the cluster, while WFC3 observations a field of about 5 arcmin^2. At $z \simeq 1.4$, the ACS *F775W* and *F850LP* bands probe the younger stellar populations in the near UV, while the WFC3 *F160W* closely corresponds to the rest-frame *R* band and traces the older stellar populations in these galaxies. The original WFC3 images have a pixels scale of 0.123 arcsec pixel^{-1} and a resolution FWHM$_{160} \simeq 0.2$ arcsec. We have re-reduced these images with the software MULTIDRIZZLE (Koekemoer et al. 2003) to match the pixel scale of the ACS images (0.05 arcsec pixel^{-1}), checking that the procedure had not introduced any spurious effects and conserved the flux.

VLT High Acuity Wide field K-band Imager (HAWK-I) observations covering a 13×13 arcmin^2 region centred on the cluster were obtained in the *J* and *Ks* filters (∼10 500 s each) under excellent seeing conditions [FWHM(*J*)≃ 0.5 arcsec and FWHM(*Ks*)≃ 0.35 arcsec]. These data are described in Lidman et al. (2008, 2013).

U-band data were obtained from VIMOS at VLT, for a total exposure of 21 000 s and FWHM of 0.7 arcsec (see Nonino et al. 2009, for details).

Spitzer data in all four Infrared Array Camera (IRAC) bandpasses (3.6, 4.5, 5.8 and 8.0 μm) were retrieved as fully reduced images from the *Spitzer* Science Archive, with exposure times of ∼ 2000 s in all bands.

2.2 Sample selection

Our sample consists of 17 galaxies that we have selected to belong to the cluster XMMU J2235–2557 at $z = 1.39$ (Mullis et al. 2005; Rosati et al. 2009). We selected our final sample following the criteria described in Saracco et al. (2014). Briefly, we first detected all the sources (∼3000) in the *F850LP* band image up to the magnitude limit $z_{850} \simeq 27$ in the ∼11 arcmin^2 region surrounding the cluster. We ran SExtractor (Bertin & Arnouts 1996) in double image mode on the *F850LP*- and *F775W*-band images, using the *F850LP*-band image as the reference image and adopted the MAG_BEST as our fiducial estimate of total magnitude. In order to perform a reliable and robust visual morphological classification, we selected galaxies with magnitudes $z_{850} \leq 24$. At this magnitude limit, the sample is 100 per cent complete. From this flux-limited sample we removed stars using SExtractor's stellarity index (CLASS_STAR >0.9) and we only considered galaxies within ≤1 Mpc (∼120 arcsec) from the cluster centre. This leaves 352 galaxies, 219 of which also have IR data from WFC3. This sample contains the five central cluster member galaxies spectroscopically confirmed by Rosati et al. (2009), three out of which, 1740, 1758 and 1782 of Table 1, are ellipticals (see below for the morphological classification). The mean colour of these five cluster member ETGs is $\langle i_{775} - z_{850} \rangle = 1.08$ with a dispersion $\sigma_{iz} = 0.06$. This colour well traces the redshift of the galaxies. In particular, for $z < 0.8$ the $i_{775} - z_{850}$ colour is always < 0.8 mag, while for $z >$0.8–0.9 its value rapidly increases and remains always > 0.8 mag, independently of the age of the stellar population considered (see e.g. Saracco et al. 2014). In Fig. 1 (right panel) we show the $i_{775} - z_{850}$ colour distribution of the 352 galaxies with $z_{850} \leq 24$, which reflects the behaviour described above. Two peaks are present. We selected all the galaxies in the colour range $0.96 < i_{775} - z_{850} < 1.2$ mag defining the second peak of the colour distribution centred at the mean colour (marked by red solid line in the figure) of the five red sequence member galaxies. The dashed red lines represent $\pm 2\sigma$ from the mean colour of the five cluster members.

According to these criteria, 50 galaxies have been selected as cluster member candidates. Thus, in order to identify the elliptical galaxies, we have performed a morphological classification based on the visual inspection of the galaxies on the ACS-*F850LP* image and on the fitting of their surface brightness profile as described in Section 3.2. We regard galaxies as ellipticals if they have regular shapes, no signs of a disc and smooth residuals after profile fitting

Table 1. Sample of 17 ETGs selected as cluster members at $z_{850} < 24$, within 1 Mpc radius from the cluster centre and having a colour $i_{775} - z_{850} = 1.08 \pm 0.12$, i.e. within 2σ from the mean colour of the five galaxies spectroscopically confirmed cluster members (Rosati et al. 2009).

ID	RA	Dec	$z_{\rm spec}$
358	22:35:27.003	−25:58:14.11	–
595	22:35:26.220	−25:56:45.54	–
684	22:35:25.804	−25:56:46.00	–
692	22:35:25.680	−25:56:58.48	–
837	22:35:24.895	−25:56:37.03	–
1284	22:35:22.814	−25:56:24.92	–
1539	22:35:22.472	−25:56:15.17	–
1740	22:35:20.839	−25:57:39.76	1.39
1747	22:35:20.588	−25:58:20.68	–
1758	22:35:20.920	−25:57:35.90	1.39
1782	22:35:20.707	−25:57:44.43	1.39
1790	22:35:20.707	−25:57:37.70	–
2054	22:35:19.078	−25:58:27.32	–
2147	22:35:19.046	−25:57:51.42	–
2166	22:35:18.168	−25:59:05.89	–
2429	22:35:17.867	−25:56:13.06	–
2809	22:35:18.251	−25:56:06.17	–

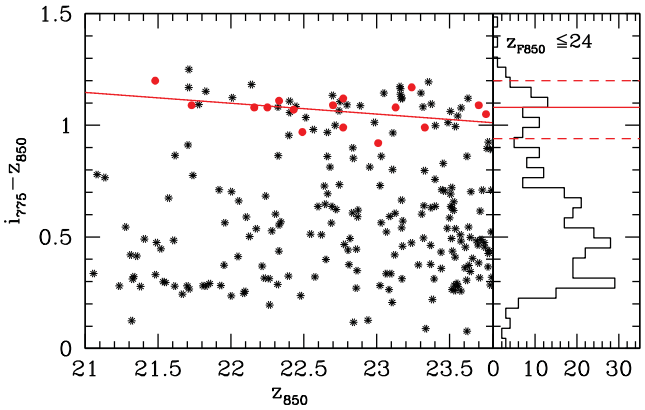

Figure 1. Left panel: colour–magnitude relation. The i_{775}–z_{850} colours of the 17 selected ellipticals (red points) as a function of z_{850} are shown together with those of the 352 galaxies with $z_{850} < 24$ (black asterisks). The solid red line is the colour–magnitude relation $(i_{775}$–$z_{850}) = 2.16(\pm 0.58)$–$0.048(\pm 0.026) z_{850}$ best fitting the 17 ellipticals. Right panel: the $i_{775} - z_{850}$ colour distribution of the 352 galaxies brighter than $z_{850} < 24$ falling within 1 Mpc from the cluster centre is shown. The red solid line marks the mean colour $\langle i_{775} - z_{850} \rangle = 1.08 \pm 0.06$ of the five cluster members spectroscopically confirmed (Rosati et al. 2009). The dashed lines represent $\pm 2\sigma$. A second peak in the distribution centred at the mean colour of the five cluster galaxies is evident.

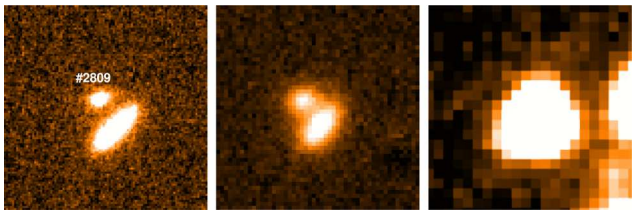

Figure 2. We show galaxy 2809, which is closed to another galaxy. The two galaxies are resolved both in the *F850LP* band image (left panel) (FWHM ∼ 0.12 arcsec) and in the HAWK-I *J*-band image (FWHM ∼ 0.5 arcsec) (central panel), whereas they are completely blended in the *Spitzer*–IRAC 3.6 μm band image due to the lower resolution (FWHM > 2.7 arcsec) and bigger pixel size (0.6 arcsec pixel^{-1}) (right panel). The *F850LP* and *J* images are 5 × 5 arcsec^2, and the IRAC 3.6 μm image is 10 × 10 arcsec^2.

and model subtraction. On this basis, 17 galaxies out of the 50 turned out to be ellipticals. The sample is summarized in Table 1.

Fig. 1 (left panel) shows the i_{775}–z_{850} colours of the 17 selected ellipticals (red points) as a function of z_{850} together with those of the 352 galaxies with $z_{850} < 24$ (black asterisks). The selected ellipticals define a red sequence, as expected. The solid red line is the colour–magnitude relation $(i_{775}–z_{850}) = 2.16(\pm0.58)–0.048(\pm0.026)z_{850}$ best fitting the 17 ellipticals.

2.3 Multiwavelength photometry

We measured the magnitudes for the 17 galaxies selected in all the available bands using SExtractor. We adopted the MAG_BEST as the best estimator of the magnitude.

As mentioned in Section 2.1, the field of view of the WFC3 is smaller than the ACS field (5 arcmin^2 instead of 11 arcmin^2); hence, only 13 ellipticals out of the 17 are covered by WFC3 observations, with galaxies 358, 1539, 2166 and 2809 falling outside.

VIMOS *U*-band observations cover the whole sample to a limiting depth of $U \simeq 28$. Thank to this depth, we detected six galaxies at this wavelength.

HAWK-I *J*- and *Ks*-band images cover the whole sample. Thanks to the excellent resolution of the images all the galaxies are resolved in both the filters.

Also *Spitzer*-IRAC observations cover the whole sample. Magnitudes have been estimated in the four IRAC bands using SExtractor in double image mode adopting the 3.6 μm image as reference. We have tested for the reliability of the flux measurement by comparing the flux of some stars in the field measured with SExtractor with the flux obtained using the IRAF task PHOT. Due to the low resolution (FWHM > 2.7 arcsec), eight galaxies (2809, 595, 692, 358, 1740, 1790, 1782 and 1758) are not resolved but appear fully blended with other close sources. For these galaxies, we have derived their magnitudes in the four IRAC bands by redistributing the total IRAC flux of the blended sources according the fluxes measured for each of them in the *F160W* and *Ks* filters. In Fig. 2 we show as example galaxy 2809, which is closed to another galaxy, in the ACS-*F850LP* (left panel), HAWK-I *J* (central panel) and *Spitzer*-IRAC 3.6 μm (right panel) images. The two galaxies are clearly resolved in the *F850LP* and in the HAWK-I *J*-band images, while they are fully blended in the *Spitzer*-IRAC 3.6 μm image.

In Table 2 we report the photometry in the 10 photometric bands for the 17 ellipticals of the sample.

3 PHYSICAL AND STRUCTURAL PARAMETERS

3.1 Global physical properties of galaxies

For each galaxy we derived the mean global stellar parameters (stellar mass, age, absolute magnitudes) by fitting the spectral energy distribution (SED) defined by the 10 available photometric points. The fit has been performed with the software HYPERZMASS (Bolzonella, Miralles & Pelló 2000) using a set of templates characterized by the composite stellar population models of Bruzual & Charlot (2003, hereafter BC03), the Chabrier initial mass function (IMF; Chabrier 2003), an exponentially declining star formation history (SFH $\propto \exp^{-t/\tau}$). In all the cases, we considered five star formation time-scale (τ = [0.1, 0.3, 0.4, 0.6, 1] Gyr) and solar metallicity $Z_\odot$. For the extinction curve we adopted the Calzetti law (Calzetti et al. 2000), with A_V left as a free parameter and allowed to vary in the range 0.0 to 0.6 mag.

The *F775W*, *F850LP* and *F160W* bands sample $\lambda_{rest} \sim 3200$Å, $\lambda_{rest} \sim 3800$Å and $\lambda_{rest} \sim 6400$Å, respectively, at the cluster redshift. Hence, we derived absolute magnitudes in *UV*, *U* and *R* bands (M_{UV}, M_U and M_R, respectively), with a *k*-correction derived from the best-fitting template. In Table 3 we report the best-fitting values for the age, the logarithm of the stellar mass, M_{UV}, M_U and M_R for the 17 galaxies of the sample.

For 14 galaxies out of the 17, the best-fitting template is defined by a SFH with $\tau = 0.1$ Gyr, while the remaining three galaxies are characterized by SFHs with $\tau = 0.3$ Gyr (837 and 1539) and with $\tau = 0.6$ Gyr (1740). The 17 ellipticals have stellar masses in the range 1.2×10^{10} M$_\odot$ < $M_* < 8.5 \times 10^{11}$ M$_\odot$ with a mean value $M_* \simeq 3 \times 10^{10}M_\odot$ and ages in the range 0.7 Gyr <age ≤ 4.3 Gyr with a mean value of ∼1.7 Gyr.

3.2 Structural parameters

We derived the structural parameters of the ellipticals of our sample by fitting their surface brightness profile with a single Sérsic law

$$\mu(r) = \mu_e + \frac{2.5b_n}{\ln(10)}[(r/r_e)^{1/n} - 1] \quad (1)$$

in the *F775W*, *F850LP* and *F160W* bands. The two-dimensional fitting has been performed using Galfit software (Peng et al. 2002), which returns as best-fitting set of structural parameters the one that minimizes the residuals between the model convolved with the PSF and the observed image. A detailed description of this procedure may be found in Appendix A. The fitting was performed both assuming *n* as a free parameter and assuming $n = 4$ (appropriate for ellipticals that have a de Vaucouleurs profile). In order to test for the dependence of our results on the PSF used, for each galaxy we have convolved the Sérsic profile with two different PSFs, derived empirically (as recommended in the Galfit manual) from two bright, unsaturated and uncontaminated stars in the field. The residual maps lacked of any structure in both the cases and the returned χ^2 values were not statistically different, showing that the results do not depend on the PSF used. Thus, we chose the mean values of the fitting results as best-fitting value for the structural parameters. The structural parameters obtained through the fit are shown in Table A1.

In order to measure colour gradients (see Section 4), we need to measure the radial surface brightness profiles in ellipses having the same orientation and ellipticity in all bands in order to prevent any artificial gradients. Hence, we re-run Galfit on the *F775W* and

Table 2. For each galaxy of the sample we report the photometry in the 10 photometric bands. Optical *U*-band and near-IR *J*- and *Ks*-band magnitudes come from VIMOS and HAWK-I VLT observations, respectively; i_{775}, z_{850} and H_{160} from ACS and WFC3 *HST* observations in the *F775W*, *F850LP* and *F160W* filters, respectively; m3.6, m4.5, m5.8 and m8.0 from the *Spitzer* archival images in the corresponding filters. We adopted the MAG_BEST provided by SExtractor as total magnitude. A detailed description of the photometric measurements is given in Section 2.3.

ID	*U*	i_{775}	z_{850}	*J*	H_{160}	*Ks*	m3.6	m4.5	m5.8	m8.0
358	>28 99	24.85 ± 0.05	23.91 ± 0.04	22.14 ± 0.1	–	20.41 ± 0.05	19.84 ± 0.1	19.69 ± 0.1	19.53 ± 0.4	19.33 ± 0.4
595	27.8±0.3	23.17 ± 0.02	22.16 ± 0.01	20.23 ± 0.03	19.35 ± 0.03	18.35 ± 0.01	16.70 ± 0.1	16.23 ± 0.1	15.99 ± 0.1	15.94 ± 0.2
684	25.9±0.1	24.19 ± 0.03	23.33 ± 0.03	21.92 ± 0.07	21.10 ± 0.06	20.11 ± 0.03	18.15 ± 0.02	17.79 ± 0.03	17.31 ± 0.1	17.41 ± 0.2
692	>28 99	24.80 ± 0.06	23.75 ± 0.04	21.90 ± 0.08	21.12 ± 0.06	19.97 ± 0.03	18.69 ± 0.1	18.46 ± 0.1	18.29 ± 0.3	18.03 ± 0.3
837	>28 99	23.76 ± 0.03	22.77 ± 0.03	20.59 ± 0.05	19.83 ± 0.04	18.61 ± 0.02	16.99 ± 0.01	16.49 ± 0.02	16.38 ± 0.08	16.10 ± 0.1
1284	>28 99	23.65 ± 0.02	22.70 ± 0.02	20.91 ± 0.04	20.22 ± 0.04	19.16 ± 0.02	17.56 ± 0.01	17.09 ± 0.02	16.77 ± 0.09	16.84 ± 0.1
1539	26.02±0.1	23.86 ± 0.02	23.01 ± 0.02	21.28 ± 0.05	–	19.34 ± 0.02	17.63 ± 0.01	17.20 ± 0.03	17.14 ± 0.1	16.87 ± 0.1
1740	24.30 0.05	22.42 ± 0.02	21.48 ± 0.02	18.55 ± 0.02	18.68 ± 0.02	17.44 ± 0.01	15.60 ± 0.1	15.17 ± 0.1	15.17 ± 0.1	14.82 ± 0.2
1747	>28 99	24.79 ± 0.05	23.70 ± 0.04	22.06 ± 0.09	21.25 ± 0.06	20.08 ± 0.03	18.73 ± 0.02	18.41 ± 0.04	18.56 ± 0.3	99.00 ± 99.0
1758	>28 99	24.16 ± 0.03	23.13 ± 0.02	20.46 ± 0.04	20.33 ± 0.04	19.09 ± 0.01	17.58 ± 0.1	17.14 ± 0.1	16.70 ± 0.1	16.89 ± 0.2
1782	24.6±0.5	23.45 ± 0.02	22.49 ± 0.02	19.97 ± 0.03	19.60 ± 0.04	18.40 ± 0.01	16.99 ± 0.1	16.58 ± 0.1	16.55 ± 0.1	16.49 ± 0.2
1790	>28 99	23.22 ± 0.02	22.25 ± 0.02	19.70 ± 0.02	19.35 ± 0.03	18.18 ± 0.01	16.34 ± 0.1	15.91 ± 0.1	15.91 ± 0.1	15.56 ± 0.2
2054	>28 99	23.43 ± 0.02	22.43 ± 0.02	20.67 ± 0.03	19.86 ± 0.04	18.83 ± 0.01	16.96 ± 0.01	16.61 ± 0.03	16.27 ± 0.1	15.79 ± 0.1
2147	>28 99	23.78 ± 0.03	22.77 ± 0.03	20.90 ± 0.04	20.15 ± 0.04	19.02 ± 0.02	16.82 ± 0.02	16.36 ± 0.03	16.37 ± 0.1	15.42 ± 0.1
2166	26.50±0.1	22.80 ± 0.01	21.73 ± 0.01	20.53 ± 0.03	–	18.73 ± 0.01	17.33 ± 0.01	17.13 ± 0.03	17.02 ± 0.1	16.68 ± 0.1
2429	>28 99	24.41 ± 0.03	23.24 ± 0.02	21.96 ± 0.08	21.04 ± 0.06	20.05 ± 0.03	18.15 ± 0.02	17.98 ± 0.04	17.91 ± 0.2	17.36 ± 0.2
2809	>28 99	23.41 ± 0.01	22.33 ± 0.01	20.92 ± 0.03	–	19.28 ± 0.01	18.36 ± 0.1	17.99 ± 0.1	17.96 ± 0.2	16.71 ± 0.2

Table 3. For each of the 17 galaxies of the sample we report the age, the logarithm of the stellar mass and the absolute magnitudes M_{UV}, M_U and M_R derived from the best-fitting template.

ID	Age [Gyr]	log M_* [$M_\odot$]	M_{UV} [mag]	M_U [mag]	M_R [mag]
358	0.72	10.08	−20.14	−20.19	−21.18
595	3.00	11.56	−21.83	−21.95	−23.62
684	1.70	10.56	−20.71	−20.79	−21.91
692	1.14	10.56	−20.23	−20.35	−21.87
837	2.50	11.47	−21.22	−21.36	−23.22
1284	1.01	11.05	−21.29	−21.41	−22.88
1539	1.80	11.01	−21.07	−21.15	−22.67
1740	3.50	11.93	−22.56	−22.65	−24.39
1747	1.02	10.55	−20.22	−20.34	−21.77
1758	1.80	11.14	−20.85	−20.99	−22.73
1782	1.90	11.57	−21.52	−21.65	−23.43
1790	4.25	11.60	−21.76	−21.89	−23.71
2054	1.70	11.22	−21.55	−21.66	−23.21
2147	1.14	11.01	−21.20	−21.31	−22.90
2166	0.90	10.99	−22.19	−22.27	−23.39
2429	0.72	10.58	−20.66	−20.76	−21.98
2809	0.65	10.73	−21.59	−21.67	−22.74
Mean	1.73	10.45	−21.21	−21.32	−22.80

the *F160W* images fixing the position angle *PA* and the axial ratio b/a to those derived for the *F850LP* image. We choose the *F850LP* image as reference band because it has better resolution (FWHM ∼0.11 arcsec) and the smallest pixel scale (0.05 arcsec pixel^{-1}). Moreover, given the shallower surface brightness, it determines the maximum radius at which we can reliably estimate radial gradients (see discussion in the next section). In Table 4 we show for each galaxy the best-fitting n, R_e [kpc] and m_{tot} in the *F775W*, *F850LP* and *F160W* bands obtained taking as reference the position angle and the axis ratio derived in the *F850LP* image. In the same table, we also show in the second row the parameters obtained assuming $n = 4$, i.e. de Vaucouleur's profile. The effective radii R_e, as derived by fitting the Sérsic law in the *F850LP* image, are in the range 0.9–7.8 kpc, with the exception of the dominant central galaxy of the cluster, which has an effective radius $R_e = 12.8$ kpc. The Sérsic index varies in the range 2.1–6, while the total magnitude m_{tot} varies in the range 20.78–23.47 mag.

We have tested the reliability of the surface brightness profile fitting and we have estimated the uncertainties on the structural parameters by using simulated galaxies, as described in Appendix A.

4 COLOUR GRADIENTS

For each of the 17 galaxies of the sample we have derived *F775W–F850LP* and *F850LP–F160W* colour gradients, corresponding to ∼($UV - U$) and ∼($U - R$) in the rest frame. The transformations to obtain the rest-frame colours are: $UV - U$= (*F775W–F850LP*) − 0.8 mag and $U - R$ = (*F850LP–F160W*) − 1.1 mag.

We have used three different methods to estimate the colour gradients: the logarithmic slope of the deconvoluted colour profiles, the ratio of the effective radii as measured in the three different filters and through the observed colour profiles. Our results are broadly independent of the method used and are in good agreement with previous work (see Section 8).

4.1 Intrinsic colour gradients

We first derived the colour gradient as the logarithmic slope of the colour profile (e.g. Peletier et al. 1990)

$$\nabla_{X-Y} = \frac{\Delta(\mu_X(R) - \mu_Y(R))}{\Delta \log R} \quad (2)$$

where μ_X(R) and μ_Y(R) are the surface brightness profiles of the galaxy in the generic *X* and *Y* bands, respectively.

We fitted the slope of the colour profile between $0.1R_e$ and $1R_e$ to be consistent with previous works. In Fig. 3 we show as an example the *F775W–F850LP* and *F850LP–F160W* colour gradients for two galaxies of our sample (1747 and 1284). The colour gradients of all other galaxies are shown in Appendix B. The black curves represent the deconvolved colour profiles, whereas the red lines are the best-fitting slopes. The 1σ error around the fit is shown as red dashed lines. The values of the colour gradients and their relative errors are reported in Table 5. We assigned as error on the colour gradient the

Table 4. For each galaxy of the sample we report the ID number, the Sérsic index n, the total magnitude and the effective radius R_e [kpc] as derived from the fitting of the surface brightness profile in the *F775W*, *F850LP* and *F160W* images, taking as reference the position angle and the axis ratio $(b/a)_{850}$ obtained in the *F850LP* image. For each galaxy we report, in the second row, the values obtained for a de Vaucouleur's profile ($n = 4$).

ID	n_{775}	$i_{775}^{\rm fit}$ [mag]	R_e^{775} [kpc]	n_{850}	$z_{850}^{\rm fit}$ [mag]	R_e^{F850} [kpc]	$(b/a)_{850}$	n_{160}	$H_{160}^{\rm fit}$ [mag]	R_e^{F160} [kpc]
358	6.0±0.4	24.5±0.2	1.1±0.1	6.0±0.4	23.5±0.1	1.5±0.2	0.6±0.1	–	–	–
”	–	24.8±0.2	0.8±0.1	4.0	23.7±0.1	1.0±0.2	–	–	–	–
595	5.7±0.3	22.9±0.1	2.2±0.3	5.6±0.3	21.6±0.1	3.5±0.5	0.9±0.1	4.5±0.1	19.2±0.1	2.5±0.1
”	–	23.1±0.1	1.5±0.3	4.0	21.9±0.1	2.2±0.5	–	–	19.2±0.1	2.3±0.1
684	6.0±0.4	24.0±0.2	0.7±0.1	6.0±0.4	22.9±0.1	1.4±0.2	0.6±0.1	4.1±0.1	20.9±0.1	0.8±0.1
”	–	24.2±0.2	0.5±0.1	4.0	23.1±0.1	1.0±0.2	–	–	20.9±0.1	0.8±0.1
692	4.5±0.2	24.3±0.2	1.3±0.1	4.1±0.2	23.5±0.2	1.5±0.2	0.7±0.1	3.0±0.1	21.0±0.1	0.9±0.1
”	–	24.7±0.2	1.3±0.1	4.0	23.5±0.2	1.5±0.2	–	–	20.9±0.1	1.1±0.1
837	6.0±0.2	23.3±0.1	5.2±0.6	6.0±0.4	21.9±0.1	7.8±1.1	0.7±0.1	6.0±0.2	19.4±0.1	5.2±0.2
”	–	23.6±0.1	2.3±0.6	4.0	22.3±0.1	8.0±1.1	–	–	19.7±0.1	7.2±0.2
1284	4.3±0.3	23.4±0.1	1.8±0.3	4.3±0.2	22.3±0.1	2.4±0.3	0.9±0.1	4.0±0.1	20.0±0.1	1.7±0.1
”	–	23.4±0.1	1.9±0.3	4.0	22.3±0.1	2.3±0.3	–	–	20.0±0.1	1.7±0.1
1539	4.8±0.3	23.7±0.2	1.1±0.1	3.5±0.2	22.7±0.1	1.5±0.2	0.6±0.1	–	–	–
”	–	23.8±0.2	1.0±0.1	4.0	22.6±0.1	1.7±0.2	–	–	–	–
1740	3.3±0.2	21.8±0.1	12.7±1.9	3.3±0.2	20.8±0.1	12.8±1.9	0.6±0.1	4.6±0.1	17.8±0.1	20.7±0.9
”	–	21.5±0.1	20.1±2.0	4.0	20.5±0.1	19.5±1.9	–	–	18.0±0.1	15.4±0.9
1747	4.3±0.2	24.6±0.2	0.8±0.1	4.8±0.3	23.3±0.1	1.7±0.2	0.6±0.1	4.0±0.2	21.1±0.1	0.9±0.1
”	–	24.7±0.2	0.7±0.1	4.0	23.4±0.1	1.5±0.2	–	–	21.1±0.1	0.9±0.1
1758	2.9±0.2	23.9±0.2	1.9±0.2	2.9±0.2	22.6±0.1	2.5±0.3	0.8±0.1	2.90±0.04	20.3±0.1	1.5±0.1
”	–	23.7±0.2	1.9±0.2	4.0	22.4±0.1	3.8±0.3	–	–	20.1±0.1	1.0±0.1
1782	2.5±0.2	23.5±0.1	1.7±0.1	3.6±0.2	22.5±0.1	3.4±0.5	0.6±0.1	3.11±0.04	19.4±0.1	2.2±0.1
”	–	22.9±0.1	3.4±0.1	4.0	22.0±0.1	3.5±0.5	–	–	19.4±0.1	2.0±0.1
1790	4.4±0.3	23.1±0.1	1.9±0.2	4.4±0.3	21.9±0.1	2.4±0.3	0.6±0.1	4.1±0.1	19.3±0.1	2.3±0.1
”	–	23.2±0.1	1.8±0.2	4.0	22.0±0.1	2.2±0.3	–	–	19.3±0.1	2.2±0.1
2054	5.1±0.3	23.2±0.1	2.9±0.4	4.4±0.3	21.9±0.1	4.2±0.6	0.7±0.1	5.1±0.1	19.5±0.1	3.7±0.2
”	–	23.3±0.1	2.2±0.4	4.0	22.0±0.1	3.7±0.6	–	–	19.6±0.1	2.9±0.2
2147	5.4±0.3	23.5±0.1	3.6±0.5	5.3±0.3	22.2±0.1	5.3±0.8	0.7±0.1	4.1±0.1	20.0±0.1	2.3±0.1
”	–	23.7±0.1	2.3±0.5	4.0	22.4±0.1	3.4±0.8	–	–	20.0±0.1	2.3±0.1
2166	3.6±0.2	22.6±0.1	1.2±0.1	3.0±0.2	21.5±0.1	1.4±0.1	0.6±0.1	–	–	–
”	–	22.6±0.1	1.3±0.1	4.0	21.4±0.1	1.7±0.1	–	–	–	–
2429	2.1±0.4	24.3±0.2	0.7±0.1	2.1±0.2	23.0±0.1	0.9±0.1	0.6±0.1	2.1±0.1	21.0±0.1	0.9±0.1
”	–	24.3±0.2	0.7±0.1	4.0	22.8±0.1	1.2±0.1	–	–	20.9±0.1	1.0±0.1
2809	4.8±0.3	23.3±0.1	1.2±0.1	3.2±0.2	22.7±0.1	1.4±0.2	0.6±0.1	–	–	–
”	–	23.3±0.1	1.1±0.1	4.0	22.0±0.1	1.6±0.2	–	–	–	–

error on the observed colour estimated within a thin circular annulus of width 0.1 arcsec and centred at $1R_e$ (if the colour gradients are fitted between $0.1R_e$ and $1R_e$) or at $2R_e$ (if the colour gradients are fitted between $0.1R_e$ and $2R_e$). This represents an upper limit to the error on the colour gradient. Indeed, we verified that, due to the lower signal-to-noise ratio (S/N), the error at $1R_e$ is, on average, approximately three times the error at $0.1R_e$.

Ellipticals in our sample have positive or null rest-frame $UV - U$ gradients. Indeed, three galaxies have a colour gradient comparable with zero at 1σ, whereas the remaining galaxies present a significant positive gradient showing the presence of a bluer stellar population towards the centre in this colour. On the contrary, these galaxies have negative or null rest-frame $U - R$ colour gradients. In particular, four galaxies have a $U - R$ colour gradient comparable with zero at 1σ, whereas the remaining ones present a significant negative gradient showing that the stellar populations are redder towards the centre in this colour. These results do not depend on the region over which the fit is carried out. The intrinsic profile from GALFIT well reproduces our observed profile up to $2R_e$ for the majority (~ 80 per cent) of the sample (see Appendix A). Hence, we have estimated the colour gradients at most up to this distance from the centre confirming the $UV - U$ and $U - R$ gradients for all the galaxies of our sample. At larger radii, we cannot reliably fit the galaxy profile as the surface brightness of galaxies falls below the level of the sky noise (see below).

We also derived the colour gradients from the ratio of the effective radii as measured in the *F775W*, *F850LP* and *F160W*: $\Delta\log R_e = \log(R_e(X)/R_e(Y))$ (La Barbera et al. 2003; De Propris et al. 2015), where X stands for the bluer band and Y stands for the redder band. As shown in Fig. 4 most of the high-redshift cluster galaxies show significant negative $\log(R_e(F775W)/R_e(F850LP))$ and simultaneously significant positive $\log(R_e(F850LP)/R_e(F160W))$. This implies positive $UV - U$ and negative $U - R$ colour gradients for most of the galaxies in agreement with the previous method. The ratios $\Delta\log(R_e)$ are also shown in Table 5.

4.2 Observed colour gradients

As a test for the robustness of our results derived by fitting the brightness profiles with GALFIT, we also derived the observed surface brightness profiles, and hence the colour profiles, by measuring the fluxes in each *HST* band within circular apertures centred on the galaxy. This method is not based on any fit of the surface brightness profile; hence, no dependence either on any assumption on the analytic function of the profile or on the fitting procedure is present.

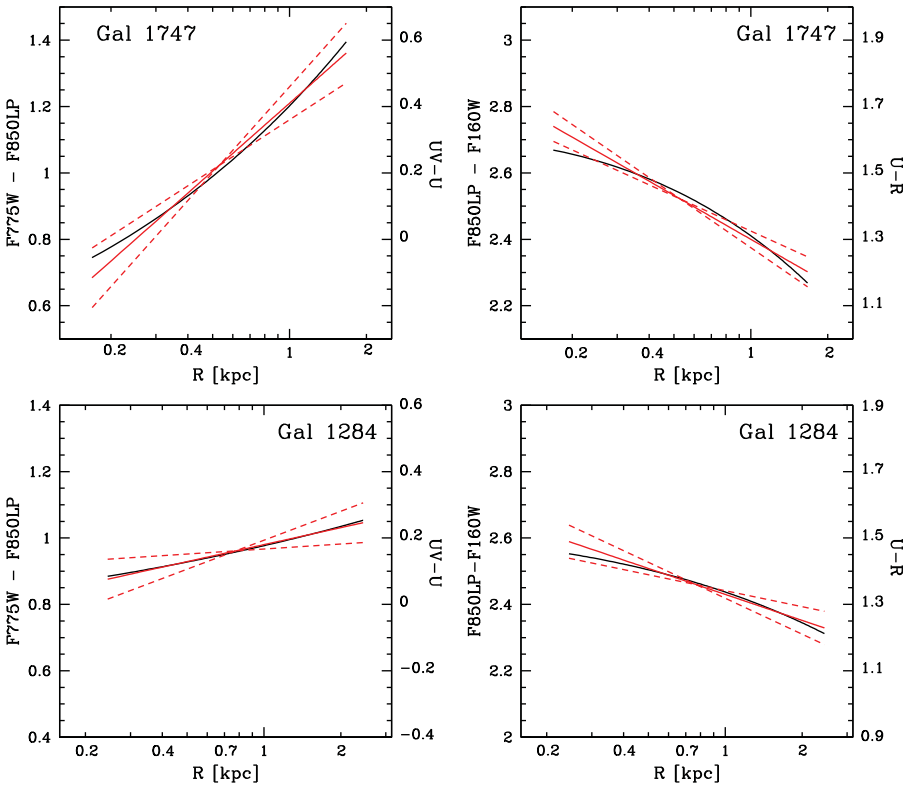

Figure 3. The *F775W–F850LP* (left panels) and *F850LP–F160W* (right panels) colour gradients of two galaxies of our sample (1747 and 1284). Black curves correspond to the intrinsic colour profiles of the galaxies fitted between $0.1R_e$ and $1R_e$ and red lines represent the best-fitted lines to the colour profile. The dashed red lines correspond to 1σ errors on colour gradients. The *y*-axis on the right shows the rest-frame $UV - U$ and $U - R$ colours. The width of the colour interval is the same (Δcolour=1 mag) for both the colours to facilitate comparison.

Table 5. For each of the 17 galaxies of the sample we report the *F775W–F850LP* and *F850LP–F160W* colour gradients derived as the logarithmic slope of the colour profile within $1R_e$ and $2R_e$ and via the ratio of the effective radii as measured in the *F775W*, *F850LP* and *F160W* filters.

ID	$\nabla_{F775W-F850LP}$	$(\nabla_{F775W-F850LP})_{2r_e}$	$\nabla_{F850LP-F160W}$	$(\nabla_{F850LP-F160W})_{2r_e}$	$\log(R_{775}/R_{850})$	$\log(R_{850}/R_{160})$
358	0.2±0.1	0.3±0.2	–	–	−0.2	–
595	0.4±0.2	0.4±0.2	−0.1 ±0.1	−0.2 ±0.2	−0.2	0.1
684	0.6±0.1	0.6±0.2	−0.3 ±0.1	−0.5 ±0.2	−0.4	0.2
692	0.2±0.2	0.2±0.2	−0.3 ±0.1	−0.5 ±0.3	−0.1	0.2
837	0.4±0.3	0.4±0.3	−0.3 ±0.2	−0.3 ±0.2	−0.3	0.2
1284	0.2±0.1	0.2±0.2	−0.3 ±0.1	−0.3 ±0.2	−0.1	0.2
1539	0.5±0.2	0.4±0.2	–	–	-0.1	–
1740	0.0±0.2	0.0±0.2	0.05±0.10	0.06±0.2	0.02	−0.2
1747	0.7±0.2	0.8±0.3	−0.4 ±0.1	−0.6 ±0.2	−0.4	0.3
1758	0.4±0.2	0.5±0.2	−0.7 ±0.2	−0.7 ±0.3	−0.1	0.2
1782	0.6±0.1	1.0±0.3	−0.3 ±0.2	−0.4 ±0.2	−0.3	0.2
1790	0.2±0.1	0.2±0.2	0.0±0.1	−0.04 ±0.02	−0.1	0.2
2054	0.5±0.1	0.4±0.2	−0.2 ±0.2	−0.2 ±0.2	−0.2	0.1
2147	0.3±0.2	0.3±0.3	−0.6 ±0.3	−0.7 ±0.3	−0.1	0.1
2166	0.3±0.1	0.3±0.2	–	–	-0.2	–
2429	0.5±0.1	0.6±0.1	0.00±0.04	0.0±0.1	−0.1	0.4
2809	0.5±0.1	0.4±0.2	–	–	−0.2	–

Since ACS *F850LP* images and WFC3 *F160W* images have a different resolution, in order not to introduce spurious gradients, we have degraded the *F850LP* image to the same PSF of the *F160W* image before deriving the *F850LP–F160W* observed colour profiles. In Fig. 5 we report as an example the observed colour profiles for the same galaxies 1747 and 1284 of Fig. 5 up to $1R_e$.

These gradients cannot be easily compared to the results in the previous subsection, as they depend on the PSF. However, both the methods provide the same systematics for all the galaxies as shown in Fig. 6, where we compare the 'intrinsic' and 'observed' *F775W–F850LP* (upper panel) and *F850LP–F160W* (lower panel) colour gradients out to 1 R_e. The 'observed' *F775W–F850LP* gradients are, on average, slightly less steep than the 'intrinsic' gradients (with an offset < 0.1 mag) due to the PSF that smooths both the profiles. The 'observed' *F850LP–F160W* colour gradients, instead, are, on average, steeper with an offset of ~ 0.3 mag. This is mainly

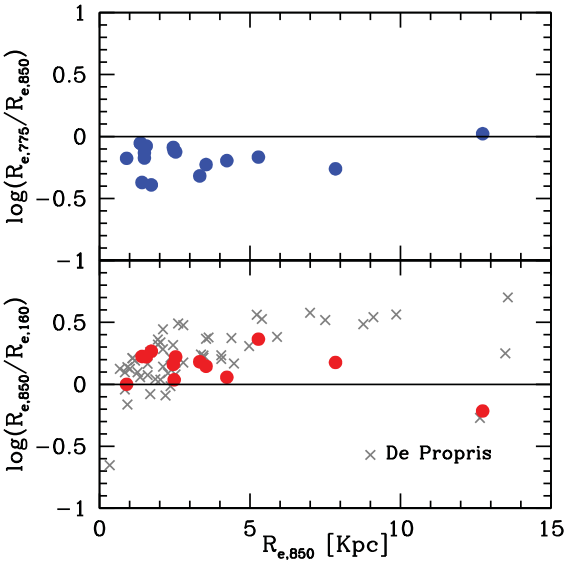

Figure 4. Colour gradients derived as log ($R_e(775)/R_e(850)$) (upper panel) and as log ($R_e(850)/R_e(160)$) (lower panel) versus the effective radius in the *F850LP* band ($R_{e,850}$). We plotted with grey crosses the cluster galaxies at $<z> \sim 1.25$ from De Propris et al. (2015) sample with n consistent with our ellipticals.

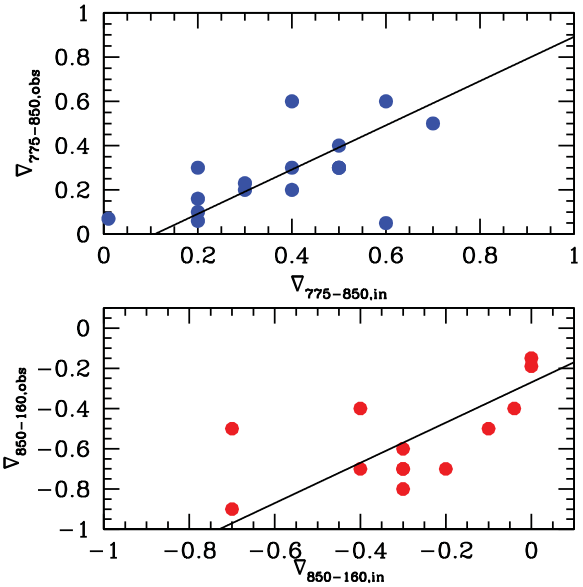

Figure 6. Comparison between the *F775W–F850LP* (upper panel) and the *F850LP–F160W* (lower panel) colour gradients derived from the intrinsic surface brightness profiles and the observed profiles.

due to the PSF-match procedure. Indeed, degrading the *F850LP* image to the same PSF of the *F160W* image, the same amount of flux of the *F850LP* image has been redistributed over a larger area. This implies a decrease of the flux in the inner region in favour to the outer region and, consequently, the gradients become steeper.

We have also checked the effect of estimating colour gradients beyond $2R_e$. Fig. C4 shows as example the observed *F850LP–F160W* colour profiles up to $3R_e$ for galaxies 595 and 837, with effective

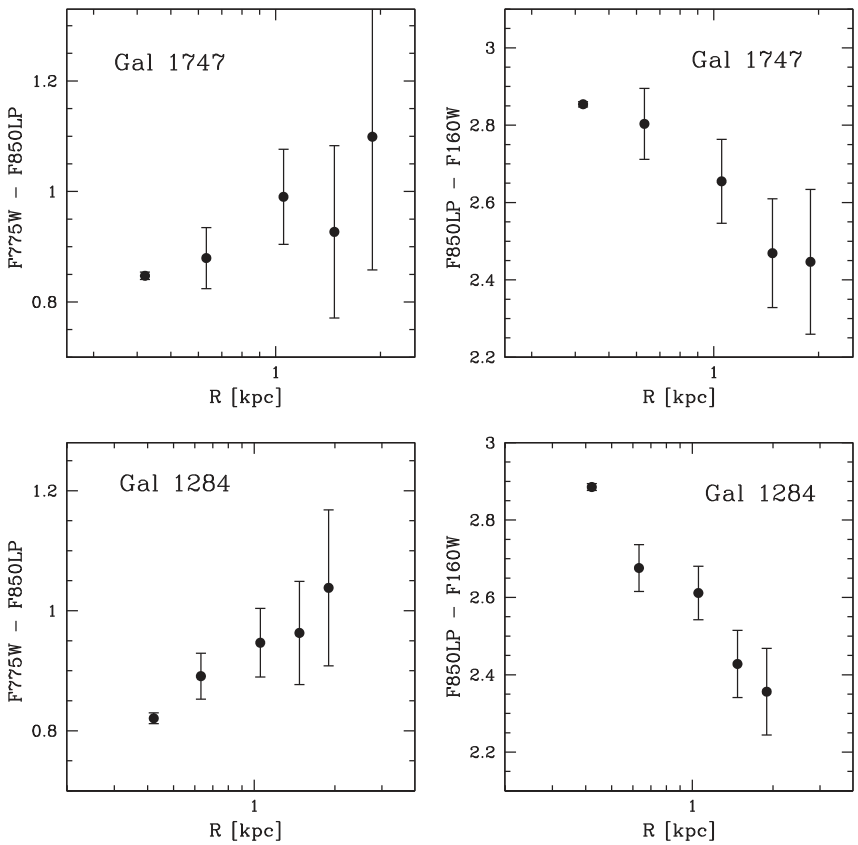

Figure 5. Observed F775W–*F850LP* (upper panels) and *F850LP–F160W* (lower panels) colour profiles derived by measuring the fluxes within circular apertures centred on each galaxy. Errors have been estimated by propagating the uncertainties on the observed brightness profiles.

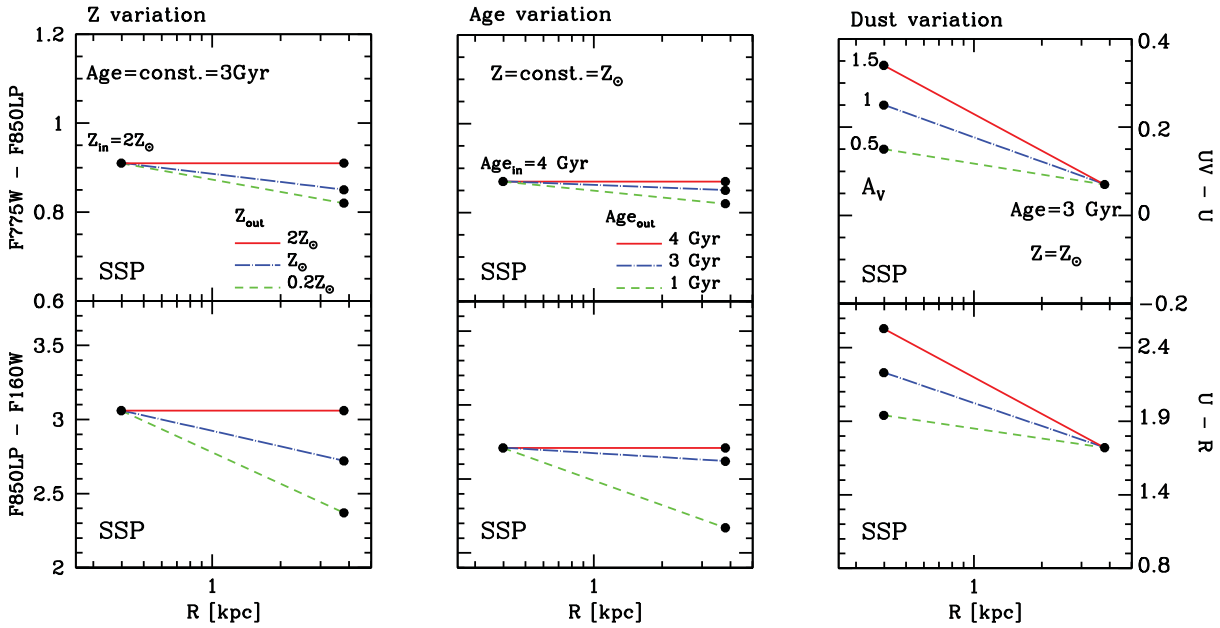

Figure 7. *F775W–F850LP* and *F850LP–F160W* colour gradient variation as a function of metallicity, age and dust. Left-hand panel: we fixed the age of the stellar population at 3 Gyr and varied the metallicity from the central region (2 $Z_{\odot}$) to the outer region [2 $Z_{\odot}$ (red solid line), $Z_{\odot}$ (blue dot–long dashed line) and 0.2 $Z_{\odot}$ (green short dashed line)]. Central panel: we fixed the metallicity at $Z_{\odot}$ and varied the age from the central region (4 Gyr) to the outer region [4 Gyr (red solid line), 3 Gyr (blue dot–long dashed line) and 1 Gyr (green short dashed line)]. Right-hand panel: the gradient variation as a function of the dust extinction A_V at fixed age and metallicity for three different values of A_V: 0.5 (green short dashed line), 1 (blue dot–long dashed line) and 1.5 (red solid line) is shown.

radius 3.5 and 7.8 kpc, respectively. We can see that at $R \gtrsim 1.5$–$2R_e$ the colour profiles reverse because the sky noise dominates the surface brightness profiles in the *F850LP* band image (see Fig. A1), introducing a spurious colour gradient. This artificially flattens the colour gradient from the steeper one measured within $2R_e$ (and with GALFIT). In agreement with what we previously found with the GALFIT fitting, estimates of the colour gradients for $R \gtrsim 2R_e$ are not reliable for most of the galaxies (∼75 per cent of the sample) since they are dominated by the background of the ACS images.

These three different methods used to derive colour gradients are mutually consistent, implying that our results are independent of the method used. We conclude that the $UV - U$ colour gradients are systematically positive (∼80 per cent) or null (∼20 per cent), never negative. On the contrary, the $U - R$ colour gradients are systematically negative (∼70 per cent) or null (∼30 per cent), never positive.

5 INVESTIGATING THE NATURE OF THE OBSERVED COLOUR GRADIENTS

The presence of colour gradients implies that one or more properties of the stellar population vary radially. In this section we test whether a radial gradient of a single parameter (age, metallicity or dust) can account for the opposite slopes of the observed $UV - U$ and $U - R$ colour gradients.

5.1 Age, metallicity and dust variation

In the local Universe, colour gradients are usually interpreted as metallicity gradients, with the possible role of age gradients being still controversial. On this basis, we first tested whether the colour gradients we measure at high redshift can be reproduced by a pure metallicity gradient.

In the left-hand panel of Fig. 7 the predicted $UV - U$ and $U - R$ colour gradients are shown as a function of metallicity. We modelled the central region of the galaxy with a 3 Gyr old simple stellar population (SSP) (the results are independent of this assumption) with supersolar metallicity (2 $Z_{\odot}$), while we modelled the outer region with the same SSP (i.e. we assume no radial age variation), but with metallicity 2 $Z_{\odot}$, $Z_{\odot}$ and 0.2 $Z_{\odot}$. It can be seen that a metallicity gradient affects the derived $U - R$ colour gradient more strongly than the $UV - U$ gradient, but the slope is always negative (e.g. for the extremes of the range, where the central region has Z_{in}=2 $Z_{\odot}$ and the outer region Z_{out}=0.2 $Z_{\odot}$, we find $\nabla_{UV-U} \sim -0.1$ mag and $\nabla_{U-R} \sim -0.7$ mag). Therefore, we cannot explain both gradients at z=1.4 with a simple metal abundance gradient as in the local Universe.

We repeated the same exercise in the case of a pure age (Fig. 7, central panel) and dust gradient (Fig. 7, right-hand panel). To investigate the effect of a pure age variation, we have modelled the central region of the galaxy with a SSP with solar metallicity and age 4 Gyr, and the external region with a SSP with the same metallicity and age 4 Gyr, 3 Gyr and 1 Gyr. Also in this case we observe that the $U - R$ colour is more sensitive to age variation and that the variation of a single parameter is not able to reproduce both the negative $U - R$ gradient and the positive $UV - U$ gradient (e.g. for a galaxy whose centre has Age_{in}=4 Gyr and Age_{out}=1 Gyr in the outskirts we obtain $\nabla_{UV-U} \sim -0.05$ mag and $\nabla_{U-R} \sim -0.6$ mag).

Finally, we considered a radial change in extinction. To model the dust variation, we fixed both the metallicity and the age and we assumed a more dusty core. The dust extinction produces an attenuation of the intrinsic flux of the galaxy that depends on the wavelength: $f_{obs}(\lambda) = f_{int}(\lambda)10^{-0.4A_{\lambda}}$, where f_{obs} and f_{int} are the observed and the intrinsic fluxes, respectively, and $A_{\lambda} = k(\lambda)A_V/R_V$ is the extinction at a wavelength λ, $k(\lambda)$ is the Calzetti law and R_V = 4.05±0.80 (Calzetti et al. 2000). In the right-hand panel of Fig. 7 it

is shown how the two colour gradients vary as a function of the dust extinction for three different values of A_V: 0.5, 1 and 1.5. Also in this case, the radial variation of dust produces concordant $UV - U$ and $U - R$ gradients, which become steeper for increasing values of A_V.

Therefore, simple radial trends in age, metallicity or dust in their own cannot reproduce the observed $UV - U$ and $U - R$ gradients at the same time. Radial trends in metallicity, age or dust (with the metal abundance, age or extinction decreasing outwards) always produce negative $UV - U$ and $U - R$ gradients (and opposite if the metallicity, age or extinction decreases inwards). Furthermore, Fig. 7 shows also that the $UV - U$ colour is much less sensitive to metallicity and age variation than the $U - R$ colour. In fact, we find that while the $U - R$ colour variations induced by the age/metallicity variations are comparable to those observed in our galaxies, the same age/metallicity variations do not produce $UV - U$ colour variations as large as those observed (see Fig. B1).

To verify whether this result is just related to our choice of the input values of metallicity/age in the toy model of Fig. 7, in the next section we check whether an age or a metallicity variation is able to reproduce the amplitude of the observed gradients or it is easier to reproduce a certain colour gradient than the other one.

5.2 Modelling of the real data

Following the analysis technique proposed by Gargiulo et al. (2012), we model the stellar content of a galaxy as composed of two main stellar populations, one population dominating towards the centre and the other one dominating towards the outskirts. We model the two populations using BC03 composite stellar populations. To test for the radial age (metallicity, Z) variation as origin of the observed colour gradients, we fixed Z (age), A_V and τ of the two populations to those derived from the fit to the global SED and leave age (Z) as free parameter of the fit. The best-fitting age of the central (external) stellar population is the one that better reproduces both the $UV - U$ and $U - R$ colours observed in the inner (outer) region of the galaxy. We also required that the sum of the stellar populations matches the global SED.

On the basis of the colour profiles (see Appendix A1), we have chosen as inner region the one enclosed within the FWHM, that is within a radius of ∼0.06 arcsec (∼0.5 kpc) and, as outer region, a circular annulus ∼ 1 kpc width centred at $1.5R_e$. We verified that for each galaxy $1.5R_e$ corresponds to at least approximately three times the radius of the PSF.

In Fig. 8, we show as an example the result obtained for the galaxy 1758, the one showing the most extreme colour gradients. In the left-hand panels we show the colour gradients from a pure age variation, whereas in the right-hand panels we show those obtained by considering a pure metallicity gradient, where we have adopted a grid of metallicity values as follows: 0.2 $Z_\odot$, 0.4 $Z_\odot$, $Z_\odot$ and 2 $Z_\odot$ The black curves represent the colour profiles of the galaxy, whereas the red lines are the observed colour gradients. The blue dashed lines represent the best-fitting colour gradients as resulting from the two-component model.

What we found is that the best-fitting procedure finds a solution to the observed $U - R$ colour gradients ($-0.7 < \nabla < -0.1$ mag; see Table 5) both in the case of an age gradient and a metallicity gradient. The resulting metallicity gradients (at fixed age) are in the range $\nabla_Z = d\log(Z)/d\log(R) < -0.8$, with a median value of ~ -0.4, consistent with the metallicity gradients derived in local and intermediate redshift ellipticals, where ∇_Z ranges from -0.2 to -0.4 (e.g. Saglia et al. 2000; Wu et al. 2005; La Barbera & de Carvalho 2009). The resulting age gradients (at fixed metallicity), instead, are in the range $\nabla_{age}=d\log(age)/d\log(R) \lesssim -0.4$. Such age gradients would be barely detectable locally. For instance, $\nabla_{age} = -0.3$ due to an age variation of 2 Gyr corresponds at z=0 to a colour gradient of -0.07 mag, smaller than the typical errors on colour gradients. On the contrary, the procedure does not find a solution for the observed large $UV - U$ colour gradients and for the opposite slopes shown by the two gradients.

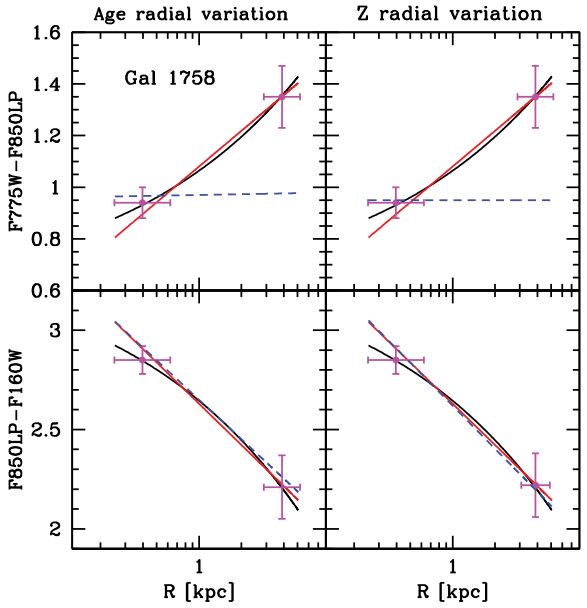

Figure 8. Left: radial age variation as origin of the observed colour gradients. The upper panel shows the *F775W–F850LP* colour profile (black line) and best-fitting slope (red line); the lower panel on this side shows the same information but for the *F850LP–F160W* gradient. In both panels, the blue dashed lines show the effect of a pure age variation as a function of radius on colour. The magenta points show the mean colour of the stellar populations in the inner and outer regions. Right: same as above but for metallicity.

It is worth noting that in the case of dust variation, to reproduce even the mean amplitude (-0.3 mag) of the $U - R$ gradients an $A_V > > 1$ mag would be needed in the inner regions, values never obtained from the fitting to the global SED of our galaxies. Hence, dust can play only a marginal role, if it has one, in the origin of the observed colour gradients.

Hence, it is easier to reproduce the negative $U - R$ colour gradients rather than the positive $UV - U$ colour gradients. $UV - U$ colour gradients cannot be accounted for by age and/or by metallicity variations. Actually, what the data show is that galaxies are bluer in the centre when the $UV - U$ colour is considered. Hence, there is an UV excess towards the galaxy central regions with respect to the external ones. Starting from this evidence, in the next section, we try to constrain the scenario that best reproduces simultaneously both the colour gradients, focusing on the nature of the bluer $UV - U$ colour in the galaxy central regions.

6 THE KEY INFORMATION STORED IN THE GALAXY CENTRAL REGIONS

While an age gradient or a metallicity gradient, as the one observed in local elliptical galaxies (e.g. Saglia et al. 2000; La Barbera et al. 2005; Wu et al. 2005; Tortora et al. 2010), can account for the $U - R$ colour gradients, the same gradient cannot produce the opposite (positive) $UV - U$ gradients. To reproduce the positive

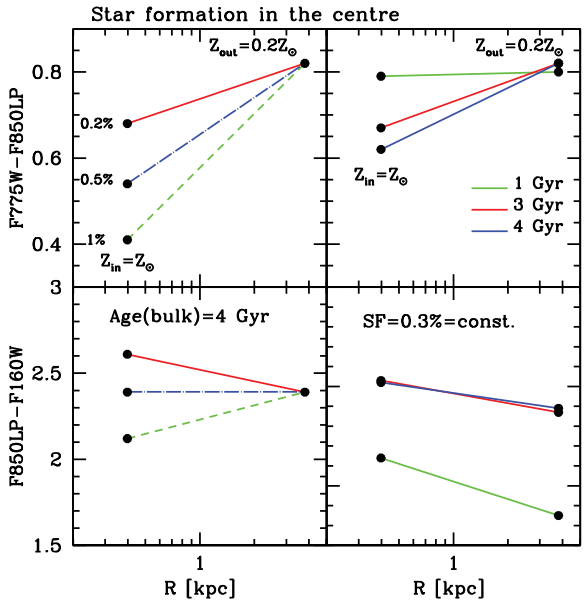

Figure 9. We show how the *F775W–F850LP* and *F850LP–F160W* colour gradients change by adding a weak star formation towards the centre. Left-hand panel: we fixed the age of the main stellar population at 4 Gyr and varied the metallicity from the centre ($Z_\odot$) to the outer region (0.2 $Z_\odot$), adding a weak star formation towards the centre. The percentages indicate the contributes in term of stellar mass of the stellar population, which is producing stars. Right-hand panel: we show how both colours change if we add a star-forming component equivalent to 0.3 per cent in stellar mass for three different ages of the main stellar population [1 Gyr (green line), 3 Gyr (red line) and 4 Gyr (blue line)] and with the same metallicity gradient.

$UV-U$ colour gradient without affecting the observed negative $U-R$ gradient, a mechanism able to efficiently enhance UV emission without altering the spectrum at longer wavelengths has to be hypothesized in the galaxy central regions. Possible mechanisms able to fulfil these requirements are the star formation, the presence of a Quasi-Stellar Object (QSO), stars in the He-burning phase or He-rich stars. In the following, we discuss each of these mechanisms.

6.1 A steady mild star formation?

One mechanism that produces UV emission is the star formation. In order to test whether weak star formation can produce positive $UV-U$ gradients without affecting the negative $U-R$ gradients, we have added in the centre a young stellar component seen while it is forming most of its stars, i.e. characterized by τ=0.1 Gyr and an age of 0.1 Gyr. The results are shown in Fig. 9. In particular, in the left-hand panel, we fixed the age of the bulk of stellar population (4 Gyr) and varied the metallicity from the centre ($Z_\odot$) to the external region (0.2 $Z_\odot$) and added different percentages (in terms of stellar mass) of star formation towards the centre. In the right-hand panel, instead, we show the same model of the left panel (metallicity varies from the central region to the outer region with different percentages of star formation in the centre) but for different constant age of the bulk of the stellar population.

We found that although the radial decrease of metallicity (at constant age) would reflect in negative $UV-U$ colour gradient (e.g. see Fig. 6), the presence of a very weak star formation in the centre is able to reverse the $UV-U$ gradient turning it from negative to positive. Moreover, the older the mean age of the stellar population the easier to produce positive $UV-U$ colour gradients. This is because the UV emission of the star-forming component tends to dominate the UV and U emission of the stellar population when it is old, enhancing the gradient with respect to the outer regions. For instance, the ratio between the UV emission of 0.3 per cent (in stellar mass) of star-forming component and the UV emission of 1 Gyr old component is ~ 0.08. This ratio increases to ~ 0.7 in the case of a 4 Gyr old component.

In order not to affect the negative $U-R$ colour gradients, the percentage in stellar mass of this star-forming component must be less than $\sim$0.5 per cent of the total stellar mass.

We applied this model to our galaxies. We built a grid where the percentage of the star-forming component ranges from 0.1 to 3 per cent with a step of 0.2. At fixed percentage of the star-forming component, we varied the age and the metallicity of the stellar population in the centre and in the outer region. The ages considered range from 1 to 4 Gyr (the age of the Universe at $z=1.39$ is $\sim$ 4.5 Gyr) with a step of 0.5. Metallicity variation has been modelled on a grid of subsolar and supersolar metallicity values: 0.2 $Z_\odot$, 0.4 $Z_\odot$, $Z_\odot$ and 2 $Z_\odot$. We found that 0.7 per cent represent an upper limit to the percentage of the star-forming component, since larger percentages produce flat or even positive $U-R$ gradients.

Six galaxies (595, 1740, 1790, 2054, 2429, 837) present $U-R$ colour gradients consistent with a null gradient at 1σ. However, these galaxies present positive $UV-U$ gradients at 1σ. The only addition of star formation towards the centre produces positive $UV-U$ gradients, but also slightly positive $U-R$ gradients. The best solutions provide for these galaxies a contribution of 0.2 per cent in mass of star formation together with either a negative age gradient of ~-0.3 (Age_{in}= 4 Gyr and Age_{out}= 2 Gyr) or a metallicity gradient of ~-0.4 ($Z_{in}=Z_\odot$ and Z_{out}= 0.4$Z_\odot$), consistent with the metallicity gradients found in local ellipticals.

Four galaxies (692, 1284, 1782, 2147) show opposite colour gradients at 1σ. For them, the best-fitting model producing simultaneously both the observed colour gradients is composed of 0.2 per cent of star-forming component in the centre superimposed to an age gradient of ~-0.3 (Age_{in}= 4 Gyr and Age_{out}= 2 Gyr) and a metallicity gradient of ~-0.4 ($Z_{in}=Z_\odot$ and Z_{out}= 0.4$Z_\odot$).

Galaxy 1758 presents an extreme value of the $U-R$ gradient at 1σ ($\nabla=-0.55$ mag). In order to produce such steep $U-R$ gradient, it is needed to consider an even lower metallicity towards the external region (Z_{out}= 0.2 $Z_\odot$). This would imply a steeper metallicity gradient ($\nabla_Z\sim-0.7$) not observed in the local ellipticals. For this galaxy, we simultaneously produce both the colour gradients by adding 0.3 per cent of star formation together with both an age gradient (Age_{in}= 4 Gyr and Age_{out}= 2 Gyr) and a metallicity gradient ($Z_{in}=Z_\odot$ and Z_{out}= 0.2 $Z_\odot$). This galaxy is shown in Fig. 10 as an example. The upper panel shows the *F775W–F850LP* colour profile (black line) with the best-fitting slope (red line), while the lower panel the *F850LP–F160W* colour profile. The blue dashed line is the colour gradient including star formation in the centre for an underlying metallicity gradient (left) and both a metallicity and an age gradient (right).

Finally, two galaxies (684 and 1747) present an extreme value of the $UV-U$ gradients at 1σ (∇= 0.47, 0.58 mag, respectively). For these galaxies, we are not able to simultaneously produce both the colour gradients. Indeed, in order to produce the steep observed UV gradients, $\gtrsim$ 1 per cent in mass of star formation is needed, but this produces positive $U-R$ gradients, even if we consider the lowest metallicity available in the external region (Z_{out}= 0.2$Z_\odot$). These galaxies are isolated; they are not the faintest in the sample

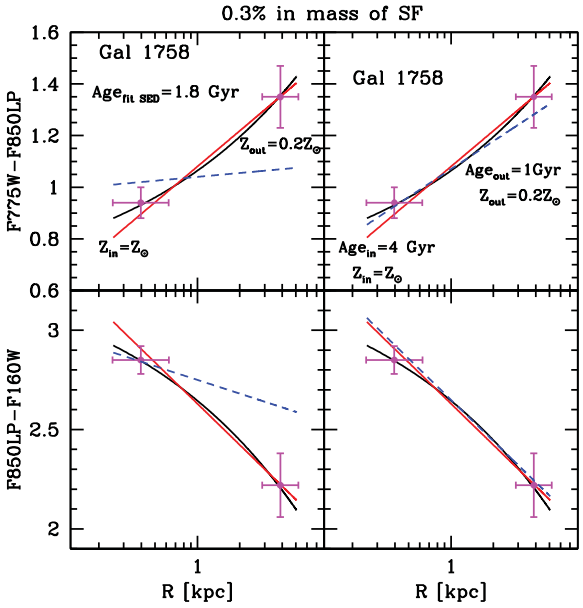

Figure 10. The two panels show the *F775W–F850LP* (upper panel) colour profile (black line) with the best-fitting slope (red line) and the *F850LP–F160W* (lower panel) colour profile (black line) with the best-fitting slope (red lines). The blue dashed lines represent the colour gradients derived from the model described in Section 6.1. In the left panel, a metallicity gradient and a weak star formation in the centre have been considered. In the right panel an age gradient has been also added. The magenta points represent the mean colour of the stellar population in the inner and outer regions.

and their structural parameters are not extreme. Hence, we have no reason to suppose that the colour gradients of these galaxies are overestimated.

In conclusion, by applying a model with star formation in the centre together with a metallicity and/or an age gradient, we are able to simultaneously produce at 1σ both the colour gradients for 11 out of the 13 ellipticals ($\sim$ 85 per cent of the sample). On the basis of this model, these ellipticals would be composed by an older and more metal-rich population in the centre, a younger and more metal-poor population in the outskirts and a small star-forming component in the core.

Taking as reference the mean value of the stellar mass ($< M_* > \sim 3 \times 10^{10}$ M$_\odot$) of the galaxies of our sample, this young star-forming component would contribute in stellar mass for just $\sim 2.7 \times 10^8$ M$_\odot$. Since the BC03 models are normalized at 1 M$_\odot$ and a stellar population of 0.1 Gyr with τ=0.1 Gyr is characterized by a SFR = 3.6×10^{-9} M$_\odot$ yr^{-1}, the SFR associated with the young central star-forming component would be SFR$\sim$1 M$_\odot$ yr^{-1}. It is worth noting that this SFR is rather stable with respect to the assumptions made: at fixed SFH (e.g. $\tau = 0.1$ Gyr) a younger stellar population (<0.1 Gyr) would be characterized by a stronger UV emission and, consequently, the required mass percentage would be lower (<0.5 per cent) leaving nearly unchanged the resulting SFR.

Following the relation

$$\mathrm{SFR}\ (\mathrm{M}_\odot \mathrm{yr}^{-1}) = (1.4 \pm 0.4) \times 10^{-41}\ L[\mathrm{O\,II}]\ (\mathrm{erg\ s}^{-1}), \qquad (3)$$

(Kennicutt 1998), the flux f[O II]λ3727 associated with a SFR of ~ 1 M$_\odot$ yr^{-1} in a galaxy at z=1.39 would be f[O II] $\sim 6 \times 10^{-18}$ erg cm^{-2} s^{-1}. Such faint f[O II] fluxes are barely detectable even at a 10 m class telescope. For instance, Cimatti et al. (2008) report the detection of such faint fluxes in three passive galaxies in the GMASS survey, all of them observed for more than 30 h. Thus, we could not directly confirm whether such a weak star formation activity is actually present in the galaxies of our sample, since it is too low to be detectable with the current instrumentations. However, some works find indirect evidence of the presence of star formation in early-type galaxies both at high-z and in the local universe. For instance, Lonoce et al. (2014), measuring the spectral indices of a sample of early-type galaxies at $0.7 < z_{\mathrm{spec}} < 1.1$, found that, in some cases, the measured H+K (Ca II) index is consistent with the presence of a small mass percentage (<1 per cent) of a young stellar component (< 1 Gyr) with recent weak star formation. Also Wagner et al. (2015), studying a sample of massive ($M > 10^{10.1}$M$_\odot$) cluster early-type galaxies at $1.0 < z < 1.5$, found that 12 per cent of them are likely experiencing star formation activity. In the local Universe, Kaviraj et al. (2008), studying $\sim$ 2100 early-type galaxies in the SDSS DR3, found that at least $\sim$30 per cent of them have UV to optical ($NUV - r$) colour consistent with recent star formation.

If the star formation is the origin of the UV excess in the galaxy central regions of our sample, this scenario requires a certain degree of fine-tuning. The fact that we observe positive $UV - U$ (or null) gradients in all the galaxies implies that all of them are experiencing star formation in their centre, otherwise we would have observed negative $UV - U$ gradients in some of them at least. This implies, in turn, that the star formation cannot be either episodic or short, but that it protracts over time in a steady fashion at low levels to allow us to observe it as it is (low) in all the galaxies. Being protracted over long time (say $\sim$1 Gyr, being at $z \sim 1.4$), this SF even if weak needs to be supplied with gas. The fuel cannot come from inflows of intracluster medium (ICM), since galaxies are in thermal equilibrium with the ICM. By the way, this kind of supplying would flatten the metallicity gradient and, consequently, the $U - R$ gradient being the ICM less metal-rich. On the contrary, such star formation should be feeded by the residual processed gas in the galaxies (closed box). This process would efficiently enhance the metallicity towards the centre (e.g. Peng, Maiolino & Cochrane 2015) producing naturally the observed negative $U - R$ gradients.

As already said, this scenario requires a fine-tuning in term of synchronism and duration of the star formation as possible origin of the observed UV excess in the centre of our galaxies. However, apart from this, we have no evidence to exclude it. Moreover, it is worth considering that this model gives rise to the observed colour gradients simultaneously reproducing both the $UV - U$ and the $U - R$ gradients (see Fig. 10) and that it would naturally produce the metallicity gradient observed also in the local ellipticals.

6.2 A possible QSO contribution?

Quasars are known to have a SED characterized by strong UV emission, peaking at $\sim$1500 Å (the so-called big blue bump; Shields 1978). To verify whether the UV excess in the galaxy central regions is the sign of the blue bump, we have added in the centre a QSO component instead of the star-forming one. We have considered the composite spectrum of Francis et al. (1991). In Fig. 11 is shown, as example, the case of the QSO component needed to produce a $UV - U$ colour gradient of $\sim$0.2 mag. In terms of absolute magnitude, this QSO is $\sim$ 2 mag fainter than the galaxy in the B-band rest-frame. In this case, the $U - R$ gradient is not significantly affected and we can reproduce simultaneously gradients in the range $\nabla(UV - U) \leq 0.25$ mag and $\nabla(U - R) > -0.3$ mag, assuming a radial decrease of metallicity and age. For instance, for galaxies 692 and 1284, having gradients in the above ranges, the QSO would have an absolute magnitudes of $M_B \sim -$ 18.7 mag

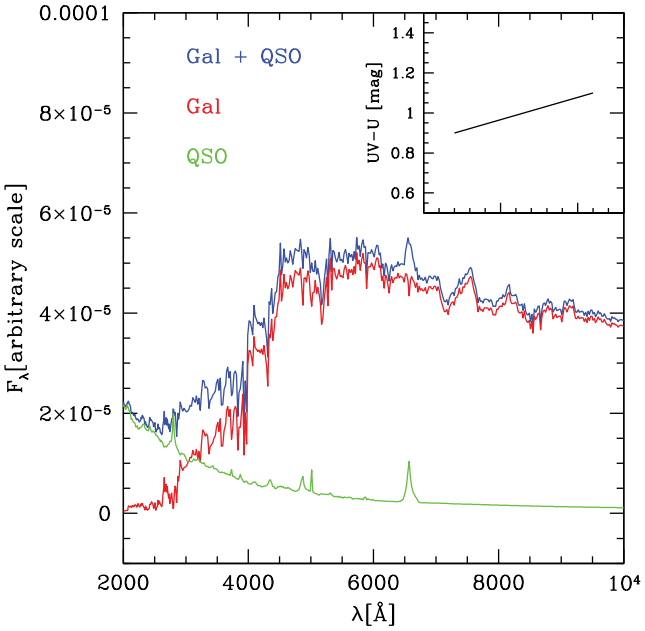

Figure 11. QSO contribution to the UV excess in the central galaxy regions. Green line represents the composite spectrum of a QSO (Francis et al. 1991), the red line is the template of a galaxy (4 Gyr old) and the blue line is the sum of the two components. The QSO is scaled to be 2 mag fainter than galaxy in the B band. The addition of this QSO component together with an age and metallicity gradient reproduces simultaneously gradients in the range $\nabla(UV-U) \leq 0.25$ mag and $\nabla(U-R) > -0.3$ mag. Brighter QSO component would flatten the $U-R$ gradients and would make the integrated $UV-U$ and $U-R$ colours of the galaxies bluer than those observed.

and $M_B \sim -19.7$ mag (Seyfert like), respectively. However, higher values of the $UV-U$ gradient cannot be accounted for by further increasing the QSO luminosity. Indeed, in this latter case, the integrated $UV-U$ and $U-R$ colours of the galaxy would be affected resulting in significantly bluer (>0.3 mag in $UV-U$ and in $U-R$) than those observed. Hence, a QSO could be present in the galaxies and contribute to the observed UV excess but cannot be the only cause. It should be superimposed to, e.g., star formation to account for the observed gradients without altering the colours of the galaxies.

6.3 Or, rather, a population of He-rich stars?

In the local Universe it has long been known that elliptical galaxies can present an UV excess in their SED, stronger at wavelengths shortwards of 2100 Å (e.g. Code & Welch 1979; O'Connell et al. 1992; O'Connell 1999), with a tail extending up to ∼3200 Å (see e.g. Greggio & Renzini 1990; Ponder et al. 1998; Dorman, O'Connell & Rood 1995). This was unexpected since ellipticals were supposed to contain mainly old and cold stellar populations. Since its discovery, the UV upturn phenomenon in elliptical galaxies has generated a big discussion about its origin. From the shape of the SED in the UV, it derives that the temperature of the stars, which give rise to the UV excess, is in the range 20000 ± 3000 K (Brown et al. 1997). This effectively ruled out young stars as the main driver of the UV upturn. The main mechanisms that are supposed to be responsible for the UV upturn are He-burning stars (e.g. Han et al. 2002, 2003; Han, Podsiadlowski & Lynas-Gray 2007; Han 2008) and He-rich stars (e.g. Yi et al. 2011; Carter et al. 2011). We have considered these scenarios to test if they can explain the blue excess we observe towards the centre of our ellipticals at $z \sim 1.4$. Indeed, even though the emission peak of the UV upturn is at wavelengths < 2100 Å, its tail extends up to ∼ 3200 Å, affecting the *F775W* band (filter range 2700 Å $\lesssim \lambda_{\rm rest} \lesssim$ 3600 Å).

6.3.1 *He-burning stars*

He-burning stars are stars that have already stopped burning hydrogen in their cores and they are burning helium. Assuming for the stellar population a formation redshift $z_f \sim 6$, at z=1.39 the population would be ∼ 4 Gyr old. Hence, at $z = 1.39$, only stars with $1.2\,M_\odot \lesssim M \lesssim 1.5\,M_\odot$ would be in the He-burning phase since their lifetime in the Main Sequence (MS) is ∼3–4 Gyr (Iben 1967). Stars with M<1.2 $M_\odot$ would still be in the MS (lifetime in MS phase $>10^{10}$ yr), whereas stars with $M>1.4M_\odot$ have already evolved (lifetime in MS phase $<10^8$ yr). The He-burning phase is characterized by a very short time-scale if compared to the MS phase and, for stars with $1.2\,M_\odot < M < 1.5\,M_\odot$ it lasts just $\sim 10^8$ yr. Hence, this very short time makes highly unlikely that the UV excess seen in the galaxy central regions is due to an excess of intermediate-mass stars in the He-burning phase.

6.3.2 *He-rich stars*

One other possibility is that the cores of elliptical galaxies host an He-rich subpopulation of stars. These stars are formed from the gas enriched by the evolution of very high mass stars. In the Λcold dark matter model the first stars are predicted to be composed principally by hydrogen (see e.g. Blumenthal et al. 1984; Komatsu et al. 2009). The absence of metals disadvantaged the formation of low- and intermediate-mass stars, since the cooling is less efficient. Results from recent numerical simulations of the collapse and fragmentation of primordial gas clouds suggest that the first stars were predominantly very massive, with typical masses $M_* > 100\,M_\odot$ (Bromm, Coppi & Larson 1999, 2002; Abel, Bryan & Norman 2000, 2002; Nakamura & Umemura 2001). These stars would evolve very quickly and the supernova (SN) explosions that ended their lives would enrich efficiently the ISM with heavy elements (see e.g. Ostriker & Gnedin 1996; Gnedin & Ostriker 1997; Ferrara, Pettini & Shchekinov 2000; Madau, Ferrara & Rees 2001). These metals would fall towards the centre of the galaxies due to the potential well naturally explaining the observed negative metallicity gradients resulting from the subsequent generations of stars.

We know that these stars exist in local ellipticals, where they contribute to the classical UV upturn (e.g. O'Connell 1999). Moreover, the UV gradients observed in Coma galaxies by Carter et al. (2011) imply that there exists an He abundance gradient, established at very early times. He-enriched stars are known to be bluer than their counterparts with standard metal abundance (see e.g. Chantereau, Charbonnel & Decressin 2015). This is observed in the bluer UV colours of He-enriched red giants in Lardo et al. (2012) and in the bluer secondary MSs of several globular clusters (e.g. Piotto et al. 2005).

Since these stars will be bluer, they will naturally produce an excess in the UV in the centre, but they will not strongly affect optical colours, as also shown by the above observations in globular clusters. Thus, an He abundance gradient, which is known to exist in the local Universe, would reproduce the observed positive $UV-U$ gradients without fine-tuning. Unfortunately, we lack population synthesis models for He-enriched populations to study this issue in detail.

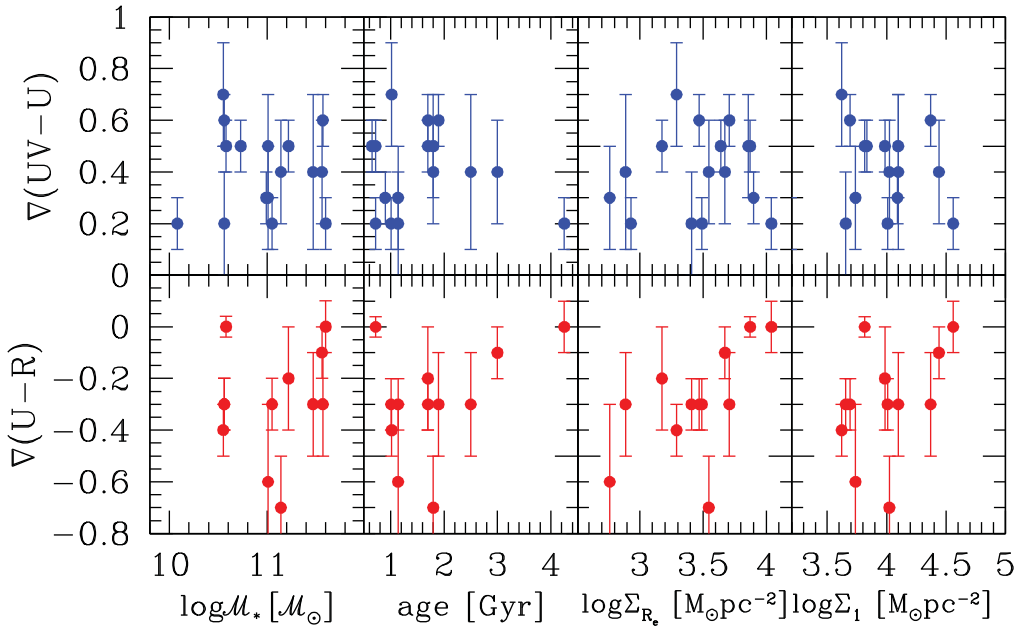

Figure 12. The $UV - U$ gradients (upper panels) and $U - R$ gradients (lower panels) versus, from left to right, log$\mathcal{M}_*$, the mean age as derived by the SED fitting, logΣ_{R_e} and logΣ_1 within 1 kpc radius.

7 COLOUR GRADIENTS AND GLOBAL PROPERTIES OF GALAXIES

To further investigate on the origin of the UV excess towards the centre and on the mechanisms producing the observed colour gradients in our galaxies, we have looked for the presence of correlations between gradients and global properties of galaxies. We considered the stellar mass $\mathcal{M}_*$, the mean age as derived by the SED fitting, the effective stellar mass density $\Sigma_{R_e} = \mathcal{M}_*/(2\pi R_e^2)$ and the central stellar mass density $\Sigma_{1\,\mathrm{kpc}}$ within 1 kpc radius, as derived in Saracco et al. (2017). Fig. 12 shows the relation between colour gradients and global properties of galaxies. The $U - R$ colour gradient seems to be weakly correlated with the effective stellar mass density of galaxies in the sense that the larger the gradient the lower the density. However, the Spearmen rank test provides a probability of just 90 per cent significance. Actually, no correlation was detected with the global properties of galaxies, both considering the $UV - U$ (upper panel) and the $U - R$ (lower panel) colour gradients. This is not surprising since colour gradients trace principally the variation of the stellar component dominating the galaxy within 1–2R_e while the other properties are derived considering the whole galaxy mass. Similar results are also found by De Propris et al. (2015, 2016) for cluster red sequence galaxies at a comparable redshift and by Gargiulo et al. (2012) for a sample of field early-type galaxies at $0.9 < z < 1.92$. We have also verified if the amplitude of the colour gradients depends on the position of the galaxy inside the cluster, namely on the radial distance from the cluster centre (i.e. on the local density). Also in this case we did not detect a correlation. The low statistics does not allow us to establish whether the local environment has affected the colour gradients of these galaxies.

8 COMPARISON WITH PREVIOUS WORKS

In this section we compare our results with those present in literature. Although colour gradients are largely studied in the local universe, still few works are focused on gradients in cluster and field galaxies at $z > 1$.

8.1 Cluster environment

Our results are in agreement with those of De Propris et al. (2015), who studied the *F850LP–F160W* colour gradients of red sequence galaxies belonging to four clusters (one of which in common with us) at $1 < z < 1.4$ using the ratio of their effective radii measured in the two bands. They found that the galaxies in their sample present significant positive log $(R_e(z)/R_e(H))$, hence negative colour gradients, larger than those observed locally (e.g. in Virgo cluster). The authors divide their red sequence galaxies in red discs (n<2) and red spheroids (n>2). Since 16 out to the 17 ellipticals of our sample have n>3, for a proper comparison, in Fig. 4 we plotted with grey crosses the galaxies of De Propris et al. (2015) sample with $n > 3$. The median value of the log $(R_e(F850LP)/R_e(F160W))$ of their cluster galaxies with n>3 is 0.18, consistent with the median value (0.21) of our cluster ellipticals. The authors interpret the negative *F850LP–F160W* gradients in term of metallicity gradients plus radial age gradients, with a younger stellar population towards the outskirts, due to the fact that star formation may have continued for a longer time in the outer regions of the galaxies (e.g. Tacchella et al. 2016). Our interpretation, as resulting from the analysis shown in Section 6.1, does not exclude a contribution of age gradient, specially to justify the most extreme $U - R$ gradients. However, it seems that the major role is played by the metallicity, as also seen in the local ellipticals. Anyway, the similarities in the colour gradients, independently found in the range $1 < z < 1.4$, suggest that cluster galaxies have experienced similar evolutionary processes in their past.

Colour gradients in cluster and field galaxies were also derived by Allen et al. (2015) at $z \sim 2$. The authors selected a mass-complete sample of 59 cluster galaxies at $z = 2.095$ and 478 field galaxies at $2 < z < 2.2$ with $\log(M_*/\mathrm{M}_\odot) \geq 9$. Galaxies in both samples are separated in quiescent and star-forming galaxies using the UVJ rest-frame colour–colour diagram (e.g. Williams et al. 2009, 2010; Wuyts et al. 2009; Wild et al. 2014). The authors stacked galaxy images both for cluster and field sample to measure average F814W–F160W ($(U - V)_{\mathrm{restframe}}$) radial colour profiles as a function of the

mass. They found no colour gradients either in field or in cluster quiescent galaxies. Unlike Allen et al. (2015), we find that most of our cluster elliptical galaxies present significative colour gradients. This suggests that from $z \sim 2$ to $z \sim 1.4$ cluster galaxies may have experienced some evolutionary processes, which have increased the amplitude of their colour gradients producing a significant radial variation of their stellar population properties.

We also compared our results with Chan et al. (2016), who studied a sample of 36 passive galaxies selected in the same cluster considered in our analysis, XMMU J2235–2557. They base their analysis only on the rest-frame $U - R$ gradient. Since we selected elliptical galaxies, only 12 galaxies are in common (for a detailed comparison see Appendix C). They derived $U - R$ colour gradients from the observed colour profile up to $3.5a_e$ (a_e is the major axis), whereas we derived colour gradients from the intrinsic colour profile and up to 2 effective radii. For the 12 galaxies in common we found a median value of the *F850LP–F160W* colour gradients of -0.3 mag, consistent with the median value (~ -0.4 mag) found by Chan et al. (2016). Anyway, for one (595) out of the 12 galaxies in common, they derive a positive gradient, whereas we measured a negative gradient. We will discuss the possible origin of this difference in Appendix C. They explain the evolution of the colour gradients from $z = 1.39$ to $z \sim 0$ through the presence of an age gradient ($\nabla_{age} \sim -0.33$) besides a metallicity gradient ($\nabla_Z \sim -0.2$). In agreement with Chan et al. (2016), we also found that the rest-frame $U - R$ gradients can be produced by the radial variation of age and metallicity. However, our analysis shows that relevant information is stored in the $UV - U$ gradient. As pointed out in Section 6, the rest-frame ultraviolet gradient is a very important key to correctly interpret the properties of the stellar population of galaxies and to constrain their history of mass accretion.

8.2 Cluster versus field

For field elliptical galaxies we first compare our results with those of Gargiulo et al. (2012). The authors have derived the *F850LP–F160W* colour gradients for 11 morphologically selected ellipticals at $1 < z < 1.9$ in the GOODS-South region. Structural parameters and gradients have been derived as in this work. They found significant negative $\nabla(F850LP - F160W)$ within $1R_e$ in $\sim$70 per cent of the galaxies, a fraction that rises up to 100 per cent when $R > R_e$ is considered, as for our sample. By considering the eight galaxies of their sample in redshift range $1.2 < z < 1.6$, to avoid evolutionary effects, we found that our cluster ellipticals show $U - R$ (*F850LP–F160W*) colour gradients of amplitudes ($<\nabla> = -0.3 \pm 0.2$ mag) comparable to those of field ellipticals ($<\nabla> = -0.5 \pm 0.3$ mag).

In a previous work (Gargiulo et al. 2011), the authors studied the *F606W–F850LP* ($(UV - U)_{restframe}$) for 20 early-type galaxies at $0.9 < z < 1.92$, only four of these in common with the other study. They detected significant radial $UV - U$ colour variation in 10 out of the 20 galaxies, five showing negative gradients and the remaining ones showing positive gradients. Hence, contrary to cluster galaxies, field galaxies at similar redshift ($1.2 < z < 1.6$) seem to present both positive and negative ultraviolet gradients. Their analysis shows that, for a minor fraction, the observed gradients can be well reproduced by a pure radial age variation or by a pure metallicity variation while, for the remaining galaxies, more than one property of the stellar population must simultaneously vary to account for the observed gradients. Hence, although the small statistic, this comparison may suggest that the environment could have already influenced the evolution of elliptical galaxies.

Finally, we compared our results with those of Guo et al. (2011), who studied the *F850LP–F160W* colour gradients for six massive ($M_* > 10^{10} M_\odot$) early-type galaxies selected at redshift $1.3 < z < 2.5$ for their early-type morphology and low SSFRs ($SSFR = SFR/M_* \leq 10^{-11} yr^{-1}$). By deriving colour gradients in concentric annular apertures up to $\approx 10\,R_e$, they found, concordantly with our results, that the inner regions are redder than the outskirts. A radial variation of a single stellar parameter (age/metallicity) does not account for the observed colour gradients. The authors found a correlation between the dust and the observed colour gradients: the redder the inner region the higher the central dust obscuration. Like Guo et al. (2011) we also found that the radial variation of a single stellar parameter cannot account for the observed colour gradients, but we do not confirm the correlation between the observed colour gradients and the dust content. However, their analysis considered only the $\sim(U - R)$ colour gradients.

9 SUMMARY AND CONCLUSIONS

In this paper, we investigated the radial variation of the stellar population properties in a sample of 17 ellipticals belonging to the cluster XMMU J2235.3–2557 at z=1.39. The galaxies have been selected on the basis of their elliptical morphology that we assigned through a visual inspection of their ACS-*F850LP* images.

Making use of the ACS images in the *F775W* and *F850LP* bands and of the WFC3 images in the *F160W* band, we derived their rest-frame $UV - U$ (*F775W–F850LP*) and $U - R$ (*F850LP–F160W*) colour gradients using three different methods: the logarithmic slope of the deconvoluted colour profiles, the ratio of the effective radii as measured in the three different filters and through the observed colour profiles. While the first two methods are both dependent on the best-fitting procedure of the colour profiles, the third method does not involve any fit of the light profiles of the galaxies.

Our main results are as follows.

(i) The $UV - U$ colour gradients are systematically positive ($\sim$80 per cent) or null ($\sim$20 per cent), never negative. On the contrary, the $U - R$ colour gradients are systematically negative ($\sim$70 per cent) or null ($\sim$30 per cent), never positive. The mean value of the $UV - U$ gradients is 0.4 ± 0.2 mag, slightly larger than the mean value of the $U - R$ gradients (-0.3 ± 0.2 mag) in spite of the much narrower wavelength interval of the $UV - U$ gradient.

(ii) The results do not depend on the method used to derive the colour gradients.

We then investigated the origin of the observed colour gradients using BC03 stellar population models. Our results are the following:

(i) The opposite slopes of the observed colour gradients cannot be accounted for by the radial variation of a single parameter (age, metallicity or dust). A variation of these parameters produces ever gradients with concordant slopes. In particular, a radial decrease in metallicity/age/dust from the central to external regions produces negative $UV - U$ and $U - R$ colour gradients and vice versa.

(ii) The amplitude of the $U - R$ colour variations observed in our galaxies can be easily accounted for by an age or by a metallicity radial decrease. On the contrary, we are not able to reproduce the amplitude of the observed $UV - U$ colour gradients through age or metallicity variation.

The $UV - U$ colour gradients we detected show the presence of an UV excess towards the centre of the galaxies with respect to the outer regions and call into question other mechanisms able to efficiently produce UV and U emission in the galaxy central

regions. We considered these possible UV and U emission sources: star formation, the presence of a QSO, stars in the He-burning phase and He-rich stars.

We found that a weak star formation ($\sim$1 $M_\odot$ yr^{-1}) superimposed to an old stellar component towards the centre and to a negative metallicity gradient can reverse the $UV - U$ colour gradient simultaneously reproducing the amplitude and the opposite slopes of the $UV - U$ and $U - R$ colour gradients. The required central star-forming component should not exceed $\sim$0.5 per cent in stellar mass not to affect the $U - R$ gradient. In this way, we are able to reproduce both the colour gradients for 10 out of the 13 ellipticals ($\sim$ 85 per cent of the sample), for which both colour gradients are available. However, if this is the cause of the bluer $UV - U$ colour towards the centre, this implies that all the galaxies are currently experiencing SF in the centre since all of them have positive or null $UV - U$ gradients. This in turn implies that the star formation should be steady and protracted over a long time (>1 Gyr) and not episodic and/or erratic.

We found that the presence of a QSO could contribute to the UV excess, but it cannot justify alone the observed $UV - U$ gradient unless flattening the $U - R$ gradient and significantly altering the integrated colours of the galaxies.

We found that it is highly unlikely that the observed UV excess we observed is due to the abundance of He-burning stars towards the centre of the galaxies. Indeed, at z=1.39, only stars with $1.2\ M_\odot \lesssim M \lesssim 1.5\ M_\odot$ would be in the He-burning phase. Since the He-burning time-scale for stars in this range of mass is very short ($\sim 10^8$ yr), it would require a very strong fine-tuning in term of synchronism to justify the UV excess observed in almost all the galaxies of our sample.

Finally, we also found that an excess of He-rich stars towards the centre of the galaxies would qualitatively explain the positive $UV - U$ gradients and the negative metallicity $U - R$ gradients as well, without introducing any fine-tuning. It is worth noting that the presence of a population of He-rich stars in the centre of elliptical galaxies would be in agreement with the NUV-UV colour gradients observed in some ellipticals in the local universe. Unfortunately, we cannot test this scenario since no suited models are available.

ACKNOWLEDGEMENTS

FC wishes to thank Paola Severgnini for the helpful comments and suggestions for the QSO discussion. We thank the anonymous referee for the useful and constructive comments. This work is based on observations collected at the European Organization for Astronomical Research in the Southern hemisphere under ESO programmes 60.A-9284 and 079.A-0758. This work is also based on observations made with the NASA/ESA *HST*, obtained from the data archive (ID 10698, 10496 and 12051) at the Space Telescope Science Institute, which is operated by the Association of Universities for Research in Astronomy, and with the *Spitzer Space Telescope*, which is operated by the Jet Propulsion Laboratory, California Institute of Technology under a contract with NASA.

REFERENCES

Abadi M. G., Moore B., Bower R. G., 1999, MNRAS, 308, 947
Abel T., Bryan G. L., Norman M. L., 2000, ApJ, 540, 39
Abel T., Bryan G. L., Norman M. L., 2002, Science, 295, 93
Allen R. J. et al., 2015, ApJ, 806, 3
Bertin E., Arnouts S., 1996, A&AS, 117, 393
Blumenthal G. R., Faber S. M., Primack J. R., Rees M. J., 1984, Nature, 311, 517
Bolzonella M., Miralles J.-M., Pelló R., 2000, A&A, 363, 476
Bromm V., Coppi P. S., Larson R. B., 1999, ApJ, 527, L5
Bromm V., Coppi P. S., Larson R. B., 2002, ApJ, 564, 23
Brown T. M., Ferguson H. C., Davidsen A. F., Dorman B., 1997, ApJ, 482, 685
Bruzual G., Charlot S., 2003, MNRAS, 344, 1000 (BC03)
Calzetti D., Armus L., Bohlin R. C., Kinney A. L., Koornneef J., Storchi-Bergmann T., 2000, ApJ, 533, 682
Carter D., Pass S., Kennedy J., Karick A. M., Smith R. J., 2011, MNRAS, 414, 3410
Cattaneo A., Dekel A., Faber S. M., Guiderdoni B., 2008, MNRAS, 389, 567
Chabrier G., 2003, PASP, 115, 763
Chan J. C. C. et al., 2016, MNRAS, 458, 3181
Chantereau W., Charbonnel C., Decressin T., 2015, A&A, 578, A117
Chiosi C., Carraro G., 2002, MNRAS, 335, 335
Cimatti A. et al., 2008, A&A, 482, 21
Clemens M. S., Bressan A., Nikolic B., Rampazzo R., 2009, MNRAS, 392, L35
Code A. D., Welch G. A., 1979, ApJ, 228, 95
Cowie L. L., Songaila A., 1977, Nature, 266, 501
De Lucia G., Springel V., White S. D. M., Croton D., Kauffmann G., 2006, MNRAS, 366, 499
De Propris R., Bremer M. N., Phillipps S., 2015, MNRAS, 450, 1268
De Propris R., Bremer M. N., Phillipps S., 2016, MNRAS, 461, 4517
Dekel A., Birnboim Y., 2006, MNRAS, 368, 2
Dorman B., O'Connell R. W., Rood R. T., 1995, ApJ, 442, 105
Drake N., Merrifield M. R., Sakelliou I., Pinkney J. C., 2000, MNRAS, 314, 768
Dressler A., Gunn J. E., 1983, ApJ, 270, 7
Eggen O. J., Lynden-Bell D., Sandage A. R., 1962, ApJ, 136, 748
Ferrara A., Pettini M., Shchekinov Y., 2000, MNRAS, 319, 539
Francis P. J., Hewett P. C., Foltz C. B., Chaffee F. H., Weymann R. J., Morris S. L., 1991, ApJ, 373, 465
Fujita Y., 1998, ApJ, 509, 587
Gargiulo A., Saracco P., Longhetti M., 2011, MNRAS, 412, 1804
Gargiulo A., Saracco P., Longhetti M., La Barbera F., Tamburri S., 2012, MNRAS, 425, 2698
Gnedin N. Y., Ostriker J. P., 1997, ApJ, 486, 581
Greggio L., Renzini A., 1990, ApJ, 364, 35
Gunn J. E., Gott III J. R., 1972, ApJ, 176, 1
Guo Y. et al., 2011, ApJ, 735, 18
Han Z., 2008, A&A, 484, L31
Han Z., Podsiadlowski P., Maxted P. F. L., Marsh T. R., Ivanova N., 2002, MNRAS, 336, 449
Han Z., Podsiadlowski P., Maxted P. F. L., Marsh T. R., 2003, MNRAS, 341, 669
Han Z., Podsiadlowski P., Lynas-Gray A. E., 2007, MNRAS, 380, 1098
Iben Jr, I.1967, ARA&A, 5, 571
Kauffmann G., 1996, MNRAS, 281, 487
Kaviraj S. et al., 2008, MNRAS, 388, 67
Kennicutt Jr, R. C.1998, ARA&A, 36, 189
Khochfar S., Silk J., 2006, ApJ, 648, L21
Kobayashi C., 2004, MNRAS, 347, 740
Koekemoer A. M., Fruchter A. S., Hook R. N., Hack W., 2003, in Arribas S., Koekemoer A., Whitmore B., eds, *HST* Calibration Workshop: Hubble after the Installation of the ACS and the NICMOS Cooling System. p. 337
Komatsu E. et al., 2009, ApJS, 180, 330
La Barbera F., de Carvalho R. R., 2009, ApJ, 699, L76
La Barbera F., Busarello G., Massarotti M., Merluzzi P., Mercurio A., 2003, A&A, 409, 21
La Barbera F., de Carvalho R. R., Gal R. R., Busarello G., Merluzzi P., Capaccioli M., Djorgovski S. G., 2005, ApJ, 626, L19
Lardo C., Pancino E., Mucciarelli A., Milone A. P., 2012, A&A, 548, A107
Larson R. B., Tinsley B. M., Caldwell C. N., 1980, ApJ, 237, 692

Lidman C. et al., 2008, A&A, 489, 981
Lidman C. et al., 2013, MNRAS, 433, 825
Lonoce I., Longhetti M., Saracco P., Gargiulo A., Tamburri S., 2014, MNRAS, 444, 2048
Madau P., Ferrara A., Rees M. J., 2001, ApJ, 555, 92
Merlin E., Chiosi C., 2006, A&A, 457, 437
Merlin E., Chiosi C., Piovan L., Grassi T., Buonomo U., Barbera F. L., 2012, MNRAS, 427, 1530
Merritt D., 1983, ApJ, 264, 24
Merritt D., 1984, ApJ, 276, 26
Mihos J. C., 1995, ApJ, 438, L75
Mullis C. R., Rosati P., Lamer G., Böhringer H., Schwope A., Schuecker P., Fassbender R., 2005, ApJ, 623, L85
Naab T., Johansson P. H., Ostriker J. P., Efstathiou G., 2007, ApJ, 658, 710
Nakamura F., Umemura M., 2001, ApJ, 548, 19
Nonino M. et al., 2009, ApJS, 183, 244
O'Connell R. W., 1999, ARA&A, 37, 603
O'Connell R. W. et al., 1992, ApJ, 395, L45
Oser L., Ostriker J. P., Naab T., Johansson P. H., Burkert A., 2010, ApJ, 725, 2312
Ostriker J. P., Gnedin N. Y., 1996, ApJ, 472, L63
Peacock1999, Nature, 399, 322
Peletier R. F., Valentijn E. A., Jameson R. F., 1990, A&A, 233, 62
Peng C. Y., Ho L. C., Impey C. D., Rix H.-W., 2002, AJ, 124, 266
Peng Y., Maiolino R., Cochrane R., 2015, Nature, 521, 192
Piotto G. et al., 2005, ApJ, 621, 777
Pipino A., Matteucci F., 2004, MNRAS, 347, 968
Ponder J. M. et al., 1998, AJ, 116, 2297
Rawle T. D., Smith R. J., Lucey J. R., 2010, MNRAS, 401, 852
Rosati P. et al., 2009, A&A, 508, 583
Saglia R. P., Maraston C., Greggio L., Bender R., Ziegler B., 2000, A&A, 360, 911
Saracco P. et al., 2014, A&A, 567, A94
Saracco P., Gargiulo A., Ciocca F., Marchesini D., 2017, A&A, 597, A122
Shields G. A., 1978, Nature, 272, 706
Sommer-Larsen J., Toft S., 2010, ApJ, 721, 1755
Tacchella S., Dekel A., Carollo C. M., Ceverino D., DeGraf C., Lapiner S., Mandelker N., Primack J. R., 2016, MNRAS, 458, 242
Tamura N., Ohta K., 2000, AJ, 120, 533
Tortora C., Napolitano N. R., Cardone V. F., Capaccioli M., Jetzer P., Molinaro R., 2010, MNRAS, 407, 144
Wagner C. R. et al., 2015, ApJ, 800, 107
Wild V. et al., 2014, MNRAS, 440, 1880
Williams R. J., Quadri R. F., Franx M., van Dokkum P., Labbé I., 2009, ApJ, 691, 1879
Williams R. J., Quadri R. F., Franx M., van Dokkum P., Toft S., Kriek M., Labbé I., 2010, ApJ, 713, 738
Wu H., Shao Z., Mo H. J., Xia X., Deng Z., 2005, ApJ, 622, 244
Wuyts S. et al., 2009, ApJ, 700, 799
Yi S. K., Lee J., Sheen Y.-K., Jeong H., Suh H., Oh K., 2011, ApJS, 195, 22

APPENDIX A: SURFACE BRIGHTNESS PROFILES

As described in Section 3.2 we have derived the surface brightness profiles by fitting a Sérsic law (equation 1).

The fitting was performed over a box of 7.5×7.5 arcsec^2 centred on the centroid of each galaxy derived by SExtractor. To fix the fitting box and the convolution box sizes ($7.5\times$ 7.5 arcsec^2), we repeatedly fitted the surface brightness profiles by increasing the boxes size until the best-fitting parameters values converged. We masked sources distant from our targets using the segmentation image generated by SExtractor, while we fitted simultaneously the sources close to the target galaxies in order to avoid the overlapping of the light profiles. For few galaxies (two in the *F775W* and in the *F850LP* images, two in the *F160W* band and one in all the three images), the fitting procedure was not able to converge. Hence, we re-performed the fit in that band several times for different fixed values of n and for each of them we obtained a set of structural parameters as output. We chose as best solution the set of structural parameters for which the χ^2 was the lowest and the residual map was lacking of residual structures. The structural parameters obtained through the fit are shown in Table A1. The goodness of the fits is shown in Fig. A1, where the observed surface brightness profiles of the galaxies are compared with the best-fitting models generated by Galfit. The surface brightness has been measured within circular annuli centred on each galaxy and it is plotted in blue (*F775W*), red (*F850LP*) and green (*F160W*). The error bars are obtained by propagating the errors on fluxes measured within the concentric annuli. In all the cases, a range of at least five magnitudes in surface brightness has been covered in the profiles of the galaxies which

Table A1. For each galaxy of the sample we report the ID number, the Sérsic index n, the total magnitude and the effective radius R_e [kpc] as derived from the fitting of the surface brightness profile in the *F775W*, *F850LP* and *F160W* images, respectively. For the *F850LP* band we also report the axial ratio $(b/a)_{850}$.

ID	n_{775}	$i^{\rm fit}_{775}$ [mag]	R_e^{775} [kpc]	n_{850}	$z^{\rm fit}_{850}$ [mag]	$R_e^{\rm F850}$ [kpc]	$(b/a)_{850}$	n_{160}	$H^{\rm fit}_{160}$ [mag]	$R_e^{\rm F160}$ [kpc]
358	6.0±0.4	24.5±0.2	1.1±0.1	6.0±0.4	23.5±0.1	1.5±0.2	0.6±0.1	–	–	–
595	5.7±0.3	22.9±0.1	2.1±0.3	5.6±0.3	21.6±0.1	3.5±0.5	0.9±0.1	4.5±0.1	19.2±0.1	2.5±0.1
684	6.0±0.4	24.1±0.2	0.6±0.1	6.0±0.4	22.9±0.1	1.4±0.2	0.6±0.1	4.0±0.1	20.9±0.1	0.8±0.1
692	4.0±0.2	24.7±0.2	1.3±0.1	4.1±0.2	23.5±0.2	1.5±0.2	0.7±0.1	3.0±0.1	21.0±0.1	0.9±0.1
837	6.0±0.2	23.3±0.1	4.3±0.6	6.0±0.4	21.9±0.1	7.8±1.1	0.7±0.1	6.0±0.2	19.4±0.1	5.2±0.2
1284	4.3±0.3	23.4±0.1	2.0±0.3	4.3±0.2	22.3±0.1	2.4±0.3	0.9±0.1	4.0±0.1	20.0±0.1	1.7±0.1
1539	4.8±0.3	23.7±0.2	1.1±0.1	3.5±0.2	22.7±0.1	1.5±0.2	0.6±0.1	–	–	–
1740	3.3±0.2	21.8±0.1	13.3±2.0	3.3±0.2	20.8±0.1	12.8±1.9	0.6±0.1	4.6±0.1	17.8±0.1	20.7±0.9
1747	4.3±0.2	24.7±0.2	0.7±0.1	4.8±0.3	23.3±0.1	1.7±0.2	0.6±0.1	4.0±0.2	21.1±0.1	0.9±0.1
1758	2.9±0.2	23.9±0.2	1.9±0.2	2.9±0.2	22.6±0.1	2.5±0.3	0.8±0.1	2.90±0.04	20.3±0.1	1.5±0.1
1782	2.6±0.2	23.5±0.1	1.6±0.1	3.6±0.2	22.5±0.1	3.4±0.5	0.6±0.1	3.11±0.04	19.5±0.1	2.2±0.1
1790	4.4±0.3	23.1±0.1	1.9±0.2	4.4±0.3	21.9±0.1	2.4±0.3	0.6±0.1	4.1±0.1	19.3±0.1	2.3±0.1
2054	5.0±0.3	23.2±0.1	2.7±0.4	4.4±0.3	21.9±0.1	4.2±0.6	0.7±0.1	5.0±0.1	19.5±0.1	3.7±0.2
2147	5.4±0.3	23.5±0.1	3.6±0.5	5.3±0.3	22.2±0.1	5.3±0.8	0.7±0.1	4.0±0.1	20.0±0.1	2.3±0.1
2166	3.6±0.2	22.6±0.1	1.2±0.1	3.0±0.2	21.5±0.1	1.4±0.1	0.6±0.1	–	–	–
2429	2.1±0.4	24.3±0.2	0.6±0.1	2.1±0.2	23.0±0.1	0.9±0.1	0.6±0.1	2.1±0.1	21.0±0.1	0.9±0.1
2809	4.8±0.3	23.3±0.1	1.2±0.1	3.2±0.2	22.7±0.1	1.4±0.2	0.6±0.1	–	–	–

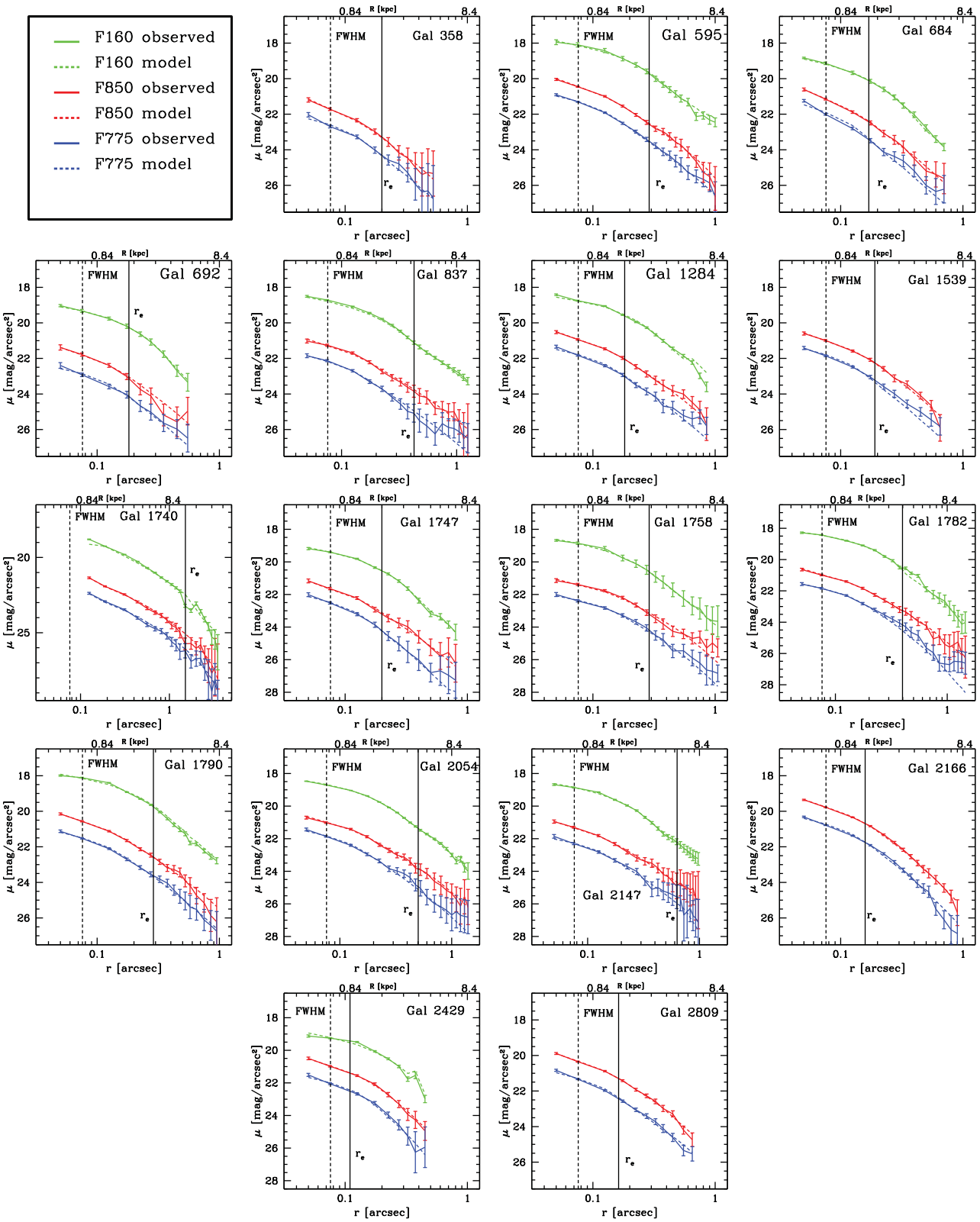

Figure A1. Comparison between the observed brightness profiles (solid lines) and the models obtained with GALFIT (dashed lines) in the three *HST* bands for the 17 ellipticals of the sample. The surface brightness profiles in the *F775W*, *F850LP* and *F160W* bands are plotted in blue, red and green, respectively. The surface brightness has been measured within circular annuli centred on each galaxy. The dashed black vertical line represents the radius of the FWHM of the PSF (∼0.06 arcsec), while the solid black vertical line corresponds to the effective radius of the galaxy as derived in *F850LP* band.

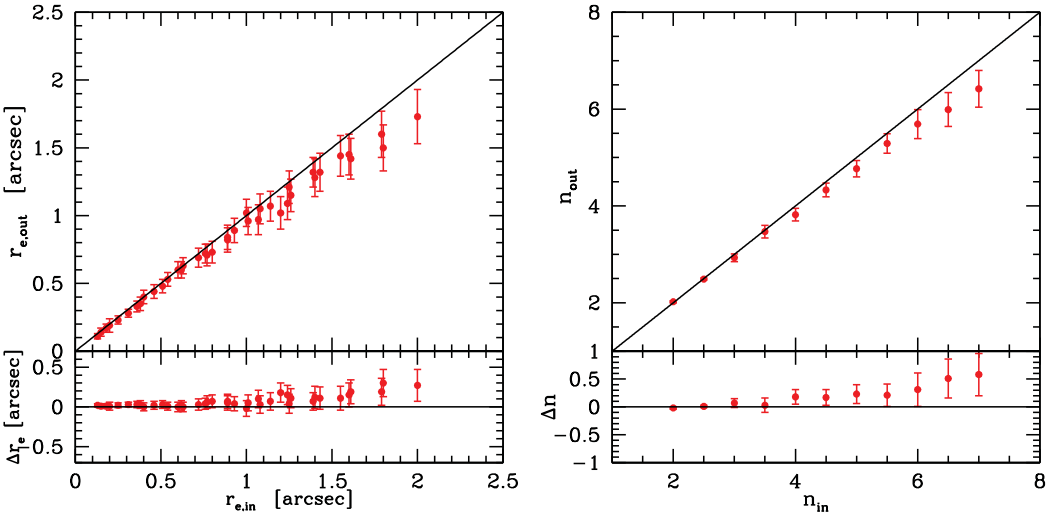

Figure A2. Comparison between the effective radius ($r_{\rm e,\,in}$) and the index of concentration ($n_{\rm in}$) of the simulated galaxies and the effective radius ($r_{\rm e,\,out}$) and the index of concentration ($n_{\rm out}$) obtained through the fitting with the Sérsic profile (upper left-hand and right-hand panels, respectively). The differences $\Delta r_{\rm e} = r_{\rm e,\,in} - r_{\rm e,\,out}$ and $\Delta n = n_{\rm in} - n_{\rm out}$ are plotted as a function of the input parameters (lower left-hand and right-hand panels, respectively).

extend up to at least $\sim 2r_{\rm e}$ for the largest galaxies. For the galaxies with a small $r_{\rm e}$ ($\sim 0.1 - 0.2$ arcsec) the observed brightness profiles extend up to $\sim 3 - 4r_{\rm e}$.

A1 Simulations

In order to test for the absence of possible systematics introduced by the fitting algorithm and to derive reliable statistical errors for the structural parameters, we performed the same fitting procedure used for real galaxies to a set of simulated galaxies. In particular, to test for the absence of systematics, we generated with GALFIT a set of ∼8000 galaxies described by a Sérsic profile with effective radius $r_{\rm e}$, index of concentration n and magnitude m assigned in the ranges $0.1 < r_{\rm e} < 2$ arcsec, $2 < n < 7$ and $20 < m < 24.5$ mag. The simulated galaxies have been convolved with the ACS-*F850LP* PSF and embedded in the real background, constructed by cutting different portions devoid of sources from the real image. For each structural parameters we verified how the output values vary as a function of the input values, keeping fixed the other two structural parameters. In Fig. A2 we show the output values $r_{\rm e,\,out}$ and $n_{\rm out}$ versus the input values $r_{\rm e,\,in}$ and $n_{\rm in}$ (left panel and right panel, respectively). For $n < 6$ and $r_{\rm e} < 1$ arcsec GALFIT recovers exactly the input values. For $n > 6$ and $r_{\rm e} > 1$ arcsec the output $r_{\rm e}$ and n are, on average, underestimated of 8 per cent and 15 per cent, respectively. These underestimates are negligible compared to the statistical errors and they are possibly due to the fact that, for galaxies having larger surface brightness profile tails, we miss a fraction of the profile since it is dominated by the background. This would drop the brightness profile and favour lower values of n in the fitting. Since the galaxies of our sample have $r_{\rm e} < 1$ arcsec and $n < 6$, we did not apply any correction to the values of the structural parameters obtained by the fitting.

We also verified for each structural parameter whether a dependence of the output values on the input values of the other structural parameters was present (e.g. output $r_{\rm e}$ versus input n and m) and no systematics were found.

To derive the statistical uncertainties of each parameter, that is how the background RMS affects the estimates of the structural parameters, we have considered a subsample of the simulated galaxies and we embedded each of them in 10 different real backgrounds. Then, for each galaxy, we have run GALFIT to derive the best-fitting parameters for the 10 different backgrounds. The standard deviation of the mean has been adopted as indicator of the statistical fluctuations.

APPENDIX B: COLOUR GRADIENTS

In this section, we show the colour gradients derived for the whole sample. In particular, in Fig. B1 we show the *F775W–F850LP* colour gradients and in Fig. B2 we show the F850LP–F160W colour gradients. In all the figures, the variation Δcolour on the y-axis is 1 mag for the *F775W–F850LP* colour and it is 0.9 mag for the *F850LP–F160W* colour.

APPENDIX C: COMPARISON WITH CHAN ET AL. 2016

In this Appendix we compare our sample with the one by Chan et al. (2016). The criteria adopted to select the two samples are different. In our analysis, we adopted the ACS-*F850LP* image for the object detection with SEXTRACTOR and as reference in the morphological and structural analysis, given its high resolution ($\simeq 0.11$ arcsec) and small pixel scale (0.05 arcsec pixel^{-1}) when compared to the WFC3-*F160W* image (FWHM$\simeq 0.22$ arcsec; 0.123 arcsec pixel^{-1}). Furthermore, we selected galaxies (see Section 2.2) at magnitudes *F850LP*<24, where the sample is 100 per cent complete, according to their F775-F850 colour and on the basis of their elliptical morphology. Chan et al., instead, used the WFC3-*F160W* image for object detection with SEXTRACTOR and as reference, and selected 36 passive galaxies according to their red sequence colour from the colour–magnitude diagram ((*F850LP–F160W*) versus *F160W*). They also applied a magnitude cut of $H_{160} < 22.5$ mag, which corresponds to a completeness of ∼ 95 per cent.

We verified that 12 out to the 17 ellipticals of our sample are in common with Chan et al. Four of our galaxies (358, 1539, 2166, 2809) are not included in their sample since they fall outside the smaller field covered by the WFC3 (5 arcmin^2 instead of 11 arcmin^2 of the ACS). Moreover, also galaxy 1747 is not included in their

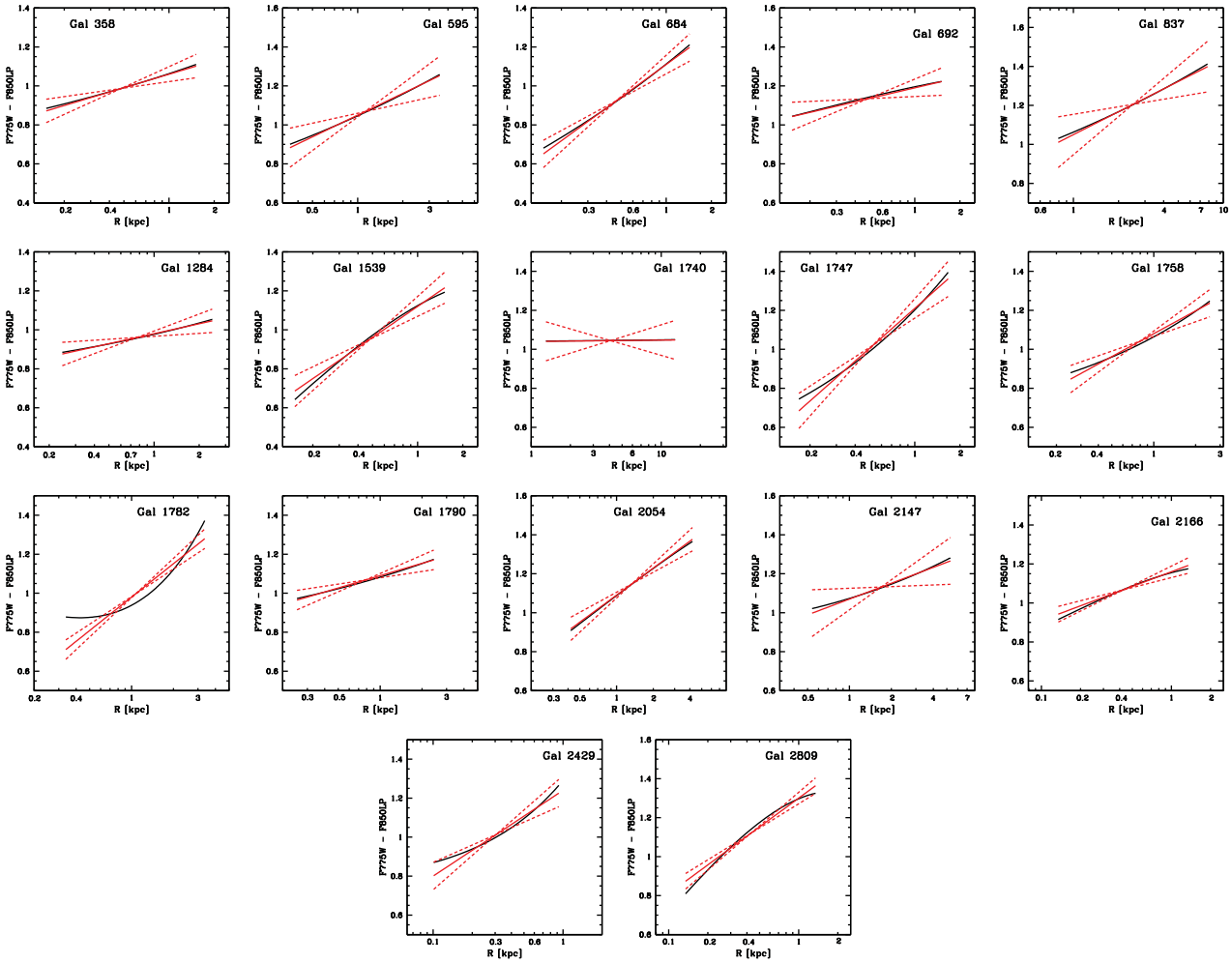

Figure B1. The *F775W–F850LP* colour gradients for the galaxies of our sample. Black lines represent the deconvolved colour profiles between $0.1R_e$ and $1R_e$ and the red solid lines are the best-fitted lines to the models. The red dashed lines set 1σ errors. For all the galaxies in the y-axis Δcolour = 1 mag. The transformation to obtain the $UV - U$ colours is: $UV - U = (F775W–F850LP) - 0.8$ mag.

sample. We verified that its *F850LP–F160W* colour would be consistent with their colour selection. However, its magnitude (*F160W* = 22.6 mag, in our sample) seems to be slightly fainter than the cut they applied. This could be the reason why it is not included in their sample. In Fig. C1 we show the comparison between the *F850LP–F160W* colour of the 12 galaxies in common, after having transformed their colours from AB to Vega magnitudes. We find that our *F850LP–F160W* colours (mean value 2.66±0.25 mag) are consistent with those derived by Chan et al. (mean value 2.62±0.19 mag).

The structural parameters of the galaxies have been derived, in both the analyses, using the software GALFIT. Since the authors do not report the structural parameters derived in the *F775W* and *F850LP* bands, we only compare the structural parameters derived in the *F160W* band. The results are shown in Fig. C2, where in the left panel we compare the Sérsic indices n and in the right panel we compare the effective radii R_e. We found a good agreement between our and their estimate of the effective radii ($<R_e/R_{e,\,Chan}> \simeq 1$) and also between the indices n. For three galaxies (595, 684 and 837) we obtained from the fit a smaller value of the index n ($< n - n_{Chan} > = -1.78$). However, we verified through the simulations that an eventual underestimate of n does not affect the estimate of the effective radii and, hence, of the colour gradients.

Finally, we compared the colour gradients. Chan et al. derived only the *F850LP–F160W* gradients from the observed colour profiles up to $3.5a_e$ (a_e=major axis), whereas we derived colour gradients through three different methods. Actually, we cannot properly compare their observed colour gradients with ours since they used elliptical apertures taking as reference the *F160W* image, whereas we measured the fluxes within circular aperture starting from *F850LP* image. The different apertures used can affect the estimates of the colour gradients, causing a scatter between the measured colour gradients. Most importantly, as discussed in Section 4, reliable estimates of colour gradients can be derived within the region where the S/N is high in all the bands considered. Fig. C4 shows the observed *F850LP–F160W* colour profiles up to $3.5a_e$ for galaxies 595 and 837, having effective radius of 3.5 and 7.8 kpc. Blue dashed line represents the effective radius of the galaxies as derived in the *F850LP* band, while red dashed line represents $3.5a_e$ as derived in the *F160W* band by Chan et al. We can see that for $R \gtrsim 1.5R_e$ the colour profiles of the two galaxies are dominated by the sky noise of the *F850LP* band, which introduces a spurious contribution in the estimate of the colour gradients. This is the reason why we derived the colour gradients at most up to $2R_e$. For $R \gtrsim 2R_e$, the estimates of the colour gradients are not reliable given the depth reached by the ACS image.

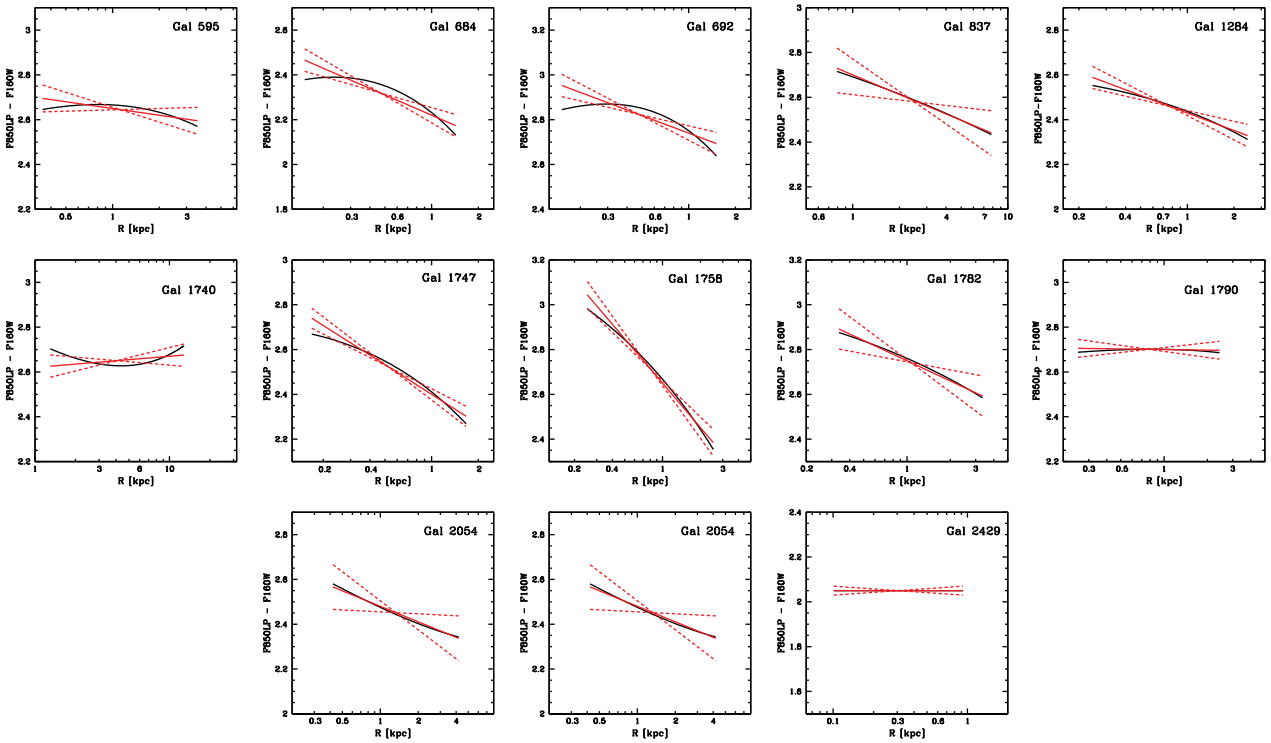

Figure B2. The *F850LP–F160W* colour gradients for the galaxies of our sample. Black lines represent the deconvolved colour profiles between $0.1R_e$ and $1R_e$ and the red solid lines are the best-fitted lines to the models. The red dashed lines set 1σ errors. For all the galaxies in the y-axis Δcolour = 0.9 mag. The transformation to obtain the $U - R$ colours is: $U - R = (F850LP - F160W) - 1.1$ mag.

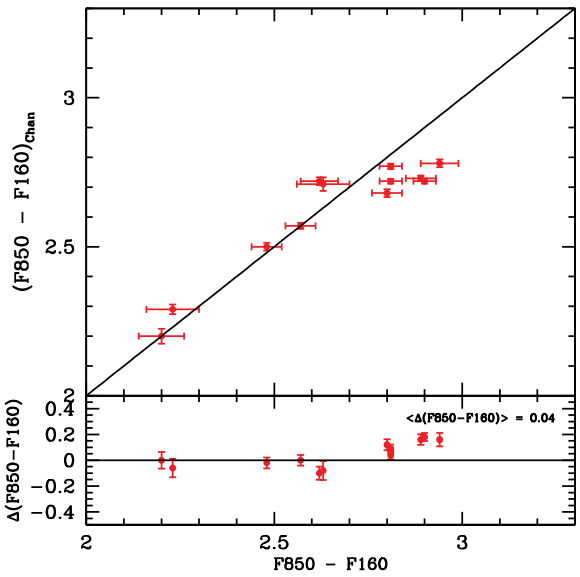

Figure C1. Comparison between the *F850LP–F160W* colours derived by Chan et al. (2016) and our *F850LP–F160W* colours for the 12 galaxies in common (upper panel). The difference $\Delta(F850 - F160) = (F850 - F160) - (F850 - F160)_{\rm Chan}$ is plotted as a function of our colours in the lower panel.

For two galaxies (595 and 684) Chan et al. derived a positive gradient, whereas we measured a negative gradient. Actually, as can be seen, one of the two (684 in our sample) is affected by a large uncertainty that makes it consistent even also with a negative gradient. In Fig. A1 we show the surface brightness profiles we derived for these galaxies in the three *HST* bands (third and fourth panels, respectively) and in Fig. B2 we show their colour profiles, which clearly present a negative trend. Since the authors do not report the effective radii in the *F850LP* band, to investigate why they derived positive gradients for these two galaxies, we compare our R_e in the *F850LP* with their R_e in the *F160W* image. The results are shown in Fig. C3 (right panel). We plotted in blue the effective radii of galaxies 595 and 684. These galaxies have a ratio $R_{e,\,850}/R_{e,\,160} > 1$, so they should present a negative colour gradient. Indeed, if this ratio is >1, the light is more concentrated in the reddest band considered and the colour gradient is negative; the opposite happens for values <1 of the ratio. Since, instead, Chan et al. measured a positive gradient for these two galaxies, it follows that the R_e they derived in the *F850LP* image is smaller than the R_e they derived in the F160W image. However, as shown in Fig. C3 (left panel), we find that systematically all the galaxies (with the exception of the central one) have the R_e in the *F160W* smaller than the R_e in the *F850LP*: $<R_{e,\,850}/R_{e,\,160}> \sim 1.5$. We are not able to explain the reason why the radii of 595 and 684 should deviate from this behaviour.

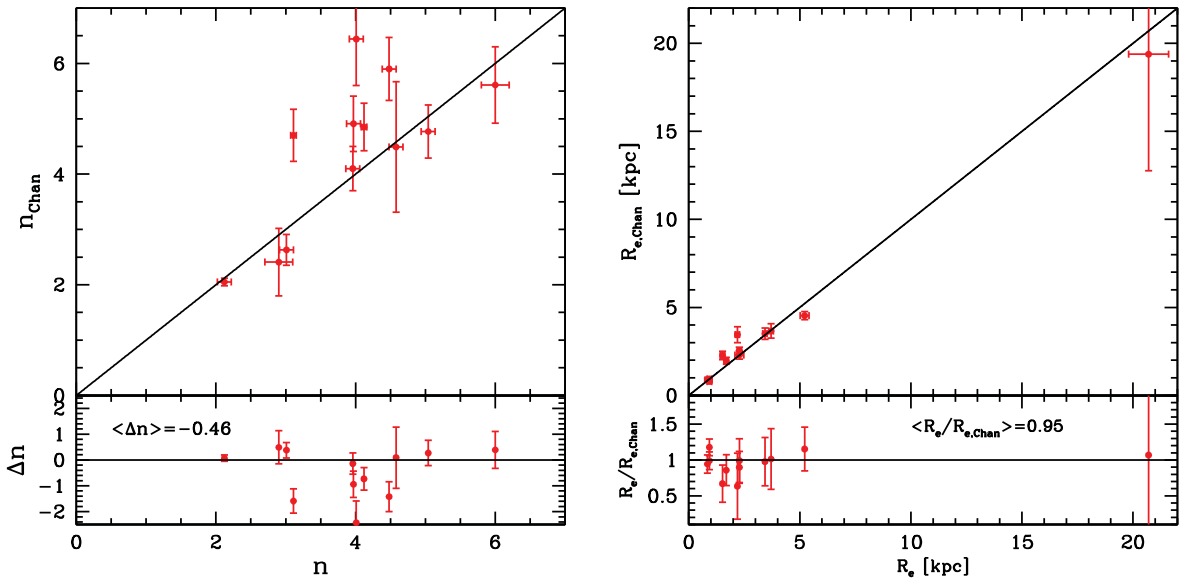

Figure C2. Left panel: comparison between the Sérsic indices n derived by Chan et al. (2016) and our Sérsic indices n for the 12 galaxies in common (upper panel). The difference $\Delta n = n - n_{\rm Chan}$ is plotted as a function of our n in the lower panel. Right panel: comparison between $R_{\rm e,\,Chan}$ derived by Chan et al. (2016) in the *F160W* band and our $R_{\rm e}$ for the 12 galaxies in common (upper panel). The ratio $R_{\rm e}/R_{\rm e,\,Chan}$ is plotted as a function of our $R_{\rm e}$ in the lower panel.

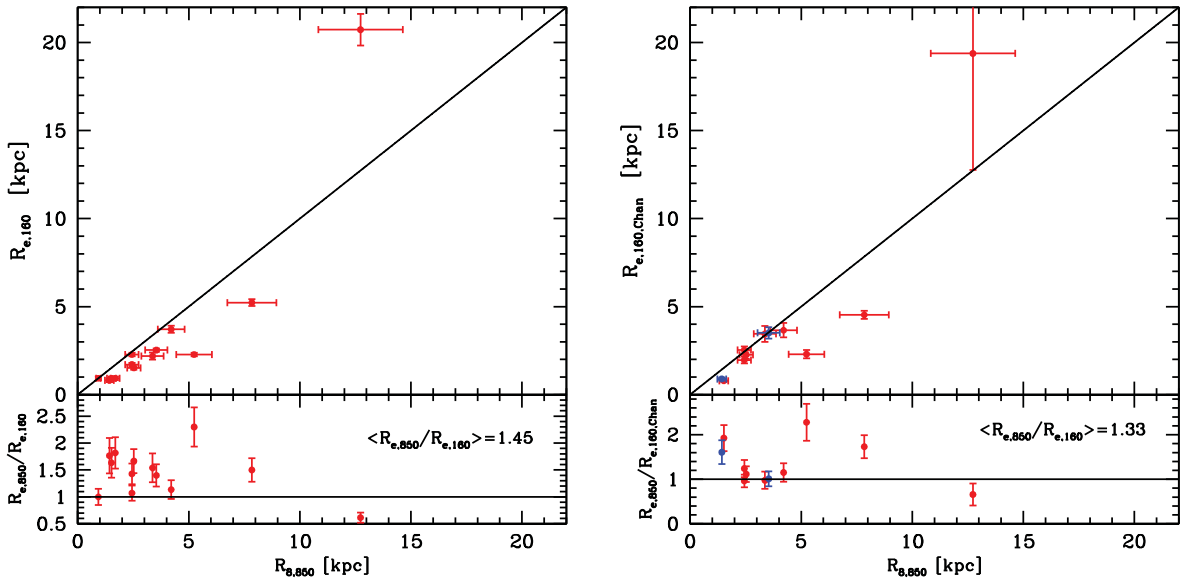

Figure C3. Left panel: comparison between $R_{\rm e}$ we derived in the *F850LP* image and the $R_{\rm e}$ derived in the *F160W* image (upper panel). The ratio $R_{\rm e,\,850}/R_{\rm e,\,160}$ is plotted as a function of $R_{\rm e,\,850}$ in the lower panel. Right panel: Comparison between $R_{\rm e}$ we derived in the *F850LP* image and the $R_{\rm e}$ Chan et al. derived in the *F160W* image (upper panel). In blue we plotted the two galaxies for which Chan et al. derived positive *F850LP–F160W* gradients. The ratio $R_{\rm e,\,850}/R_{\rm e,\,160,\,Chan}$ is plotted as a function of our $R_{\rm e,\,850}$ in the lower panel.

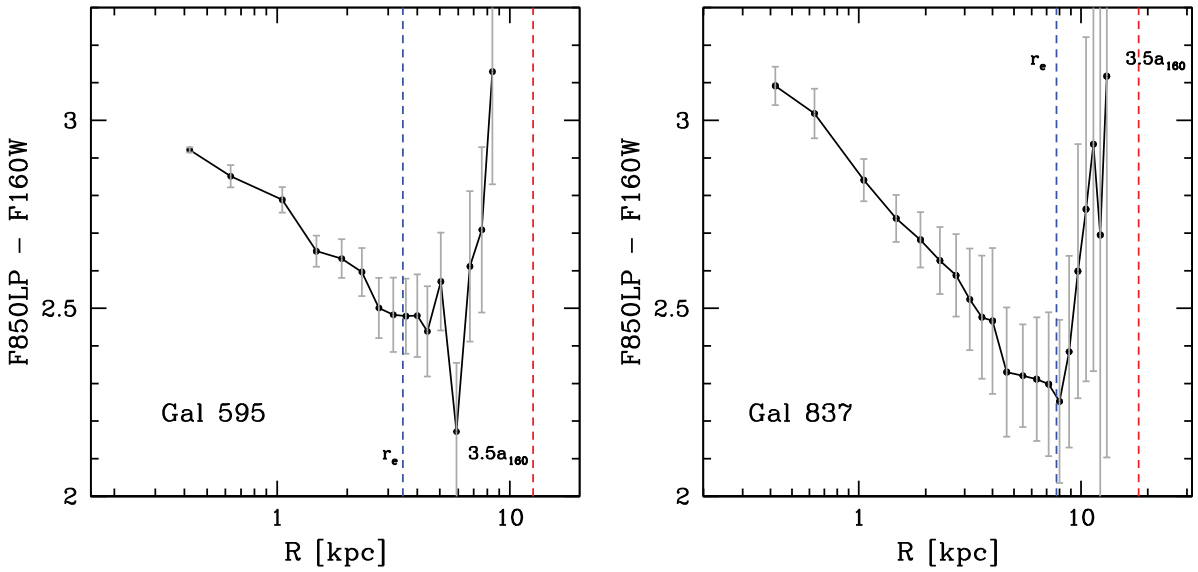

Figure C4. Observed *F850LP–F160W* colour profiles derived by measuring the fluxes within circular apertures centred on each galaxy. Blue dashed line represents the effective radius of the galaxies as we derived in the *F850LP* band, while red dashed line represents 3.5a (major axis) as derived in the F160W band by Chan et al.

This paper has been typeset from a TEX/LATEX file prepared by the author.